RECONSTRUCTION OF NEUTRAL-TRIGGERED RECOIL JETS IN $\sqrt{S} = 200$ GEV P+P COLLISIONS AT THE STAR EXPERIMENT

A Thesis

by

DEREK MURPHY ANDERSON

Submitted to the Graduate and Professional School of
Texas A&M University
in partial fulfillment of the requirements for the degree of

DOCTOR OF PHILOSOPHY

Chair of Committee,	Saskia Mioduszewski
Committee Members,	Carl Gagliardi
	Rainer Fries
	Charles M. Folden III
Head of Department,	Grigory Rogachev

May 2022

Major Subject: Physics

ABSTRACT

The collision of relativistic heavy-ion such as the AuAu-collisions studied at the Relativistic Heavy-Ion Collider produce a hot, dense medium with properties consistent with that of a state of matter in which quarks and gluons become deconfined, the Quark-Gluon Plasma. Collimated sprays of hadrons known as jets are produced by the fragmentation of quarks and gluons during the early stages of a heavy-ion collision, and offer a valuable probe of this medium. In particular, jets recoiling from energetic direct photons offer a "golden channel" through which we may study the complex dynamics of the medium produced in heavy-ion collisions. However, to understand the interplay between jets and the produced medium, a high-precision reference is needed in which no medium is produced.

Thus, this thesis presents a high precision measurement of the semi-inclusive yields of charged jets recoiling from energetic γ_{dir} and π^0 triggers in $\sqrt{s} = 200$ GeV pp-collisions recorded by the STAR detector during the 2009 running year. The recoil jets were reconstructed from charged particles using the anti-k_{T} algorithm with jet resolution parameters 0.2 and 0.5. A regularized unfolding scheme was employed to correct the measured per-trigger recoil jet yields for finite reconstruction efficiency and resolution. The energy resolution of the triggers was assessed using a simulation of the STAR electromagnetic calorimeter. The effect of a finite trigger resolution was applied to recoil jet spectra generated by PYTHIA 8.185 using a weighting scheme, and the corrected data were compared against the weighted recoil jet spectra from PYTHIA 8.185.

DEDICATION

For my parents and sister, and especially for my grandparents. This work would not be possible without their love and support.

ACKNOWLEDGMENTS

No scientific work is done alone, and I am immensely grateful for all the support I received throughout my time as a graduate student. Especially, I would like to thank my advisor Dr. Saskia Mioduszewski for her constant patience, support, and guidance. I couldn't have asked for a better mentor. I would also like to thank Dr. Nihar Sahoo: his guidance and help – especially in the beginning stages of my studies – was invaluable; and I would like to thank Dr. Peter Jacobs for his insightful feedback and guidance throughout the analysis presented in this thesis. Furthermore, I would like to thank my group-mates, Yanfang Liu and Jace Tyler, and Dr. Alexander Schmah.

Lastly, I wish to extend thanks to all the faculty, students, and staff at the Texas A&M Cyclotron Institute and Department of Physics and Astronomy who helped and supported me along this journey. In particular, I would like to thank Tarini Konchady, Eames Bennet, Sven Dildick, Naomi Schroeder, James Gerity, Lauren Aldoroty, and Mike Roosa. There are too many more to list here, but I am grateful for all the support and friendship throughout my time at Texas A&M.

CONTRIBUTORS AND FUNDING SOURCES

Contributors

This work was supported by a thesis committee consisting of advisor Dr. Saskia Mioduszewski and members Dr. Carl Gagliardi and Dr. Rainer Fries of the Department of Physics and Astronomy, and member Dr. Cody Folden III of the Department of Chemistry. I am grateful for their invaluable feedback and advice on the preparation of this document.

Figure 7.4 was prepared by Dr. Saskia Mioduszewski and the Off-Axis Cone spectra in figure 8.5 were prepared by Dr. Nihar Sahoo of Shandong University. All other work conducted for this thesis was completed by the student independently.

Funding Sources

The material presented in this this thesis is based upon work supported by the Texas A&M University Department of Physics and Astronomy and by the United States Department of Energy under grant number DE-SC0015636.

NOMENCLATURE

ADC	Analog-to-Digital Conversion
AdS/CFT	Anti-de Sitter/Conformal Field Theory
AGS	Alternating Gradient Synchotron
AJP	Adjacent Jet Patch
ALICE	A Large Ion Collider Experiment
AMY	Arnold, Moore, Yaffe
AnDY	A_N, Drell-Yan
AP	Altarelli-Parisi
AS	Away Side
ASW	Armesto, Salgado, Wiedemann
ASW-MS	Armesto, Salgado, Wiedemann-multiple soft
ASW-SH	Armesto, Salgado, Wiedemann-single hard
AtR	Alternating Gradient Synchotron-to-Relativistic Heavy Ion Collider
BAMPS	Boltzmann Approach to Multiparticle Scattering
BBC	Beam-Beam Counter
BDMPS-Z	Baier, Dokshitzer, Mueller, Peigneé, Schiff, Zhakarov
BEMC	Barrel Electromagnetic Calorimeter
BHT2	Barrel High Tower 2
BHT3	Barrel High Tower 3
BNL	Brookhaven National Laboratory

BRAHMS	Broad Range Hadron Magnetic Spectrometer
BSMD	Barrel Shower Maximum Detector
BW-MLLA	Borghini-Wiedemann Modified Leading Logarithmic Approximation
C/A	Cambridge/Aachen
CBT	Central Barrel Trigger
CERN	Conseil Européen pour la Recherche Nucléaire
CGC	Color Glass Condensate
CoLBT	Coupled Linear Boltzmann Transport
CoLBT-hydro	Coupled Linear Boltzmann Transport and hydrodynamics
DAQ	Data Acquisition
DCA	Distance of Closest Approach
DGLV	Dynamic Gyulassey, Levai, Vitev
DIS	Deep Inelastic Scattering
EEMC	Endcap Electromagnetic Calorimeter
EMC	Electromagnetic Calorimeter
ESMD	Endcap Shower Maximum Detector
FF	Full Field
FMS	Forward Meson Spectrometer
FPD	Forward Pion Detector
FTPC	Forward TPC
GLV	Gyulassey, Levai, Vitev
HT	Higher Twist
HTL	Hard Thermal Loop
IP	Interaction Point

IRC	Infrared and Collinear
IV	Interaction Vertex
JADE	Japan, Deutschland, and England
JER	Jet Energy Resolution
JES	Jet Energy Scale
JP1	Jet-Patch 1
L0	Level-0
L1	Level-1
L2	Level-2
LBT	Linear Boltzmann Transport
LCPI	Light Cone Path Integral
LHC	Large Hadron Collider
LINAC	Linear Accelerator
LO	Leading Order
LPM	Landau-Pomeranchuk-Migdal
lQCD	lattice Quantim Chromodynamics
MB	Minimum Bias
MWPC	Multi-Wire Proportional Chambers
NLO	Next-to-Leading Order
nPDF	nuclear Parton Distribution Function
NS	Near Side
PHENIX	Pioneering High-Energy Nuclear Interaction Experiment
PIV	Primary Interaction Vertex
PMT	Photomultiplier Tube

pQCD	perturbative Quantum Chromodynamics
PRS	Preshower
PU	Pile-Up
PV	Primary Vertex
QCD	Quantum Chromodynamics
QED	Quantum Electrodynamics
QFT	Quantum Field Theory
QGP	Quark-Gluon Plasma
RFF	Reverse Full Field
RHIC	Relativistic Heavy-Ion Collider
SLAC	Stanford Linear Accelerator
SMD	Shower Maximum Detector
SPEAR	Stanford Positron Electron Asymmetric Ring
sPHENIX	super Pioneering High-Energy Nuclear Interaction Experiment
SSD	Silicon Strip Detector
STAR	Solenoidal Tracker at RHIC
SU	Special Unitary
SVT	Silicon Vertex Tracker
TER	Trigger Energy Resolution
TES	Trigger Energy Scale
TOF	Time of Flight
TPC	Time Projection Chamber
TSP	Transverse Shower Profile
TVdG	Tandem Van de Graaf

UE	Underlying Event
VPD	Vertex Position Detector
VPDMB	VPD Minimum Bias
YaJEM	Yet another Jet Energy-loss Model
ZB	Zero Bias
ZDC	Zero-Degree Calorimeter
ZOWW	Zhang, Owens, Wang, and Wang

TABLE OF CONTENTS

Page

LIST OF FIGURES

FIGURE Page

LIST OF TABLES

1. Introduction

> "By substance I understand what is in itself and is conceived through itself; that is, that the concept of which does not require the conception of another thing from which it has to be formed." – Spinoza, Definition 3 of *The Ethics* [20]

What *is* the world? Is there some fundamental constituent, some indivisible atom[1], from which our experiential world of matter is built? If so, what characterizes it? Or in the words of Spinoza, what are its "attributes," that "which the intellect perceives of a substance as constituting its essence?" [20]. These sorts of questions have long occupied humanity's curiosity, and have motivated philosophy and science both ancient and modern.

In fact, science (particularly physics) as we understand it today has largely developed up to this point as an effort to understand *the* substance (matter) from which our world is built and its attributes. In its own way of grappling with the flux of sensory data that we experience, science renders the world comprehensible by constructing quantitative theories which describe causal relations between various bodies of nature [21]. The theory which describes nature at its smallest scale (at time of writing) is *the Standard Model* [22], a profound achievement of 20th century particle physics, and represents our current understanding of what matter is.

1.1 The Standard Model

The Standard Model consists of seventeen fundamental particles whose attributes are described by a handful of so-called *quantum numbers*. For instance, we can class these seventeen particles into two types: *fermions*, which comprise matter, and *bosons* which mediate fundamental interactions between the fermions. These classes are indexed by a

[1] From *atomus* (Greek), literally "uncuttable."

particle's intrinsic spin, angular momentum intrinsic to a particle rather than being due to any sort of motion of the particle. The spins of fermions come in half-integer multiples of the fundamental unit of angular momentum (the reduced Planck Constant[2], $\hbar$), while the spins of bosons come in integer multiples. In addition to spin, other quantum numbers which describe the nature of a particle are its rest mass, which describes the strength of its gravitational interaction with other objects; its parity or handedness, which is the orientation of its intrinsic spin relative to its momentum; its flavor (described below); and its electric charge, weak isospin/charge, and color charge which each describe which interactions the particle participates in. Figure 1.1 shows the set of particles comprising the Standard Model.

Each fundamental interaction consists of the exchange of a gauge boson between particles. For example, particles which carry an electric charge participate in the electromagnetic interaction by exchanging photons. Those which carry weak isospin participate in the charged weak interaction by exchanging $W^{\pm}$, while those which carry weak charge participate in the neutral weak interaction by exchanging Z^0 bosons. And those with color charge participate in the strong interaction via the exchange of gluons. The strong interaction and color charge will be described in detail in chapter 2.

We may then further subdivide the fermions into sub-classes according to which interactions each participates in: the *quarks*, which carry color charge and compose the proton and neutron, and the *leptons*, which do not carry color charge. Both the quarks and leptons, however, participate in the weak and electromagnetic interactions.

The quarks come in six *flavors* – up (u), down (d), charm (c), strange (s), top (t), and bottom (b) – which are arranged into three *generations*, doublets made of an "up-type" quark, which carries $+2/3$ units of electric charge, and a "down-type" quark, which carries $-1/3$ units of electric charge:

[2]Its value is $\approx 1.054 \times 10^{-34}$ J·s in SI units or $\approx 6.582 \times 10^{-22}$ MeV·s in eV units [6].

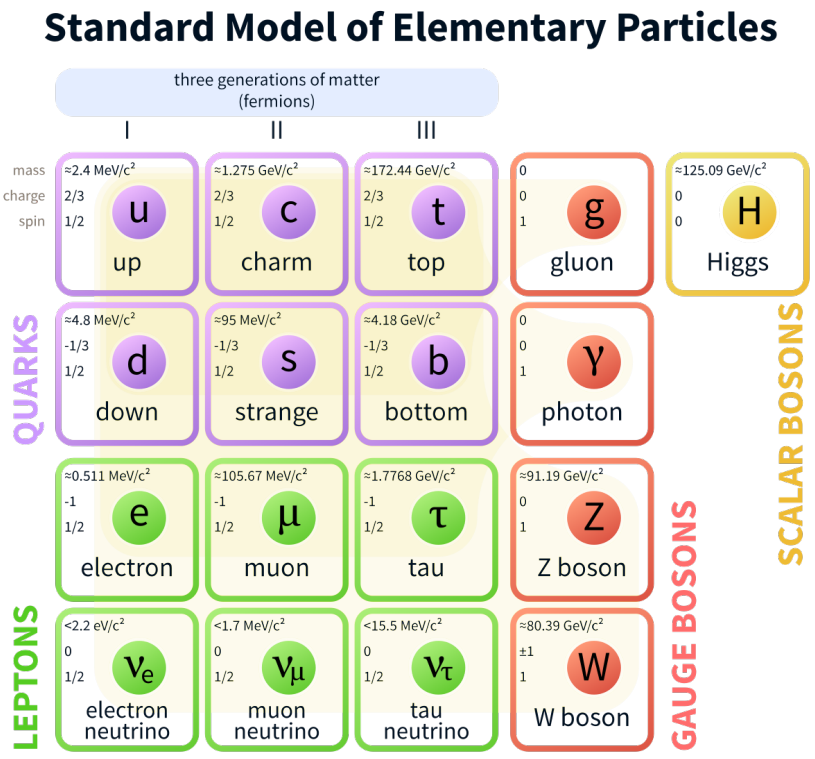

Figure 1.1: The particles of the Standard Model of Physics. From [1].

$$\{q\} = \begin{pmatrix} u \\ d \end{pmatrix} \oplus \begin{pmatrix} c \\ s \end{pmatrix} \oplus \begin{pmatrix} t \\ b \end{pmatrix} \tag{1.1}$$

Here the top row of each of doublet is the up-type quark, and the bottom row the down-type. The mass, electric charge, and spin of each quark are listed below in table 1.1. The generations are ordered according to increasing mass of each pair, where the first consists of the least massive quarks, the up and down, and the last consists of the most massive quarks, the top and bottom.

When a quark participates in the charged weak interaction, it emits or absorbs a $W^{\pm}$ boson which transforms it from one flavor into another. For instance, an up quark can

Name	Mass	Electric Charge	Intrinsic Spin
Up (u)	$2.16^{+0.49}_{-0.26}$ MeV/c^2	$+2e/3$	$1/2$
Down (d)	$4.67^{+0.48}_{-0.17}$ MeV/c^2	$-e/3$	$1/2$
Strange (s)	93^{+11}_{-5} MeV/c^2	$-e/3$	$1/2$
Charm (c)	1.27 ± 0.02 GeV/c^2	$+2e/3$	$1/2$
Bottom (b)	$4.18^{+0.03}_{-0.02}$ GeV/c^2	$-e/3$	$1/2$
Top (t)	172.76 ± 0.30 GeV/c^2	$+2e/3$	$1/2$

Table 1.1: The six quarks and their mass, electric charge, and intrinsic spin. The listed value of the top mass is derived from direct measurements. All values are from [6].

transform into a down quark by emitting a W^-. Note that these transformations do not occur between quarks of the same type, e.g. a charm quark will never transform into an up quark via $W^\pm$ exchange. Oddly, only left-handed quarks – quarks whose spin is anti-parallel with their momentum – have been observed to participate in the charged weak interaction.

Like the quarks, the leptons also come in three generations of doublets. Each doublet is composed of an electron-type lepton, which carries one unit of electric charge, and a corresponding electrically neutral neutrino:

$$\{l\} = \begin{pmatrix} e^- \\ \nu_e \end{pmatrix} \oplus \begin{pmatrix} \mu^- \\ \nu_\mu \end{pmatrix} \oplus \begin{pmatrix} \tau^- \\ \nu_\tau \end{pmatrix} \tag{1.2}$$

Here the top row of the doublets are the three flavors of electron-type leptons – the electron (e^-), muon (μ^-), and tau (τ^-) – and the bottom row are the three corresponding flavors of neutrinos, referred to as the electron, muon, and tau neutrinos. The leptons and their mass, electric charge, and spin are listed in table 1.2. As with the quarks, the generations are ordered according to increasing mass of the electron-type lepton with the electron being the least massive and the tau being the most massive.

Also like the quarks, only left-handed leptons participate in the charged weak interac-

Name	Mass	Electric Charge	Intrinsic Spin
Electron (e^-)	$0.5109989461 \pm 3.1 \times 10^{-9}$ MeV/c^2	$-e$	$1/2$
Muon (μ^-)	$105.6583745 \pm 2.4 \times 10^{-6}$ MeV/c^2	$-e$	$1/2$
Tau (τ^-)	1776.86 ± 0.12 MeV/c^2	$-e$	$1/2$
The Neutrinos (ν_e, ν_μ, and ν_τ)	< 1.1 eV/c^2	0	$1/2$

Table 1.2: The six leptons and their mass, electric charge, and intrinsic spin. All values are from [6].

tion: an electron-type lepton can transform into its neutrino counterpart by emitting a $W^\pm$ boson and vice versa. As before, transformation between leptons of the same type cannot occur through $W^\pm$ exchange. It is worth noting here that while right-handed quarks and electron-type leptons and – whose spin is parallel with their momentum – abound in nature, no right-handed neutrinos have been observed (as of time of writing).

There are two remaining particles in the Standard Model to be discussed, the Z^0 and Higgs bosons. The Z^0 boson mediates the neutral weak interaction which, in contrast to the charged weak interaction, only involves transfers of spin or momentum between particles. Some examples of neutral weak interactions are the elastic scattering of neutrinos in matter, or the decay of a Z^0 into a fermion-anti-fermion pair.

The Higgs boson carries no electric or color charge, and is the only currently known fundamental particle to carry zero spin. It mediates the famous Higgs Interaction which is responsible for generating the mass of the fermions and the $W^\pm$/Z^0 bosons. Table 1.3 summarizes the mass, electric charge, and spin of the gauge bosons of the Standard Model.

Lastly, for each electrically charged particle there is a corresponding *antiparticle* with opposite quantum numbers but identical mass. The neutral bosons, the photon and Z^0, are their own antiparticles, but (at time of writing) it is not known whether or not neutrinos are

Name	Mass	Electric Charge	Intrinsic Spin
Photon (γ)	0 ($< 10^{-18}$) eV/c^2	0	1
Gluon (g)	0 eV (Theoretical value)	0	1
$W^{\pm}$	80.739 ± 0.012 GeV/c^2	$\pm e$	1
Z^0	91.1876 ± 0.0021 GeV/c^2	0	1
Higgs (H^0)	125.25 ± 0.17 GeV/c^2	0	0

Table 1.3: The gauge and Higgs bosons and their mass, electric charge, and intrinsic spin. All values are from [6].

their own antiparticles. Antiparticles are typically notated with a bar (e.g. the antiparticle of the u quark is denoted $\bar{u}$) or with a specific symbol. For example, the positron, the antiparticle of the electron, is denoted e^+. By convention, the species of particle which is **not** naturally occurring (like the e^+) is taken to be the antiparticle of the pair.

The laws of physics are almost identical between particles and antiparticles. However, violations of this symmetry have been observed in the decays of neutral kaons (particles made up of pairs of up or down and strange quarks) [23] and in the decays of charmed D^0 particles (particles containing up and charm quarks) [24].

These seventeen particles, the corresponding antiparticles, and their interactions form the basis of the Standard Model. It is worth noting that this model is strangely asymmetric. For instance, why is it that only left-handed particles participate in the charged weak interaction? Why are there no right-handed neutrinos? Moreover, there are glaring omissions in the Standard Model, particularly dark matter and the gravitational interaction. There are many ongoing efforts to extend the Standard Model to include these, but efforts have thus far proved inconclusive due to a lack of sufficient empirical evidence and/or due to the immense theoretical challenges involved.

Suffice to say, the asymmetry and blind spots of the Standard Model are superb examples of the ways in which the phenomenal world constantly spills over the bounds of our

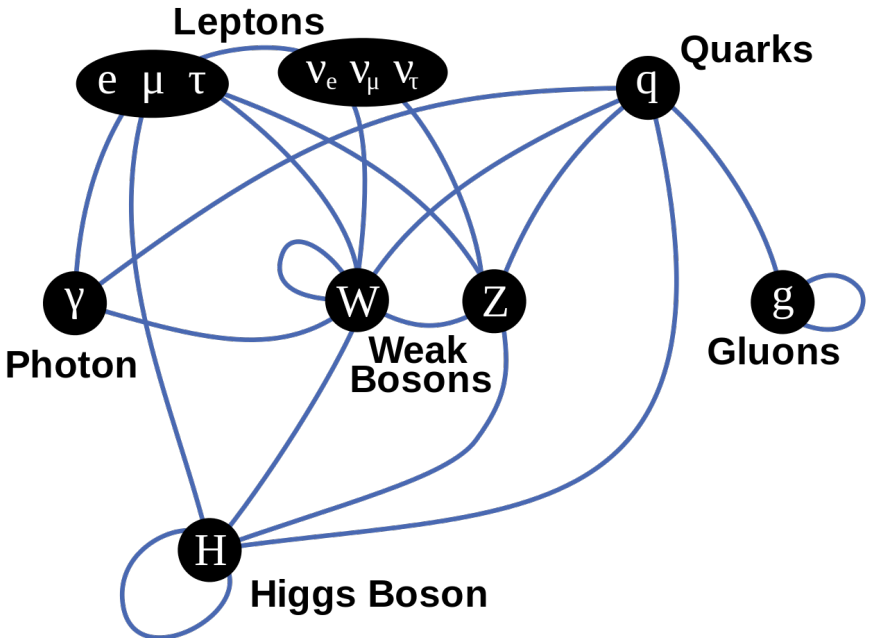

Figure 1.2: The interactions of the Standard Model of Physics. Interactions are visualized as blue lines connecting the participating particles. From [2].

conceptual frameworks and presents us with novelty that forces us to think, to revise, and to expand our picture of just what the world is.

1.2 Manuscript Organization

The focus of this thesis, though, are the quarks, gluons, and their interactions in relation to a state of matter known as the **Q**uark-**G**luon **P**lasma (QGP). This state of matter existed microseconds after the big bang and is created in the extreme conditions of the heavy-ion collisions studied at colliders such as the **R**elativistic **H**eavy-**I**on **C**ollider (RHIC) or the **L**arge **H**adron **C**ollider (LHC).

When nuclear matter is subjected to high enough energy densities, the nucleons (protons and neutrons) melt away leaving a strongly-coupled liquid of *deconfined* quarks and gluons. In other words, nuclear matter transitions to a locally thermally equilibrated state of matter in which its color degrees of freedom – the constituent quarks and gluons of the

nucleons – become manifest over *nuclear* rather than nucleonic volumes [25].

This thesis will discuss out the physics behind and elaborate on the details of a precise measurement of the momentum spectra of a certain observable known as *jets* recoiling from high energy neutral particles - neutral pions (π^0) and *direct photons* (γ_{dir}) - in proton-proton (pp) collisions, where no QGP-like medium is thought to be created. This measurement will serve as the vacuum-fragmentation (i.e. without the presence of a QGP-like medium) reference for a similar measurement in gold-gold (AuAu) collisions, wherein a QGP-like medium is created. Thus this thesis is organized as follows.

Chapter 2 will give a brief summary of concepts and techniques from Quantum Field Theory relevant to the content of this thesis, and then will proceed to give a brief account of **Q**uantum **C**hromo**d**ynamics (QCD), the mathematical description of the strong interaction, and will then proceed to a description of the phase diagram of nuclear matter suggested by QCD and detail the origin and nature of the QGP.

Chapter 3 will define the concept of a *jet* and its role as an observable of QCD.

Chapter 4 will proceed to discuss the interaction of a jet with the QGP and detail several theoretical models describing the phenomenon of *jet quenching*.

Chapter 5 will define the concept of a direct photon, and discuss why they are a valuable observable in relation to jets and jet quenching.

Chapter 6 will then transition to an account of experimental techniques. In particular, this chapter will describe the RHIC complex, and give a detailed overview of the **S**olenoidal **T**racker **A**t **R**HIC (STAR) detector, the machine used to collect the data used in this thesis.

Chapter 7 will detail how direct photons and neutral pions are measured using the STAR experiment.

Chapter 8 will proceed to give the details of the measurement presented in this thesis such as the steps involved in going from raw data to a refined measurement and the various criteria applied to ensure a clean signal.

Chapter 9 will describe the two simulation frameworks used to estimate the response of the STAR detector.

Chapter 10 will elaborate on how the data are corrected for biases and distortions through a process known as *regularized unfolding*.

Chapter 11 will detail how the systematic uncertainties of this measurement are estimated and applied to the data.

Chapter 12 will describe the simulation framework used to estimate the response of the STAR detector to the photons and neutral pions used as triggers in this measurement.

Chapter 13 will discuss the response of the STAR detector to photons and neutral poins is accounted for in this measurement before concluding the thesis with a comparison between the fully corrected data and simulation.

2. Quantum Chromodynamics and the Quark Gluon Plasma

The particles of the Standard Model and their interactions are described mathematically in the language of **Q**uantum **F**ield **T**heory (QFT)[1]. In a QFT, both fermions and bosons are conceptualized as local excitations of an underlying *field*, a mathematical construct which assigns a mathematical object – such as a number (scalar), vector, tensor, etc. – to every point in space-time. This picture accommodates two facts that have been observed about nature: (1) that fundamental particles are identical everywhere, an electron observed at one point in the universe has the exact same properties as an electron observed at another; and (2) that particle number is not conserved [26].

The quantum aspect of QFT indicates that these fields are inherently quantum mechanical in nature, and thus the uncertainty principle holds:

$$\Delta E \Delta t \geq \frac{\hbar}{2} \tag{2.1}$$

Energy conservation may be violated by amount ΔE for a period of time Δt so long as that time satisfies $\Delta t \sim \hbar/2\Delta E$. This is what enables the fundamental interactions of the Standard Model: a particle emits a boson – violating the conservation of energy – which travels a distance $\Delta t/c$ to be absorbed by another particle, restoring the conservation of energy. These ephemeral particles that only exist due to the uncertainty principle are referred to as *virtual*. Furthermore, the uncertainty principle also means that the vacuum of space-time is not so much of a vacuum after all: it is filled with pairs of virtual particles and antiparticles that flicker into existence for a brief period of time Δt only to annihilate back into the vacuum again [26].

Such processes are visualized with Feynman Diagrams [28]: diagrams which depict

[1] For an accessible introduction to the topic see [26] or [27].

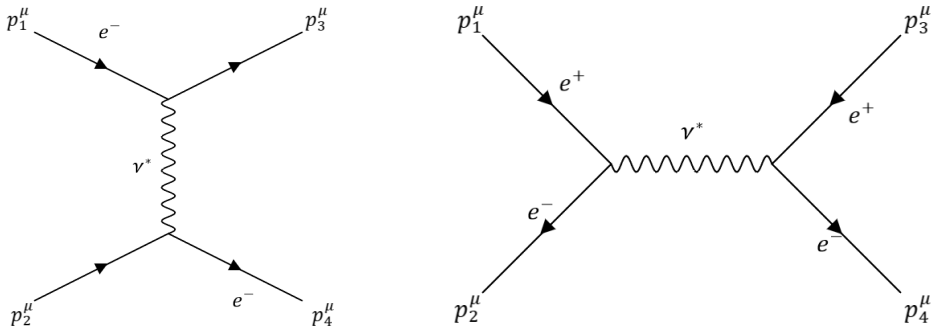

(a) e^- scattering (b) e^+e^- annihilation

Figure 2.1: Two example Feynman diagrams: the scattering of two e^- by the exchange of a virtual γ (2.1a), and the annihilation of an e^+e^- pair (2.1b) with their 4-momenta labeled.

physical processes and function as visual mnemonics for the calculations that describe the probability of each process occurring. For instance, figure 2.1a shows the scattering of two electrons by the exchange of a virtual γ, and figure 2.1b shows the annihilation of a e^-e^+ pair into a virtual photon which splits into an outgoing e^+e^- pair. The x-axis of these diagrams is frequently taken to be time and the y-axis to be space. Unless stated otherwise, this is the convention which will be followed in this thesis. Lines pointing backwards in time indicate antiparticles, and those pointing forwards indicate regular particles.

Lastly, it should be noted that the kinematics of $2 \rightarrow 2$ scattering events such as the ones depicted in figure 2.1 are encoded in *Mandelstam Variables* [29]:

$$\begin{aligned} s &= (p_1 + p_2)^2 = (p_3 + p_4)^2 \\ t &= (p_1 - p_3)^2 = (p_2 - p_4)^2 \\ u &= (p_1 - p_4)^2 = (p_2 - p_3)^2 \end{aligned} \tag{2.2}$$

where p_i are the 4-momenta[2] of the two incoming and two outgoing particles as labeled in figure 2.1. These variables are *Lorentz Invariant*, meaning that they are the same regardless of the reference frame used. Of the three, s and t also correspond to the square of the *center-of-mass energy* of the two incoming particles[3] and the *momentum transfer* of the process (i.e. the momentum of the virtual photon in figure 2.1).

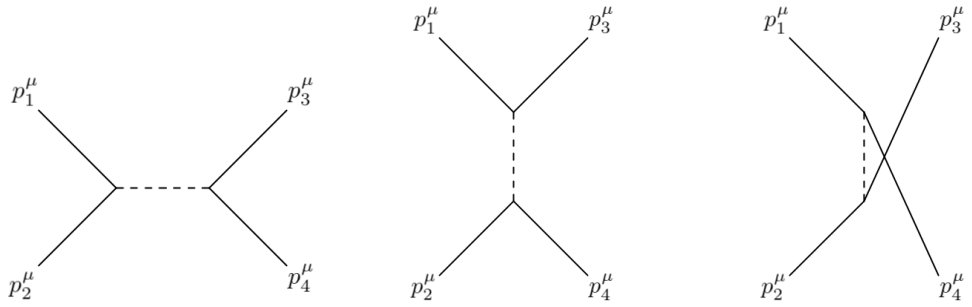

(a) s-channel (b) t-channel (c) u-channel

Figure 2.2: Prototypical diagrams of s-channel (2.2a), t-channel (2.2b), and u-channel (2.2c) scattering processes. Note that the u-channel is simply the t-channel with the roles of the outgoing particles reversed.

These three variables are also used to label certain configurations of $2 \to 2$ scattering processes. These processes are visualized in figure 2.2. These "channels" correspond to processes where the 4-momentum squared carried by the intermediate, virtual particle is given by s in the s-channel (s for **s**pace), t in the t-channel (t for **t**ime), and u in the u-channel. With all of these concepts in hand, we are now ready to discuss quarks, gluons, and QCD in more detail.

[2] $p^\mu = (E, p_x, p_y, p_z)$ where E is the energy of a particle and $p_{x,y,z}$ are the x, y, and z components of the 3-momentum, $\vec{p}$.

[3] The "center-of-mass frame" is the reference frame in which $\vec{p}_1 + \vec{p}_2 = 0$.

2.1 Quantum Chromodynamics

We have introduced quarks as fundamental particles. However, in sharp contrast to electrons, we never interact with quarks directly. Rather, the matter we interact with day-to-day is composed of atoms which are in turn composed of electrons, protons, and neutrons. The protons and neutrons are examples of *baryons*[4], particles composed of three quarks. Two u quarks and a d quark make up a proton (notated $p = uud$), and two d quarks and a u make up a neutron ($n = udd$). This reproduces the observed properties of the proton and neutron such as intrinsic spin or electric charge:

$$\begin{aligned} Q_p &= \sum_q Q_q = \frac{2e}{3} + \frac{2e}{3} - \frac{e}{3} = +e \\ Q_n &= \sum_q Q_q = \frac{2e}{3} - \frac{e}{3} - \frac{e}{3} = 0 \end{aligned} \tag{2.3}$$

There are many more members of the baryon family such as the Δ^{++} or the Hyperons, baryons which contain a strange quark such as the $\Lambda^0 = uds$. Table 2.1 lists a few baryons and some key properties.

In addition to baryons, the quarks can form *mesons*[5], bosons composed of a quark and an antiquark. These were originally proposed by Hideki Yukawa to be the carriers of the force that holds together the nucleus [30], their name deriving from the fact that their predicted mass lay in the middle of the electron and proton. The most common meson in nature are the pions, the lightest of the mesons. These include the $\pi^+ = u\bar{d}$, $\pi^- = d\bar{u}$, and the $\pi^0 = 2^{-1/2}\left(u\bar{u} + d\bar{d}\right)$[6]. Another example of a meson are the kaons: mesons composed

[4]From the Greek word *barýs* meaning "heavy."

[5]From the Greek world *mesos* meaning "intermediate."

[6]Since there is no way to experimentally distinguish $u\bar{u}$ from $d\bar{d}$ the π^0 must be described as a superposition of the two states. This is what the $+$ indicates here. Moreover, the prefactor is for normalization of the wavefunction.

Name	Quark Composition	Mass [MeV/c^2]	Electric Charge	Intrinsic Spin
Proton (p)	uud	$938.272081 \pm 0.6 \times 10^{-5}$	$+e$	$1/2$
Neutron (n)	udd	$939.565413 \pm 0.6 \times 10^{-5}$	0	$1/2$
Δ^{++}	uuu	1232 ± 2	$+2e$	$3/2$
Λ^0	uds	1115.683 ± 0.006	0	$1/2$
Ω^-	sss	1672.45 ± 0.29	$-e$	$3/2$
Ξ_{cc}^{++}	ucc	3621.6 ± 0.4	$+2e$	?

Table 2.1: A few baryons and their quark composition, mass, electric charge, and intrinsic spin. All values are from [6].

Name	Quark Composition	Mass [Mev/c^2]	Electric Charge	Intrinsic Spin
$\pi^{\pm}$	$u\bar{d}$, $d\bar{u}$	139.57039 ± 0.0001	$\pm e$	0
π^0	$2^{-1/2}\left(u\bar{u} + d\bar{d}\right)$	134.9768 ± 0.0005	0	0
$K^{\pm}$	$u\bar{s}$, $s\bar{u}$	493.677 ± 0.016	$\pm e$	0
K^0	$d\bar{s}$	497.611 ± 0.013	0	0
Φ	$s\bar{s}$	1019.461 ± 0.019	0	1
J/ψ	$c\bar{c}$	3096.900 ± 0.006	0	1
$\Upsilon\,(1S)$	$b\bar{b}$	9460.30 ± 0.26	0	1

Table 2.2: A few mesons and their quark composition, mass, electric charge, and intrinsic spin. All values are from [6].

of u, d, and s quarks. There are also the *quarkonia:* mesons composed of the heavy quarks such as the $J/\psi = c\bar{c}$. Table 2.2 lists a few mesons and their properties.

Together, the baryons and mesons constitute the *hadrons*[7], particles composed of various combinations of quarks and antiquarks. This is the quark model, independently proposed by Murray Gell-Mann and George Zweig [31, 32, 33]. The quarks which compose the hadrons and the gluons that hold them together are collectively referred to as *partons*,

[7]From the Greek word *hadrós* for "thick" or "stout."

a term coined by Richard Feynman [34]. A question naturally arises here: is it possible to have hadrons made of two quarks, qq? Or a hadron made up of four antiquarks, $\bar{q}\bar{q}\bar{q}\bar{q}$? What combinations of quarks are possible?

Moreover, the Δ^{++} baryon presents a puzzle. It is composed of three u quarks, all with their spins pointed in the same direction. Fermions obey so-called *Fermi-Dirac Statistics*, meaning that no two fermions can occupy the same quantum state. For example, consider a spin up ($+1/2$) proton: the quark composition would be a d quark with spin up, a u quark with spin up, and a u quark with spin down ($-1/2$). All three quarks are in different quantum states. However, in the Δ^{++}, the magnitude of whose spin is $3/2$, there are three quarks of the same flavor with their spins pointing in the same direction. Thus all three seem to be occupying the same state. How is this possible?

The answer to these questions lies in the fact that there is an additional quantum number at play: color, the charge associated with the strong interaction.

2.1.1 Color Charges

Color is the strong interaction analogue of the electric charge. Whereas the electric charge can either be positive or negative – e.g. the electron carries one unit of negative electric charge and the positron carries one unit of positive electric charge – color can take on three values referred to as **r**ed (R), **g**reen (G), and **b**lue (B) in analogy (and **only** in analogy) with visible color. A quark carries one unit of color (R, G, or B), and an antiquark carries one unit of *anticolor*: antired ($\bar{\text{R}}$), antigreen ($\bar{\text{G}}$), and antiblue ($\bar{\text{B}}$).[8]

When dealing with electric charge, there is exactly one way to produce an electrically neutral state: an equal mixture of positive and negative electric charge, such as in the hydrogen atom. There are three ways, however, to obtain a color neutral (or "white") state:

(a) an equal mixture of all three colors, RGB $= 0$;

[8]The anticolors are also referred to as "cyan" ($\bar{\text{R}}$), "magenta" ($\bar{\text{G}}$), and "yellow" ($\bar{\text{B}}$).

(b) an equal mixture of all three anticolors, $\bar{\mathrm{R}}\bar{\mathrm{G}}\bar{\mathrm{B}} = 0$;

(c) or an equal mixture of color and the corresponding anticolor, such as $\mathrm{R}\bar{\mathrm{R}} = 0$.

This explains the two species of hadrons. Baryons (and antibaryons) are composed of three quarks (antiquarks) each carrying a different color (anticolor), and the mesons are composed of a quark of one color and an antiquark of the corresponding anticolor. Moreover, this answers one of the questions posed in the last section. Particles like the Δ^{++} are observed because the three u quarks which compose it are each in different color states, and thus satisfy Fermi-Dirac Statistics.

No bare color charges have ever been observed, however, and thus we stipulate that all observed particles must be color neutral. This is ensured in QCD by the mechanism of *confinement* which confines color charges to color neutral combinations, and will be discussed in section 2.1.2.

This answers the other question posed in the last section. As all observable particles are color neutral, particles with quark compositions such as qq or $\bar{q}\bar{q}\bar{q}\bar{q}$ should never be observed. Rather, all observed particles must either be a color neutral triplet of (anti-) quarks, a color neutral pair of quarks and antiquarks, or more exotic color neutral combinations of those two such as the tetraquark ($q\bar{q}q\bar{q}$) [35] or the pentaquark ($qqqq\bar{q}$) [36].

As mentioned before, the strong interaction is mediated by the exchange of gluons. An example of such a process is depicted in figure 2.3. QCD necessarily conserves color. This means that the gluon in figure 2.3a must also carry color. Supposing that the upper incoming quark is red and the lower incoming quark is blue, then to conserve color the gluon must carry a unit of blue and a unit of antired: gluons are in fact *bicolored*. This is represented by the two vertical lines in figure 2.3b which depicts how color flows from one quark to another (the horizontal lines) in a gluon exchange. From the perspective of the incoming red quark, it absorbs an antired-blue gluon, negating its red color and imbuing

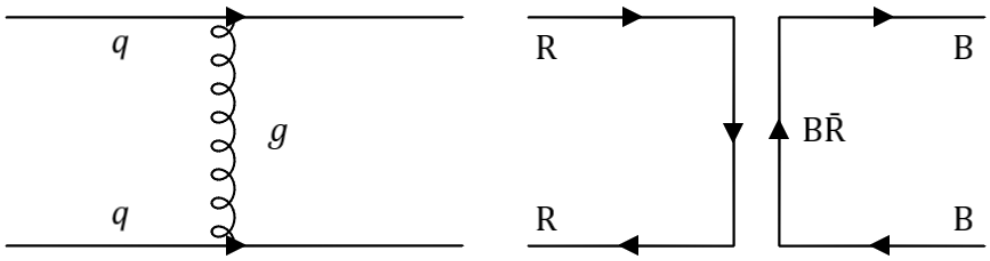

(a) qg exchange (b) color lines

Figure 2.3: The exchange of a gluon by two quarks (2.3a) and the corresponding color lines (2.3b).

it with blue color. While from the perspective of the incoming blue quark, it emits an antired-blue gluon carrying away its blue color while "taking away" a unit of antired color to imbue it with red color.

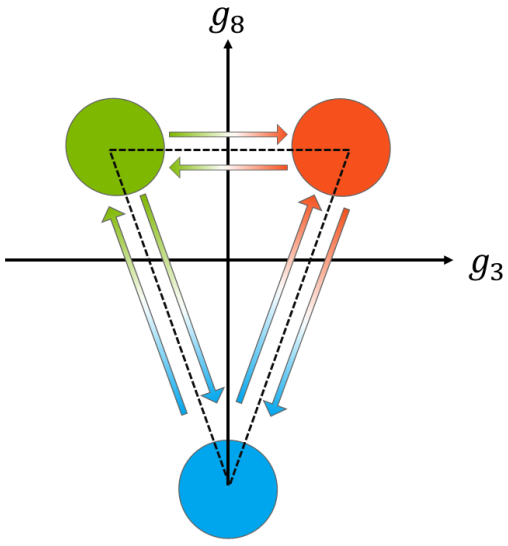

Figure 2.4: A visualization of the SU(3) symmetry underlying QCD interactions.

We can conceptualize such processes in QCD by considering a three dimensional space

in which the color states of the quarks are taken to be basis vectors [37, 38]:

$$R = \begin{pmatrix} 1 \\ 0 \\ 0 \end{pmatrix}, G = \begin{pmatrix} 0 \\ 1 \\ 0 \end{pmatrix}, B = \begin{pmatrix} 0 \\ 0 \\ 1 \end{pmatrix}. \tag{2.4}$$

Rotations between these three states are described by 3×3 hermitian traceless matrices with unit determinant, referred to as *generators*. It can be worked out there are eight such matrices which are linearly independent [37, 38]. These are also known as the *Gell-Mann Matrices*. Only two of these are diagonalizable, and may be written as:

$$G_3 = \begin{pmatrix} 1 & 0 & 0 \\ 0 & -1 & 0 \\ 0 & 0 & 0 \end{pmatrix}, G_8 = \begin{pmatrix} 1 & 0 & 0 \\ 0 & 1 & 0 \\ 0 & 0 & -2 \end{pmatrix} \tag{2.5}$$

With these, we can visualize the symmetry underlying QCD interactions. Let g_3 and g_8 be the eigenvalues of R, G, and B corresponding to the G_3 and G_8 matrices respectively. The quark color states may then be plotted according to their eigenvalues as in figure 2.4, where the arrows correspond to the actions of the other six generators on the quark states [37].

These eight generators constitute what is called the *color octet* and correspond to the eight gluons of QCD. The quarks, then, correspond to the *color triplet* of the three vectors above. The triplet and octet are both *representations* of the same symmetry group, SU(3)[9]: the triplet being the *fundamental* representation and the octet being the *adjoint* representation.

However, the fact that the gluons carry a unit of color and a unit of anticolor might lead one to wonder why there is no ninth gluon. This additional gluon would be a *color singlet*

[9] "SU" for **S**pecial **U**nitary

gluon. It would be color neutral, and so, in light of confinement, it should appear as a free particle and be exchanged between other color singlets such as the proton. Since the gluon is massless, this interaction should be long-range (like the electromagnetic interaction) and have the coupling strength of the strong interaction. This would mean that there would be an observable long range strong interaction between hadrons. This is emphatically **not** observed, and thus the color singlet gluon is disallowed on observational grounds [39].

Lastly, QCD is a *non-abelian* theory meaning that the mediating bosons themselves also carry the associated charge of the interaction. In contrast, **Q**uantum **E**lectro**d**ynamics (QED), the theory describing the electromagnetic interaction, is an *abelian* theory as the photon is electrically neutral. The non-abelian nature of QCD means that since the gluons carry color, they can interact with themselves. This is responsible for two of the most striking characteristics of QCD: confinement and asymptotic freedom.

2.1.2 Confinement and Asymptotic Freedom

The strength of a fundamental interaction is quantified by what are coupling constants in QFT, commonly denoted α. For instance, the coupling constant of the electromagnetic interaction is denoted by α_{em} (also known as the *fine structure constant* for historical reasons). These coupling constants are directly related to the charges associated with each fundamental interaction described in the introduction. The electric charge is related to α_{em} by

$$e = \sqrt{4\pi\alpha_{\text{em}}} \tag{2.6}$$

in natural units. A similar relation holds for the strong interaction: $g_s = \sqrt{4\pi\alpha_s}$ where α_s is the strong coupling constant and g_s is the QCD analogue of the unit electric charge [37]. These "constants" are also referred to as *running coupling constants* for reasons that will become clear shortly.

The charge associated with a fundamental interaction is related to its strength. Thus, if one wished to measure the electric charge, one could go about it by gradually moving a *test charge* (e.g. a single electron) closer and closer to some electrically charged target (e.g. another single electron) and measuring the coulomb repulsion between the two charges. As the test charge gets closer to the target charge, the electric field between the two will grow in strength. The increasing strength of this field will cause an increasingly dense cloud of virtual e^+e^- pairs to sublime out of the vacuum. The e^+e^- pairs closer to the target charge will orient themselves such that the e^+ is preferentially closer to the target charge [37].

This means that as the test charge penetrates the cloud of virtual e^+e^-, the cloud becomes increasingly dense with more and more e^+ on the target side and more and more e^- on the test side. Hence, the test charge feels an increasingly large negative electric charge. This phenomenon is known as *screening* [37].

We can imagine a similar thought experiment for QCD wherein we gradually move a test color charge towards a target color charge of the same color and measure the QCD analogue of coulomb repulsion between the two. The experiments proceeds much like it did in the QED case: as the test and target charges draw close, the color field between the two will increase in strength. However, this will result in an increasingly dense cloud of not just virtual $q\bar{q}$ pairs, but also virtual gluons. The color charge carried by these virtual gluons will effectively "smear" the color of the target charge. Rather than feeling an increasingly strong charge like in QED, the test charge will feel an increasingly dilute color charge. This phenomenon is (fittingly) referred to as *anti-screening* [37].

To summarize: the electromagnetic interaction *increases* in strength (the effective electric charge grows) with decreasing separation between electric charges due to screening. In contrast, the strong interaction *decreases* in strength (the effective color charge shrinks) with decreasing separation between color charges due to anti-screening. In both cases the

coupling of the theory "runs," or varies with changing length scales [37].

For QCD, the running coupling constant α_s is given by the equation

$$\alpha_s\left(Q^2\right) = \frac{12\pi}{(33 - 2n_f)\log\left(Q^2/\Lambda^2_{\text{QCD}}\right)} \tag{2.7}$$

where Q^2 is the squared momentum transfer between two color charges, n_f is the number of "active" quark flavors being considered (a number between 2 and 6), and Λ_{QCD} is the *QCD Scale*, a constant with dimensions of mass [37]. When Q^2 is large (i.e. $Q^2 \gg \Lambda^2_{\text{QCD}}$, meaning large energy scales and small length scales), α_s is small ($\alpha_s \ll 1$). The strong interaction grows weak with increasing Q^2, meaning that the quarks asymptotically approach acting as free, noninteracting particles. This is *Asymptotic Freedom* [40, 41].

At low energies, the coupling becomes strong again. Consider a $q\bar{q}$ pair: the self interactions of the gluons mean that rather than spreading out in space like photons, the exchanged gluons between the $q\bar{q}$ pair are compressed into a dense tube of gluons called *color flux tubes* or *QCD strings*. If the $q\bar{q}$ pair is roughly static (i.e. their relative motion is much smaller than the frequencies of the gluons exchanged), then the potential between may be well approximated by the phenomenological potential

$$V_{q\bar{q}}\left(r\right) = \frac{-a}{r} + \lambda r \tag{2.8}$$

where a and λ are constants and r is the separation between the quarks [42]. The constant $a = 4\alpha_s/3$ comes from the asymptotically-free regime, and the constant λ may be interpreted as the tension of the color flux tube, which is roughly 0.9 fm^{-1} [42].

Note that as r increases, V increases. This is *confinement*, also known as *Infrared Slavery*. As one tries to increase the separation of the $q\bar{q}$ pair, the potential grows and pulls them back into the color neutral $q\bar{q}$ configuration[10]. In sharp contrast, the coulomb

[10]This pictures holds up to a certain threshold in separation which will be discussed in chapter 3

potential in QED goes like $V_{\text{coulomb}}(r) \sim 1/r$, and so quickly falls off as r increases.

The QCD Scale Λ_{QCD} is a constant of integration that is introduced in the derivation of equation 2.7. It is a free parameter and so must be provided by experiment. For $Q^2 \gg \Lambda^2_{\text{QCD}}$, color charges are asymptotically free, but for $Q^2 \lesssim \Lambda^2_{\text{QCD}}$, the strong interaction becomes strong again and the principle of confinement dominates. Hence, we can understand Λ_{QCD} as the scale at which the familiar world of color-neutral hadrons gives way to a world of asymptotically free color. For this reason we should expect this constant to be near the typical mass of a hadron. Indeed, for 5 active quark flavors, $\Lambda_{\text{QCD}} \approx 210 \pm 14$ MeV [6]. This is close to the length of 1 fm (10^{-15} meters or roughly 197.3 MeV in natural units), roughly the diameter of a nucleon.

This scale also demarcates the *perturbative* and *non-perturbative* regions of QCD. In **p**erturbative QCD (pQCD)[11], one performs calculations by expanding the QCD Lagrangian in a power series on α_s. The Lagrangian is a mathematical object which encodes the possible interactions and their strengths allowed by a QFT. Each term in this series corresponds to a particular Feynman diagram and carries a weight α_s^λ where λ is the order of the diagram (given by the number of vertices). For large Q^2 (much greater than Λ^2_{QCD}), α_s is small and the series can be safely truncated, allowing the calculation to be carried out.

For Q^2 on the order of Λ^2_{QCD}, however, α_s is large. Even higher order terms will carry a non-negligible weight, and so any calculation would require an infinite number of diagrams to be computed. For energy scales relevant to describing every-day, confined matter, pQCD fails and the equations of QCD remain unsolved. Despite this, many techniques for approximating the non-perturbative regime of QCD have been developed. One powerful approach to calculating non-perturbative processes in QCD is that of **l**attice QCD

[11] For brief introductions to pQCD, see [37, 43, 42]

(lQCD)[12] In this approach, one defines QCD on a lattice. The quarks occupy lattice sites, and the gluons occupy the links between the sites. The finite spacing of the lattice imposes a minimum length and time scale which renders calculations tractable.

2.2 The Quark-Gluon Plasma

By confinement, color charges only exist as part of the color neutral hadrons that constitute our phenomenal day-to-day world. However, by asymptotic freedom, there should exist a state of matter in which these color charges – the quarks and gluons – become *deconfined*, free to roam as individual entities. This state of matter is known as the Quark-Gluon Plasma [42, 43].

Above a critical temperature, the strong interaction is anti-screened and becomes weak, causing the hadrons to melt away and leave only a viscous fluid of deconfined quarks and gluons. To reiterate the definition from earlier: the QGP is a state of matter in which its color degrees of freedom become manifest over *nuclear* rather than merely nucleonic volumes [25].

Lattice calculations suggest that the transition from hadronic matter to the QGP occurs for a critical temperature somewhere in the range of 150 to 200 MeV. An early lattice prediction for the critical temperature was roughly $T_c \sim 170$ MeV [44], or roughly **2 trillion K**. For reference, the core of the sun is estimated to be a mere 15 million K. The critical temperature corresponds to an energy density of roughly $\epsilon_c \sim 0.7$ GeV/fm^3 [45]. The density of a proton[13] is about $\rho_p = 0.16$ fm^{-3}, which means its rest energy density approximately $\epsilon_p = m_p \rho_p \approx 0.15$ GeV/fm^3.

Consequently, there are two paths toward the creation of a QGP: compressing nuclear matter to densities above the critical density ρ_c, or heating nuclear matter to temperatures above T_c. Figure 2.5 shows the phase diagram of strongly interacting (i.e. quark) matter as

[12] See chapter 5 of [42] for a brief introduction to the subject.
[13] using the proton's charge radius, ~ 0.84 fm, and mass, ~ 0.94 GeV [6]

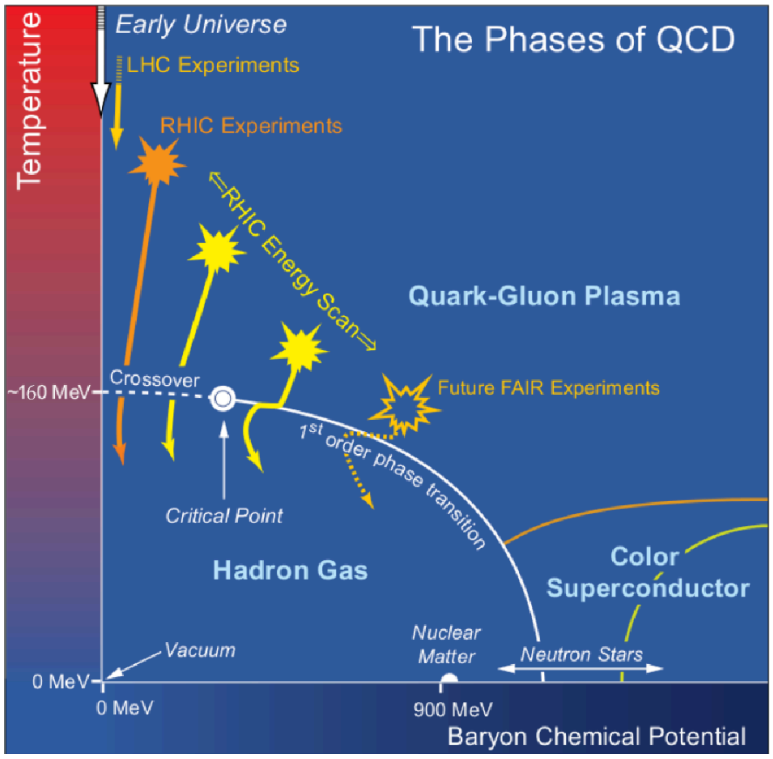

Figure 2.5: The phase diagram of strongly interacting matter. From [3].

a function of temperature and baryon chemical potential (a proxy for baryon density). The diagram in figure 2.5 also indicates where physical systems reside, as well as the regions past and future experiments have probed and will probe.

Along the high density path, we may imagine a scenario where a finite number of baryons are compressed adiabatically until they reach ρ_c. At this point, the baryons will overlap and form a degenerate, deconfined mass of quarks. There is a possibility that this situation may exist at the cores of neutron stars where the densities may reach 5-10 times that of normal nuclear matter [42, 46].

Along the high temperature path, we can imagine raising the temperature of a finite region of space. At low temperatures, the vacuum excitations will necessarily be color neutral hadrons (by confinement). However, as the temperature increases the frequency

and number of excitations will increase. At T_c these excitations will overlap, leaving only a sea of deconfined quarks and gluons [42, 43]. The early universe, microseconds after the big bang, is predicted to have been at temperatures well in excess of Λ_{QCD} and T_c. Thus the early universe may well have existed in a QGP-like state [46].

Unfortunately, neutron stars and the early universe are not available on demand in a laboratory. However, there is the possibility of creating a QGP in relativistic heavy-ion collisions [46]. Early experimental results from the Relativistic Heavy-Ion Collider at Brookhaven National Lab suggest that the almost head-on collisions of gold ions (denoted AuAu collisions) at its top center-of-mass energy of $\sqrt{s_{NN}} = 200$ GeV per nucleon achieves energy densities well in excess of the necessary ϵ_c, with the lower bound being roughly 10 GeV/fm^3 [47]. Thus, relativistic heavy-ion collisions provides us with the **only** laboratory setting in which we may study the QGP.

Ample evidence that a hot, dense medium which satisfies the definition stated earlier has been generated at both the Relativistic Heavy-Ion Collider at **B**rookhaven **N**ational **L**aboratory (BNL) and the Large Hadron Collider at the **C**onseil **E**uropéen pour la **R**echerche **N**ucléaire (CERN) in Geneva [25, 46]. The evidence includes (but is not limited to):

1. strong momentum anisotropy exhibited by low to mid transverse momentum particles produced in heavy-ion collisions;

2. the suppression of higher angular momentum Υ states (e.g. the 2S and 3S) alongside the non-modification of the Υ ground state relative to pp-collisions; and

3. an opacity to energetic particles, i.e. a suppression of energetic particles relative to pp-collisions.

The third piece of evidence, the opacity to energetic particles (a phenomenon known as *jet quenching*), offers not only a clear signal of the formation of a hot, dense medium, but

also a prime channel through which we may quantitatively explore the properties of the produced medium. This will be the focus of this thesis, and so the next three chapters will first elaborate the concept of a jet (chapter 3), then will discuss various theoretical models of jet quenching (chapter 4), and finally will discuss how recoil jets correlated with *direct photons* offer a well-calibrated probe with which to experimentally measure jet quenching (chapter 5).

3. Jets

Isolated partons have never been observed; they are always confined to color-neutral systems such as the proton or pion. The property of confinement, however, has dramatic consequences for any partons who are liberated from their hadronic prisons via process like **D**eep **I**nelastic **S**cattering (DIS). In DIS, an electron-type lepton is scattered off of a nucleon by the exchange of a virtual photon. For sufficiently high momentum exchange between the lepton and nucleon, the nucleon is shattered and a constituent quark is kicked out. This produces an collimated spray of hadrons roughly collinear with the momentum of the freed quark: these are called *jets*.

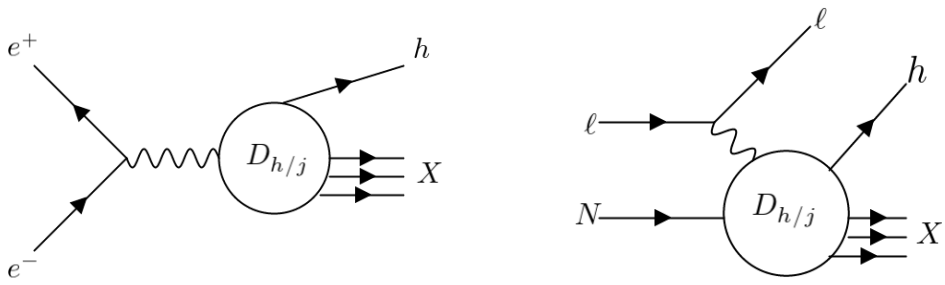

(a) (b)

Figure 3.1: Feynman diagrams for e^+e^- annihilation (3.1a) and DIS (3.1b). Here l indicates an electron-type lepton, N a nucleon, h a hadron, and $D_{h/j}$ a fragmentation function.

Jets were postulated as an experimental signature of the quark model that would be observable in both DIS and $e^+e^- \to q\bar{q}$ processes (visualized in figure 3.1) [48, 49, 50, 51]. While free quarks can never be observed, we can infer their existence in the jets they produce. In 1975, just such an observation was made in e^+e^- collisions studied at the **S**tanford **P**ositron **E**lectron **A**symmetric **R**ing (SPEAR) detector at the **S**tanford **L**inear

Accelerator (SLAC) [52, 53].

We can understand the phenomenon of jets by recalling that the color field lines between two or more color charges are compressed into dense tubes of gluons with roughly constant energy density per unit length due to the self-interactions of the gluons. This gave rise to a potential that is directly proportional to the distance r between the charges, $V(r) \propto r$. As r increases, so too does the potential, thereby confining the color charges.

In the case of e^+e^- collisions, the e^+ and e^- annihilate into a virtual photon. The photon can then decay into a $q\bar{q}$ pair for sufficient energies, carrying the momentum of the original e^+e^- pair. The color field lines are stretched to the point where they exceed the threshold for creating a new $q\bar{q}$ pair. The new pair pops into existence, and acting as new end points for the color field lines snap the original tube of gluons in half, reducing the overall energy of the system. The quarks and antiquarks continue along their trajectory, stretching and splitting the gluon tubes in the same manner until the system finally has zero net color charge and the produced hadrons have sufficiently low internal momentum [37].

This picture gives a solid intuition for why jets occur, but it is simplified: baryons are also produced in the fragmentation of jets. One possible mechanism for the creation of baryons in jets would be that first three pairs of quarks are produced – a R$\bar{\text{R}}$, a B$\bar{\text{B}}$, and a G$\bar{\text{G}}$ pair – which then recombine into a baryon and anti-baryon [54].

3.1 Fragmentation Functions

The process of a parton fragmenting into hadrons is known as hadronization, and is intrinsically non-perturbative. It is phenomenologically described by the fragmentation functions, $D_{h/j}(z)$. These functions describe the probability of a parton (jet) j with momentum $\hat{p}$ fragmenting into a hadron of type h with momentum fraction $z = p_h/\hat{p}$. Necessarily they must satisfy both probability and momentum conservation:

$$\begin{aligned}\sum_h \int_0^1 z D_{h/j}(z)\, dz &= 1 \\ \sum_j \int_{z_{\text{min}}}^1 D_{h/j}(z)\, dz &= n_h\end{aligned} \tag{3.1}$$

where z_{min} corresponds to the threshold energy for producing a hadron of mass m_h, $p_{\text{min}} = 2m_h/Q$[1], and n_h is the average number of produced hadrons of type h. These functions are obtained by global fits to data from a wide variety of sources such as e^+e^- collisions, DIS, and pp collisions. For two recent reviews see [55] and [56].

The differential cross-section for the production of hadrons from the collision of two nuclei A and B is then described as a convolution of the partonic hard scatter cross-section $\sigma^{ab\to cX}$ (which is calculable in pQCD), the **n**uclear **P**arton **D**istribution **F**unction (nPDF) which describes the partonic composition of a given nucleus, and the fragmentation function which describes the process of hadronization. As a function of the hadron transverse momentum and rapidity, this is written as:

$$\frac{d^3\sigma^h}{d^2p_{\text{T}}dy} = \frac{1}{\pi}\int dx_a \int dx_b f_a^A(x_a)\, f_b^B(x_b)\, \frac{d\sigma^{ab\to cX}}{d\hat{t}_c}\frac{D_{h/c}(z)}{z} \tag{3.2}$$

where $x_{a,b} = \hat{p}_{a,b}/p_{A,B}$ are the momentum fractions of partons a and b which are found in nuclei A and B respectively. The momenta of the nuclei are p_A and p_B. Then $\hat{t}_c = (\hat{p}_c - x_a\langle p_A\rangle)^2 = Q^2$ is the momentum transfer squared between an outgoing parton c with momentum $\hat{p}_c$ and an incoming parton a with momentum $x_a\langle p_A\rangle$, and $\langle p_A\rangle$ is the average momentum of a nucleon in nucleus A. The terms $x_{a,b}f_{a,b}^{A,B}(x_{a,b})$ are the nPDFS, which can be interpreted as the probability of finding a parton of type a with x_a in nucleus A and vice versa. Much like the fragmentation functions, they are intrinsically connected

[1] Q being the Q-value of the hadron.

to non-perturbative processes in QCD and must be obtained from global fits to data. For a recent review of parton distribution functions in nucleons and nuclei see [57].

3.2 Jet Finding Algorithms

Given that jets are nothing more than collimated sprays of hadrons, an ambiguity arises: how do we decide which hadron should be associated with which jet? At the level of observation, we have no access to the partons themselves and thus no way of associating each hadron with its parent parton. Even at the level of the partons this ambiguity persists. Suppose a quark radiates a gluon. If the gluon is roughly collinear with the quark, then it makes sense to include it in the jet of the initial quark. If the gluon is emitted at a substantially wide angle relative to the quark, however, should it still be counted as part of the initial quark's jet?

Thus, we can only define jets operationally: a jet is the output of an algorithm which clusters together objects according to some criteria (be those objects tracks in a time projection chamber, towers in a calorimeter, or particles in a simulation). This is in line with the Snowmass Accord, a standard regarding jet definitions that was settled upon at the 1990 Snowmass Meeting [58]: whatever definition of a jet is used, both theory and experiment must use the same definition and this definition must be theoretically well-motivated.

Broadly speaking, there are two classes of clustering algorithms: cone algorithms (e.g. [59] or [60]) and "sequential recombination" algorithms (e.g. [4]). The following sections will present a detailed discussion of each class in turn.

3.2.1 Cone Algorithms

Historically, the cone algorithms were the first algorithms to be developed. They attempt to define a jet as a core around some dominant flow of energy, reflecting the fact that jets should be collimated in momentum-space. Let $\mathcal{C} = \{c_i\}$ indicate the input to a Cone Algorithm, the set of objects to be clustered, each of which have 4-momentum p_i^μ.

Let $\mathcal{J} = \{j_i\}$ indicate the output of the algorithm, a set of stable cone jets. Lastly, let $\mathcal{R}(a^\mu) = \{r_i | r < R_{\text{jet}}\}$ indicate the set of objects lying within a distance R_{jet} away from the point a^μ in the (y, φ) plane. A Cone Algorithm would proceed in manner like so:

Algorithm 1 A schematic outline of cone algorithms. This algorithm is defined by two parameters: the cone radius R_{jet}, and the max number of iterations, N_{pass}.

1: **do**

2: Select a "seed object" to define the axis of a trial cone from the set $\mathcal{C}$.
Denote its 4-momentum p^μ_{seed}.

3: Sum the 4-momenta of all objects lying in $\mathcal{R}(p^\mu_{\text{seed}})$, $p^\mu_{\text{sum}} = \sum_{j \in \mathcal{R}} p^\mu_j$

4: **if** $p^\mu_{\text{seed}} \neq p^\mu_{\text{sum}}$, **then**

5: Select a new seed object.

6: **else**

7: The cone is stable. Add the cone to the list of stable cones, $\mathcal{J}$.

9: Remove all objects contained in $\mathcal{R}(p^\mu_{\text{seed}})$ from $\mathcal{C}$.

8: **while** $\mathcal{C}$ is not empty **and** the number of iterations is $\leq N_{\text{pass}}$.

Typically the seed object is the most energetic object in the set $\mathcal{C}$. While computationally easy to implement, such algorithms quickly produce ambiguities in complex situations. For instance, it might be that two jets overlap. In such a case, there is an ambiguity as to which jet the objects in the overlap belong to. This is typically resolved by introducing an "overlap parameter," f_{merge}. If $p_{\text{T}}^{\text{overlap}} < f_{\text{merge}} p_{\text{T}}^{\text{hard}}$ – $p_{\text{T}}^{\text{hard}}$ being the p_{T} of the harder of the two jets – then each object shared between them is assigned to the jet whose axis is closer. Otherwise, the two jets are merged into a single jet.

However, a more serious ambiguity arises when we consider the algorithm in the infrared limit[2]. Suppose a seed of infinitesimal p_{T} is introduced between two stable cones, the algorithm may group the two original cones into a single cone centered on the new seed upon re-running. Similarly, if simulated partons are used as input for the algorithm, the hardest parton can easily be changed by a quasi-collinear, infrared splitting[3] leading to divergences in the output of the algorithm. As such, these algorithms are said to be *Infrared Unsafe* [60, 61].

3.2.2 Sequential Recombination Algorithms

While the Cone Algorithms present a very tidy picture of parton radiation, they can be quite unwieldy in high multiplicity, high background environments such as those present at a hadron collider. Sequential recombination algorithms may be more suitable for such environments. These algorithms proceed by attempting to play the parton shower in reverse: they sequentially combine hadrons or their proxies (TPC tracks, calorimeter towers, etc.) into jets according to a best guess as to how the parton shower proceeded. This gives sequential recombination algorithms the necessary flexibility in defining jets to more cleanly parse the desired hard radiation from background radiation in such noisy environments like hadron collisions [61].

3.2.2.1 The k_T Algorithm

One example of a sequential recombination is the k_T algorithm [62]. This algorithm is descended from algorithms developed by the JADE[4] Collaboration for $e^+e^- \rightarrow h^+h^-$ collisions. It utilizes the fact that QCD showers are "momentum ordered," meaning that hard partons fragment into progressively softer partons.

The algorithm begins by defining two distance metrics in phase space:

[2] i.e. when $p_T \approx 0$

[3] The Δr between the original 4-momenta and the split is approximately 0.

[4] **JA**pan, **D**eutschland, and **E**ngland

$$
\begin{aligned}
d_{ij} &= \min\{k_{\mathrm{T},i}^2, k_{\mathrm{T},j}^2\} \left(\frac{\Delta_{ij}}{R_{\text{jet}}}\right)^2 \\
d_{iB} &= k_{\mathrm{T},i}^2
\end{aligned}
\tag{3.3}
$$

where $\Delta_{ij}^2 = (\eta_i - \eta_j)^2 + (\varphi_i - \varphi_j)^2$ and $k_{\mathrm{T},i}$ is the transverse momentum of the i^{th} object. Here R_{jet} is an angular length scale, and thus carries units of angular length, which functions as a parameter which controls the relative size of the jets produced. By convention, values of R_{jet} will be quoted from hereon without any reference to units. Finally, the metric d_{ij} encodes the distance in phase-space between pairs of objects; while d_{iB} encodes the distance in phase-space between the i^{th} object and the beam.

Once again, let $\mathcal{C} = \{c_i\}$ indicate the set of objects to be clustered with 4-momentum k_i^μ, and $\mathcal{J} = \{j_i\}$ indicate the output of the algorithm. In the context of sequential recombination algorithms, whatever objects are being clustered are frequently referred to as "proto-jets." The k_T algorithm then proceeds like so:

Algorithm 2 A schematic outline of the k_T algorithm. This algorithm is defined by one parameter, R_{jet}, which functions as an angular cut-off: objects with $\Delta_{ij} > R_{\text{jet}}$ will never be merged.

1: Set the list of proto-jets $\mathcal{P} = \{p_i\}$ equal to the set of inputs, $\mathcal{C}$.
2: **do**
3: **for** each pair of objects $p_i, p_j \in \mathcal{P}$ **do**
4: Compute d_{ij} and d_{iB}.
5: **if** $d_{ij} < d_{iB}$, **then**
6: Merge the two proto-jets into a new proto-jet, p', with 4-momentum $k^{\mu\prime} = k_i^\mu + k_j^\mu$.

7: Add p' to $\mathcal{P}$.

8: Remove the old proto-jets p_i, p_j from $\mathcal{P}$.

9: **else**

10: p_i is a stable jet. Add it to the list of stable jets $\mathcal{J}$.

11: Remove p_i from $\mathcal{P}$.

12: **end if**

13: **end for**

14: **while** $\mathcal{P}$ is **not** empty.

While this algorithm can easily handle high-multiplicity, high-background environments and it eliminates the ambiguities inherent in the cone algorithm, it has its own issues. As the lowest k_{T} objects are merged first, arbitrarily small k_{T} objects can become jets. Moreover, since it begins by merging soft objects first working up towards harder objects, it tends to construct irregularly-shaped jets which depend on the detailed distribution of soft radiation in an event. Thus k_{T} jets tend to be harder to calibrate due to their irregular shape, and are quite sensitive to any unrelated radiation that may be present [4, 61].

3.2.2.2 The C/A Algorithm

A related algorithm is the **C**ambridge/**A**achen (C/A) Algorithm [63]. The algorithm is identical to the k_T algorithm in every respect except the phase-space distance metrics are modified to be:

$$\begin{aligned} d_{ij} &= \left(\frac{\Delta_{ij}}{R_{\text{jet}}}\right)^2 \\ d_{iB} &= 1 \end{aligned} \tag{3.4}$$

Thus, the only information factored into whether or not two proto-jets are merged is the distance between them. The C/A algorithm centers the "angular ordering" of QCD showers, i.e. the last emissions are the ones farthest from the initial parton. It was developed to strike a balance between approximating the structure of a QCD shower and maintaining some degree of insensitivity to soft radiation.

3.2.2.3 The Anti-k_T Algorithm

A third example of a sequential recombination algorithm is the "anti-k_T" algorithm [4]. This algorithm proceeds in a manner identical to the k_T and C/A algorithms, but – once again – the distance metrics are adjusted:

$$\begin{aligned} d_{ij} &= \min\{\frac{1}{k_{\mathrm{T},i}^2}, \frac{1}{k_{\mathrm{T},j}^2}\} \left(\frac{\Delta_{ij}}{R_{\text{jet}}}\right)^2 \\ d_{iB} &= \frac{1}{k_{\mathrm{T},i}^2} \end{aligned} \tag{3.5}$$

This results in the algorithm running in the "opposite direction" of the k_T algorithm: it clusters the hardest objects first, identifying the hard cores of jets, and it clusters the softest objects last. The anti-k_T algorithm abandons any attempt to replicate the structure of QCD showers, but nonetheless, it does present a very intuitive picture of a jet: a hard core surrounded by a soft, roughly conical corona.

This algorithm has very desirable properties. The anti-k_T algorithm is manifestly **I**nfra**r**ed and **C**ollinear (IRC) safe: an additional infinitesimally soft particle or quasi-collinear split will have a negligible impact on the clustered jets. Additionally, since the soft objects have minimal impact on the hard core of the jet, this algorithm tends to cluster objects out to distances R_{jet} away from the jet core. Thus, the algorithm is relatively insensitive to soft background radiation, and yields very regularly-shaped (and thus very

easy to calibrate) jets [4].

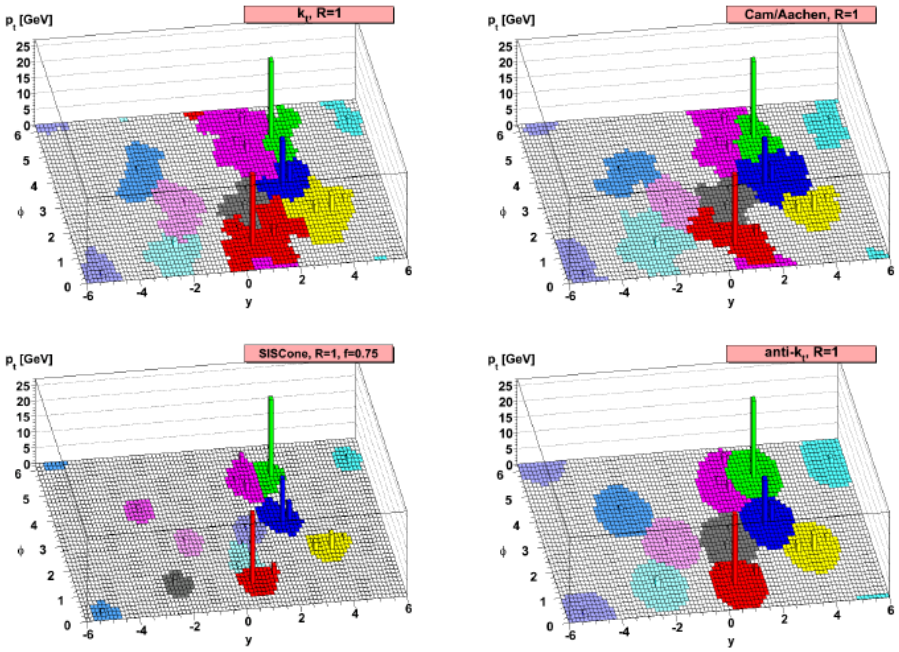

Figure 3.2: A comparison of the jets produced by the different jet algorithms discussed in this chapter. In each case, the same event is clustered but with a different algorithm. The areas of each jet are visualized with random ghosts as discussed in section 3.3. Used with permission from [4].

Recall that the cone algorithm produced ambiguities when two cones overlapped. The anti-k_T algorithm sidesteps these ambiguities by definition. Consider two hard particles with $R_{\text{jet}} < \Delta_{12} < 2R_{\text{jet}}$: the anti-$k_T$ algorithm will produce two jets, but they won't be conical. If the two transverse momenta are roughly equal, $k_{\text{T},1} \approx k_{\text{T},2}$, then the produced jets will be clipped by a boundary defined by ${}^{\Delta_{1b}}/_{k_{\text{T},1}} = {}^{\Delta_{2b}}/_{k_{\text{T},2}}$ where $\Delta_{1,2b}$ are the distances between the boundary and the hard particles.

Similarly, if the two hard particles have $\Delta_{12} < R_{\text{jet}}$, the behavior of the algorithm can be worked out. If $k_{\text{T},1} \gg k_{\text{T},2}$, then the algorithm will simply produce a single, conical

jet centered on $k_{\mathrm{T},1}$. However, if $k_{\mathrm{T},1} \approx k_{\mathrm{T},2}$, then two jets will be produced (both with a radius less than R_{jet}) with a more complex shape. Such behavior can be seen in the green vs. magenta and blue vs. yellow jets in the upper right-hand corner of the lower right panel of figure 3.2.

However, if there are no additional hard particles (or no hard particles at all) within R_{jet}, then the algorithm produces a perfectly conical jet of radius R_{jet}. All of these scenarios can be seen in figure 3.2 which compares the results of all four jet algorithms discussed in this chapter.

The key feature in all of this is that soft particles do not modify the shape of the produced jet, only hard particles do [4]. This property has made the anti-k_T algorithm ideal for the complex, high background environments of hadron collisions, and it has since become the default algorithm of analyses at RHIC and the LHC [61].

3.3 Jet Area

In practice, particles produced by hard partonic interactions are inevitably accompanied by multiple sources of background, especially so in relativistic nuclear collisions. There are two primary sources of background in such collisions: the so-called **U**nderlying **E**vent (UE) and **P**ile-**U**p (PU). The UE consists of radiation from non-perturbative effects between the nucleon beams (e.g. color recombination), and PU consists of diffuse radiation from additional **M**inimum **B**ias (MB) collisions occurring at the same bunch crossing simultaneously with the primary hard interaction.

Of the two, the UE is substantially more difficult to understand as it cannot be disentangled from the products of the hard interaction. Pile-up, on the other hand, is diffuse, and is completely uncorrelated with the hard interaction of interest. These two sources of background can affect jet measurements in two ways: by adding energy to the jet by being clustered with the hard interaction products, or by modifying which particles are

clustered into which jets. The impact of the former can easily be assessed by introducing the concept of a *jet catchment area,* or simply *jet area* [64].

Defining the area of a jet is not a straightforward matter. Since jets are composed of point particles, strictly speaking, their area will always be zero. Using a geometric construction such as the convex hull of the jet constituents leads to ambiguities. For instance, two adjacent jets with uneven borders will lead to overlapping convex hulls. It is possible, however, to define a meaningful jet area that avoids these pitfalls by exploiting the infrared safety of modern jet algorithms. Two such definitions will be discussed here, *passive area* and *active area*, both of which are based on the idea introducing "ghost particles" with infinitesimal energy into the clustering process.

3.3.1 Passive Jet Area

The *passive area* of a jet measures its susceptibility to a point-like UE [64]. It's calculated by scanning a ghost particle over (y, φ) space and determining the region in which the ghost particle is clustered into the jet, i.e.

$$\begin{aligned} a\left(J_i\right) &= \int dyd\varphi\, \Theta\left[g\left(y,\varphi\right), J_i\right] \\ a^{\mu}\left(J_i\right) &= \int dyd\varphi\, \frac{g^{\mu}}{g_{\mathrm{T}}}\, \Theta\left[g\left(y,\varphi\right), J_i\right] \end{aligned} \tag{3.6}$$

Here $a\left(J_i\right)$ and $a^{\mu}\left(J_i\right)$ denote the scalar and 4-vector passive areas of the i^{th} jet J_i, and g denotes a ghost particle with a 4-momentum of g^{μ}. The function $\Theta\left[g, J\right]$ is 1 when $g \in J$, and 0 otherwise. The 4-vector passive area is defined such that its transverse component coincides with the scalar passive area.

3.3.2 Active Jet Area

The *active area* of a jet measures its susceptibility to a diffuse UE [64]. Here, a randomly generated distribution of ghost particles is overlaid on (y, φ) space. The active area is then simply the number of ghost particles clustered into each jet. In regions with no hard particles, ghost particles will cluster into jets themselves. Thus they play an active role in the jet clustering process, giving this definition of jet area its name.

Like the passive area, the active area comes in scalar and 4-vector areas:

$$\begin{aligned} A\left(J_i | \left\{g_j\right\}\right) &= \frac{N_g\left(J_i\right)}{\nu_g} \\ A^\mu\left(J_i | \left\{g_j\right\}\right) &= \frac{1}{\nu_g\left(g_{\mathrm{T}}\right)} \sum_{g_j \in J_i} g_j^\mu \end{aligned} \tag{3.7}$$

Here ν_g indicates the number density of ghost particles in the distribution $\{g_j\}$, and $N_g\left(J_i\right)$ is the number of ghost particles in the i^{th} jet J_i. The randomness inherent in distributing the ghost particles will propagate to the calculated jet area. Hence, in order to ensure a unique answer for each jet that is independent of the particular ghost distribution used, the active area is more properly given by

$$\begin{aligned} A\left(J_i\right) &= \lim_{\nu_g \to \inf} \left\langle A\left(J_i | \left\{g_j\right\}\right)\right\rangle_g \\ A^\mu\left(J_i\right) &= \lim_{\nu_g \to \inf} \left\langle A^\mu\left(J_i | \left\{g_j\right\}\right)\right\rangle_g \end{aligned} \tag{3.8}$$

where $\langle \star \rangle_g$ indicates an average over different ghost distributions. In practice, however, it is usually sufficient to use one appropriately dense ghost distribution and forego the limiting process [64].

3.3.3 Jet Area-Based Background Correction

Using either of these definitions of jet area, it can be shown that the impact on a jet's transverse momentum due to a diffuse background from the UE, PU, or other sources of background is given by

$$\Delta p_{\mathrm{T}}^{\mathrm{jet}} = A^{\mathrm{jet}}\rho \pm \sigma\sqrt{L} - L \tag{3.9}$$

where ρ measures the level of diffuse noise, σ measures the size of fluctuations in ρ, and L is the gain or loss of energy due to jet consituents being gained or lost as a result of the clustering process being affected by the presence of the diffuse background [65].

Assuming that σ and L are small, the corrected jet p_{T} can easily be calculated:

$$\begin{aligned} p_{\mathrm{T}}^{\mathrm{jet}} &= p_{\mathrm{T}}^{\mathrm{meas}} - \left(\rho \cdot A^{\mathrm{jet}}\right) \\ p_{\mu}^{\mathrm{jet}} &= p_{\mu}^{\mathrm{meas}} - \left(\rho \cdot A_{\mu}^{\mathrm{jet}}\right) \end{aligned} \tag{3.10}$$

In the limit where the background is sufficiently uniform and dense, ρ would simply be $p_{\mathrm{T}}^{\mathrm{jet}}/A^{\mathrm{jet}}$. However, local fluctuations in PU will cause values of $p_{\mathrm{T}}^{\mathrm{jet}}/A^{\mathrm{jet}}$ to be distributed about ρ, and so a reasonable measurement of ρ would be the median of this distribution:

$$\rho = \text{median}\left\{\frac{p_{T,j}^{\mathrm{jet}}}{A_j^{\mathrm{jet}}}\right\} \tag{3.11}$$

Similarly, σ can determined by requiring that $(1-x)/2$ jets satisfy

$$\frac{p_{\mathrm{T}}^{\mathrm{jet}}}{A^{\mathrm{jet}}} < \rho - \frac{\sigma}{\sqrt{A^{\mathrm{jet}}}} \tag{3.12}$$

where $x = \mathrm{Erf}\left(1/\sqrt{2}\right)$. For simplicity, $\sqrt{A}$ is frequently replaced with $\sqrt{\langle A\rangle}$.

This correction scheme is valid if three conditions are met: (1) that PU noise is in-

dependent of y and φ; (2) that R_{jet} is greater than the minimum distance between PU particles; and (3) that the number of PU jets is substantially larger than the number of hard jets [65].

Throughout this thesis, only the active area will be used in calculations. Hence "jet area" will unambiguously refer to the active definition. Moreover, as the observable of interest here – jet momentum spectra – does not depend on the jet direction, only the scalar area will be utilized.

It should be noted here that the $\rho \cdot A^{\text{jet}}$ subtraction used in this thesis is not the only method to correct for the UE in pp collisions. A notable alternative is the *Perpendicular Cones* or *Off-Axis Cones* method which has been used by both the ALICE[5] collaboration at the LHC [66] and the STAR Collaboration [67, 68].

In contrast to the $\rho \cdot A^{\text{jet}}$ method, which measures the UE on an event-by-event basis, the Off-Axis Cone method measures the UE on a jet-by-jet basis. Following [67], two cones of radius of R_{jet} are drawn centered at the same pseudorapidity as the axis of a given jet but displaced by $\pm\pi/2$ in relative azimuth. Then the energy density contained within the $+\pi/2$ and $-\pi/2$ cones respectively is:

$$\sigma^{\pm} = \frac{\Sigma_i \varpi_{\text{T}}^i}{\pi R_{\text{jet}}^2} \tag{3.13}$$

where ϖ_{T}^i is the transverse momentum of the i^{th} object (particle, TPC track, etc.) falling in the $+$ or $-\pi/2$ cone. The densities of the two cones are then averaged together, and the corrected jet transverse momentum is given by:

$$p_{\text{T}}^{\text{jet}} = p_{\text{T}}^{\text{meas}} - \left(\bar{\sigma} \cdot A^{\text{jet}}\right) = p_{\text{T}}^{\text{meas}} - \frac{A^{\text{jet}}}{2}\left(\sigma^{+} + \sigma^{-}\right). \tag{3.14}$$

A comparison of the $\rho \cdot A^{\text{jet}}$ and Off-Axis Cone methods as applied to the data analyzed in

[5] **A** **I**on **C**ollider **E**xperiment

this thesis can be seen in figure 8.5.

3.4 Jet Observables

Before proceeding, it will be useful to define a few terms and observables commonly associated with jet measurements in heavy-ion collisions (for a recent review see [69]). Such measurements can make use of the reconstructed jets themselves, or use single particles that stand in as proxies for the reconstructed jets. For jet proxies, two common objects of study are inclusive single hadron spectra and dihadron correlations.

A common observable in heavy-ion collisions that makes use of inclusive single hadron spectra is the ratio R_{AA}, or more generally, R_{AB}. This quantifies the extent to which particle production is modified by the environment of a collision between two nuclei A and B relative to pp collisions. It is defined to be the ratio of the inclusive cross-section of a given observable as measured in AB collisions (σ_{AB}) over the inclusive cross-section in pp collisions (σ_{pp}) scaled to account for the number of independent nucleon-nucleon collisions in AB:

$$R_{AB} = \frac{d^3\sigma_{AB}/dp_{\mathrm{T}}dy}{\langle T_{AB}\rangle d^3\sigma_{pp}/dp_{\mathrm{T}}dy} \tag{3.15}$$

where p_{T} and y are the transverse momentum and rapidity of the produced particle, $\langle T_{AB}\rangle = \langle N_{\mathrm{coll}}\rangle/\sigma_{pp}^{\mathrm{inel}}$ is the "nuclear overlap function," $\langle N_{\mathrm{coll}}\rangle$ is the average number of inelastic binary nucleon-nucleon collisions that happens in an AB collision, and $\sigma_{pp}^{\mathrm{inel}}$ is the total cross-section of inelastic pp collisions. The notation R_{AA}, then, designates R_{AB} for a symmetric collision system such as AuAu or PbPb.

If an AA collision were simply the superposition of multiple binary pp collisions, then $R_{AA} \approx 1$ for hard (large momentum transfer) processes such as jet production. Then $R_{AA} > 1$ indicates an enhancement of particles relative to what would be expected from pp (appropriately scaled), and $R_{AA} < 1$ indicates a suppression. While such measurements

are conceptually easy, interpreting them can be challenging due to the possible interplay of nuclear mechanics besides those of the QGP (so called "cold matter effects").

A common alternative is R_{CP}, the ratio of an inclusive spectra in central AA collisions over the same inclusive spectra in peripheral AA collisions:

$$R_{CP} = \frac{\langle N^{P}_{\text{coll}} \rangle}{\langle N^{C}_{\text{coll}} \rangle} \frac{d^3 N^{C}_{AA}/dp_{\text{T}}dy}{d^3 N^{P}_{AA}/dp_{\text{T}}dy} \tag{3.16}$$

where P and C indicate quantities associated with *peripheral* and *central* collisions respectively. The terms peripheral and central refer to the *centrality* of a collison, the extent of overlap between the two colliding ions. A central collision is one in which there is substantial overlap between the two, and a peripheral collision is one in which there is minimal overlap. The quantities $\langle N^{\star}_{\text{coll}} \rangle$ in equation 3.16 are the average number of binary nucleon-nucleon collisions in central and peripheral collisions respectively. This ratio is frequently used in situations where no pp reference is available or the uncertainties on the pp reference are large relative to the AA sample.

In dihadron correlations, events are identified which contain a high p_{T} hadron (or electroweak boson, as will be discussed in chapter 5) which is used to define the coordinate system of a collision. The high p_{T} hadron is referred to as a *trigger*, and is a good proxy for the axis of the jet from which it originated due to its high energy. The hadrons which are produced in the same jet or contained in a recoil jet are referred to as *correlated* or *associated* hadrons. The trigger then defines a **N**ear **S**ide (NS) of the collision – the region near the trigger with a relative azimuth of $\Delta\varphi \sim 0$[6] – and an **A**way **S**ide (AS) of the collision – the region opposite the trigger with a relative azimuth of $\Delta\varphi \sim \pi$.

A common observable in heavy-ion collisions which makes use of dihadron correlations is I_{AA}, the ratio of per-trigger (conditional) yield of correlated hadrons in a heavy-ion

[6] $\Delta\varphi = \varphi_{\text{trg}} - \varphi_{\text{assoc}}$

collision (D^{AA}) over the corresponding per-trigger yield of correlated hadrons in pp (D^{pp}):

$$I_{AA} \equiv \frac{D^{\mathrm{AA}}(\star)}{D^{pp}(\star)} \tag{3.17}$$

where $\star$ indicates some independent variable such as z_{T} or p_{T} of the correlated jet or jet proxy. Like R_{AA}, I_{AA} quantifies the extent to which a heavy-ion collision modifies the per-trigger yield relative to pp. However, I_{AA} has the benefit that the per-trigger yields that form the ratio are self-normalizing: the normalization is the number of measured triggers. In contrast, R_{AA} requires that the inclusive spectra be absolutely normalized, and thus one needs to know the integrated luminosity corresponding to the measured sample. Recent STAR and PHENIX measurements of I_{AA} will be discussed in chapter 5.

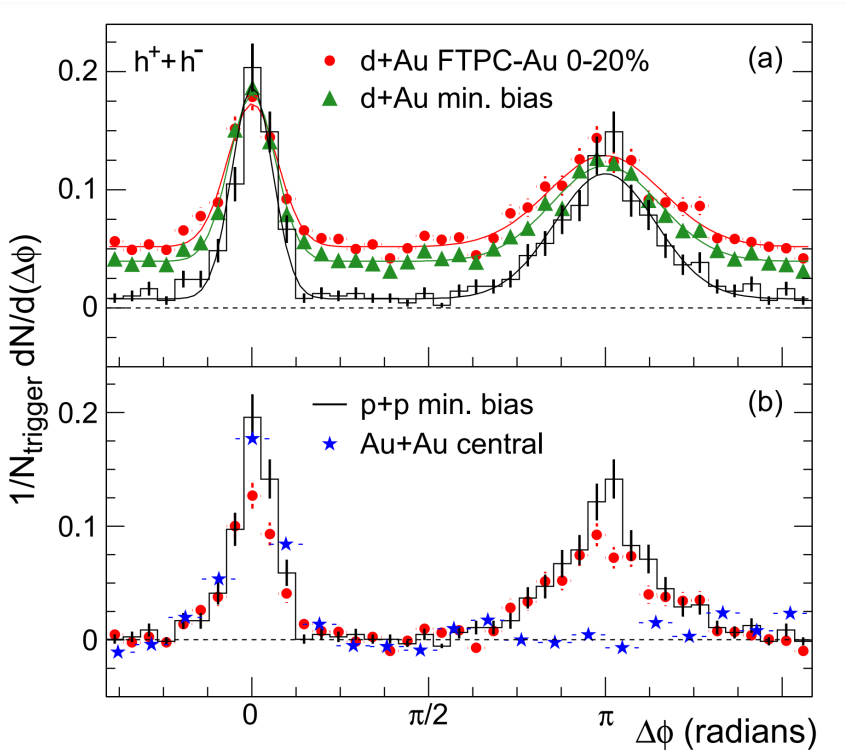

Figure 4.1: Azimuthal dihadron correlations as measured by STAR in 2003 in pp, dAu, and AuAu collisions. Used with permission from [5].

One of the most strking observations made by RHIC in its first years of running was that of *Jet Quenching:* the suppression of energetic hadrons in AA collisions relative to small collision systems such as pp. Figure 4.1 shows azimuthal dihadron correlations measured by the STAR collaboration in 2003 [5]. In both pp and dAu collisions, a clear NS and AS peak are observed. However, in AuAu – in which a hot, dense QGP-like medium was anticipated to be produced – the AS peak is absent.

Jet quenching has long been postulated as a one of the consequences of the formation

of a QGP in AA collisions [70]. The phenomenon is believed to be the result of partons traversing the medium and through interactions with the medium, losing energy. The details of this in-medium partonic energy loss depend intimately on the characteristics of the medium. Thus a quantitative understanding of the energy lost by a parton as it moves through the medium would yield valuable information about the properties of the QGP.

4.1 Radiative Energy Loss

The total energy lost by a parton in medium can be described as the sum of the energy lost via *collisional interactions* and that lost via *radiative interactions*. In collisional interactions, the traversing parton experiences 2-to-2 *elastic* scatterings with medium constituents. While in radiative interactions, the traversing parton experiences *inelastic* scatterings.

To elaborate further: in QED, an electrically charged particle (such as an electron) moving past another charged particle nearby (such as a nucleus) may be deflected, causing the moving particle to decelerate and lose kinetic energy. In this case, the lost kinetic energy is carried off by a photon radiated by the deflected particle. This radiation is called *bremsstrahlung*[1]. An analogous process occurs for a parton moving through the QGP wherein it is deflected by a nearby color charge (a medium constituent) and emits a gluon as bremsstrahlung. This is what is meant by radiative energy loss in the QGP.

For muons moving through copper, the dominate mode of energy loss for low momentum (between 10 MeV/c and 100 GeV/c or so) is collisional: this is the region indicated by "Bethe" in figure 4.2. For high energies, though, the dominate mode becomes radiative (the region indicated by "Radiative"). However, muons in copper and partons in a QGP are not directly comparable, and it has been shown that radiative losses become dominant at far lower energies in the QGP case [71, 72].

[1] "Braking radiation" (German).

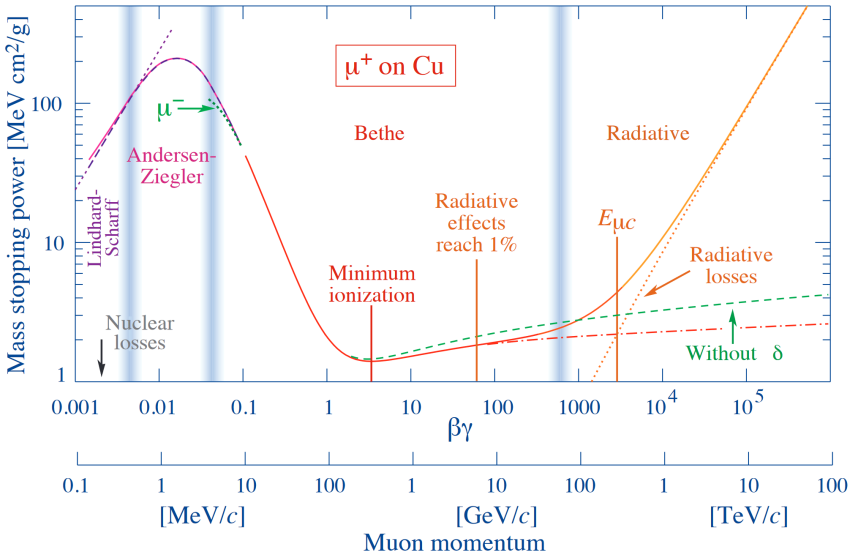

Figure 4.2: The energy lost per unit length $-dE/dl$ ("stopping power") for μ^- in Copper as a function of momentum (lower axis). The vertical bars indicate shifts in the dominate mode of energy loss. From [6].

For instance, an important phenomenon to consider in the case of splitting partons and medium-induced gluon radiation is the "**L**andau-**P**omeranchuk-**M**igdal (LPM) Effect" [73, 74]. It will take a finite amount of time to complete the process of a hard parton emitting a collinear (small angle) gluon, the formation time of which is $\tau_f \sim 2\omega/k_{\mathrm{T}}^2$ where ω and k_{T} are the energy and transverse momentum of the radiated gluon. If τ_f is larger than the mean free path λ of the hard parton, then the multiple scatterings the parton will undergo in the medium cannot be considered independent and so will experience quantum interference. This results in an induced radiation spectrum which is more suppressed than if these scatterings were incoherent (as in the case of the muon moving through copper). However, the non-abelian nature of QCD means that the radiated gluons will rescatter with soft gluons in the medium, which results in an overall enhancement in the induced radiation spectrum than in the QED case.

4.2 Jet Quenching Formalisms

As radiative energy losses dominate for hard partons moving through a QGP, understanding radiative energy loss is crucial for understanding the phenomenon of jet quenching. There are four major pQCD-based formalisms though which radiative energy loss of light quarks and gluons is modeled:

1. the **B**aier-**D**okshitzer-**M**ueller-**P**eigné-**S**chiff and **Z**hakarov (BDMPS-Z) formalism;
2. the **G**yulassey-**L**evai-**V**itev (GLV) formalism;
3. the **H**igher **T**wist (HT) formalism; and
4. the **A**rnold-**M**oore-**Y**affe (AMY) formalism.

These formalisms fall into two categories: the BDMPS-Z and GLV formalisms calculate the in-medium radiated gluon spectrum, and the HT and AMY formalisms calculate the impact on the final distribution of hard particles due to medium interactions. For recent reviews and comparisons of these formalisms see [75, 76, 77]. Each formalism will be described in detail below.

Each of these formalisms approaches the task of characterizing in-medium radiative energy loss by considering a parton produced in a hard process (referred to as the "hard" or "traversing" parton below) which traverses the medium with a path-length L. Each formalism will take a different approach in characterizing the medium, but a few key variables which describe the properties of the medium that will be mentioned are the medium temperature T; its Debye mass $m_D(T) \sim gT$, where g is the parton-medium coupling, which is inversely proportional to the color screening length and related to the scale of typical momentum exchanges with the medium; and the *jet transport coefficient* or *quenching parameter* $\hat{q}$:

$$\hat{q} = \frac{\langle \Delta p_{\mathrm{T}}^2 \rangle}{L} = \frac{m_D^2}{\lambda} \tag{4.1}$$

which characterizes the color scattering power of the medium with the average momentum squared $\langle p_{\mathrm{T}}^2 \rangle$ exchanged with the medium per unit length [78, 79, 80]. Here λ is the mean free path of a parton in the medium.

4.2.1 The BDMPS-Z/ASW-MS Formalism

The BDMPS-Z framework was developed by Baier, Dokshitzer, Mueller, and Schiff [81, 82], and independently by Zhakarov under the name the "**L**ight **C**one **P**ath **I**ntegral" (LCPI) approach [83]. Numerical implementations of this framework were developed by **A**rmesto, **S**algado, and **W**iedemann [84] in its **m**ultiple **s**oft scattering limit. Hence this formalism is frequently labeled as ASW-MS as well.

This framework approaches the task of describing radiative energy loss by considering a hard parton moving though a medium which consists of a set of static colored scattering centers with some density ρ and undergoing a series of soft scatters with these centers, emitting gluons in the process. The effect of an expanding medium is simulated by decreasing ρ with increasing path-length of the traversing hard parton.

The propagation of the hard parton through the medium is described by a path integral over the fields of the parton and scattering centers. This leads to a resumming of the multiple soft scatters experienced by the hard parton. In the ASW-MS implementation, this reults in a set of "quenching weights" $P_E\left(\epsilon|\hat{q}\right)$ which are applied to the vacuum fragmentation function $D_{h/i}^{\mathrm{vac}}$ to obtain the in-medium fragmentation function $D_{h/i}^{\mathrm{med}}$:

$$D_{h/i}^{\mathrm{med}}\left(z'\right) = P_E\left(\epsilon|\hat{q}\right) \otimes D_{h/i}^{\mathrm{vac}}\left(z\right) \tag{4.2}$$

where $\epsilon = \Delta E/E$ is the fraction of energy lost by a parton of energy E, z is the momentum

fraction of a produced hadron with respect to the undegraded parton energy, and z' is the momentum fraction of a produced hadron with respect to the degraded parton energy.

The spectrum of radiated gluons in medium in the BDMPS-Z framework is proportional to the term $(\hat{q}L)^{-1} \exp\left[-Q_{\mathrm{T}}^2/\hat{q}L\right]$ where Q_{T}^2 is the momentum transfer squared of the hard interaction which produced the traversing hard parton. Thus, the properties of the medium here are fully defined by $\hat{q}$.

There are two major assumptions in this approach: (1) that the hard parton only undergoes soft scatters, and (2) that any sort of gluon emission by the scattering centers (i.e. any sort of recoil motion of the centers) is negligible.

4.2.2 The GLV/ASW-SH Formalism

The GLV framework was developed by **G**yulassey, **L**evai, and **V**itev [85, 86, 87], and independently by Wiedemann [88, 89]. It was shown that this framework is a limiting case of the BDMPS-Z framework wherein the hard parton only undergoes a single hard scatter [88, 84, 90]. For this reason the formalism is frequently labeled ASW-SH (for **s**ingle **h**ard scatter) as well.

The GLV framework shares its description of the medium with the BDMPS-Z framework, but differs in how it approaches gluon emission. Here the single hard gluon spectrum is expanded in a power series in orders of *opacity*, the number of scatters experienced in a medium. In a single scattering, the traversing hard parton gains transverse momentum from the medium and then radiates a gluon before or after the scattering. Multiple scatterings experienced by the traversing parton are accounted for by a recursive diagrammatic procedure.

For a given opacity, each emission is assumed to be independent and distributed according to a Poisson distribution. Then quenching weights $P_n\left(\epsilon, E\right)$ similar to the ASW-MS approach may be calculated which describe the probability of a parton of energy E

losing an energy fraction ϵ due to n emissions. Summing over n gives the total probability P of a parton losing ϵ, and thus the medium-modified fragmentation function is given by $D_{h/i}^{\text{med}}(z') = P(\epsilon, E) \otimes D_{h/i}^{\text{vac}}(z)$ just like in ASW-MS. Most phenomenological calculations only use the 1st order in opacity.

Here the medium is characterized by two parameters: the Debye mass m_D which regulates the infrared behavior of the single scattering cross-section, and the initial density ρ of the scattering centers, which must be extracted from data. The primary assumptions made in this approach are that (1) multiple gluon emissions are independent, and (2) that the scattering centers are static. However, the framework was later extended to include **d**ynamic scattering centers in the DGLV implementation of the framework by Djordevic and Heinz [91].

4.2.3 The HT Formalism

The HT formalism was developed by Guo and Wang [92, 93]. In its initial formulation, it only included single scatterings per gluon emission, but the approach was later extended to include multiple scatterings per emission by Majumder [94].

In this framework, the medium is encoded in "higher twist" matrix elements – meaning matrix elements involving higher-order moments of QCD operators – which modify the LO, vacuum jet production cross section with a power series ordered according to the number of scatterings per gluon emission. The jet production cross section is factorized into a nPDF piece (re. section 3.1) and the HT piece which describes interactions between the traversing parton and the medium. This factorization is valid to LO in parton path-length.

The HT matrix elements result in an additive correction to the vacuum fragmentation function:

$$D_{h/i}^{\text{med}} = D_{h/i}^{\text{vac}} + \Delta D_{h/i} \tag{4.3}$$

where $\Delta D_{h/i}$ is the correction and is proportional to $\Delta P_{ij}^{\text{med}}$, the medium modified **A**ltarelli-**P**arisi (AP) QCD splitting function which is proportional to $P_{ij}^{\text{vac}} C_A \alpha_s T_{qg}^A$. Here P_{ij}^{vac} is the vacuum AP QCD splitting function, which describes how energy is distributed across $1 \to 2$ partonic splittings, and T_{qg}^A is the nuclear quark-gluon correlation term. This term encodes *all* of the medium effects in the HT approach. In contrast to the GLV formalism, HT makes use of only the LO moment of the exchanged p_{T} distribution in computing T_{qg}^A. This means that T_{qg}^A is characterized exclusively by $\hat{q}$.

The nuclear quark-gluon correlation term needs to be normalized. This can be done by fitting the computed cross-section to a data point wherein one can calculate $D_{h/i}^{\text{med}}$ directly and then calculate the final hadron spectrum. The normalization factor is related to the average energy loss suffered by a traversing parton.

The primary assumption made in this formalism is the factorization of the cross-section. Both the GLV and HT formalisms make use of an expansion in terms of opacity, and, much like in the GLV formalism, phenomenological calculations frequently use only the single scattering per emission term.

4.2.4 The AMY Formalism

The AMY formalism was originated by Arnold, Moore, and Yaffe [95, 96, 97]. In it, the medium is assumed to be a thermally equilibrated, weakly coupled state in the sense of **H**ard **T**hermal **L**oop theory (for a brief discussion of HTLs and finite temperature QFTs, see chapter 4 of [42]). This means that the relation $T \gg gT \gg g^2T$ holds with g being the parton-medium coupling constant and T being the medium temperature. Thus, the properties of the medium are determined solely by its temperature.

In this framework, the traversing parton scatters off the medium with momentum trans-

fers on the order of $\mathcal{O}(gT)$. These scatterings are encoded in a $1 \to 2$ scattering rate Γ^a_{bg} wherein a parton a splits into an outgoing parton b and a radiated gluon g. The original parton distribution P_a is then evolved along with the medium over a time τ according to a Fokker-Planck type equation:

$$\frac{dP_a}{d\tau} = \int dk \left[P_b(p+k) \frac{d\Gamma^b_{ac}(p+k,p)}{dk d\tau} - P_a(p) \frac{d\Gamma^a_{bc}(p,k)}{dk d\tau} \right] \tag{4.4}$$

where k is the momentum transferred in the scatter.

The medium-modified fragmentation function is then described as a convolution of the final (medium-modified) hard parton distribution P_f and $D^{\text{vac}}_{h/i}$:

$$D^{\text{med}}_{h/i}(z) = \int dp_f \frac{z'}{z} \sum_a P_a(p_f|p_i) D^{\text{vac}}_{h/a}(z') \tag{4.5}$$

where p_i, p_f are the initial and final momenta of the traversing parton, and $z' = p_h/p_f$, $z = p_h/p_i$ are the momenta fractions of a produced hadron with momentum p_h with respect to the final and initial momenta of the traversing parton respectively.

The major assumption made by this framework is that of thermal equilibrium. It is still very much an open question as to the extent to which this assumption holds in heavy ion collisions (see for instance [98]). Furthermore, AMY was initially developed assuming an infinitely large medium. Caron-Huot and Gale later extended the formalism to include finite size effects [99]. Lastly, the assumption that the medium is weakly coupled made by the framework necessarily means that it is only applicable to a very high temperature QGP.

4.3 Comparisons of the Quenching Formalisms

Each of the four formalisms discussed above has advantages and disadvantages, and each captures different aspects of in-medium energy loss. There are nonetheless several

points of similarity and contrast between the four. For instance, both the BDMPS-Z and GLV formalisms share the formulation of the medium as a set of static scattering centers and both implement multi-gluon emission by repeatedly invoking a 1-gluon emission kernel. In contrast, both the HT and AMY formalisms deploy an approach which makes use of a coupled evolution between the hard parton and the medium. This enables HT and AMY to keep track of the relative quark and gluon distributions within a jet as well as its gradual degradation in energy [76, 77].

However, the BDMPS-Z and GLV approaches work well for both thick (large L) and thin (small L) media. Though HT shares the opacity expansion with GLV, the HT formalism is more applicable to thin media. On the other hand, the HT formalism enables studies of multiparticle correlations and the direct calculation of the medium-modified fragmentation function [75].

One advantage shared by the three formalisms other than AMY is that they all can accommodate vacuum radiation and the interference between vacuum and medium radiation [76]. However, AMY has the advantage that it is the only formalism which allows for situations in which the hard parton absorbs energy from the medium. Furthermore, both AMY and HT are the only two which account for energy flow *into* the medium [75].

Lastly, while the four formalisms each make specific assumptions in their construction, there are several assumptions which they share in common. For instance, all four make use of the *eikonal approximation:* the energy E of the hard parton and the energy ω of the radiated gluon are stipulated to be such that they are much larger than the transverse momentum exchanged between them q_{T}, i.e. $q_{\mathrm{T}} \ll E, \omega$. Furthermore, the gluon energy is frequently stipulated to be soft ($\omega \ll E$) in phenomenological calculations using these formalisms (aside from AMY) [77].

All four also stipulate that the radiated gluons be collinear (small-angle) with respect to the hard parton, and all assume that the momentum transfers between the hard parton

and the radiated gluon are *localized.* This means that the mean free path λ of the radiated gluon is much smaller than the screening length L_D, i.e. $\lambda \ll L_D = 1/m_D$. A closely related assumption that all four make is that the remaining path-length of the traversing hard parton does *not* degrade with lost energy. However, this is an immensely challenging problem to address as one would have to keep track of local information, finite size effects, *and* interference between radiation across the medium. All of this would result in a description of medium-induced gluon radiation that is decidedly non-local [77].

4.4 Other Approaches to Jet Quenching and Modeling the QGP

In addition to the four formalisms discussed above there are several alternative approaches to modeling in-medium partonic energy loss. For instance, another popular approach to in-medium energy loss is the use of *Transport Models.* The Fokker-Planck rate equation (equation 4.4) used in the AMY formalism is an example of just such a transport model. By solving equation 4.4, one obtains the time evolution of both a hard parton as it propagates through the medium and the medium itself. As noted, such an approach enables one to keep track of both the hard and thermal quark and gluon populations over time. A similar transport approach was recently implemented in a **L**inear **B**oltzmann **T**ransport (LBT) model wherein both the hard partons of the jet shower and the medium response partons are simulated using a linearized Boltzmann Equation [100, 101, 102].

However, the most popular approach to modeling the QGP itself in energy-loss models is that of *Viscous Relativistic Hydrodynamics*. For two recent reviews of hydrodynamic techniques in heavy-ion collisions see [103, 104]. Observables related to collective flow in relativistic heavy-ion collisions have been found to be well described by hydrodynamics [105]. Thus, many jet quenching models use hydrodynamic simulations to model the medium through which a parton propagates. For example, a recent iteration on the LBT approach – the **C**oupled LBT and **hydro**dynamics (CoLBT-hydro) model [106] – developed

by Chen *et al.* describes the process of jet quenching by coupling a (3+1)d hydrodynamic model of the QGP to a linearized Boltzmann Equation. The hydrodynamic model provides the local temperature and viscosity of the medium while the Boltzmann Equation simulates the propagation of the parton through the fluid medium.

Moreover, the collective flow observed in heavy-ion collisions suggests that the medium formed is very strongly coupled [107, 108, 109] meaning that non-perturbative dynamics may play a significant role in heavy-ion phenomenology. A common approach to describing these non-perturbative aspects of such a system is to make use of the **A**nti-**d**e **S**itter/**C**onformal **F**ield **T**heory (AdS/CFT) correspondence [110, 111]. For a recent review of AdS/CFT techniques see [112]. The Ads/CFT correspondence states that a 4-dimensional strongly coupled conformal field theory is equivalent to a weakly coupled gravity described by a string theory in a 5-dimensional Anti-de Sitter space (meaning that it has constant negative curvature). Thus analytic calculations can be carried out perturbatively with the string theory in the 5d AdS space and then mapped "holographically" onto the non-perturbative dynamics of the 4d CFT. Jet quenching can be described using the AdS/CFT by replacing the AdS space with an AdS black hole, where the Hawking Temperature of the black hole corresponds to the temperature of the medium [113, 114, 115]. Then the propagation of a parton through the medium is described by the stretching of a string in the presence of the AdS black hole. Solving the equations of motion for the string enables the extraction of medium properties such as $\hat{q}$.

5. Neutral Triggers and Energy Loss

The phenomenon of in-medium energy loss is experimentally well established (e.g. [5]). However obtaining a quantitative understanding of the phenomenon is extremely challenging due to the complex interplay of various physical mechanisms, geometric biases, experimental limitations, and backgrounds involved in observables associated with energy loss. The study of recoil jets opposite direct photons, though, offers a "golden channel:" a penetrating, well-calibrated probe through which we can study in-medium energy loss.

5.1 Prompt and Direct Photons

Photons are produced at every stage of a heavy-ion collision (for a recent review of the theory and experimental techniques behind photons in heavy ion collisions, see [116]). However, these photons can be classed into two broad categories based on their production source: *direct photons* (γ_{dir}) and *decay photons*. Decay photons are those produced in the decay of hadrons such as π^0 or η. Direct photons then encompass photons from various sources that can be further divided into two sub-categories.

Prompt Photons: these are photons produced by the hard-scattering of partons [117] and potentially "pre-equilibrium" sources, conjectured states of matter that precede the onset of local thermalization in the QGP (e.g. [118, 119]).

Thermal Photons: radiated photons from the locally-thermalized, expanding QGP or a hadron gas [120] analogous to blackbody radiation.

Of particular interest are the prompt photons (γ_{prompt}). There are two sources of prompt photons at **l**eading **o**rder (LO): quark-gluon Compton Scattering ($qg \rightarrow q\gamma$) and quark-

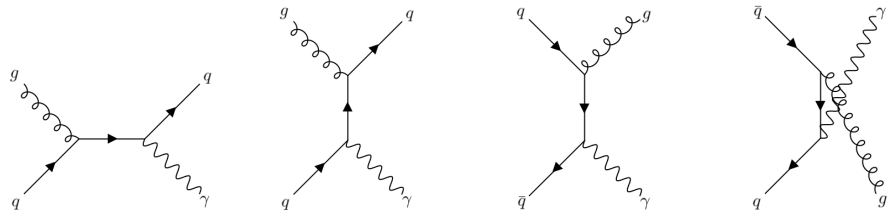

(a) (b) (c) (d)

Figure 5.1: LO diagrams of γ_{prompt} production: the s- (5.1a) and u-channels (5.1b) of qg Compton Scattering, and the t- (5.1c) and u-channels (5.1d) of $q\bar{q}$ annihilation.

antiquark annihilation ($q\bar{q} \to g\gamma$). The relevant Feynman diagrams can be seen in figure 5.1.

For these processes, the Mandelstam variables for qg Compton Scattering are $s_c = (p_g + p_q)^2$, $t_c = (p_g - p_\gamma)^2$; and $u_c = (p_q - p_\gamma)^2$, and those for $q\bar{q}$ annihilation are $s_a = (p_q + p_{\bar{q}})^2$, $t_a = (p_q - p_\gamma)^2$, $u_a = (p_{\bar{q}} - p_\gamma)^2$.[1] For massless partons, the cross-sections for each process are [121]:

$$\begin{aligned} \frac{d\sigma}{dt}(qg \to q\gamma) &= \frac{-\pi\alpha_{\text{em}}\alpha_{\text{s}}e_q^2}{3s_c^2}\left(\frac{u_c}{s_c} + \frac{s_c}{u_c}\right) \\ \frac{d\sigma}{dt}(q\bar{q} \to g\gamma) &= \frac{8\alpha_{\text{em}}\alpha_{\text{s}}e_q^2}{9s_a^2}\left(\frac{u_a}{t_a} + \frac{t_a}{u_a}\right) \end{aligned} \tag{5.1}$$

where α_{em} and α_{s} are the electromagnetic and strong coupling constants, and e_q is the electric charge of the quark. Note that the $q\bar{q}$ annihilation process is suppressed compared with the qg Compton Scattering due to a lack of valence $\bar{q}$ present in the nucleons, however.

The biggest contributions to these are when $u_c \to 0$ ($p_q \approx p_\gamma$) in the case of Compton Scattering, and when $t_a \to 0$ ($p_q \approx p_\gamma$) or $u_a \to 0$ ($p_{\bar{q}} \approx 0$) in the case of $q\bar{q}$ annihilation. Or in other words, the biggest contributions to each are when the γ_{prompt} is collinear with

[1] Here $p_\star$ indicates the 4-momentum of each particle.

the original q ($\bar{q}$). Thus, a measurement of the energy of a γ_{prompt} gives a direct measurement of the initial energy of the recoiling parton. That is **if** the γ_{prompt} are unmodified by the environment of a heavy-ion collision.

Indeed, we should expect that the γ_{prompt} escape the collision unmodified as they are both color and electrically neutral. They will not interact strongly with the produced medium, and the mean free path for electromagnetic interactions of a γ_{prompt} with energy E_γ in medium can be estimated from its equilibration time τ_γ [121]:

$$\tau_\gamma = \frac{9}{10\pi\alpha_{\text{em}}\alpha_{\text{s}}}\frac{E_\gamma}{T^2}\frac{e^{E_\gamma/T+1}}{e^{E_\gamma/T-1}}\frac{1}{\ln\left(3.7388E_\gamma/4\pi\alpha_{\text{s}}T\right)} \tag{5.2}$$

where T is the temperature of the medium. For $\alpha_{\text{s}} = 0.4$ and $T = 200$ MeV, then for even a relatively low energy of E_γ the equilibration time is $\tau_\gamma \approx 481$ fm/c. This is substantially larger than the roughly 10 fm/c lifetime of the medium [122], and will only increase with increasing E_γ.

It should be clarified that there is no experimental method to distinguish γ_{prompt} from the other sources of γ_{dir} such as fragmentation photons, and thus only an admixture of all sources of γ_{dir} is measured. At high energies, though, the contribution from thermal photons to the γ_{dir} signal is vanishingly small and γ_{prompt} overwhelmingly dominate. While decay photons cannot be completely excluded, their contamination in the γ_{dir} signal due to fragmentation or decay photons can be mitigated via a statistical subtraction (see chapter 7).

Moreover, "high energy" can be a somewhat arbitrary designation. Throughout this thesis it will be taken to mean photon energies in excess of 5 GeV. In this regime, the γ_{dir} cross-section is almost exclusively due to the hard scattering of partons – primarily qg Compton Scattering – and so high energy γ_{dir} and γ_{prompt} will be taken to be interchangeable from here on unless a distinction between the two is needed.

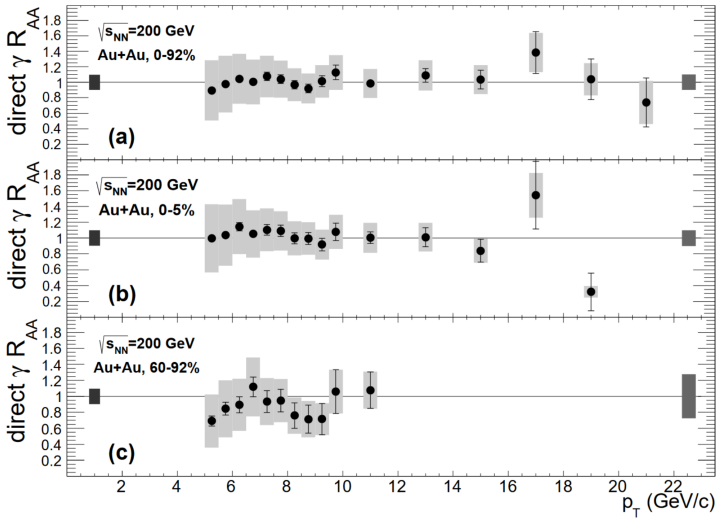

Figure 5.2: R_{AA} for γ_{dir} across three different centralities in $\sqrt{s_{NN}} = 200$ GeV AuAu collisions. Used with permission from [7].

That γ_{prompt} are unmodified by the medium has been confirmed experimentally through measurements of the R_{AA} of high energy γ_{dir}. PHENIX measured the R_{AA} of energetic γ_{dir} in $\sqrt{s_{NN}} = 200$ GeV AuAu collisions in 2012 for several different centralities [7]. All three R_{AA} were consistent with unity (meaning no modification in AuAu) across γ_{dir} p_{T}, and are shown in figure 5.2. Similar results were reported by the LHC [123, 124, 125]. This demonstrates that the γ_{dir} really are unmodified by the environment of a heavy ion collision, and further corroborates that the suppression of energetic hadrons observed in [5] or in [126] is indeed due to jet-quenching.

5.2 Direct Photons and the QGP

As seen in the last section, high energy γ_{dir} do not interact strongly with the produced medium of heavy-ion collisions and so are unmodified by it. Thus (to leading order) the measurement of the γ_{dir} transverse energy (E_{T}^{γ}) is a good approximation of the initial transverse energy of the parton (E_{T}^{0}) they scattered from. This sets the energy scale of the recoiling jets in events tagged by these γ_{dir}, and so makes the measurement of energetic

γ_{dir} and the recoiling jets opposite them an extremely well-calibrated probe of in-medium energy loss.

In 1996 Wang, Huang, and Sarcevic proposed to use hadrons correlated with energetic γ_{dir} to measure the energy lost per unit length by partons as they traverse the medium [8]. They constructed a model of energy loss wherein partons lose energy by radiating gluons with an average energy of ϵ some number of times n over a path-length ΔL through the medium, after which they escape from the medium and fragment according to the usual vacuum fragmentation pattern. Here n is drawn from a Poisson distribution:

$$P(n) = \frac{(\Delta L/\lambda)^{-n}}{n!} e^{-\Delta L/\lambda} \tag{5.3}$$

where λ is the inelastic scattering mean-free path of a parton in the medium, and $P(n)$ is the probability of radiating a gluon n times. The total number of radiations N was limited to $N = E_{\text{T}}^{0}/\epsilon$ to conserve energy, and for large N the average number of scatterings in ΔL is approximately $\langle n \rangle \approx \Delta L/\lambda$.

They then define the inclusive fragmentation function to be:

$$D^{\gamma} = \sum_{jh} r_j \left(E_{\text{T}}^{\gamma}\right) D_{h/j}(z) \tag{5.4}$$

where $r_j\left(E_{\text{T}}^{\gamma}\right)$ is the fractional cross-section of producing a jet of species j correlated with a γ_{dir} with energy E_{T}^{γ}, $D_{h/j}$ are the fragmentation functions discussed in section 3.1 and whose vacuum fragmentation parameterizations are taken from [127], and the indices h and j respectively run over the hadron and jet species considered. The dependence of $D_{h/j}$ on the scale Q^2 here is suppressed as it is set to be E_{T}^{γ}.

Using their energy loss model, they then calculated the inclusive fragmentation functions without energy loss (notated D_{pp}^{γ}) and with energy loss (notated D_{AA}^{γ}), which corresponds to the situation in a central nucleus-nucleus collision. Thus D_{AA}^{γ} is given by:

$$D^{\gamma}_{AA} = \int \frac{d^2 r t^2_A(r)}{T_{AA}(0)} \sum_{jh} r_j\left(E^{\gamma}_{\mathrm{T}}\right) D_{h/j}\left(z, \Delta L\right) \tag{5.5}$$

where $T_{AA}(0) = \int d^2 r t^2_A(r)$ is the nuclear overlap function at an impact parameter of 0; $t_A(r)$ is the nuclear thickness function,[2] and ΔL is the path-length of a parton through the medium. Both D^{γ}_{pp} and D^{γ}_{AA} were calculated for all produced hadrons at mid-rapidity[3] satisfying $|\varphi_h - \varphi_\gamma| \leq 1$. The experimental analogues of $D^{\gamma}_{AA,pp}$ would be the conditional yields of hadrons in the same kinematic region correlated with γ_{dir} triggers in nucleus-nucleus and pp collisions respectively.

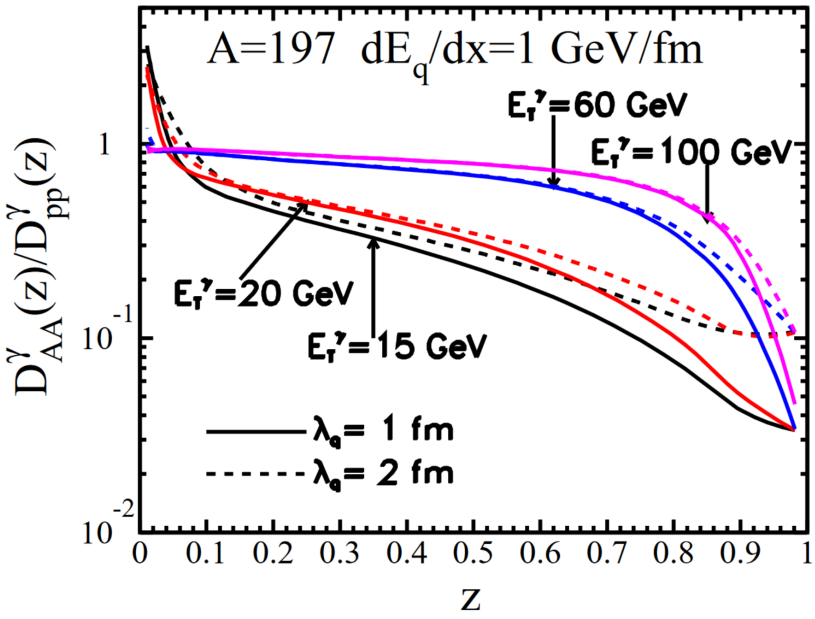

Figure 5.3: The ratio of inclusive fragmentation functions for γ_{dir}-tagged jets with and without energy loss. The energy loss per unit length is fixed to 1 GeV/fm here. Used with premission from [8].

[2]This is normalized such that $\int d^2 r t_A(r) = A$, where A is the mass number of a nucleus.

[3]$|y| \leq 0.5$

The authors then formed the "Suppression Factor" by taking the ratio of the inclusive fragmentation functions with energy loss over that without. This is shown in figure 5.3 for different values of E_{T}^{γ} as a function of the produced hadrons' z ($= p_{\mathrm{T}}^{h}/E_{\mathrm{T}}^{0}$). This suppression factor corresponds to the experimental observable of I_{AA}. If the suppression factor is unity, the fragmentation function is un-modified by energy loss. As E_{T}^{γ} increases, the suppression factor approaches unity across z. However, for lower E_{T}^{γ} there is a substantial suppression, especially at moderate z. Thus the authors propose that there will be a sweet spot for measuring this suppression for E_{T}^{γ} between 10 and 20 GeV, in which backgrounds will be relatively low for $\sqrt{s_{NN}} = 200$ GeV nucleus-nucleus collisions.

Within the framework of their model, the suppression factor at high z is given by $\langle \exp\left(-\Delta L/\lambda\right)\rangle$, which is independent of the total jet energy $E_{\mathrm{T}}^{0} = E_{\mathrm{T}}^{\gamma}$ and the energy loss per unit length dE/dx. At intermediate values of z ($\approx 0.2 - 0.5$), the energy loss per scattering will be much smaller than the total jet energy, $\epsilon \ll E_{\mathrm{T}}^{0} = E_{\mathrm{T}}^{\gamma}$. Since the total energy lost by the leading[4] parton is $\langle \Delta E_{\mathrm{T}} \rangle = \langle n \rangle = \langle \Delta L \rangle dE/dx$, the suppression factor will depend very weakly on the mean free path.

In principle, a measurement of the suppression factor at high z would then enable the extraction of λ, and an additional measurement at mid z would enable the extraction of dE/dx. As noted in [128], the energy loss per unit length, dE/dx, experienced by a parton is approximately:

$$\frac{dE}{dx} \approx -\alpha_{\mathrm{s}} \langle Q^2 \left(\Delta L\right) \rangle = \frac{\alpha_{\mathrm{s}} \mu^2 \Delta L}{\lambda} = \alpha_{\mathrm{s}} \hat{q} \Delta L \tag{5.6}$$

in the BDMPS-Z formalism. Here Q^2 is the squared momentum-transfer in the original hard scattering, μ is the mean momentum transfer per hard scatter, and $\hat{q}$ is the jet transport coefficient. Hence such a measurement described by the authors would enable the

[4] i.e. hardest

calculation of the jet transport coefficient.

Since the authors' proposal, precise measurements of I_{AA} of recoiling hadrons correlated with γ_{dir} have been furnished by multiple collaboration, particularly PHENIX [10] and STAR [9]. These measurements will be discussed in detail in section 5.4. Using the data from these measurements, theorists have been able to extract $\hat{q}$ (e.g. [128, 129]). For instance, in [128] $\hat{q}$ was found to be 1.2 ± 0.38 GeV^2/fm for lower values of p_{T}^h and 0.24 ± 0.096 GeV^2/fm for higher values of p_{T}^h (for a weighted average of 0.30 ± 0.09 GeV^2/fm) assuming a path-length of $\Delta L \approx 7$ fm in central AuAu collisions. These values are close to or less than the value of $\hat{q} \approx 1.2 \pm 0.3$ GeV^2/fm calculated by the JET collaboration using measurements of R_{AA} [130].

5.3 Neutral Pions vs. Direct Photons

In contrast to γ_{dir}, hadron triggers – such as neutral pions (π^0) – are not good approximations of the initial energy of the recoiling parton. This is because hadrons are produced in the fragmentation of a parton and thus can only carry a fraction of the initial energy of the scattered parton. The PYTHIA Monte Carlo simulator [131], for instance, suggests that energetic π^0 triggers with $p_{\text{T}}^{\text{trg}} > 12$ GeV/c can carry 80% ($\pm$ 5%) on average of the scattered parton's initial p_{T} [9].

Nevertheless, it is still interesting to compare the energy loss experienced by jets recoiling from γ_{dir} triggers (γ_{dir}+jet) against those recoiling from π^0 (π^0+jet) triggers as the difference in production mechanisms between π^0+jet and γ_{dir}+jet could lead to observable difference between their measured suppression. This could give insight into the path-length and color factor (quark vs. gluon) dependence of in-medium energy loss.

Firstly, there is a difference in the geometric biases between π^0 and γ_{dir} triggers at RHIC energies [132]. Energetic π^0 are likely to have been produced close to the surface of the medium, while γ_{dir} have no such bias as their mean free path is significantly larger than

the produced medium. This would suggest that, on average, the partons recoiling from π^0 have a longer path-length than those recoiling from γ_{dir} which would lead to a difference in suppression between the two. However, the interplay between the kinematics of the observed jets or jet proxies (such as charged hadrons, $h^{\pm}$) and their geometrical biases must be considered.

Next-to-**L**eading **O**rder (NLO) pQCD calculations suggest that geometric biases can affect the production of hadrons at different momentum fraction $z_{\text{T}} = p_{\text{T}}^{\text{had}}/p_{\text{T}}^{\text{trg}}$, the ratio of the hadronic p_{T} to the trigger p_{T} [133]. The calculations suggest that high z_{T} hadrons correlated with γ_{dir} triggers tend to originate from hard scatterings that occurred close to the AS of the medium. This is because scatterings occurring deeper in the medium will result in the recoiling parton traversing more of the medium and so losing more energy, resulting in a suppression of energetic hadrons.

In contrast, high z_{T} hadrons correlated with a π^0 trigger tend to originate from scatterings wherein the AS parton recoils tangential to the medium (such as was suggested by the observations from the 2013 study of multihadron correlations by STAR [134]). These two biases would lead to any differences in the observed suppression of charged hadrons at high z_{T} being washed out. Thus it is at low z_{T} where one would expect to observe differences in the observed suppression of π^0+jet and γ_{dir}+jet due to differences in path-length.

Secondly, quark-gluon compton scattering dominates the production cross-section of γ_{dir}. This means that the AS of γ_{dir} triggers are dominated by quark jets. In contrast, at leading order dijet production (and so the jet recoiling from a π^0) comes from both quarks and gluons. However, recent calculations suggests that π^0 with a high energy relative to the total jet energy are somewhat more likely to come from quark jets [135, 136], and so the AS correlated with such π^0 will more likely be gluons [137].

Thus the AS of γ_{dir} triggers is dominated by quark jets, and the AS of energetic π^0 may be dominated by gluon jets. This would lead one to expect the recoil jets of energetic π^0

will experience more suppression than those γ_{dir} due to the larger color factor associated with the gluon. The strengths of the processes of a quark emitting a gluon and a gluon emitting a gluon are proportional to the so-called *color factors* $C_F = 4/3$ (quarks) and $C_A = 3$ (gluons) respectively[5]. Hence it is more likely for a gluon to emit another gluon than it is for a quark to emit a gluon (2.25$\times$ in fact). This leads to gluon jets being more diffuse and soft than quark jets, and so more susceptible to energy-loss.

These two facts – that on average the recoiling partons of π^0 have a longer path-length than their γ_{dir} counterpart, and that the recoiling partons of γ_{dir} tend to be quark jets – would lead one to expect the suppression observed in the recoil jets correlated with π^0 and γ_{dir} to differ, i.e. that π^0+jet would be more suppressed than γ_{dir}+jet. This would manifest experimentally as a difference in the measured I_{AA} between the two systems [10].

5.4 Previous Measurements of I_{AA}

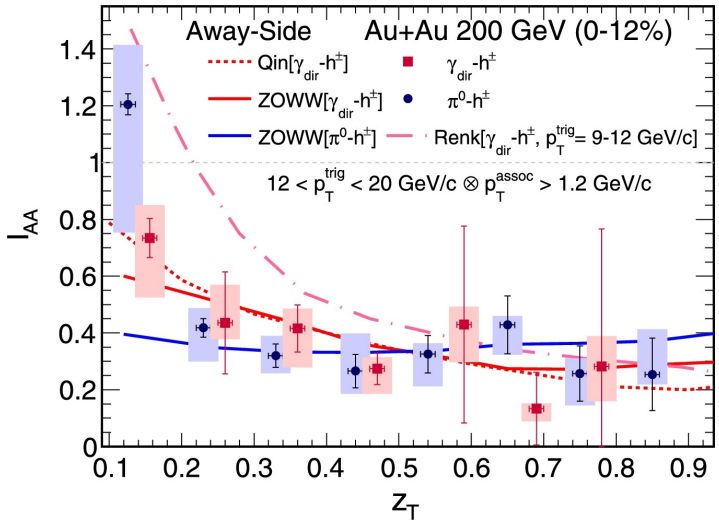

Figure 5.4: I_{AA} for $\gamma_{\text{dir}} + h^{\pm}$ (red boxes) and $\pi^0 + h^{\pm}$ (blue boxes) measured by the STAR collaboration in 2016. The solid curves are theoretical predictions. From [9].

[5]The subscripts refer to the **f**undamental (quark) and **a**djoint (gluon) representations of the SU(3) symmetry group

In 2016 the STAR collaboration measured I_{AA} for AS charged hadrons ($h^{\pm}$) correlated with γ_{dir} and energetic π^0 [9]. In this context, "away side" specifically designates a relative azimuth of $\Delta\varphi^{\text{had}} \in (\pi - 1.2, \pi + 1.2)$ with respect to the trigger. Thus the $h^{\pm}$ here function as proxies for the recoiling jets opposite the γ_{dir} and π^0 triggers. Figure 5.4 shows the measured I_{AA} for $h^{\pm}$ correlated with γ_{dir} ($\gamma_{\text{dir}} + h^{\pm}$) and π^0 ($\pi^0 + h^{\pm}$) as a function of the hadron's z_{T} compared against three theoretical models: Qin [138], ZOWW (**Z**hang, **O**wens, **W**ang, and **W**ang) [133, 139], and Renk [140].

As discussed, the difference in production mechanisms between π^0+jet and γ_{dir}+jet systems might lead one to anticipate a difference in the suppression – and so in the measured I_{AA} as well – experienced by the recoiling jets. Yet STAR observed no difference in the reported I_{AA} of $\gamma_{\text{dir}} + h^{\pm}$ and $\pi^0 + h^{\pm}$ within uncertainties for the sampled kinematic range. However, the low z_{T} hadrons are noticeably less suppressed than those at high z_{T}; $I_{AA} \leq 1$ across the kinematic range of the measurement.

Nonetheless, the comparison between the included theoretical predictions and the data in figure 5.4 is quite compelling. All three incorporate in-medium partonic energy loss in some capacity for γ_{dir}+jet (red lines) and π^0+jet in the case of ZOWW (blue line). The Qin model utilizes the AMY framework [95, 96, 97] with a medium provided by (3+1)d ideal relativistic hydrodynamics; ZOWW utilizes HT techniques for initial jet production [141] with the **B**oltzmann **A**pproach to **M**ultiparticle **S**cattering (BAMPS) [142, 143] model for the non-equilibrium evolution of a (3+1)d ideal relativistic hydrodynamic medium; and Renk utilizes both the ASW-MS framework [84] and YaJEM (**Y**et **a**nother **J**et **E**nergy-loss **M**odel) [144, 145, 146] in a 3d hydrodynamical model.

The Qin and ZOWW models reasonably reproduce the data across z_{T}. However, only the Renk model incorporates redistribution of lost partonic energy into the medium, leading to a large rise in I_{AA} at low z_{T} that is not observed in the data.

In fact, the PHENIX Collaboration also measured I_{AA} for AS $h^{\pm}$ correlated with γ_{dir}

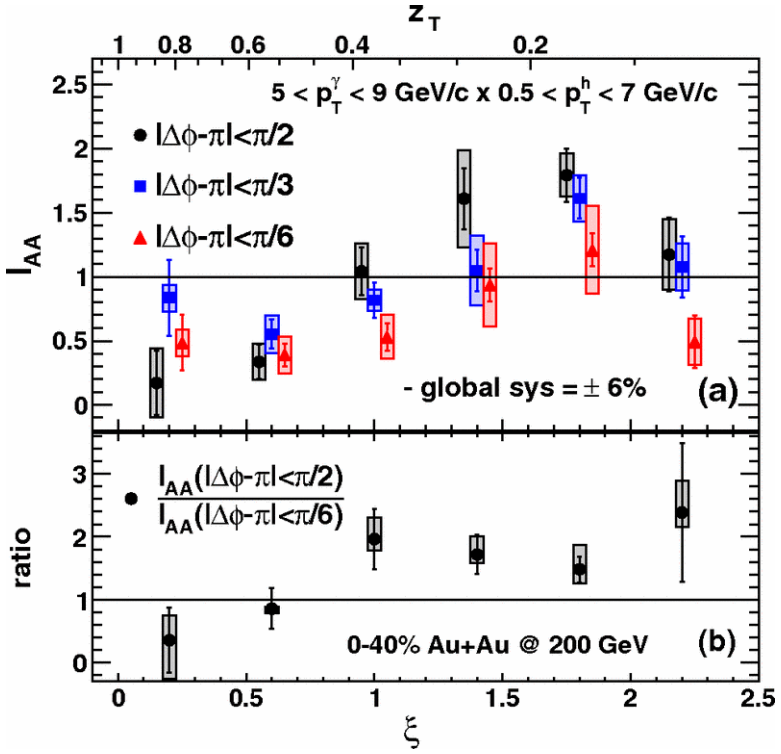

Figure 5.5: I_{AA} for $\gamma_{dir} + h^{\pm}$ and $\pi^0 + h^{\pm}$ measured by the PHENIX collaboration in 2013 for different AS $\Delta\varphi^{\text{had}}$ integration windows. Used with permission from [10].

triggers in 2013 [10] and reported a distinct *enhancement* for low z_{T} $h^{\pm}$. This can be seen in figure 5.5 which shows the measured I_{AA} for $\gamma_{\text{dir}} + h^{\pm}$ and $\pi^0 + h^{\pm}$ in different AS $\Delta\varphi^{\text{had}}$ integration windows as a function of $\xi = \ln(1/z_{\text{T}})$[6].

We can resolve the tension between the STAR measurement and the PHENIX measurement by considering the kinematic windows of the of the two measurements. For fixed range of $z_{\text{T}} \in (0.1, 0.4)$, STAR measured $h^{\pm}$ with $p_{\text{T}}^{\text{had}}$ in the range of $1.2 - 8$ GeV/c correlated with γ_{dir} triggers with $E_{\text{T}}^{\text{trg}} \in (12, 20)$ GeV. Whereas PHENIX measured $h^{\pm}$ with $p_{\text{T}}^{\text{had}}$ in the range of $0.5 - 3.6$ GeV/c correlated with γ_{dir} triggers with $E_{\text{T}}^{\text{trg}} \in (5, 9)$ GeV.

If the energy lost by a parton as it traverses the medium is redistributed into the medium

[6]Thus high ξ corresponds to low z_{T} and vice versa.

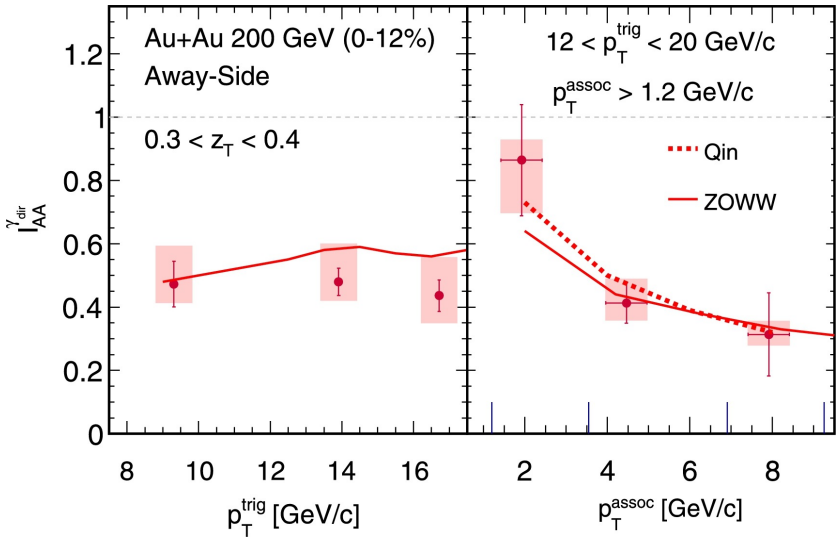

Figure 5.6: I_{AA} of $\gamma_{\text{dir}} + h^{\pm}$ as a function of $p_{\text{T}}^{\text{had}}$ measured by STAR in 2016. From [9].

as soft radiation below a fixed $\mathbf{p}_{\text{T}}$ around 2 GeV/c rather than below a fixed $\mathbf{z}_{\text{T}}$, then both measurements are consistent [9]. This is what one would expect from models such as YaJEM which include energy redistribution into the medium, as can be seen in the prediction for the STAR data provided by Renk. Indeed, STAR also measured the I_{AA} for $\gamma_{\text{dir}} + h^{\pm}$ as a function of $p_{\text{T}}^{\text{had}}$, as shown in figure 5.6, and the low p_{T} $h^{\pm}$ are less suppressed than the high p_{T}.

This picture of in-medium energy loss is further corroborated by other measurements. For instance, PHENIX measured the I_{AA} of $\gamma_{\text{dir}} + h^{\pm}$ using enhanced statistics in 2020 [11]. The enhanced statistics enabled a measurement of I_{AA} differential in the $E_{\text{T}}^{\text{trg}}$ of the γ_{dir} trigger. The I_{AA} for $\gamma_{\text{dir}} + h^{\pm}$ across the three ranges of $E_{\text{T}}^{\text{trg}}$ is shown in figure 5.7. If the energy is redistributed into the medium occurred at fixed z_{T} – that is if the redistribution scaled with the total energy of the jet – then the transition between $I_{AA} < 1$ and $I_{AA} > 1$ should occur at a single z_{T} for all $E_{\text{T}}^{\text{trg}}$ [8]. This is not observed in the data: this transition occurs at increasing ξ (i.e. *decreasing* z_{T}) as $E_{\text{T}}^{\text{trg}}$ increases. The measured data agree well with predictions from a CoLBT calculation [106] and a BW-MLLA (**B**orghini-**W**iedemann

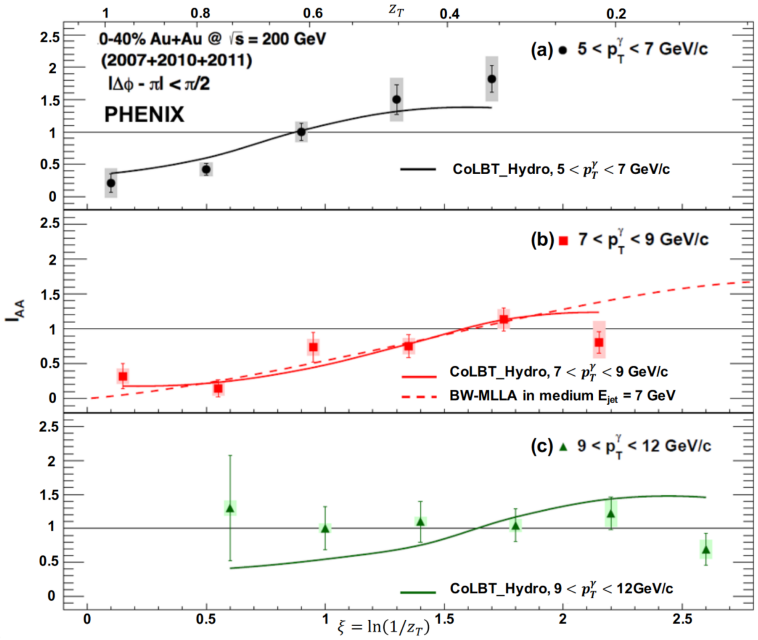

Figure 5.7: I_{AA} for AS $h^{\pm}$ with $p_{\mathrm{T}}^{\mathrm{had}} = 0.5 - 7$ GeV/c measured by PHENIX in 2020 correlated with γ_{dir} for three different ranges of $E_{\mathrm{T}}^{\mathrm{trg}}$. The data are plotted as a function of the hadrons' ξ. From [11].

Modified **L**eading **L**ogarithmic **A**pproximation) calculation [147], both of which assume that the lost jet energy is redistributed into thermal (soft) excitations in the medium.

Additionally, STAR measured D_{AA} for charged AS $h^{\pm}$ correlated with reconstructed jets in 2014 [12]. The observable D_{AA} measures the difference in transverse momentum of jets or jet proxies associated with a high p_{T} trigger between AuAu and pp collisions:

$$D_{AA}\left(p_{\mathrm{T}}^{\mathrm{assoc}}\right) \equiv Y_{\mathrm{AuAu}}\left(p_{\mathrm{T}}^{\mathrm{assoc}}\right) \cdot \left\langle p_{\mathrm{T}}^{\mathrm{assoc}}\right\rangle_{\mathrm{AuAu}} - Y_{pp}\left(p_{\mathrm{T}}^{\mathrm{assoc}}\right) \cdot \left\langle p_{\mathrm{T}}^{\mathrm{assoc}}\right\rangle_{pp} \tag{5.7}$$

where $Y_{\mathrm{AuAu},pp}$ indicate the integrated yield of AS $h^{\pm}$ and $\left\langle p_{\mathrm{T}}^{\mathrm{assoc}}\right\rangle_{\mathrm{AuAu},pp}$ indicate the per-trigger yields mean $p_{\mathrm{T}}^{\mathrm{assoc}}$ of a given bin of $p_{\mathrm{T}}^{\mathrm{assoc}}$ in AuAu and pp respectively. Any deviation from $D_{AA} = 0$ indicates a modification of the jet. Figure 5.8 shows the reported D_{AA} for AS $h^{\pm}$ correlated with reconstructed NS jets compared against calculations from

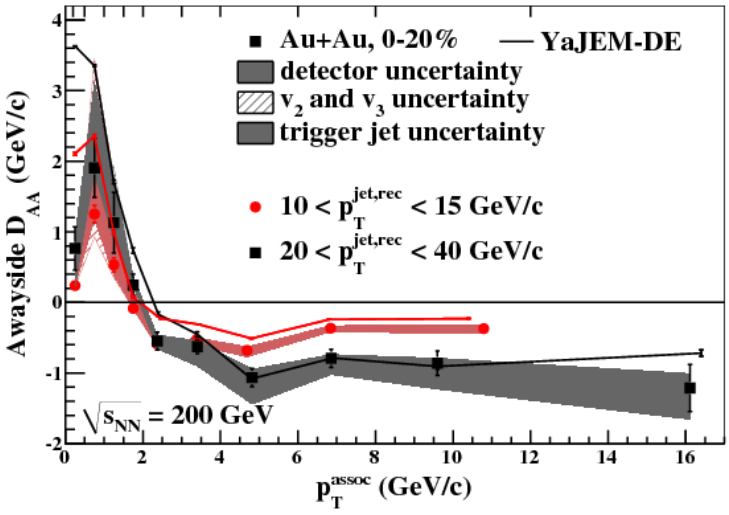

Figure 5.8: The momentum difference D_{AA} of AS $h^{\pm}$ correlated with reconstructed jets for two ranges of $p_{\mathrm{T}}^{\mathrm{jet}}$ measured by STAR in 2014. Used with permission from [12].

the YaJEM-DE[7] model [148]. The data show an enhancement of AS $h^{\pm}$ ($D_{AA} > 0$) for $p_{\mathrm{T}}^{\mathrm{assoc}} < 2$ GeV/c and a suppression ($D_{AA} < 0$) for $p_{\mathrm{T}}^{\mathrm{assoc}} > 2$ GeV/c. which is reproduced by the model calculation.

By summing D_{AA} over $p_{\mathrm{T}}^{\mathrm{assoc}}$, we can check whether or not the enhancement at low $p_{\mathrm{T}}^{\mathrm{assoc}}$ balances the suppression at high $p_{\mathrm{T}}^{\mathrm{assoc}}$: $\Sigma D_{AA} = \Sigma_{p_{\mathrm{T}}^{\mathrm{assoc}}} D_{AA}$. STAR reported values of ΣD_{AA} between -0.6 ± 0.2 and -1.0 ± 0.8, suggesting that the high $p_{\mathrm{T}}^{\mathrm{assoc}}$ suppression is largely balanced by the low $p_{\mathrm{T}}^{\mathrm{assoc}}$ enhancement [12]. All of this further corroborates the picture of in-medium energy loss wherein lost energy is redistributed into soft radiation beneath a fixed p_{T} of roughly 2 GeV/c.

These measurements demonstrate that jet proxies such as correlated hadrons can yield important insights into the mechanisms of in-medium energy loss. However, they are no substitutes for the jets themselves which can track the *complete* energy flow, both the hard

[7]The "DE" here indicates that the model incorporates both path-length dependence of radiative energy-loss and elastic energy loss.

radiation of the jet and the soft radiation of medium excitations. The true test of the various energy-loss models is whether or not they can reproduce both single particle observables *and* complex multiparticle observables such as jets.

Thus, the aim of this thesis is to contribute to extending the techniques utilized in [9] to observables which incorporate reconstructed jets, enabling a more precise account of the energy flow down to lower and lower transverse momenta ($p_{\mathrm{T}} \sim 0.2$ GeV/c). This is accomplished by furnishing a precise measurement of the p_{T} spectra of charged recoil jets correlated with γ_{dir} and π^0 triggers in pp collisions. These spectra will serve as the vacuum fragmentation reference for a measurement of I_{AA} for γ_{dir}+jet and π^0+jet.

6. Experimental Apparatus

6.1 The RHIC Accelerator Complex

The RHIC accelerator complex was the first machine in the world capable of colliding ions as heavy as gold at relativistic energies, and the first and only machine in the world capable of colliding spin-polarized protons. Its physics goal is twofold: (1) to create and study the Quark-Gluon Plasma by colliding heavy-ions, and (2) to elucidate the source of the proton's spin by colliding spin-polarized protons.

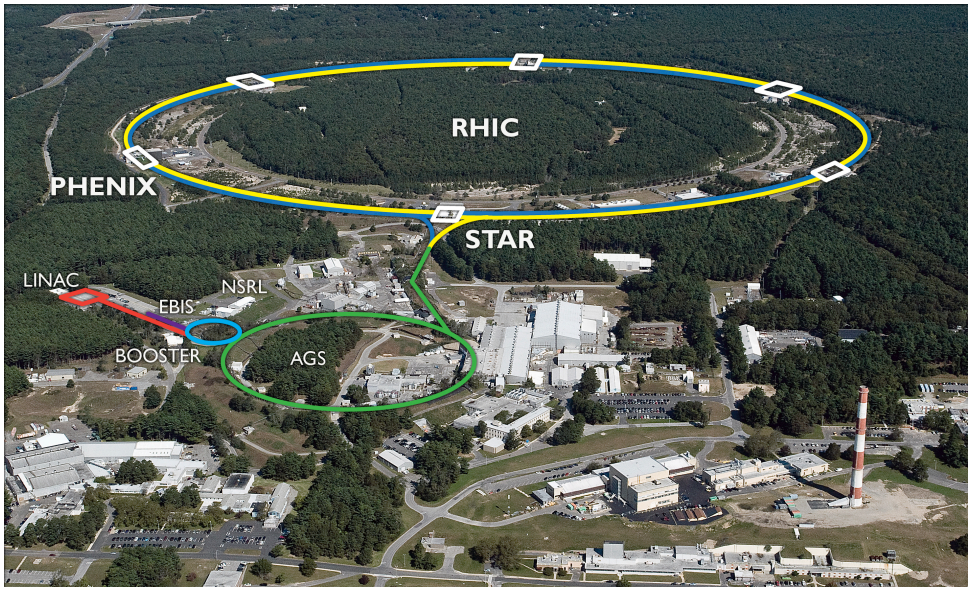

Figure 6.1: An aerial view of the RHIC complex at BNL. From [13].

The RHIC complex became operational in 2000 after ten years of development. Figure 6.1 shows an aerial view of the complex with its constituent systems highlights. It is located at BNL on Long Island, New York. The main ring – shown in blue and yellow in figure 6.1 – has a circumference of 3.8 km (2.4 mi.) and consists of two quasi-circular,

counter-rotating rings which intersect at six independent points. The facility is capable of colliding heavy-ions up to a center-of-mass energy of $\sqrt{s_{NN}} = 200$ GeV/ per nucleon – well above the anticipated onset of the Quark-Gluon Plasma – and capable of colliding polarized and un-polarized protons up to a little above a center-of-mass energy of $\sqrt{s} = 200$ GeV. Thus the machine has ample capability to produce jets across a wide kinematic range in a variety of collision systems.

There are three major stages from beam production to collisions: (1) beam production and injection into the **A**lternating **G**radient **S**ynchotron (AGS), (2) preparation for injection into RHIC by the AGS, and finally (3) injection into RHIC for final acceleration and collisions. Beams are produced in one of two facilities: a **T**andem **V**an de **G**raaf (TVdG) for heavy-ions, and a **Line**ar **Ac**celerator (LINAC) for protons. For example, a heavy-ion collision system such as AuAu begins by producing Au ions with a charge state of +1 from a pulsed sputter ion-source at the TVdG. The ions are partially stripped of their electrons by a stripping foil, and then accelerated by the TVdG up to an energy of 1 MeV per nucleon.

As the Au ions exit the TVdG, they are further stripped to a charge state of +32. Bending magnets select and guide the +32 Au ions to the Booster Synchotron. The booster accelerates the ions to an energy of 95 MeV per nucleon, about 37% the speed of light. The Au ions are stripped again by stripping foil to a charge state of +77 as they exit the booster and are injected into the AGS. The AGS prepares the Au ions for injection into RHIC proper by accelerating them to 10.8 GeV per nucleon, around 99.7% the speed of light. The Au ions exit the AGS and undergo one last stripping, achieving a charge state of +79. The **A**GS-**t**o-**R**HIC (AtR) Beam Transfer Line injects the fully-stripped beams into RHIC. There they are accelerated to their desired collision energy (e.g. 200 GeV per nucleon, 99.995% the speed of light) and steered towards collisions by the machine's helium-cooled superconducting 3.5 T magnets.

Producing *pp*-collision systems is far more straight-forward. Protons are produced and accelerated to 200 MeV in the LINAC. The 200 MeV proton beam is injected into the AGS booster, further accelerated into the AGS proper, and finally injected into RHIC via the AtR line for final ramping before collisions.

The RHIC complex is an extremely versatile facility. It is able to produce a wide variety of collision systems at a wide range of collision energies. For instance, the first phase of the Beam Energy Scan program explored the QCD phase diagram – probing the onset of deconfinement and investigating a possible critical point – by utilizing the RHIC facility's wide range of collision energies, running AuAu-collisions at center-of-mass energies of 7.7, 11.5, 14.5, 19.6, 27, 39, and 62 GeV. As of writing, RHIC has run collisions of pp, pAl, pAu, dAu, hAu, OO, CuCu, CuAu, ZrZr, RuRu, AuAu, and UU with center-of-mass energies ranging between 8 and 510 GeV [149]. This versatility makes a RHIC a unique and ideal machine to explore QCD and the Quark-Gluon Plasma in a quantitative and systematic manner.

6.2 Experiments at RHIC

When RHIC came online, four major experiments were commissioned – two smaller experiments, PHOBOS and BRAHMS, and two large experiments, PHENIX and STAR – to create a comprehensive, varied program of heavy-ion research. Of the four, only STAR is still actively taking data as of 2021. Both PHOBOS and BRAHMS completed their scientific programs in 2006, and PHENIX completed its data-taking operations in 2016. While STAR will be described in detail in section 6.3, this section shall give a brief overview of the other experiments that have made their homes on the RHIC ring.

The PHOBOS experiment [150], which occupied the 10 'o clock position on RHIC, was designed around the fact that at the time very little was known *a priori* about the properties of the fireball produced in heavy-ion-collisions beyond that such collisions were

going to be rare. Thus the experiment was designed to have a very large acceptance, reach to very low momentum particles, and a high trigger rate such that PHOBOS could analyze large numbers of unselected collisions and give global information about collisions where a fireball was produced, such as the temperature, size, and density of the fireball. Some of its major measurements were of the pseudorapidity and centrality dependence of charged particles [151, 152]. These measurements showed that the energy and particle densities produced in a head-on AuAu collisions were far higher than what would be anticipated for a mere superposition of pp collisions.

Similarly, the **B**road **Ra**nge **H**adron **M**agnetic **S**pectrometer (BRAHMS) which occupied the 2 o' clock position on RHIC was designed to measure charged particles over a wide range of rapidity and momentum in order to understand the reaction mechanisms of heavy-ion-collisions [153]. Thus it was designed to provide strong momentum resolution and particle identification over a very large range of rapidity. One of its most striking measurements was of the centrality and pseudorapidity dependence of the nuclear modification factor in dAu collisions (R_{dA}) [154]. This, when compared to similar measurements in AuAu collisions, provides evidence for and constraints on a possible precursor to the QGP, the so-called **C**olor **G**lass **C**ondensate (CGC) [155].

The largest of the four RHIC experiments, the **P**ioneering **H**igh **E**nergy **N**uclear **I**nteraction e**x**periment (PHENIX) located at the 8 o' clock position on RHIC, was designed with an emphasis on detecting rare probes of the Quark-Gluon Plasma such as high momentum particles, heavy quarkonia, and electromagnetic particles such as muons and photons [156]. The PHENIX collaboration has produced many important results over the years. Of particular relevance to this thesis are its measurements of the direct-photon production cross-section [7], neutral pion suppression in heavy-ion collisions [157], and its measurement of the suppression of charged hadrons opposite direct-photons and neutral pions in heavy-ion collisions discussed in sections 5.3 and 5.4. While PHENIX has ceased its

data-taking operations, the collaboration continues to remain very active. Construction is already underway on the successor of PHENIX, **S**uper PHENIX (sPHENIX) [158]. The sPHENIX detector will emphasize jet measurements, especially jets at high transverse momentum, and heavy quarkonia, such as Υ particles.

Two additional small scale experiments have occupied the BRAHMS position on the RHIC ring at various times: pp2pp and A_NDY. These were aimed exclusively at understanding polarized pp-collisions. The A_NDY experiment was a feasibility study which operated during the running years of 2012 and 2013, and was commissioned to study the feasibility of measuring large x_F (momentum fraction), low mass $e^{\pm}$ pairs from Dell-Yann[1] processes in pp-collisions at $\sqrt{s} = 200$ GeV at RHIC. For instance, in 2015 the A_NDY collaboration measured the production cross-sections and single-spin asymmetry A_N of forward jets in polarized pp-collisions at $\sqrt{s} = 500$ GeV [159]. Elements of this study were later incorporated into upgrades in the forward region of STAR.

The pp2pp experiment was designed to study elastic and inelastic pp-collisions at extremely small scattering angles and in the region of extremely small squared four-momentum transfer region ($|t| \in (4 \times 10^{-4}, 1.3]$ (GeV/c)^2) [160]. The design of pp2pp consists of four *roman pots* – cylindrical vessels in which detectors can be mounted and moved close to the beam while remaining protected from the beam vacuum – each containing four silicon strip detectors and a scintillator. The four detectors are stationed approximately 50 or 60 m downstream in each pipe from the interaction region. This is necessary to catch the scattered protons after they have passed through the bending magnets. After being operated as a standalone experiment during 2002, it was incorporated into the STAR experiment. A recent result produced by the STAR collaboration using this detector array was a precision measurement of A_N in polarized pp-collisions [161].

[1] $q\bar{q} \to e^+e^-$

6.3 The STAR Detector

The STAR experiment [162] resides at the 6 o' clock position of the RHIC ring, and is the second largest of the four commissioning experiments at RHIC weighing in at 1200 tons. It is also the focus of this thesis. The experiment covers the largest solid angle of the RHIC experiments, covers a large phase space, and consists of a wide variety of detectors with a large range of capabilities, all of which make it a highly versatile experiment. Thus it is well-suited for a highly diverse set of measurements such as particle identification, di-electron and heavy flavor measurements, forward measurements, and – importantly for this thesis – jets.

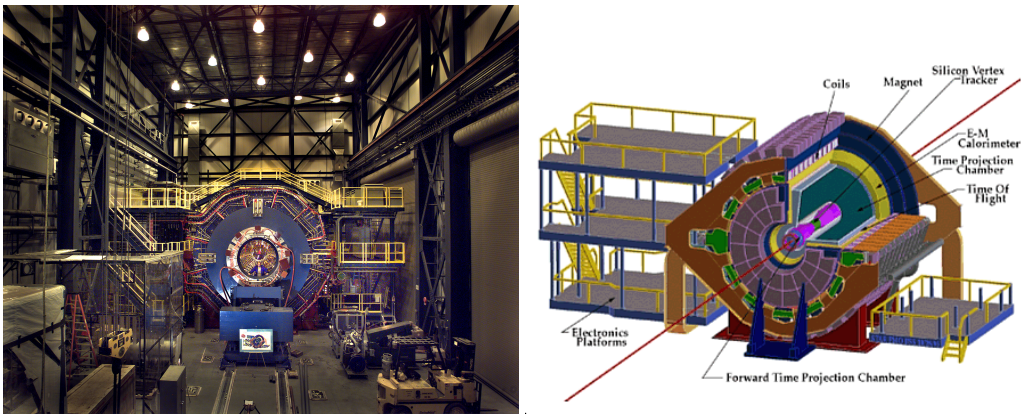

(a) The STAR experiment. (b) Layout of STAR detectors.

Figure 6.2: A front-end view of the STAR experiment (6.2a), and an isometric view of STAR with certain sub-systems labeled (6.2b). From [14] and [15] respectively.

Figure 6.2 gives a bird's-eye view of the experiment as well as cross-section showcasing some of its major subsystems. Four major categories of STAR hardware will be detailed here: the solenoidal magnet, event characterization detectors, the **T**ime **P**rojection **C**hamber (TPC), and the **E**lectro**m**agnetic **C**alorimeter (EMC).

6.3.1 Detector Coordinates

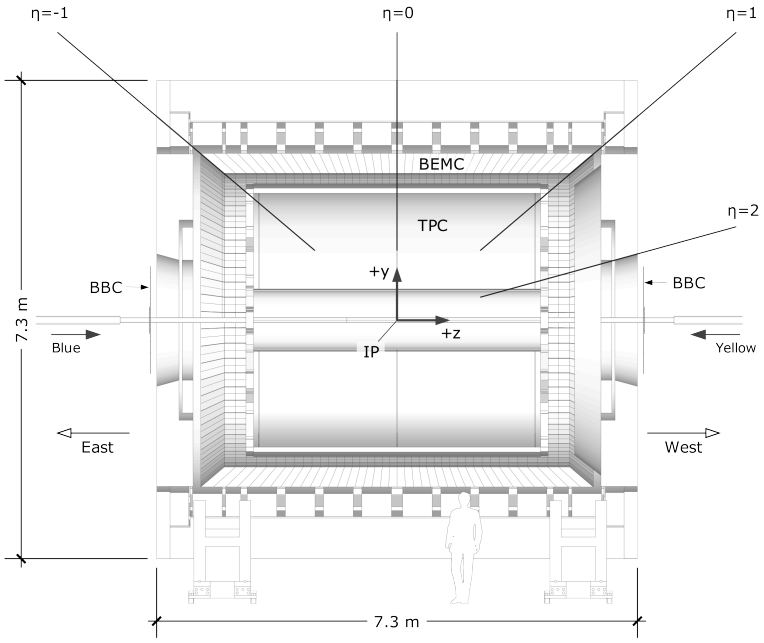

Figure 6.3: An illustration of the coordinate system used at STAR. Used with permission from [16].

Before proceeding, it will be useful to clarify the coordinate system used at STAR. The major points of reference used to define these coordinates are the center of STAR, referred to as the **I**nteraction **P**oint (IP), and the collision, labeled the **P**rimary **I**nteraction **V**ertex (PIV) or just **P**rimary **V**ertex[2]. The IP is used in establishing the absolute coordinates of STAR. The z-axis is oriented along the beamline with the positive z direction pointing westward and $z = 0$ set at the IP. The x- and y-axes define the plane transverse to the beamline.

[2]**I**nteraction **V**ertex (IV) is another common term.

Despite the two incoming beams having equal and opposite momentum and thus having a primary vertex corresponding to the center of momentum in pp- and AuAu-collisions, Cartesian coordinates are not suitable for describing the physics of hadron colliders: the z-component of the 3-momentum is *not* boost invariant. Physical phenomena may be conflated with irrelevant boosts along the beamline that would be averaged out if the system is treated relativistically.

Thus, a particle with 4-momentum $p^\mu = (E, \overrightarrow{p})$ is expressed in the coordinates $p^\mu \doteq (E, p_T, \varphi, y)$. Here p_T and φ encode the magnitude and orientation of the transverse component of the 3-momentum, and the rapidity y encodes the magnitude and direction of the longitudinal component. Rapidity is additive under boosts along the beamline, and so variations will be averaged out over a large enough sample size. It is given by:

$$y = -\frac{1}{2}\ln\left(\frac{E + p_z}{E - p_z}\right)$$

And the other two coordinates are given by:

$$\begin{aligned} p_T &= \sqrt{p_x^2 + p_y^2} \\ \varphi &= \tan^{-1}\left(p_x/p_y\right) \end{aligned} \tag{6.1}$$

Relativistic hadron collisions typically produce particles with rest masses substantially smaller than their total momentum. Moreover, the identity of measured particles must be deduced offline and the rest masses of particles are frequently unknown at the time of measurement. Thus it is usually convenient to express the polar coordinate in terms of pseudorapidity η:

$$\eta = \frac{1}{2}\ln\left(\frac{p + p_z}{p - p_z}\right) = -\ln\left[\tan\left(\frac{\theta}{2}\right)\right]$$

For $|p| \gg m_0$, the pseudorapidity is approximately equal to the rapidity. The STAR coordinate system is illustrated in figure 6.3. Note that the momenta of particles are calculated with respect to the PV.

6.3.2 The Solenoidal Magnet

The "Solenoidal" in STAR comes from the large solenoidal magnet which houses the TPC and other detectors [163]. The magnet is cylindrical, with a length of 6.85 m and inner and outer diameters of 5.27 m and 7.32 m respectively. It establishes a strong axial[3] magnetic field of up to $|B_z| = 0.5$ T which bends the trajectories of charged particles within the TPC which enables the precise measurement of their momenta.

The absolute field varies within 0.5 Gauss of its nominal value at a rate of less than 0.1 Gauss every 12 hours. The radial and azimuthal deviations of the field are less than 50 and 3 Gauss respectively. This stability enables the tracking of energetic electrons to within 200 μm. The magnet can also operate in two different field configurations: $B_z = \pm 0.5$ T, referred to as "**F**ull **F**ield" (FF, $+$) and "**R**everse **F**ull **F**ield" (RFF, $-$).

6.3.3 Event Characterization Detectors

Multiple detectors are used by STAR to trigger on and characterize potentially interesting events [164, 165]. Note that the term "trigger" is used very generally here. A "trigger" could be simply a signal that a collision may have occurred, or it could a signal that indicates that the collision may have a unique feature such as a high energy photon. During data taking, STAR employs several triggers running simultaneously to select events and sort them into data streams. The primary detectors used for triggering and event characterization are the BBC, ZDC, VPD, FPD/FMS, CTB/TOF, and the EMC.

The **B**eam-**B**eam **C**ounter (BBC) [166] is a fast detector used for min-bias triggering[4],

[3] i.e. along the length of

[4] i.e. the bare minimum to indicate that a collision has occured

monitoring luminosity, and vertex positioning in *pp*-collisions. There are two BBC detectors each placed 3.7 m away from the IP on either side of STAR. They consist of two layers of packed, hexagonal scintillators arranged into two rings each: one with small tiles, and one with larger tiles. These small tiles cover a pseudorapidity range of $|\eta| \in (3.4, 5.0)$ and 2π in azimuth.

To measure the position of the IV, the BBC utilizes the difference in timing between coincident signals in the east and west BBCs: $v_z^{\text{BBC}} = c \cdot (\Delta t_{\text{BBC}}/2)$ where Δt_{BBC} is the difference in timing between the two and c is the speed of light. Additionally, the BBC can be used as a local polarimeter when RHIC is running polarized proton beams.

The **Z**ero-**D**egree **C**alorimeter (ZDC) [167] fulfills a similar role to the BBC in heavy-ion collisions. The two ZDCs are placed at the first bending magnets on either side of STAR, about 18 m away from the IP, and cover extremely small angles ($\theta < 4$ mrad) close to the beamline. Each ZDC consist of alternating tungsten absorbers and scintillating fibers which feed into photomultiplier tubes.

At the ZDCs, charged collision fragments are mostly swept away by magnetic fields, and the neutral fragments and secondaries are negligible. This leaves only spectator neutrons, which the ZDCs use the coincidence of to determine if a collision has occurred. Like the BBC, the ZDCs measure the IV via the timing difference between signals in the east and west ZDCs. Thus the ZDCs are used as a min-bias trigger, a luminosity monitor, and vertex positioning.

The **V**ertex **P**osition **D**etectors (VPDs) [168] are similar in function to the BBCs and ZDCs. They provide MB triggering, vertex positioning, and luminosity monitoring. Each VPD unit is composed of 19 individual detectors which consist of an aluminum cylinder filled with a 6.4 mm thick lead absorber next to a 10 mm thick scintillator. Each scintillator is then connected to a PMT by way of an optically transparent silicon adhesive. This design aimed to provide high timing resolution between signals in each VPD. Each VPD

is placed about 5.6 mm away from the IP on both sides covering a pseudorapidity range of $|\eta| \in (4.24, 5.10)$ and 2π in azimuth.

The **F**orward **P**ion **D**etectors (FPDs) [169] are fast electromagnetic calorimeters positioned on either side of the IP with a pseudorapidity range of $|\eta| \in (2.5, 4)$ but a limited azithumal coverage. These were developed for π^0 detection in highly forward regions, but they also provide triggering capabilities as well as local polarimetry. Each FPD consists of 4 lead glass calorimeters placed above, below, and to the sides of the beam pipe. The FPDs on the sides of the beam pipes are a 7-by-7 array of calorimeter towers, while the FPDs above and below are 5-by-5 arrays.

In 2004, the FPD in the positive pseudorapidity region was replaced with the **F**orward **M**eson **S**pectrometer (FMS) [169]. The FMS is very similar in design and in physics goals to the FPD, and covers the same pseudorapidity range as the FPD. However, it does expand the azimuthal coverage to a full 2π.

The **C**entral **B**arrel **T**rigger (CBT) (described in [164]) was a fast detector array consisting of 240 scintillator slats covering a pseudorapidity range of $|\eta| < 1$. It was used to identify central AuAu-collisions with a high multiplicity of high p_T particles. The CBT was eventually succeeded by the **T**ime **o**f **F**light (TOF) detector [170] which was installed over a period starting in 2002 and ending in 2010.

In addition to the above, the EMC, which will be described in detail below, can be used to identify events in which a large amount of energy is deposited in a small area, e.g. dijet events or direct photons.

6.3.4 The TPC

The primary tracking detector – and namesake of – STAR is the Time Projection Chamber [17]. The TPC is a long cylindrical chamber filled with P10 gas[5] held at 2

[5] 10% Methane and 90% Argon.

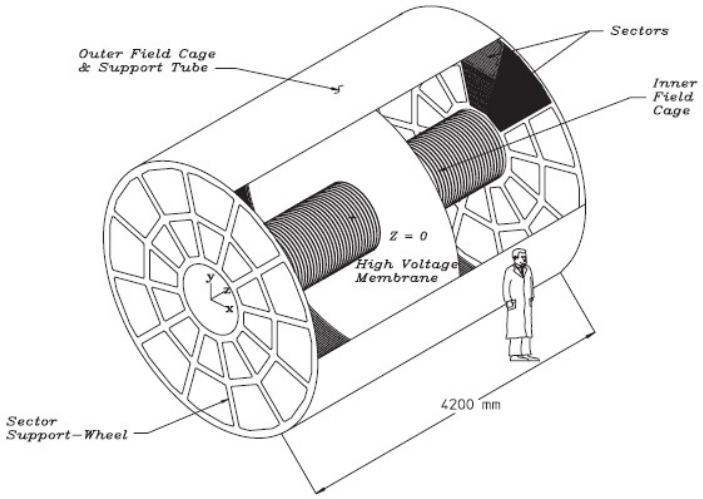

Figure 6.4: A schematic of the STAR TPC, with scientist for scale. Used with permission from [17].

mbar above atmospheric pressure measuring 11.2 m in length and 4 m and 1 m in outer and inner diameter respectively. It is bounded by an outer and inner field cage and two anode endcaps, and divided into an east and west chamber by a central cathode membrane held at a high voltage. Figure 6.4 provides a schematic diagram of the TPC.

A strong electric field is established parallel (and anti-parallel) to the axial magnetic field induced by the solenoidal magnet by holding the central membrane at +25 kV and the endcaps at ground. A key design criterion of the TPC was to ensure high stability and uniformity of its electric field such that electron paths longer than 2 meters can still be reconstructed with sub-millimeter precision. In order to help achieve this, the inner and outer field cages are segmented into rings whose individual voltages may be varied to maintain a uniform electric field.

Charged particles are ejected from a nuclear collision; as they move through the bulk of the TPC, their trajectories are bent into helices by the magnetic field. These particles interact with the P10 gas and leave behind a trail of ionized P10 molecules. The associated

electrons are swept to the endcaps by the electric field at a well-defined drift velocity[6].

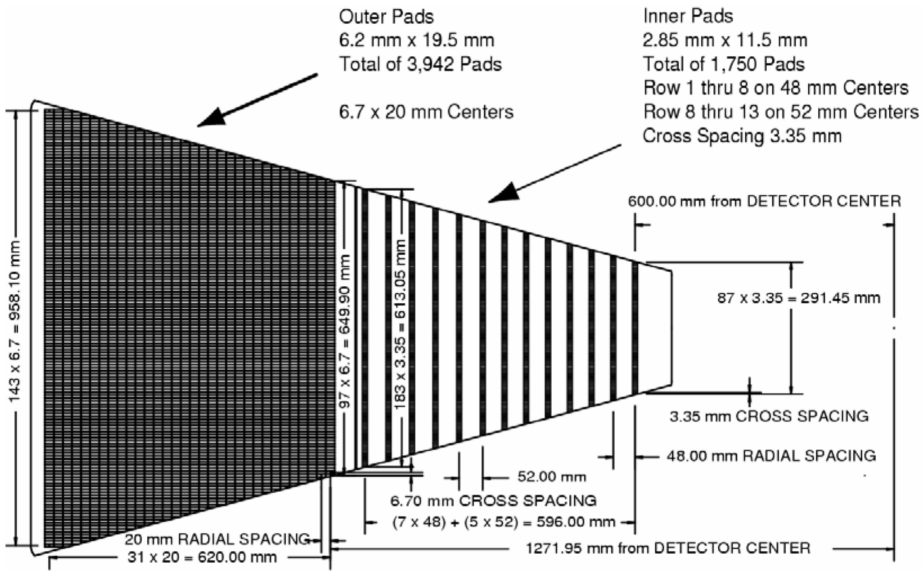

Figure 6.5: An example sector of an endcap with inner (on the right) and outer (on the left) pad rows labeled. The inner pad rows consist of small pads spaced widely, while the outer pad rows consist of large pads spaced tightly. Used with permission from [17].

Each TPC endcap consists of 12 highly pixelated sectors arranged like a clock. These sectors are further divided into an inner and outer sub-sector which each consist of a grid of read-out pads. In total, there are 1,750 small pads across 13 "rows" in the inner sector, and 3,942 large pads across 32 rows in the outer sector. The design of the anode sectors can be seen in figure 6.5. The pads are based on **m**ulti-**w**ire **p**roportional **c**hambers (MWPCs): drift electrons registered by the endcap read-out pads by avalanching in a strong electric field. The design goals of the endcaps were two-fold: (1) good resolution of tracks in the inner sector for vertex finding, and (2) fine resolution of tracks in the outer sector for optimizing dE/dx measurements (see below).

[6]In fact, the P10 gas was selected for the TPC due to its stable and high drift velocity of 5.45 cm/μs.

Thus, the "track" of a charged particle moving through the TPC gets recorded as a series of discrete points – referred to as "hits" – in the (x, y) plane. Additionally, the arrival time of an electron at its read-out pad is recorded in discrete "time buckets" measured relative to the time of collision. Using the data (x, y positions and arrival time), the trajectories of charged particles are reconstructed post-hoc enabling measurement of the x, y, and z components of the particles' momentum.

In order to identify particles, an additional datum is needed from the TPC: energy loss per unit length, dE/dx. The dE/dx a particle experiences as it moves through the TPC depends on its species and its momentum. Below 1 GeV/c, pions, kaons, and protons can be cleanly separated into different bands of dE/dx; above that, their bands begin to overlap. However, pions can be reliably separated from non-pions statistically thanks to the relativistic rise in dE/dx. The integrated dE/dx over the length of the TPC of a particle is small compared to its total energy: for a 1 GeV particle, the integrated dE/dx will be on the order of 100 MeV.

The primary functions of the TPC are to measure the 3-momentum and identify particles over a p_T range of 0.1 to 30 GeV/c with a phase coverage spanning the full 2π in azimuth and $|\eta| < 1.3$ in pseudorapidity. Though, since the reconstruction efficiency of tracks drops rapidly above $|\eta| = 1$ due to high pseudorapidity tracks crossing fewer numbers of pad rows, its effective range is $|\eta| < 1$. Using the reconstructed tracks, the TPC complements the VPD in identifying the IV. It can also be used to identify the secondary vertices of cascading decay chains.

In addition to the TPC, there have been additional tracking elements incorporated into STAR at various points in time. Notably, the **S**ilicon **V**ertex **T**racker (SVT) [171] and **S**ilicon **S**trip **D**etector [172] have been used to facilitate tracking close to the beamline, and the **F**orward TPC (FTPC) [173] was used to facilitate tracking at highly forward pseudorapidities.

6.3.5 The BEMC

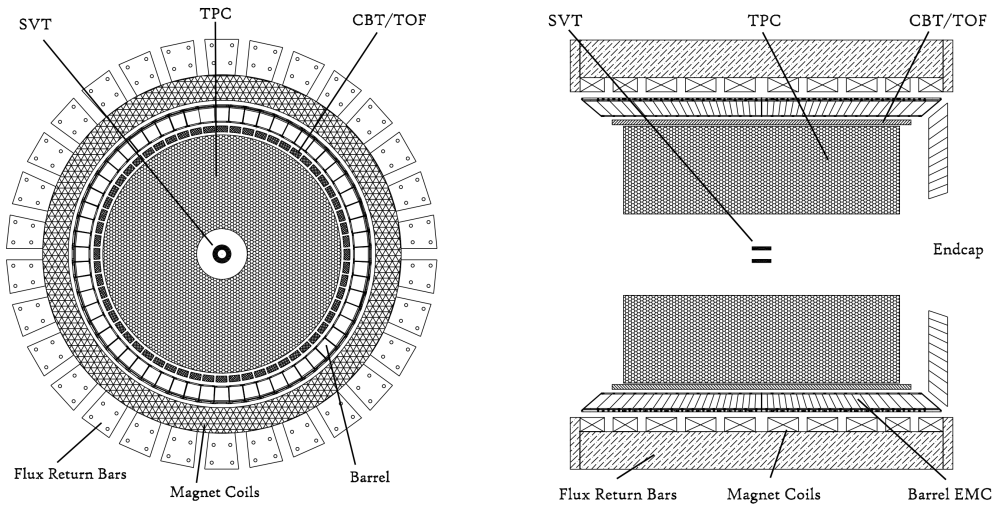

Figure 6.6: A cross-section of the STAR BEMC. Used with permission from [18].

Situated between the TPC and the yokes of the solenoid magnet sits the **B**arrel EMC (BEMC) [18]. The BEMC covers 2π in azimuth and a pseudorapidity range of $|\eta| < 1$, matching the coverage of the TPC. Its inner face runs parallel to the beamline and has a radius of 223.5 cm. It provides a variety of capabilities: it can identify (where tracking is available) and distinguish between photons, electrons, and neutral mesons such as π^0, η, etc.; it can measure the energy deposited by particles and is thus suitable for jet measurements; and it can be used to trigger on events in which a large amount of energy is deposited in a small area such as events associated with dijets, isolated photons, W/Z decays, and heavy quark production. A cross-section of the BEMC can be seen in figure 6.6.

The calorimeter is segmented into 120 modules, 60 in azimuth and 2 in pseudorapidity, subtending 6° (~ 0.1 rad) of φ and 1 unit of η each. Each module is then further segmented

into 40 towers, 2 in φ and 20 in η, for a total of 4800 towers subtending 0.05 by 0.05 in (φ, η). The modules are each 20 cm wide and 293 cm long; the towers each are about 30 cm deep, 23.5 cm of which is "active" (i.e. where interactions occur), and the remaining 6.5 cm or so consists of structural plating (1.9 cm of that structural planting is located at the front, inner surface of the module).

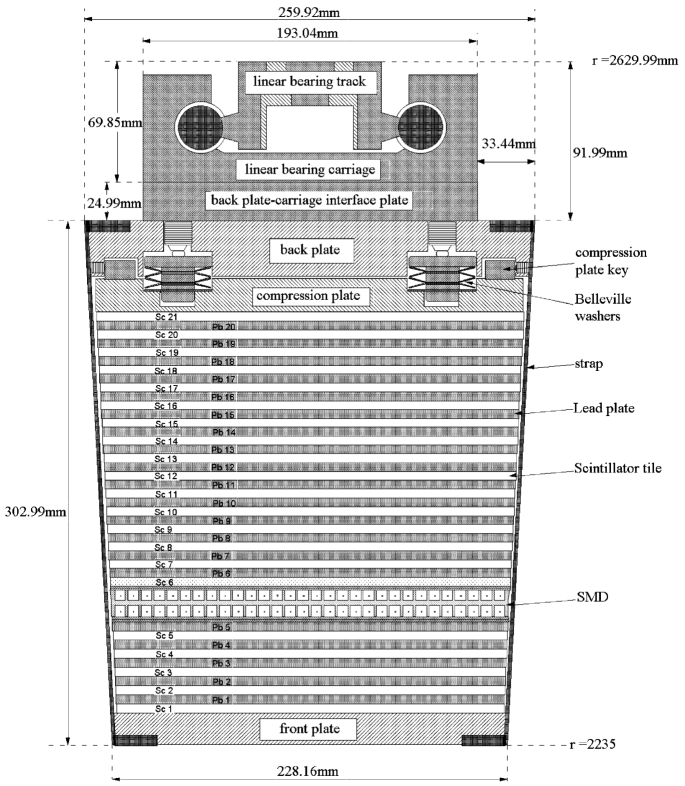

Figure 6.7: A cross-section of an individual BEMC tower, including its structural plating and mounting apparatus. Used with permission from [18].

The individual towers consist of alternating lead and plastic scintillator tiles: 20 layers of 5 mm thick lead plates, 19 layers of 5 mm thick plastic scintillator tiles[7], and 2 layers

[7]The scintillators are Kuraray SCSN81 specifically, which is machined into sheets of "mega tiles" consisting of 40 (1 each tower) tiles of optically isolated scintillator per sheet.

of 6 mm thick scintillator tiles. A diagram of an individual tower can be seen in figure 6.7. In total, the active depth of the towers at $\eta = 0$ spans about 20 radiation lengths (denoted X_0).

The thicker tiles, located at the front (i.e inner face) of each tower, constitute the **Pre**shower (PRS) Detector. The PRS was designed to distinguish electrons from hadrons based on the speed at which their electromagnetic (hereafter E/M) showers develop. The E/M showers associated with electrons develop faster in the calorimeter, with electrons having an 84% probability of interaction within the 1st two layers, while those associated with hadrons develop slower, with hadrons having a 6% probability of interaction within the 1st two layers. And situated between the 5th and 6th layers of each tower is the Shower Maximum Detector. As it is vital to the offline trigger selection used in this thesis, it will be described in detail below.

Each tower is equipped with independent readout capabilities: the PRS, SMD, and all 21 layers of scintillator are independent. The signal from each scintillator tile is transported via wave-length shifting fibers to decoder boxes located outside the STAR magnet. These boxes then merge the signals from the 21 scintillator tiles into a single **P**hoto**m**ultiplier **T**ube (PMT), also located outside the magnet, whose signal is then digitized using 12-bit flash **A**nalog-to-**D**igital **C**onversion (ADC).

In addition to the BEMC, two other major detectors at STAR provide electromagnetic calorimetry: the **E**ndcap EMC (EEMC) [174] and the FMS. The EEMC is identical to the BEMC in its general design (aside from its shape), and is equipped with its own PRS and SMD detectors. It consists of 720 calorimeter towers in each of STAR's endcaps, and covers the pseudorapidity range of $|\eta| \in (1, 2)$ and 2π in azimuth.

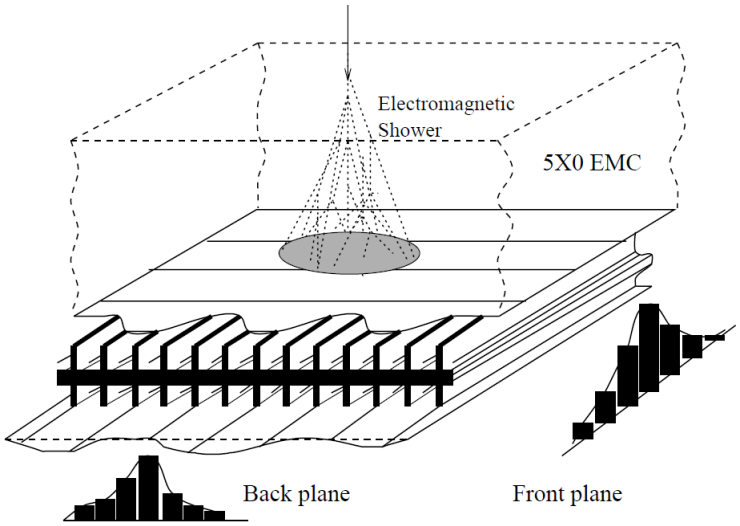

Figure 6.8: A cross-section of the SMD showcasing the two layers of read-out wires and the aluminum extrusion. Used with permission from [18].

6.3.6 The BSMD

Each calorimeter module is also equipped with a **S**hower **M**axiumum **D**etector (SMD), which is situated after the 5$^{\text{th}}$ layer of lead (as stated above). At $\eta = 0$, this is about $5.6X_0$ into the BEMC tower. The SMD is a MWPC consisting of two cathode boards with strips etched into them, housing an aluminum "extrusion" with channels guiding gold-plated tungsten read-out wires that run the length of each calorimeter module. On one cathode plate, the etched strips are parallel to the read-out wires, and on the other the etched strips are perpendicular to the read-out wires. Each of these strips are 1.33 cm wide and are either 0.1 radians in φ (about 23 cm) or 0.0064 radians in η (about 1.5 cm at small η) long, covering a total of 30 wire channels. Figure 6.8 shows the internal construction of the SMD.

In total, there are 36,000 strips throughout the barrel calorimeter which are split up into 1200 distinct areas (0.1×0.1 in $\eta - \varphi$) with 15 η strips and 15 φ strips in each. This grid of strips enables the measurement of the spatial profile of the electromagnetic shower as it

develops in the calorimeter with a granularity of approximately 0.007×0.007 in $\eta - \varphi$.

The primary use of the SMD is to distinguish hadrons from electrons and isolated photons based on the longitudinal (η) and transverse (φ) profiles of their E/M showers. In this thesis, it is specifically used in the offline trigger selection to identify neutral pions and potential direct photons as described in detail in chapter 7.

For reference, the energy resolution of the SMD is nominally

$$\frac{\sigma_E}{E} = 0.12 \oplus \frac{0.86 \text{ GeV}^{-1/2}}{\sqrt{E}}$$

at the front (inner) plate, and the energy resolution is about 3 - 4% worse on the back plate. Thus the front and back plates of the SMD respectively have spatial resolutions of

$$\begin{aligned} \frac{\sigma_r^{\text{front}}}{r_{\text{shower}}} &= 2.4 \oplus \frac{5.6 \text{ GeV}^{-1/2}}{\sqrt{E}} \\ \frac{\sigma_r^{\text{back}}}{r_{\text{shower}}} &= 3.2 \oplus \frac{5.8 \text{ GeV}^{-1/2}}{\sqrt{E}} \end{aligned} \tag{6.2}$$

in natural units.

The EEMC is also equipped with an analogous SMD, the **E**ndcap SMD (ESMD). However, the EEMC and the ESMD are not utilized in this thesis. Thus, "SMD" will unambiguously refer to the SMD installed in the BEMC, the **B**arrel SMD (BSMD), throughout.

7. Identifying Neutral Pions and Photons With STAR

As mentioned in the previous chapter, the STAR SMD plays a key role in identifying energetic π^0 and photons. Utilizing its ultra-fine granularity, one can measure the spatial distribution of an electromagnetic shower as it develops within the towers of the BEMC. The "shape" of these showers is quantified in what is called the **T**ransverse **S**hower **P**rofile (TSP), and this quantity is used to select identified π^0's and γ_{dir} candidates. This chapter will describe the calculation of the TSP and the procedure by which the background due to hadronic decays is removed from the sample of γ_{dir} candidates.

7.1 Calculation of the TSP

First, clusters consisting of one to two BEMC towers and fifteen BSMD strips in both the η and φ directions satisfying certain conditions are formed according to the algorithm described below. Then, the TSP corresponding to a cluster is given by [175]:

$$\text{TSP} = \frac{E^{\text{clust}}}{\sum_i e_i^{\text{strip}} r_i^{1.5}} \tag{7.1}$$

Here E^{clust} is the total energy of the cluster – i.e. either the energy of the sole constituent tower for a 1-tower cluster or the sum of the energies of the two constituent towers for a 2-tower cluster –, e_i^{strip} is the energy of the i^{th} BSMD strip, and r_i is the distance from the i^{th} BSMD strip to the centroid of the cluster. The exponent of 1.5 on r_i was tuned to give maximal separation between π^0's (which produce broader electromagnetic showers) and isolated γ's (which produce more narrow electromagnetic showers) [176].

Let $a_{\text{strip}} = 0.007$ and $a_{\text{twr}} = 0.05$ indicate the grid-spacing of the BSMD strips and the side-length of a BEMC tower respectively in units of pseudorapidity. Then let $\mathcal{H} = \{\eta_i\}$ indicate the set of all η BSMD strips in the BEMC, each of which has an energy e^η, an

angular coordinate $(\eta^\eta, \varphi^\eta)$, and a cartesian coordinate $\mathbf{r} = (x^\eta, y^\eta, z^\eta)$ in the coordinates of STAR. Similarly, let $\mathcal{F} = \{\varphi_i\}$ indicate the set of all φ BSMD strips in the BEMC, each of which has an energy e^φ, an angular coordinate $(\eta^\varphi, \varphi^\eta)$, and a cartesian coordinate $\mathbf{r} = (x^\varphi, y^\varphi, z^\varphi)$. Furthermore, let $\mathcal{T} = \{t_i\}$ indicate the set of all BEMC towers, each of which has an energy E^{twr} and an angular coordinate $(\eta^{\text{twr}}, \varphi^{\text{twr}})$. Lastly, let $\mathcal{N}(t) = \{n_i\}$ indicate the set of up to 8 neighboring towers adjacent to a tower t, each of which has an energy E^{adj}, an angular coordinate $\left(\eta^{\text{adj}}, \varphi^{\text{adj}}\right)$, and a cartesian coordinate $\mathbf{r}^{\text{adj}} = \left(x^{\text{adj}}, y^{\text{adj}}, z^{\text{adj}}\right)$. These four sets define the input into algorithm 3 which constructs trigger clusters that serve as candidate π^0's and γ's.

Algorithm 3 The procedure for constructing candidate π^0 and γ_{dir} BEMC clusters [175]. Quantities associated with the central BSMD strips and leading and sub-leading BEMC towers will be marked with an asterisk, and the indices A, B number the 7 neighboring strips on either side of a central η, φ strip respectively.

---

for each η BSMD strip $\eta_i \in \mathcal{H}$ registering a hit, **do**
  if $e_i^\eta < 0.05$ GeV, **continue**
  else designate η_i as the central η strip of the cluster, η_i^*.
  if $\exists A, e_i^{\eta*} < e_i^{\eta A}$, **continue**
  if any one of the ± 1 and ± 2 neighboring strips are the 1st or last η strip in a BEMC module, **continue**
  for φ BSMD strip $\varphi_j \in \mathcal{F}$ registering a hit, **do**
    if $|\eta_i^{\eta*} - \eta_j^\varphi| \geq a_{\text{twr}}$, **continue**
    if $e_j^\varphi < 0.05$ GeV, **continue**
    else
      Designate φ_j as the central φ strip of the cluster, φ_j^*. The position of

the intersection of η_i^* and φ_j^* is given by $\mathbf{r}_{ij}^{\text{strip}*} = \left(x_j^{\varphi*}, y_j^{\varphi*}, z_i^{\eta*}\right)$.

if $\exists B, e_j^{\varphi*} < e_j^{\varphi B}$, **continue**

if any one of the ± 1 and ± 2 neighboring strips are the 1st or last strip φ strip in a BEMC module, **continue**

for each BEMC tower $t_k \in \mathcal{T}$ registering a hit, **do**

if t_k is *not* in the same BEMC module as η_i^* and φ_j^*, **continue**

if $e_k^{\text{twr}} < 6$ GeV, **continue**

if $\left(\eta_i^{\eta*} - \frac{a_{\text{strip}}}{2} \geq \eta_k^{\text{twr}} - \frac{a_{\text{twr}}}{2}\right) \vee \left(\eta_i^{\eta*} + \frac{a_{\text{strip}}}{2} \geq \eta_k^{\text{twr}} + \frac{a_{\text{twr}}}{2}\right)$, **continue**

if $\left(\varphi_j^{\varphi*} - \frac{a_{\text{strip}}}{2} \geq \varphi_k^{\text{twr}} - \frac{a_{\text{twr}}}{2}\right) \vee \left(\varphi_j^{\varphi*} + \frac{a_{\text{strip}}}{2} \geq \varphi_k^{\text{twr}} + \frac{a_{\text{twr}}}{2}\right)$, **continue**

Designate this tower as the lead tower, t_k^*.

Calculate the difference in η and φ between t_k^* and η_i^*, φ_j^*:

$$\Delta\eta_{ik}^{\text{twr}*} = |\eta_k^{\text{twr}*}| - |\eta_i^{\eta*}|$$

$$\Delta\varphi_{jk}^{\text{twr}*} = |\varphi_k^{\text{twr}*}| - |\varphi_j^{\varphi*}|$$

if $(|\Delta\eta_{ik}^{\text{twr}*}| \leq 0.018) \wedge \left(|\Delta\varphi_{jk}^{\text{twr}*}| \leq 0.018\right)$, **then**

No additional tower will be added to the cluster.

else

for each adjacent BEMC tower $n_l \in \mathcal{N}\left(t_k^*\right)$ registering a hit, **do**

Calculate the displacement between the primary interaction vertex and n_l and the intersection of η^* an φ^*:

$$\tilde{\mathbf{r}}_l^{\text{adj}} = \mathbf{r}_l^{\text{adj}} - \mathbf{PV}$$

$$\tilde{\mathbf{r}}_{ij}^{\text{strip}*} = \mathbf{r}_{ij}^{\text{strip}*} - \mathbf{PV}$$

where $\mathbf{PV}$ is the coordinates of the primary interaction vertex.

Then calculate the angle $\theta_{ijl}^{\text{adj}}$ between $\tilde{\mathbf{r}}_l^{\text{adj}}$ and $\tilde{\mathbf{r}}_{ij}^{\text{strip}*}$:

$$\theta_{ijl}^{\text{adj}} = \frac{\tilde{\mathbf{r}}_l^{\text{adj}} \cdot \tilde{\mathbf{r}}^{\text{strip}*}}{|\tilde{r}_l^{\text{adj}}||\tilde{r}_{ij}^{\text{strip}*}|}$$

end for

27: Designate the adjacent tower with the smallest $\theta_{ijl}^{\text{adj}}$ to be the sub-leading tower of the cluster, n_l^*. The total energy of the cluster is then $E^{\text{clust}} = E^{\text{twr}*} + E^{\text{adj}*}$.

28: **end else**

29: The TSP of the cluster is then given by:

$$\text{TSP} = \frac{E_{\text{clust}}}{\sum_A e_A^\eta \left(r_A^\eta\right)^{1.5} + \sum_B e_B^\varphi \left(r_B^\varphi\right)^{1.5}}$$

30: Add cluster to the list of candidate π^0 and γ_{rich}.

31: **end for**

32: **end for**

33: **end for**

With the TSP calculated, the trigger candidates may be sorted into identified π^0's and a sample with an enhanced fraction of γ_{dir} based on their TSP values as listed in table 7.2. Triggers that fall into this latter category are referred to as γ_{rich}.

Trigger Species	**TSP Range**
π^0	TSP $\in (0, 0.08)$
γ_{rich}	TSP $\in (0.2, 0.6)$

Table 7.2: The range of TSP values identifying π^0 and γ_{rich} triggers.

These values were determined via Monte Carlo simulation [176]. Figure 7.1 shows the distribution of measured TSP values from the Run9 *pp* data. The tight TSP cuts applied to select the π^0 sample ensure that the sample contains very little contamination from background sources, such as decay products or γ_{dir} with a low TSP value. The *purity* (the

percentage of correctly identified π^0) is roughly 90% for pp-collisions. However, there is a significant background present in the γ_{rich} sample which must be corrected for.

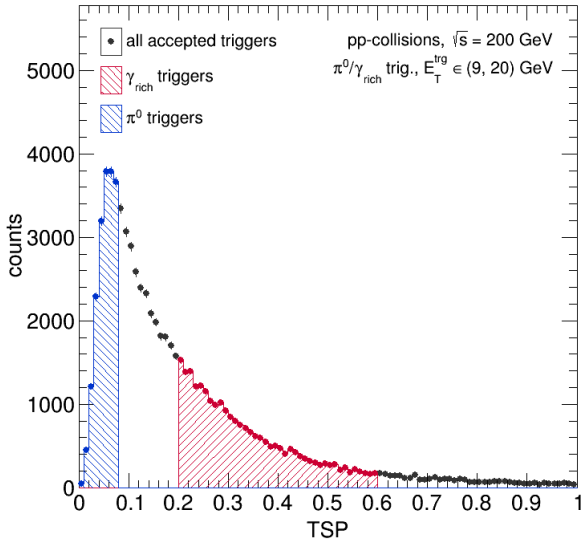

Figure 7.1: Measured trigger yields of TSP (black, light red, and light blue markers). Shaded regions indicate TSP cuts applied to select π^0 and γ_{rich} triggers.

7.2 Photon Background Correction

The γ_{rich} sample will contain contributions from multiple sources dominated by asymmetric π^0 and η decays. This contribution is removed at the level of event-averaged distributions via a statistical subtraction utilizing a data-driven estimation of the background present as a function of the trigger's transverse energy [176].

The estimation relies on comparing the NS per-trigger yields of TPC tracks between π^0 and γ_{rich} triggers. The following calculation makes two major assumptions:

Assumption 1, that γ_{dir} produce **zero** NS yield of charged hadrons; and

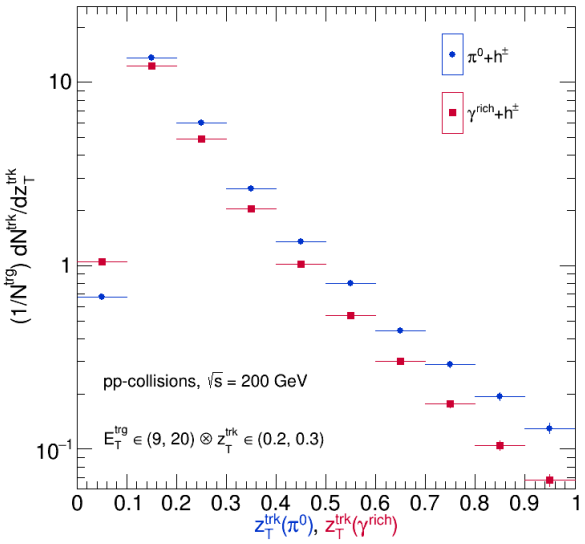

Figure 7.2: z_T^{trk} of primary tracks with $p_{\text{T}} > 1.2$ GeV/c correlated with γ_{rich} and π^0 triggers with $E_{\text{T}}^{\text{trg}} > 9$ GeV.

Assumption 2, that the spectral shape of the π^0 NS yield of charged hadrons is the same as that of the asymmetric π^0/η decays.

First events are selected which satisfy all the event selection criteria listed in tables 8.1 and 8.2 excluding the TSP criterion. From these events, primary tracks are selected which satisfy $p_{\text{T}}^{\text{trk}} \in (1.2, 20)$ GeV/c as well as all of the track selection criteria listed in 8.4.

Figure 7.2 shows the $z_{\text{T}}^{\text{trk}} = p_{\text{T}}^{\text{trk}}/E_{\text{T}}^{\text{trg}}$ distribution of all selected tracks, and figure 7.3 shows the per-trigger yield of selected primary tracks as a function of $\Delta\varphi^{\text{trk}}$ relative to the trigger azimuth for selected tracks with a $z_{\text{T}}^{\text{trk}} \in (0.2, 0.3)$. The cut on $z_{\text{T}}^{\text{trk}}$ was to select a clean sample of NS primary tracks: the region $(0.2, 0.3)$ strikes a nice balance between providing sufficient statistics without being dominated by too much background. This was determined by considering the signal to background levels in the correlation plots by inspection.

The $\Delta\varphi^{\text{trk}}$ per-trigger yields were fit with two gaussians, one each for the NS and AS

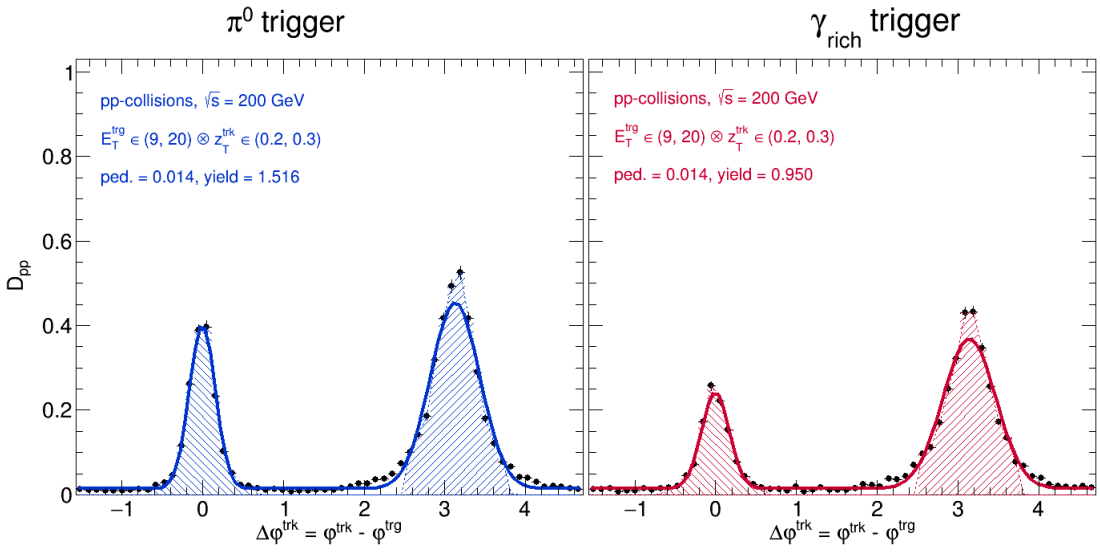

Figure 7.3: $\Delta\varphi^{\text{trk}}$ of primary tracks selected for the calculation of the γ_{rich} purity integrated over $E_{\text{T}}^{\text{trg}}$. The solid lines indicate fits consisting of two gaussians and a constant, and the fill areas indicate the NS and AS regions.

peaks, and a constant to capture the average background, referred to as the "pedestal," i.e.

$$f\left(\Delta\varphi^{\text{trk}}\right) = a_0 e^{-\left(\Delta\varphi^{\text{trk}}\right)^2/2\sigma_0^2} + a_1 e^{-\left(\Delta\varphi^{\text{trk}}-\pi\right)^2/2\sigma_1^2} + a_2 \tag{7.2}$$

where a_i and σ_i are fit parameters. Once fitted, the per-trigger NS yields were extracted by subtracting the pedestal from the per-trigger yield (determined by counting the bin contents) in each bin of $\Delta\varphi^{\text{trk}}$ and then integrating over the NS region, defined to be $\Delta\varphi^{\text{trk}} \in (-0.63, 0.63) \approx \left(-\frac{\pi}{5}, \frac{\pi}{5}\right)$ (the shaded regions in figure 7.3):

$$D_{\text{NS}}^{pp}\left(E_{\text{T}}^{\text{trg}}|\star\right) = \int_{-0.63}^{0.63} \left[\frac{1}{N^{\text{trg}}\left(E_{\text{T}}^{\text{trg}}|\star\right)} \frac{dN^{\text{trk}}\left(E_{\text{T}}^{\text{trg}}|\star\right)}{d\Delta\varphi^{\text{trk}}} - a_2\right] d\Delta\varphi^{\text{trk}} \tag{7.3}$$

where $D_{\text{NS}}^{pp}\left(E_{\text{T}}^{\text{trg}}|\star\right)$ indicates the NS per-trigger yield as a function of $E_{\text{T}}^{\text{trg}}$ for a given species of trigger (π^0 or γ_{rich}). Taking the ratio between the NS per-trigger yields of the two species gives

$$\mathcal{B}\left(E_{\mathrm{T}}^{\mathrm{trg}}\right) = \frac{D_{\mathrm{NS}}^{pp}\left(E_{\mathrm{T}}^{\mathrm{trg}}|\gamma_{\mathrm{rich}}\right)}{D_{\mathrm{NS}}^{pp}\left(E_{\mathrm{T}}^{\mathrm{trg}}|\pi^{0}\right)} \tag{7.4}$$

where $\mathcal{B}$ is the background level of the γ_{rich} sample, the fraction of γ_{rich} triggers which are **not** γ_{dir}. The purity (the fraction of γ_{rich} triggers which **are** γ_{dir}) is then

$$\mathcal{R} = 1 - \mathcal{B}. \tag{7.5}$$

7.3 Measurement of $\mathcal{B}$ and Systematic Uncertainties

Before measuring the value of $\mathcal{B}$, the second assumption in this calculation, needs to be remarked on here. The p_{T} of a decay photon's parent might be different than the p_{T} of the measured photon itself, and this may impact the shape of the D_{NS}^{pp} for background contaminants in the γ_{rich} sample. To test this, a quick Monte-Carlo was used wherein the maximum impact was estimated by assuming that the background in the γ_{rich} sample is due to decay photons exclusively.

First, values of decay photon p_{T} ($p_{\mathrm{T}}^{\mathrm{decay}}$) were sampled according to the measured γ_{rich} E_{T} distribution. For each $p_{\mathrm{T}}^{\mathrm{decay}}$, the p_{T} of the parent π^0/η ($p_{\mathrm{T}}^{\mathrm{parent}}$) was calculated. For each simulated trigger, a pseudo-event was formed by sampling a certain number of near-side tracks according to the measured $p_{\mathrm{T}}^{\mathrm{trk}}$ and $\Delta\varphi^{\mathrm{trk}}$ distributions.

Then the NS per-trigger yields were computed as a function of $z_{\mathrm{T}}^{\mathrm{trk}}$ twice: once where $z_{\mathrm{T}}^{\mathrm{trk}}$ was calculated with respect to the decay photon ($p_{\mathrm{T}}^{\mathrm{trk}}/p_{\mathrm{T}}^{\mathrm{decay}}$), this will be labeled $D_{\mathrm{NS}}^{pp}\left(z_{\mathrm{T}}^{\mathrm{trk}}|\gamma_{\mathrm{decay}}\right)$; and once with respect to the parent meson ($p_{\mathrm{T}}^{\mathrm{trk}}/p_{\mathrm{T}}^{\mathrm{parent}}$), which will be labeled $D_{\mathrm{NS}}^{pp}\left(z_{\mathrm{T}}^{\mathrm{trk}}|\pi^{0}\right)$. The ratio was found to agree with unity within 5% agreement for $z_{\mathrm{T}}^{\mathrm{trk}} \in (0.2, 0.3)$ and within at most 20% otherwise. This indidcates that the impact on $\mathcal{B}$ due to differences in the shape of $D_{\mathrm{NS}}^{pp}\left(E_{\mathrm{T}}^{\mathrm{trg}}|\gamma_{\mathrm{decay}}\right)$ is negligible.

With this confirmed, $\mathcal{B}$ was calculated as a function of $z_{\mathrm{T}}^{\mathrm{trk}}$ for the three ranges of $E_{\mathrm{T}}^{\mathrm{trg}}$

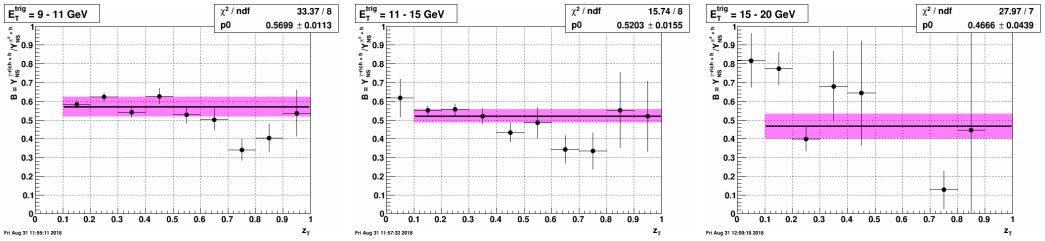

(a) $E_{\mathrm{T}}^{\mathrm{trg}} = 9 - 11$ GeV (b) $E_{\mathrm{T}}^{\mathrm{trg}} = 11 - 15$ GeV (c) $E_{\mathrm{T}}^{\mathrm{trg}} = 15 - 20$ GeV

Figure 7.4: $\mathcal{B}$ as a function of $z_{\mathrm{T}}^{\mathrm{trk}}$ for three ranges of $E_{\mathrm{T}}^{\mathrm{trg}}$. Solid line indicates the average over $z_{\mathrm{T}}^{\mathrm{trk}}$, and the solid band indicates 1σ.

used in this analysis. The background level was then averaged over all $z_{\mathrm{T}}^{\mathrm{trk}} \in (0.1, 1)$. The calculated $\mathcal{B}$ and their average for each of the three ranges of $E_{\mathrm{T}}^{\mathrm{trg}}$ are shown in figure 7.4. The bin $z_{\mathrm{T}}^{\mathrm{trk}} < 0.1$ was excluded as backgrounds were too high to reliably extract a NS per-trigger yield. These averages were taken to be *the* background levels of each range of $E_{\mathrm{T}}^{\mathrm{trg}}$. Table 7.3 lists the average values of $\mathcal{B}$ and their uncertainties in pp-collisions for each of the three bins of $E_{\mathrm{T}}^{\mathrm{trg}}$. The bin $z_{\mathrm{T}}^{\mathrm{trk}} \in (0, 0.1)$ was not used due to high backgrounds.

$\mathbf{E_T^{trg}}$ **[GeV]**	$\mathcal{B}$	$\pm\delta\mathcal{B}$
9 - 11	0.570	0.054
11 - 15	0.520	0.036
15 - 20	0.470	0.068

Table 7.3: Measurements of $\mathcal{B}$ and their uncertainties as a function of $E_{\mathrm{T}}^{\mathrm{trg}}$.

The systematic uncertainty is approximately 10% across $E_{\mathrm{T}}^{\mathrm{trg}}$. This uncertainty is primarily due to the choice of $z_{\mathrm{T}}^{\mathrm{trg}}$. The choice of integration window in extracting D_{NS}^{pp} produces a negligible uncertainty.

8. Analysis Details

The data analyzed in this thesis were recorded by the STAR experiment between April 19th and May 9th, 2009 (Run9). The collisions selected for analysis are pp-collisions which are part of the "high luminosity" dataset recorded during Run9 with a center-of-mass energy of $\sqrt{s} = 200$ GeV. Note that "event" and "collision" will be used interchangeably throughout. Both will refer to collisions which have been successfully registered, processed, and recorded by STAR.

Events are selected using an online trigger system at STAR which consists of three layers of decision making. The first layer of trigger electronics, **L**evel-**0** (L0), determines which events to accept at the hardware level based on data from the fast detectors (EMC, BBC, ZDC, CTB, and FPD). The second layer, **L**evel-**1** (L1), is an intermediate stage which passes the data from accepted events to be processed by the final layer of trigger processing, **L**evel-**2** (L2). The L2 tier sorts the accepted events into data streams and pass it on to the **d**ata **ac**q**u**isition units (DAQ) to be saved to tape.

The events discussed herein satisfy the "L2gamma" online trigger. This trigger is designed to identify events which are more likely to contain energetic photons. At the L0 level, L2gamma events must satisfy the **VPD** **M**in-**B**ias (VPDMB) and **B**arrel **H**igh **T**ower **2** (BHT2) triggers. These are defined as so:

(a) **VPDMB Trigger:** in the event there must be coincident activity in the east and west VPD detectors; and

(b) **BHT2 Trigger:** there must be an EMC tower in the event which contains at least 4.3 GeV.

And at the L2 level, L2gamma events must contain a 3×3 cluster of EMC towers whose

two most energetic towers contain a sum total transverse energy of 7.44 GeV. In total, approximately 11,327 million events were recorded that satisfy the L2gamma trigger during Run9 for an integrated luminosity of roughly 23 pb^{-1}.

Schematically, the process of going from these raw L2gamma events to fully corrected π^0- and γ_{dir}-triggered charged recoil jet spectra looks like so:

1. **Apply Clusterizer:** L2gamma events are processed by an algorithm (referred to as the *clustering algorithm* or *clusterizer* from hereon) to identify candidate π^0 and γ_{rich} triggers as described in chapter 7. Events with identified candidates are passed on to the next stage.

2. **Reconstruct Jets:** From the selected events, those with real π^0 and γ_{rich} triggers are selected via the event and trigger selection criteria described in section 8.1. Charged jets are then reconstructed event-by-event from primary tracks which satisfy the track selection criteria described in section 8.2. And from these charged jets, only recoil jets satisfying the jet selection criteria described in section 8.3 are accumulated into raw per-trigger yields (spectra).

3. **Correct Detector Effects:** the raw data are then corrected for various distortions induced by the experimental apparatus described in chapter 9 via a "regularized unfolding" scheme described in chapter 10.

4. **Evaluate Systematic Uncertainties:** After correction, the various sources of uncertainty in the measurement process are assessed and assigned to the corrected data as described in chapter 11.

5. **Determine Trigger Energy Scale and Resolution:** Before comparing the corrected data to theory, it is necessary to determine the distribution of actually sampled π^0 and γ_{dir} energies. This calculation is detailed in chapter 12.

6. **Compare to Theory:** Finally, once the actual distributions of π^0 and γ_{dir} energy have been determined, the fully corrected data can be compared against the relevant calculated and simulated charged recoil jet distributions. This is discussed in chapter 13.

8.1 Event and Trigger Selection

Criterion	Description
$\lvert v_z \rvert < 55$ cm	z-component of PV must be within 55 cm of the IP.
$\lvert v_r \rvert < 2$ cm	radial component of PV must be within 2 cm of the IP.

Table 8.1: Criteria applied to the primary vertex of events retained for analysis.

L2gamma events are processed by the tower clustering algorithm described in chapter 7 to identify those events which contain candidate π^0 and γ_{rich} triggers, clusters of 1 – 2 BEMC towers and up to 15 η and 15 φ BSMD strips. In order to select real π^0 and γ_{rich} triggers and ensure a clean signal, the events retained for further analysis need to satisfy certain section criteria on their primary vertex and their associated trigger. These are listed in tables 8.1 and 8.2.

Note that the criteria on e^*_η and e^*_φ are built into the clusterizer algorithm, and thus guaranteed to be satisfied by all accepted triggers. Furthermore, events from data-taking runs determined to be bad and whose associated trigger cluster contains a "hot" tower are not retained for further analysis. The list of bad runs and hot towers can be found in appendix A alongside more information about the L2gamma stream.

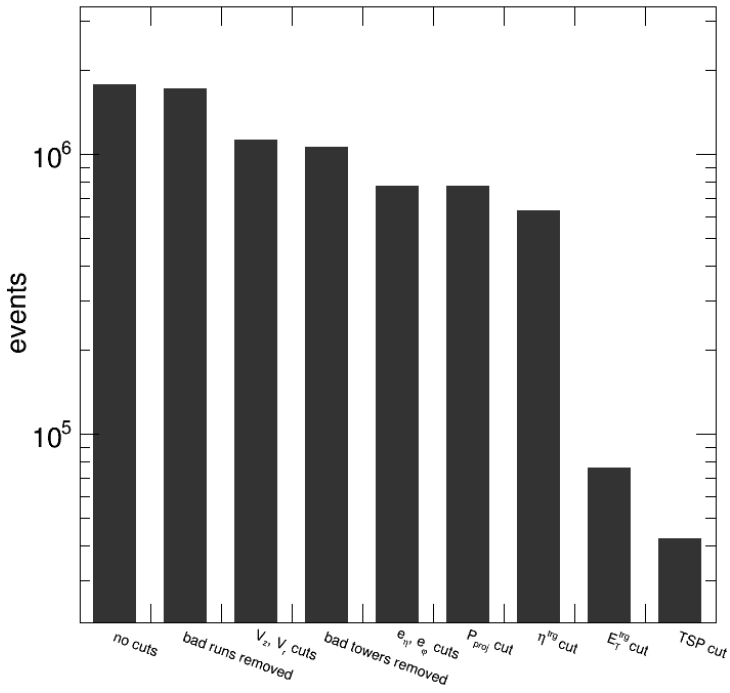

Figure 8.1: The number of events left after each successive event and trigger selection criteria is applied.

Figure 8.1 shows the number of events remaining after each successive cut is applied: only 42,508 events remain after all event and trigger selection criteria have been applied. Table 8.3 breaks down these remaining events according to the transverse energy and species (π^0 vs. γ_{rich}) of their associated trigger. The various distributions to which these criteria are applied are shown in appendix B.

8.2 Track Selection

From the events selected for analysis, primary tracks are selected for jet reconstruction according to the criteria listed in table 8.4. The $N_{\text{fit}}/N_{\text{poss}}$ criterion is required in order to ensure that split tracks are not double-counted, and the N_{fit} criterion is required in order to ensure precision in the fitting of the track and thus in the calculation of its 3-momentum.

Criterion	Description
$\Sigma p_{\text{match}} \leq 3$ GeV/c	Total 3-momentum of tracks matched to central tower of trigger must be less than 3 GeV/c.
$e^*_\eta \geq 0.5$ GeV	Energy of central η strip must be greater than 0.5 GeV.
$e^*_\varphi \geq 0.5$ GeV	Energy of central φ strip must be greater than 0.5 GeV.
$\lvert\eta^{\text{trg}}\rvert < 0.9$	The cluster's pseudorapidity, as defined by the position of the towers in the BEMC, must be within $(-0.9, 0.9)$.
$E_{\text{T}}^{\text{trg}} \in (9, 20)$ GeV	Cluster transverse energy must be within $(9, 20)$ GeV.
TSP $\in (0, 0.08) \cup (0.2, 0.6)$	TSP must be within $(0, 0.08)$ or $(0.2, 0.6)$.

Table 8.2: Criteria applied to the trigger of events retained for analysis.

$\mathbf{E}_{\text{T}}^{\text{trg}}$ **[GeV]**	π^0	γ_{rich}
9 - 11	12,869	15,232
11 - 15	4,918	7,328
15 - 20	699	1,522
Total	18,426	24,082

Table 8.3: Number of events containing a trigger passing all event and trigger selection criteria versus the trigger transverse energy, $E_{\text{T}}^{\text{trg}}$.

Furthermore, the global **D**istance of **C**losest **A**pproach (DCA) – i.e. the distance of closest approach of a global (in the frame of the IP) track to the nominal PIV – criterion is required to exclude background due predominantly to pile-up; though this cut will also reduce the number of secondary decay products included. These three criteria help improve the precision with which the 3-momentum – $p \doteq (p_{\text{T}}, \eta, \varphi)$ – is calculated. The various distributions to which the track selection criteria are applied are shown in appendix B.

Criterion	Description
$N_{\text{fit}} \geq 15$	The number of fit points comprising the selected track must be ≥ 15.
$N_{\text{fit}}/N_{\text{poss}} \geq 0.52$	Selected track must use $\geq 52\%$ of the possible fit points.
DCA < 1 cm	Selected track must have a DCA of < 1 cm from the PV when the track is fit as a global track (c.f. section 6.3.4).
$\lvert\eta^{\text{trk}}\rvert < 1$	Selected track's pseudorapidity as defined relative to the IV must fall within $(-1, 1)$.
$p_{\text{T}}^{\text{trk}} \in (0.2, 30)$ GeV/c	Selected track must have a p_{T} in the range of $(0.2, 30)$ GeV/c.

Table 8.4: Criteria applied to primary tracks selected for jet reconstruction.

8.3 Jet Selection

Once the relevant primary tracks have been selected in an event, they are clustered into "charged" jets[1]. Here, jets are clustered according to the anti-k_{T} algorithm via the FastJet 3.0.6 software [177]. Two jet resolution parameters are used in this analysis, $R_{\text{jet}} = 0.2$ and 0.5. These were chosen to match the resolution parameters used in the parallel analysis of AuAu-collisions (publication forthcoming) since the fully-corrected pp data presented here will be the denominator in the forthcoming measurement of I_{AA}. The rationale behind these two values is to select a relatively small and a relatively large R_{jet} in order to study how I_{AA} changes with increasing jet radius. If $I_{\text{AA}} \rightarrow 1$ as R_{jet} increases, this would indicate that the energy lost by a jet due to medium interactions is redistributed into soft radiation at large angles relative to the jet axis.

Jet areas are measured using the "active area" definition discussed in section 3.3.2. This choice is, once again, to match the analysis of AuAu-collisions. However, the contribution due to pile-up here is small: for $R_{\text{jet}} = 0.2$, $\langle \rho \cdot A_{\text{jet}} \rangle \sim 0$ across $E_{\text{T}}^{\text{trg}}$; and for $R_{\text{jet}} = 0.5$,

[1] Meaning that only the charged component of the jet is reconstructed.

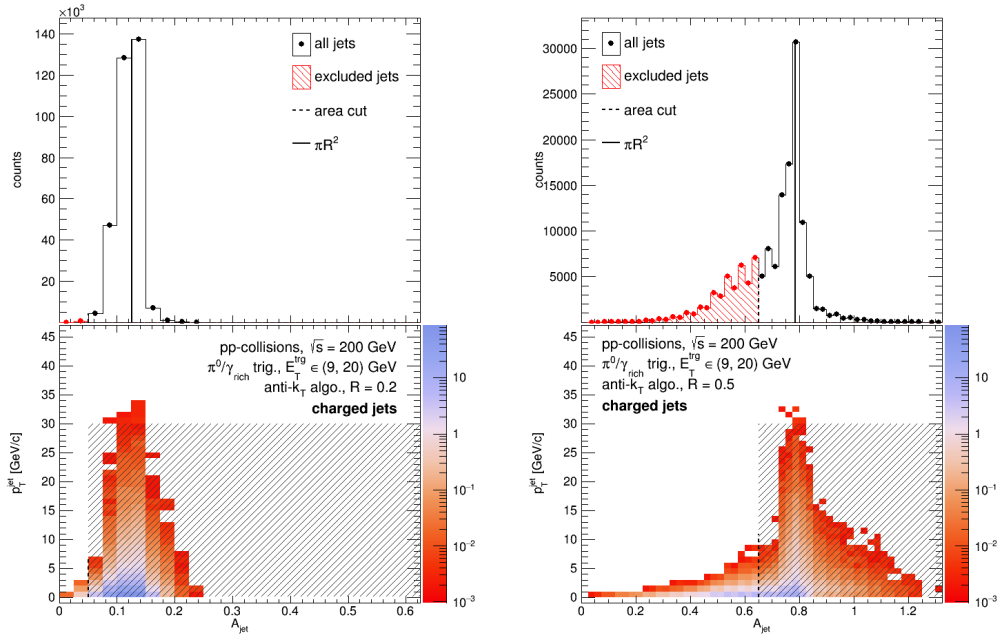

(a) $R_{\text{jet}} = 0.2$ jets (b) $R_{\text{jet}} = 0.5$ jets

Figure 8.2: Jet areas integrated over $p_{\text{T}}^{\text{jet}}$ (upper panels) and as a function of $p_{\text{T}}^{\text{jet}}$ for R_{jet} = 0.2 (8.2a) and 0.5 (8.2b). The dotted lines and shading in the upper panel indicates regions excluded by the jet section criteria, and the solid lines indicate the value of πR_{jet}^2. The shaded boxes in the lower panels indicate the jets passing the jet area and $p_{\text{T}}^{\text{jet}}$ selection criteria.

$(\rho \cdot A_{\text{jet}})$ rarely surpasses 1 GeV/c across $E_{\text{T}}^{\text{trg}}$. Figure 8.2 shows A_{jet} for both values of R_{jet}, and figure 8.3 illustrates how $\rho \cdot A_{\text{jet}}$ varies with $p_{\text{T}}^{\text{jet}}$, the raw (uncorrected) jet transverse momentum.

Once reconstructed, jets are selected according to the criteria listed in table 8.5. The cut on η^{jet} ensures that the reconstructed jets are fully contained within STAR's acceptance. The A_{jet} criteria are chosen to match the criteria applied in [178]. Only "recoil jets" are recorded. These are jets whose axis falls in the quadrant opposite the trigger in relative azimuth, $\Delta\varphi^{\text{jet}} = \varphi^{\text{jet}} - \varphi^{\text{trg}}$. In other words, a recoil jet is one who satisfies $|\Delta\varphi^{\text{jet}} - \pi| < \pi/4$.

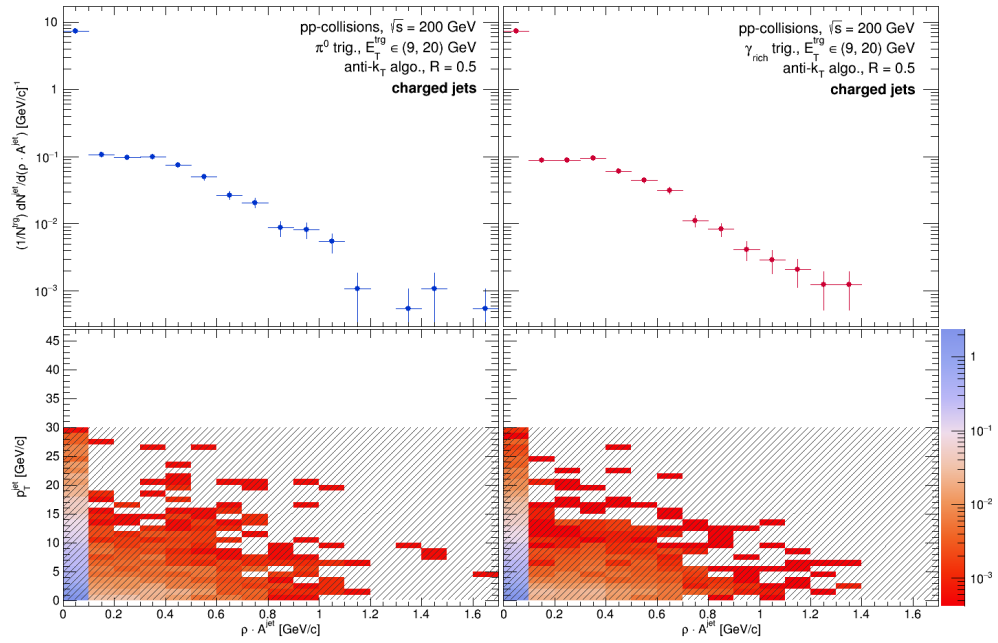

Figure 8.3: The correction term $\rho \cdot A_{\text{jet}}$ integrated over $p_{\text{T}}^{\text{jet}}$ (upper panel) and as a function of $p_{\text{T}}^{\text{jet}}$ (lower panel) for $R_{\text{jet}} = 0.5$ jets. For $R_{\text{jet}} = 0.2$, the correction term is zero.

Criterion	**Description**
$\lvert\eta^{\text{jet}}\rvert < 1 - R_{\text{jet}}$	The pseudorapidity of the selected jet's axis has to fall within $(R_{\text{jet}} - 1, 1 - R_{\text{jet}})$.
$p_{\text{T}}^{\text{jet}} \in (0.2, 30)$ GeV/c	The raw p_{T} of the selected jet must be within $(0.2, 30)$ GeV/c.
$A_{\text{jet}} > 0.05, 0.65$	The selected jet's area has to be greater than 0.05 (for $R_{\text{jet}} = 0.2$) or 0.65 (for $R_{\text{jet}} = 0.5$).
$\lvert\Delta\varphi^{\text{jet}} - \pi\rvert < \pi/4$	Only recoil jets are selected for analysis.

Table 8.5: Criteria applied to reconstructed jets selected for analysis.

The p_{T} of the selected recoil jets are corrected event-by-event to account for the average background energy density according to equation 3.10. Let the corrected jet p_{T} be denoted $p_{\text{T}}^{\text{reco}}$. However, as discussed in section 3.3.3, $\rho \cdot A_{\text{jet}}$ is not the only method by which one can correct for the UE; there is also the Off-Axis Cone method. Figure 8.5 shows

the $R_{\text{jet}} = 0.5$ π^0- and γ_{rich}-triggered uncorrected recoil jet spectra compared against the spectra of recoil jets corrected with the $\rho \cdot A_{\text{jet}}$ method, those corrected with the Off-Axis Cone method, and the magnitude of the Off-Axis corrections. At most 10% differences in the corrected $R_{\text{jet}} = 0.5$ jet spectra were observed for $p_{\text{T}}^{\text{reco}} < 3$ GeV/c. Above this, they were found to be consistent. The two methods were found to be consistent across $p_{\text{T}}^{\text{reco}}$ for $R_{\text{jet}} = 0.2$.

The choice to use the $\rho \cdot A_{\text{jet}}$ method over any other was made in order to match the analysis of the AuAu-collisions. Ultimately, however, so long as the same UE subtraction method is used both on the raw data and in deriving the corrections to be applied to the raw data, the fully corrected jet spectra should be largely independent of the particular method used.

The $\Delta\varphi^{\text{jet}}$ distributions of all selected jets with the recoil jet region demarcated can be seen in figure 8.4. These recoil jets are accumulated into semi-inclusive distributions normalized by the number of triggers per range of $E_{\text{T}}^{\text{trg}}$ and trigger species which are visualized in figure 8.6. The $p_{\text{T}}^{\text{reco}}$ bin sizes of the distributions were defined such that the statistical uncertainty on each datum is at most 30% relative to its central value.

In total, there are 146,752 $R_{\text{jet}} = 0.2$ recoil jets and 39,509 $R_{\text{jet}} = 0.5$ recoil jets passing all jet selection criteria within the 42,508 analyzed events. Table 8.6 lists the number of recoil jets broken down according to the $E_{\text{T}}^{\text{trg}}$ and species of their correlated trigger.

$\mathbf{E_T^{trg}}$ **[GeV]**	π^0		γ_{rich}	
	0.2	0.5	0.2	0.5
9 - 11	44,994	11,997	51,208	13,917
11 - 15	17,348	4,646	25,673	6,901
15 - 20	2,216	650	5,313	1,398
Total	64,558	17,293	82,194	22,216

Table 8.6: Number of selected recoil jets versus the species and $E_{\text{T}}^{\text{trg}}$ of the correlated trigger, and the jet resolution parameter.

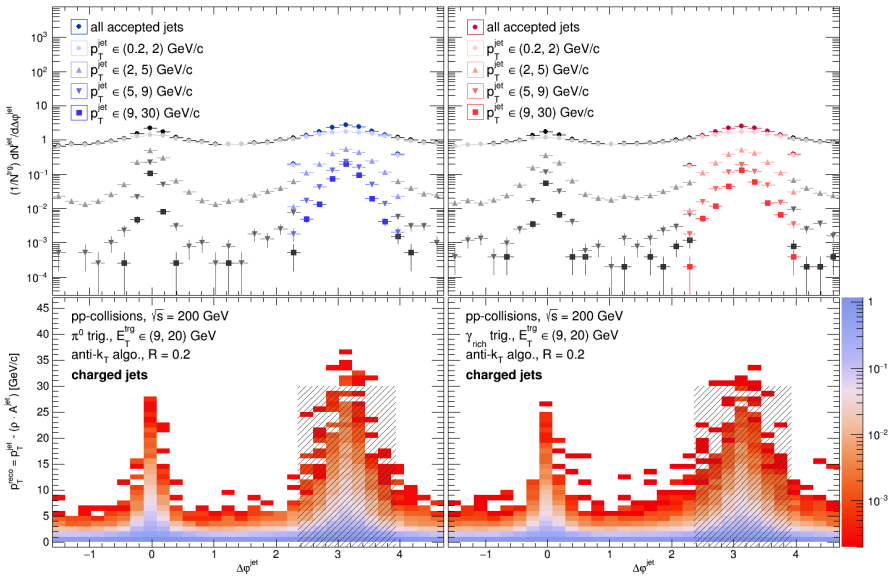

(a) $R_{\text{jet}} = 0.2$

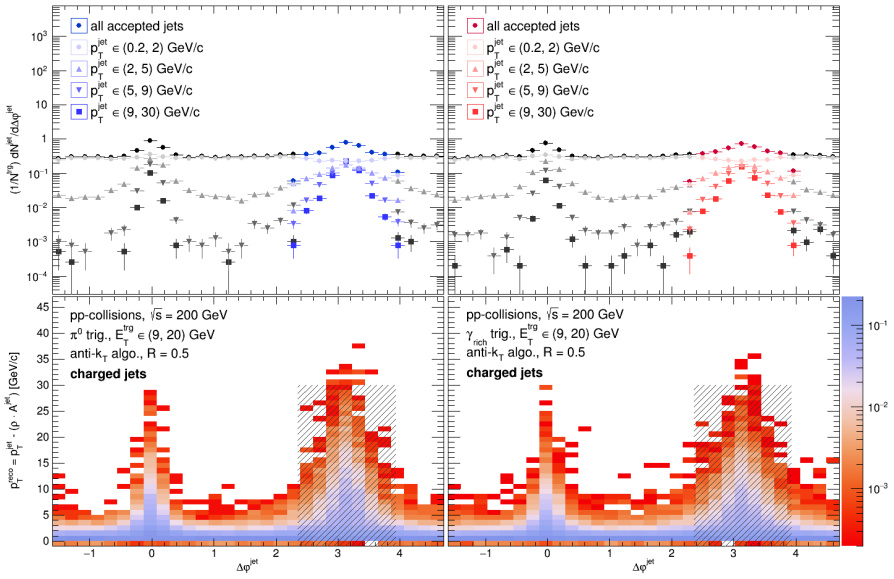

(b) $R_{\text{jet}} = 0.5$

Figure 8.4: $\Delta\varphi$ distributions of all accepted R_{jet} = 0.2 (8.4a) and 0.5 (8.4b) jets. The recoil jet acceptance window is indicated with colored markers in the upper panels and the shaded region in the lower panels.

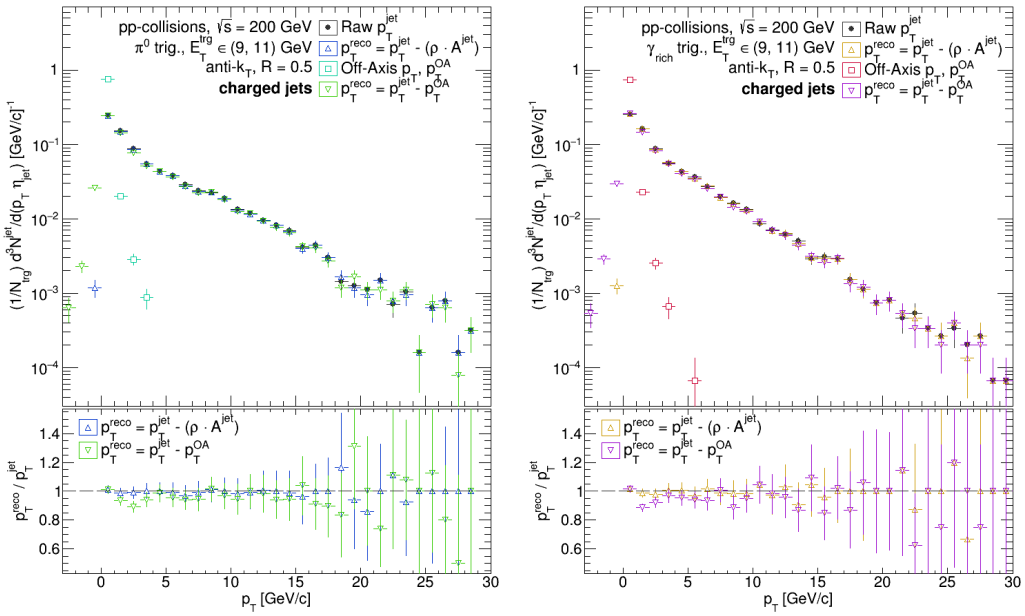

(a) π^0 trigger

(b) γ_{rich} trigger

Figure 8.5: Raw p_{T} spectra (solid black circles) of $R_{\text{jet}} = 0.5$ π^0- (8.5a)and γ_{rich}-triggered (8.5b) recoil jets compared against jet spectra corrected via the $\rho \cdot A_{\text{jet}}$ and Off-Axis methods (open triangles) and the spectra of the magnitude of the Off-Axis corrections (open squares). The lower panels show the ratio of the corrected spectra to the uncorrected spectra.

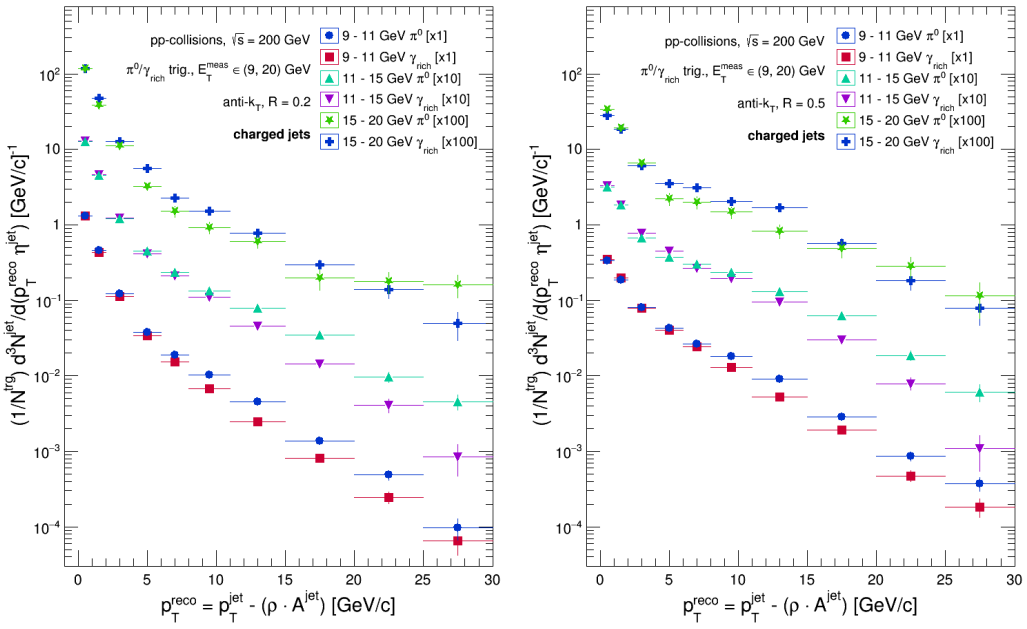

(a) $R_{\text{jet}} = 0.2$, π^0 vs. γ_{rich}

(b) $R_{\text{jet}} = 0.5$, π^0 vs. γ_{rich}

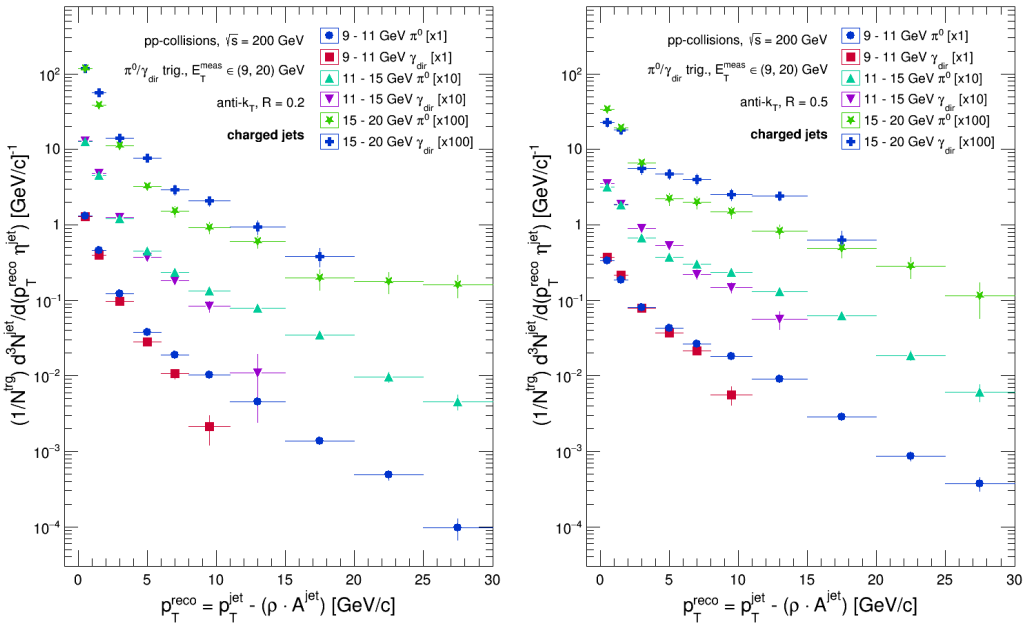

(c) $R_{\text{jet}} = 0.2$, π^0 vs. γ_{dir}

(d) $R_{\text{jet}} = 0.5$, π^0 vs. γ_{dir}

Figure 8.6: Raw semi-inclusive distributions of charged R_{jet} = 0.2 (8.6a, 8.6c) and 0.5 (8.6b, 8.6d) recoil jets as a function of $E_{\text{T}}^{\text{trg}}$ for π^0 vs. γ_{rich} (8.6a, 8.6b) and γ_{dir} (8.6c, 8.6d) triggers.

9. Simulation Framework and Detector Response Estimation

The STAR detector, being a physical measurement apparatus, has fundamental limits with which it can measure physical quantities such as the momentum of a particle. These limitations manifest as effects such as a finite momentum resolution or the reconstruction efficiency of single particles in the TPC. To gauge the size of these effects, this analysis makes use of two separate simulation samples.

The first simulation will be described in detail in section 9.1. It consists of dijet events[1] embedded into real **Z**ero-**B**ias (ZB) pp-data[2] recorded by STAR during the running year 2009. This simulation is used to estimate the tracking efficiency, the probability of reconstructing a charged particle of a given momentum, and the tracking resolution, the precision with which the transverse momentum of a charged particle may be measured, of the STAR TPC. The tracking efficiency and resolution are then parameterized and applied on a particle-by-particle basis to the second simulation, described in section 9.2, which consists of both dijet and γ-jet events.

Throughout this thesis, "particle-level" will be used to refer to simulated events and their corresponding sets of triggers, particles, or jets contained therein before any sort of detector response – via a Geant simulation of STAR or a parameterized function – has been applied. The term "detector-level" will then be used to refer to simulated events, triggers, particles, or jets after a detector response has been applied.

9.1 The Run9 Dijet Embedding Sample

The simulation used to estimate the tracking efficiency and resolution consists of roughly 21 million simulated dijet events at $\sqrt{s} = 200$ GeV using PYTHIA 6.426 [179]

[1] pp-collisions containing two roughly back-to-back jets
[2] pp-collisions recorded without requiring an online trigger

Hard QCD Processes	Electroweak Processes
$gg \to gg$	$qg \to q\gamma$
$gg \to q\bar{q}$	$q\bar{q} \to g\gamma$
$gq \to qg$	$gg \to g\gamma$
$qq \to qq$	$q\bar{q} \to \gamma\gamma$
$q\bar{q} \to gg$	$gg \to \gamma\gamma$
$q\bar{q} \to q\bar{q}$	

Table 9.1: $2 \to 2$ hard scatter QCD and electroweak processes used in the Py6⊕Geant (left column only) and Py8⊕Param (left and right columns) simulations.

with the "Perugia 0" tune [180]. These dijet events are simulated using the $2 \to 2$ hard scatter QCD processes listed in table 9.1 which are then processed by the GSTAR framework, a simulation package based on GEANT-3 [181] that models the response of STAR's detectors. For this reason, this simulation will be frequently referred to as Py6⊕Geant throught this thesis. Once the simulated dijet events have been processed by GSTAR, the simulated detector responses are mixed with real detector responses from ZB pp-data recorded during 2009 to simulate the effect of pile-up. Due to operator error during running, the number of recorded pp-collisions with TPC hits was a factor of 10 lower than what was needed for this simulation. Thus, the available ZB collisions had to be reused several times.

The simulated EMC response is used to select simulated events which would have satisfied several key online triggers: the **J**et-**P**atch 1 (JP1), **A**djacent **J**et **P**atch (AJP), and **B**arrel **H**igh **T**ower 3 (BHT3) triggers. These are defined as so:

(a) **JP1 Trigger:** a nominal transverse energy of $E_T \geq 5.4$ GeV was deposited into a 0.4×0.2, 0.4×0.4, or 0.6×0.4 patch – referred to as "jet patches" – of (η, φ) space of the calorimeter;

(b) **AJP Trigger:** a nominal transverse energy of $E_T \geq 3.5$ GeV was deposited into

two adjacent jet patches; and

(c) **BHT3 Trigger:** a nominal energy of $E \geq 7.5$ GeV was deposited in a 2×2 cluster of BEMC towers.

This is called "trigger filtering." Without it, the computational time and space requirements necessary to simulate sufficient statistics would far outstrip what was available at the time of simulation. Of the total 21 million events, only 2 million events (roughly 8.5%) passed the trigger filtering and were reconstructed. All 21 million of the initial, simulated events are available, however, to allow for corrections back to the initial, unbiased sample.

In order to obtain necessary statistics at high jet $p_{\mathrm{T}}^{\mathrm{jet}}$, the simulation was generated in 10 different bins of partonic p_{T}, $\hat{p}_T$. Each bin of $\hat{p}_{\mathrm{T}}$ is weighted such that an unbiased $\hat{p}_{\mathrm{T}}$ distribution is recovered when summed over all 10 bins. The necessary statistics in each bin of $\hat{p}_{\mathrm{T}}$ was generated so as to ensure that the statistical uncertainty of each bin of simulated p_T^{jet} was well below a quarter of the statistical uncertainty of the corresponding bin of measured p_T^{jet}. This is to avoid large statistical fluctuations in the derived corrections.

However, the statistics of the Py6⊕Geant sample were tuned with inclusive jet measurements in mind, **not** coincidence measurements such as the one presented in this thesis. The available statistics for deriving corrections *after* applying the event, trigger, and jet selection criteria discussed in sections 9.1.1 and 9.1.3 are comparable to the data.

Lastly, it should be noted that the full Py6⊕Geant sample is divided into two subsamples: an FF configuration, and a RFF configuration.

9.1.1 Estimation of the Tracking Efficiency

To calculate the tracking efficiency, events from the Py6⊕Geant framework were selected which satisfy the event selection criteria applied to data (those listed in table 8.1) and which contain a simulated π^0 that has a transverse energy in the range of 9 - 11, 11 - 15, or 15 - 20 GeV and has a pseudorapidity between -0.9 and 0.9. In total, there are

31,627 such events from the Py6⊕Geant framework. Table 9.2 breaks the number of accepted events versus the partonic p_{T} of the event's hard scatter, $\hat{p}_{\mathrm{T}}$, $E_{\mathrm{T}}^{\mathrm{trg}}$ of the trigger π^0, and FF/RFF sub-sample.

$\hat{p}_{\mathrm{T}}$ [GeV/c]	9 – 11 GeV		11 – 15 GeV		15 – 20 GeV	
	FF	**RFF**	**FF**	**RFF**	**FF**	**RFF**
4 - 5	0	1	0	0	0	0
5 - 7	11	2	1	0	0	0
7 - 9	70	92	16	7	0	0
9 - 11	259	360	56	53	3	4
11 - 15	568	686	206	226	9	9
15 - 25	1,569	1,753	1,136	1,210	232	230
15 - 35	3,488	2,721	3,633	2,878	1,759	1,440
>35	1,268	1,066	1,437	1,262	960	855
Total	7,234	6,681	6,485	5,636	2,963	2,538
FF + RFF	14,005		12,121		5,501	

Table 9.2: Number of Py6⊕Geant events containing a trigger passing all event and trigger QA criteria versus the event's $\hat{p}_{\mathrm{T}}$, the $E_{\mathrm{T}}^{\mathrm{trg}}$ of its associated trigger, and the event's sub-sample.

From these events, both primary TPC tracks were selected which satisfy the same conditions applied to data (those listed in table 8.4) and final-state simulated particles which satisfy the conditions listed in table 9.3. When the simulation was created, the reconstructed tracks were matched to simulated particles by comparing the fit points used in constructing the TPC tracks to the trajectories of the simulated particles. This allows for the comparison of various track quantities such as its transverse momentum ($p_{\mathrm{T}}^{\mathrm{reco}}$) to the transverse momentum of the particle that created it ($p_{\mathrm{T}}^{\mathrm{MC}}$). Here, for a track to be declared as *matching* a simulated particle, at least 50% of the fit points comprising the track must match the trajectory of the particle.

Criterion	Description
$Q_{\text{mc}} \neq$	Selected final-state particle must be charged.
$\Delta\varphi^{\text{mc}} = \varphi^{\text{mc}} - \varphi^{\text{trg}} \in (\frac{\pi}{2}, \frac{3\pi}{2})$	Selected final-state particle must lie in the away-side hemisphere.
$\lvert\eta^{\text{mc}}\rvert < 1$	Selected final-state particle must have a pseudorapidity must fall within $(-1, 1)$.
$p_T^{\text{mc}} > 0.2$ GeV/c	Selected final-state particle must have a p_{T} greater than 0.2 GeV/c.

Table 9.3: Criteria applied to Py6⊕Geant final-state MC particles selected for particle-level jet reconstruction.

The selected simulated particles were then accumulated into a histogram p_i which records the weighted (by $\hat{p}_{\text{T}}$) number of particles falling in a bin i of p_{T}^{MC}. Next, the selected tracks were then accumulated into two distinct histograms. Those selected tracks which were successfully matched to a simulated particle were accumulated into a histogram d_i which records the $\hat{p}_{\text{T}}$ weighted number of matched tracks who fall in a bin i of their progenitor's p_{T}^{MC}; and **all** selected tracks were accumulated into a histogram $\tilde{d}_i$ which records the weighted number of tracks falling in a bin i of $p_{\text{T}}^{\text{reco}}$.

After normalizing p_i, d_i, and $\tilde{d}_i$ by the weighted number of triggers, two ratios were calculated: the proper tracking efficiency ϵ_{trk} and a *pseudo-efficiency* ($\tilde{\epsilon}_{\text{trk}}$).

$$\begin{aligned} \epsilon_{\text{trk},i} &= \frac{d_i}{p_i} \\ \tilde{\epsilon}_{\text{trk},i} &= \frac{\tilde{d}_i}{p_i} \end{aligned} \tag{9.1}$$

Since the tracking efficiency's denominator only includes tracks from the original simulated sample, it gives the absolute probability of reconstructing such a particle of transverse momentum p_{T}^{MC}. The pseudo-efficiency, however, also includes tracks produced by parti-

cles associated with sources other than the original simulated sample, namely pile-up and the decays of short-lived particles (so-called *secondary decays*). Thus $\tilde{\epsilon}_{\text{trk}}$ gives the relative surplus or loss of objects with a particular transverse momentum at the detector-level versus the particle-level.

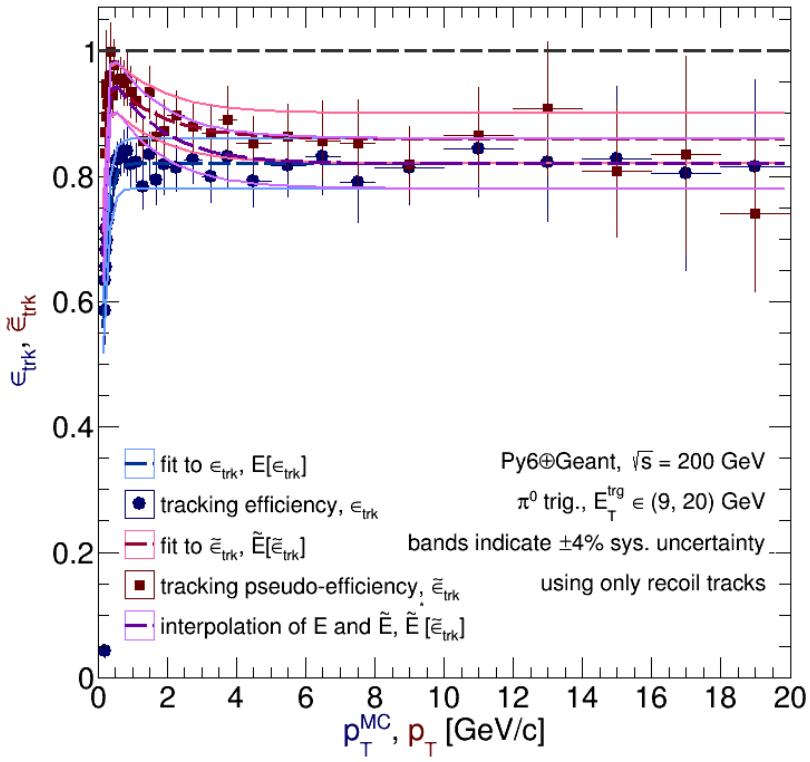

Figure 9.1: The calculated ϵ_{trk} and $\tilde{\epsilon}_{\text{trk}}$ from the Py6⊕Geant framework, and the fit functions E and $\tilde{E}$ applied to ϵ_{trk} and $\tilde{\epsilon}_{\text{trk}}$ respectively. The magenta curve $\tilde{E}^*$ is the interpolation of E and $\tilde{E}$.

The calculated ϵ_{trk} and $\tilde{\epsilon}_{\text{trk}}$ are shown in figure 9.1. Due to the statistical limitations of the Py6⊕Geant sample, there are noticeable statistical fluctuations in the ratios. To mitigate these fluctuations, both ratios are fit with functions that capture their shape:

$$
\begin{aligned}
E\left[\epsilon_{\text{trk}}\right] &= \epsilon_0 \left(1 + e^{-\sigma_1 p_{\text{T}}^{\text{MC}}}\right) \\
\tilde{E}\left[\tilde{\epsilon}_{\text{trk}}\right] &= \epsilon_0 + \epsilon_1 e^{-\sigma_1 p_{\text{T}}} + \epsilon_2 e^{-\sigma_2 p_{\text{T}}^2}
\end{aligned}
\tag{9.2}
$$

where ϵ_i and σ_i are fit parameters. Since pile-up and secondary decays produce soft radiation, $\tilde{\epsilon}_{\text{trk}}$ should converge to ϵ_{trk} at high p_{T}. Thus, a third function, $\tilde{E}^*$, which has the same functional form as $\tilde{E}$ is introduced which interpolates $\tilde{E}$ and E by requiring the parameter ϵ_0 to be that of E. These three functions are shown in figure 9.1. The bands on these functions indicate an absolute uncertainty of $\pm 4\%$, the precision with which STAR is able to measure its tracking efficiency [182]. The extracted fit parameters are listed in table 9.4

Fit Parameter	**E**	$\tilde{\mathbf{E}}$	$\tilde{\mathbf{E}}^*$
(ϵ_i)	0.82	$(0.86, -1.81, 0.12)$	$(0.82, -2.18, 0.18)$
(σ_i)	7.59	$(13.00, 0.67)$	$(13.00, 0.67)$

Table 9.4: Parameters extracted from the fits to ϵ_{trk} and $\tilde{\epsilon}_{\text{trk}}$.

The functions E and $\tilde{E}^*$ constitute **the** parameterized tracking efficiency and pseudo-efficiency which can be utilized in the fast simulation described in section 9.2. The use of both were explored in constructing the fast simulation. However, as no simulation of pile-up was included in the fast simulation and secondary decays were handled differently at the particle-level between it and the Py6$\oplus$Geant framework, $\tilde{E}^*$ was selected as the parameterization to be used in the fast simulation in order to emulate these effects.

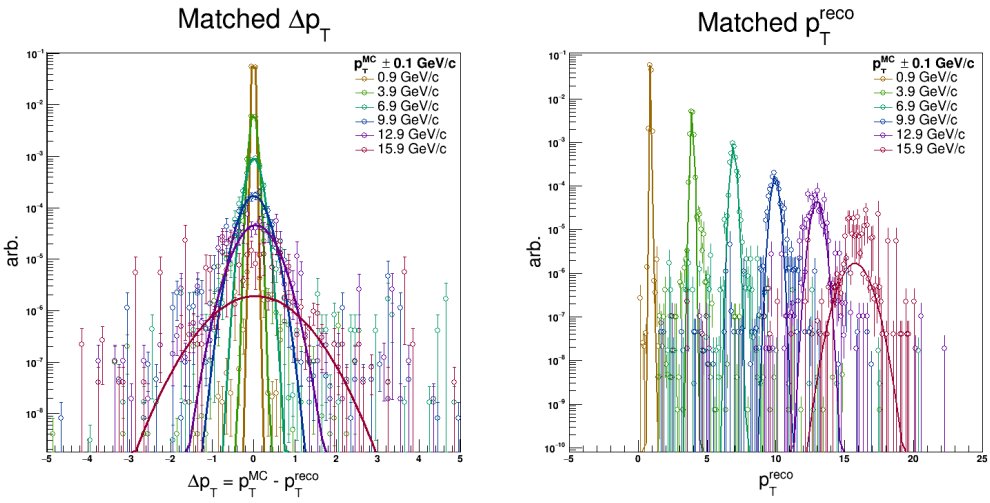

(a) r_{ij}^{diff} (b) r_{ij}^{dist}

Figure 9.2: Projections of matched track Δp_{T} (9.2a) and $p_{\text{T}}^{\text{reco}}$ (9.2b) for select values of simulated particle p_{T}^{MC}. The solid curves are Gaussian fits to the projections.

9.1.2 Estimation of the Tracking Resolution

The parameterization of the tracking resolution $\Delta p_{\text{T}}^{\text{trk}}$ is calculated in a manner analogous to the parameterization of ϵ_{trk}. The same pairs of matched tracks and simulated particles used to calculate ϵ_{trk} were accumulated into two histograms: r_{ij}^{diff} (for **diff**erence), which records the $\hat{p}_{\text{T}}$ weighted number of matched tracks falling in a bin i of progenitor p_{T}^{MC} and in a bin j of difference in progenitor and reconstructed track $p_{\text{T}}^{\text{reco}}$, $\Delta p_{\text{T}} = p_{\text{T}}^{\text{reco}} - p_{\text{T}}^{\text{MC}}$; and r_{ij}^{dist} (for **dist**ribution), which records the $\hat{p}_{\text{T}}$ weighted number of matched tracks falling in a bin i of progenitor p_{T}^{MC} and in a bin j of reconstructed track $p_{\text{T}}^{\text{reco}}$. Each histogram was normalized such that the integral over a slice of p_{T}^{MC} is unity. Then each normalized slice was fit with a gaussian function. These two histograms are visualized as projections of Δp_{T} and $p_{\text{T}}^{\text{reco}}$ in figure 9.2, and the fits are shown as solid lines.

Let σ denote the width of each of the fits with $\sigma\left(\Delta p_{\text{T}} | p_{\text{T}}^{\text{MC}}\right)$ corresponding to the fits to r_{ij}^{diff} and $\sigma\left(p_{\text{T}}^{\text{reco}} | p_{\text{T}}^{\text{MC}}\right)$ corresponding to the fits to r_{ij}^{dist}. These are estimates of the tracking

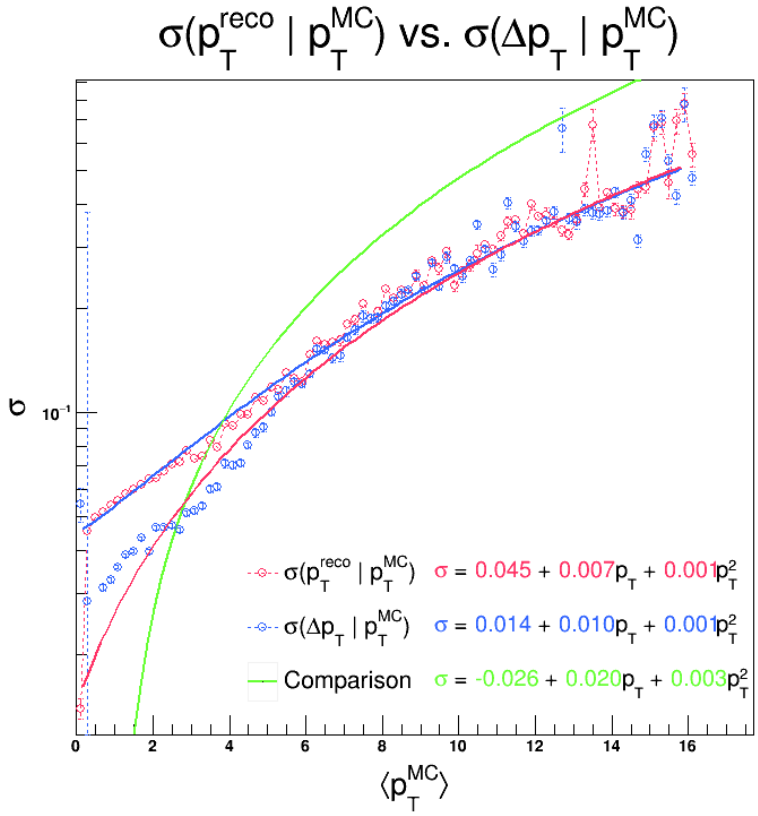

Figure 9.3: Extracted $\sigma\left(\Delta p_{\mathrm{T}}|p_{\mathrm{T}}^{\mathrm{MC}}\right)$ and $\sigma\left(p_{\mathrm{T}}^{\mathrm{reco}}|p_{\mathrm{T}}^{\mathrm{MC}}\right)$ as a function of p_{MC}. Solid lines indicate polynomial fits, and the green curve indicates the fit to $\sigma\left(p_{\mathrm{T}}^{\mathrm{reco}}|p_{\mathrm{T}}^{\mathrm{MC}}\right)$ used in the measurement of the dijet imbalance A_J made by STAR in 2017 [19].

resolution, $\Delta p_{\mathrm{T}}^{\mathrm{trk}}$. To parameterize the tracking resolution, each σ was fit with a second order polynomial R:

$$\begin{aligned} R^{\mathrm{diff}}\left[\sigma\left(\Delta p_{\mathrm{T}}|p_{\mathrm{T}}^{\mathrm{MC}}\right)\right] &= \varsigma_0 + \varsigma_1 p_{\mathrm{T}}^{\mathrm{MC}} + \varsigma_2\left(p_{\mathrm{T}}^{\mathrm{MC}}\right)^2 \\ R^{\mathrm{dist}}\left[\sigma\left(p_{\mathrm{T}}^{\mathrm{reco}}|p_{\mathrm{T}}^{\mathrm{MC}}\right)\right] &= \varsigma_0 + \varsigma_1 p_{\mathrm{T}}^{\mathrm{MC}} + \varsigma_2\left(p_{\mathrm{T}}^{\mathrm{MC}}\right)^2 \end{aligned} \tag{9.3}$$

where ς_i are fit parameters. The extracted fit parameters are listed in table 9.5. An additional parameterization is included in figure 9.3 and table 9.5 as another point of comparison. This parameterization was extracted from a fit to $\sigma\left(p_{\mathrm{T}}^{\mathrm{reco}}|p_{\mathrm{T}}^{\mathrm{MC}}\right)$ calculated utilizing

an embedding sample using ZB data recorded by STAR during the 2012 running year, and was used in the measurement of the dijet imbalance $A_J = \left(p_{\mathrm{T}}^{\mathrm{lead}} - p_{\mathrm{T}}^{\mathrm{sublead}}\right) / \left(p_{\mathrm{T}}^{\mathrm{lead}} + p_{\mathrm{T}}^{\mathrm{sublead}}\right)$ made by the STAR Collaboration in 2017 [19].

Fit Parameter	$\mathrm{R}^{\mathrm{diff}}$	$\mathrm{R}^{\mathrm{dist}}$	**Run12**
ς_0	0.0045	0.0142	-0.026
ς_1	0.0070	0.0107	0.020
ς_2	0.0013	0.00132	0.0030

Table 9.5: Extracted parameters from the fits to $\Delta p_{\mathrm{T}}^{\mathrm{trk}}$, and the fit parameters used in the measurement of the dijet imbalance A_J made by STAR in 2017 [19].

The parameterization R^{diff} was arbitrarily taken to be the default tracking resolution used in the fast simulation. The R^{dist} and Run12 were then reserved to be used as checks when evaluating the systematic uncertainty associated with the tracking resolution.

9.1.3 Jet Reconstruction in the Run9 Dijet Embedding Sample

From the set of selected MC particles and reconstructed TPC tracks, particle- and detector-level jets were reconstructed with the anti-k_{T} algorithm via FastJet 3.0.6 using resolution parameters of $R_{\mathrm{jet}} = 0.2$ and 0.5 in the same manner as jets were reconstructed in the measured data. The same prescription to account for the average background energy density was applied event-by-event to jets in the Py6$\oplus$Geant framework as in data.

After reconstruction, particle- and detector-level recoil jets were selected according to the criteria listed in table 8.5. These selected jets were retained to be used to calculate the response matrix described in Section 10.1. In total, there were 229,744 $R_{\mathrm{jet}} = 0.2$ and 89,516 $R_{\mathrm{jet}} = 0.5$ particle-level recoil jets in the Py6$\oplus$Geant sample, and 95,196 $R_{\mathrm{jet}} = 0.2$ and 23,421 $R_{\mathrm{jet}} = 0.5$ detector-level recoil jets. Table 9.6 lists the number of

particle-level recoil jets broken down according to the $E_{\mathrm{T}}^{\mathrm{trg}}$ of their correlated trigger, and table 9.7 lists the corresponding number of detector-level recoil jets.

$\mathbf{E_T^{trg}}$ **[GeV]**	$\mathbf{R_{jet} = 0.2}$			$\mathbf{R_{jet} = 0.5}$		
	FF	**RFF**	**FF + RFF**	**FF**	**RFF**	**FF + RFF**
9 - 11	27,220	24,667	51,817	10,101	9,317	19,367
11 - 15	24,729	21,640	46,328	9,072	8,032	17,076
15 - 20	11,636	10,108	21,707	4,404	3,890	8,257
Total	63,585	46,307	119,852	23,577	21,239	44,700

Table 9.6: Number of selected Py6⊕Geant particle-level recoil jets versus sub-sample and $E_{\mathrm{T}}^{\mathrm{trg}}$ of the correlated trigger.

$\mathbf{E_T^{trg}}$ **[GeV]**	$\mathbf{R_{jet} = 0.2}$			$\mathbf{R_{jet} = 0.5}$		
	FF	**RFF**	**FF + RFF**	**FF**	**RFF**	**FF + RFF**
9 - 11	21,548	19,682	41,158	5,251	4,958	10,164
11 - 15	19,484	17,326	36,769	4,670	4,143	8,786
15 - 20	9,237	8,059	17,259	2,406	2,102	4,471
Total	50,269	45,067	95,196	12,327	11,203	23,421

Table 9.7: Number of selected Py6⊕Geant detector-level recoil jets versus sub-sample and $E_{\mathrm{T}}^{\mathrm{trg}}$ of the correlated trigger.

9.2 The Fast Simulation

The parameterized functions $\tilde{E}^{*}$ and R^{diff} were applied on a particle-by-particle basis to events generated by PYTHIA 8.185 [131]. This standalone simulation, labeled

Py8⊕Param, has two advantages over the Py6⊕Geant simulation: (1) that it enables control over the simulated detector response; and (2) that it can simulate additional collisions with minimal computing requirements. In light of the latter advantage, the Py8⊕Param will also be referred to as a "Fast Simulation" interchangeably.

The Py8⊕Param sample consists of simulated events which contain π^0 or γ_{dir} triggers with $p_{\text{T}}^{\text{trg}} > 8$ GeV/c and $|\eta^{\text{trg}}| < 1$. The π^0-triggered events were generated using the same $2 \to 2$ hard scatter QCD processes listed in table 9.1, and the γ_{dir}-triggered events were generated using the following $2 \to 2$ electroweak listed in the same table. In both cases, the $\hat{p}_{\text{T}}$ was required to be greater than 4 GeV/c. These events were generated using the default tune (the "Monash Tune") of PYTHIA 8.185.

Generated events with π^0- or γ_{dir}-triggers satisfying $p_{\text{T}}^{\text{trg}} \in (9, 20)$ GeV/c and $|\eta^{\text{trg}}| < 0.9$ were selected to be analyzed. In these events, the parameterized detector response was applied particle-by-particle via Algorithm 4 below. Let $\mathcal{P} = \{p_i\}$ indicate the set of charged particles with 4-momentum $p_i^{\text{MC},\mu}$ for a given event which pass the p_{T} and η requirements applied to MC particles in section 9.1.1.

Algorithm 4 Procedure for applying parameterized detector response in the Fast Simulation.

1: **for** each particle $p_i \in \mathcal{P}$, **do**

2: Let Δ be a value randomly sampled from a Gaussian distribution with mean $\mu = 0$ and standard deviation $\sigma = R^{\text{diff}}\left(p_{\text{T},i}^{\text{MC}}\right)$.

3: The smeared transverse momentum is then $p_{\text{T},i}^{\text{reco}} = p_{\text{T},i}^{\text{MC}} + \Delta$.

4: Randomly sample a value ϵ_{test} between 0 and 1 from a uniform distribution.

4: **if** $\epsilon_{\text{test}} > \tilde{E}^*\left(p_{\text{T},i}^{\text{reco}}\right)$, **then**

5: The particle is discarded as an inefficiency.

6: **else**

7: Recalculate the components of the particle's 4-momentum in terms of its $p_{\mathrm{T}}^{\mathrm{reco}}$, η, and φ.

8: Add it to the set $\mathcal{D}$.

9: **end if**

10: **end for**

The set $\mathcal{D} = \{d_i\}$ then represents the particles with smeared 4-momentum $p_i^{\mathrm{reco},\mu}$ which are not lost due to tracking inefficiencies. The sets $\mathcal{P}$ and $\mathcal{D}$ are then passed along to the jet-finder to create sets of particle-level and detector-level jets.

Parameters such as the geometry of the simulated STAR detector and its simulated ϵ_{trk} and $\Delta p_{\mathrm{T}}^{\mathrm{trk}}$, what type of events (dijets, γ-triggered, etc.), the momentum transfers sampled, the number of events, and so on were all fixed when the Py6$\oplus$Geant sample was initially generated. This presents challenges when assessing the systematic uncertainties associated with the ϵ_{trk} and $\Delta p_{\mathrm{T}}^{\mathrm{trk}}$ as they cannot be varied with ease. The fast simulation allows for these to be easily varied, though. However, the parameterization of the detector response used in the fast simulation may not fully capture the effects present in the data. In contrast, the Py6$\oplus$Geant framework – with its full simulation of STAR and the process of reconstructing data – is certain to. Thus the Py6$\oplus$Geant framework alone is used to correct the measured jet yields, while the fast simulation is reserved to assess the systematic uncertainties associated with the uncertainties on ϵ_{trk} and $\Delta p_{\mathrm{T}}^{\mathrm{trk}}$.

10. Correction of Detector Effects

Any detector used in the study of physics is a physical one, and thus will always have a finite resolution and efficiency. These "detector effects" can cause highly nonlinear distortions in the distribution of physical quantities we aim to measure. This is especially so for the steeply-falling spectra that are frequently studied in high energy nuclear physics such as the recoil jet spectra of this thesis.

To correct for the finite momentum resolution and particle reconstruction efficiency, a strategy known as *regularized unfolding* (or simply *unfolding*) is deployed. Generally speaking, in an unfolding one encodes the relevant effects into a response matrix R_{ij} which maps a true, undistorted spectrum (t_i) onto the measured, distorted spectrum (m_i):

$$m_i = R_{ij} t_j \tag{10.1}$$

The matrix is then "inverted" (in a certain sense) and applied to the measured data, yielding the "true" spectrum with distortions removed. Section 1 of this chapter will explain how the response matrix is calculated in the context of this measurement, Section 2 will describe how Bayes' Theorem can be used to regularize the inversion of this matrix, Section 3 will describe its application, and Section 4 will discuss the outcomes of this correction scheme.

10.1 Calculation of the Response Matrix and Jet Matching Efficiency

As discussed in Chapter 9, the Py6⊕Geant and Py8⊕Param simulations consist of a set of events $\mathcal{E} = \{e_i\}$ each with a π^0 or $h^{\pm}$ trigger with 3-momentum $\left(E_T^{\text{trg}}, \eta^{\text{trg}}, \varphi^{\text{trg}}\right)$, a set of particle-level jets $\mathcal{P}_i = \{p_{ij}\}$ with 3-momentum $(p_{\text{T}}^{\text{par}}, \eta^{\text{par}}, \varphi^{\text{par}})$, and a set of detector-level jets $\mathcal{D}_i = \{d_{ij}\}$ with 3-momentum $\left(p_{\text{T}}^{\text{det}}, \eta^{\text{det}}, \varphi^{\text{det}}\right)$. The response matrix R_{ij} is calculated

by matching simulated particle-level jets to their reconstructed detector-level counterparts. Let $\Delta\eta^{\text{par, det}} = \eta^{\text{par, det}} - \eta^{\text{trg}}$ and $\Delta\varphi^{\text{par, det}} = \varphi^{\text{par, det}} - \varphi^{\text{trg}}$. Then the algorithm by which this is accomplished is described in algorithm 5.

Algorithm 5 The algorithm for matching simulated particle-level jets to reconstructed detector-level jets to calculate a response matrix R_{ij} and jet matching efficiency ϵ_{jet}.

---

for each event $e_i \in \mathcal{E}$, **do**
  if the $\pi^0/h^{\pm}$ trigger does *not* satisfy the criteria listed in table 8.2, **continue**
  for each particle-level recoil jet $p_{ij} \in \mathcal{P}_i$, **do**
    if p_{ij} does *not* satisfy the criteria listed in table 8.5, **then**
      continue
    else
      Add p_{ij} to the histogram P_{eff}.
    end if
    for each detector-level recoil jet $d_{ik} \in \mathcal{D}_i$, **do**
      if d_{ik} does *not* satisfy the criteria listed in table 8.5, **continue**
      Calculate the displacement Δr^{jet} between p_{ij} and d_{ik} and their p_{T} fraction $q_{\text{T}}^{\text{jet}}$:

$$\Delta\eta^{\text{jet}} = \Delta\eta_{ij}^{\text{par}} - \Delta\eta_{ik}^{\text{det}},$$
$$\Delta\varphi^{\text{jet}} = \Delta\varphi_{ij}^{\text{par}} - \Delta\varphi_{ik}^{\text{det}},$$
$$\Delta r^{\text{jet}} = \sqrt{\left(\Delta\eta^{\text{jet}}\right)^2 + \left(\Delta\varphi^{\text{jet}}\right)^2},$$
$$q_{\text{T}}^{\text{trg}} = \frac{p_{\text{T},ik}^{\text{det}}}{p_{\text{T},ij}^{\text{par}}}.$$

      if $\left(\Delta r^{\text{jet}} < \Delta R^{\text{match}}\right) \wedge \left(q_{\text{T}}^{\text{jet}} \in Q_{\text{T}}^{\text{match}}\right)$, **then**
        d_{ik} is a candidate match for p_{ij}, so add it to the list of match

candidates C_{ij}.

15: **end if**

16: From $\mathcal{C}_{ij}$, *the* match will be the candidate which "matches best," i.e. the candidate which has a $q_{\mathrm{T}}^{\mathrm{jet}}$ closest to 1 *and* the smallest Δr^{jet}. Label this candidate m_{ij}.

17: Add m_{ij} to the histogram D_{eff} and the pair (p_{ij}, m_{ij}) to the the response matrix R.

18: **end for**

19: **end for**

20: **end for**

21: Compute the jet matching efficiency $\epsilon_{\mathrm{jet},i} = D_{\mathrm{eff},i}/P_{\mathrm{eff},i}$.

Thus the response matrix is given by $R_{ij} = R\left(p_{\mathrm{T}}^{\mathrm{det}}, p_{\mathrm{T}}^{\mathrm{par}}\right)$. The response matrix is normalized such that

$$\int R\left(p_{\mathrm{T}}^{\mathrm{det}}, p_{\mathrm{T}}^{\mathrm{par}}\right) dp_{\mathrm{T}}^{\mathrm{det}} = 1. \tag{10.2}$$

This enables the response matrix to be interpreted as encoding the conditional probability of obtaining a reconstructed jet with transverse momentum $p_{\mathrm{T}}^{\mathrm{det}}$ given a simulated jet with transverse momentum $p_{\mathrm{T}}^{\mathrm{par}}$. The histograms $P_{\mathrm{eff},i}$ and $D_{\mathrm{eff},i}$ record the number of particle-level jets to match and the number of matched reconstructed jets falling in a bin i of $p_{\mathrm{T}}^{\mathrm{par}}$.

This algorithm requires two parameters to be specified: $\Delta R^{\mathrm{match}}$, which sets the maximum distance a reconstructed jet can be from a simulated jet in $(\eta, \Delta\varphi)$ space to be considered a match candidate, and $Q_{\mathrm{T}}^{\mathrm{match}} = \left(q_{\mathrm{T}}^{\mathrm{min}}, q_{\mathrm{T}}^{\mathrm{max}}\right)$, which sets the allowable range of momentum fraction which a reconstructed jet can have to be considered a match candidate.

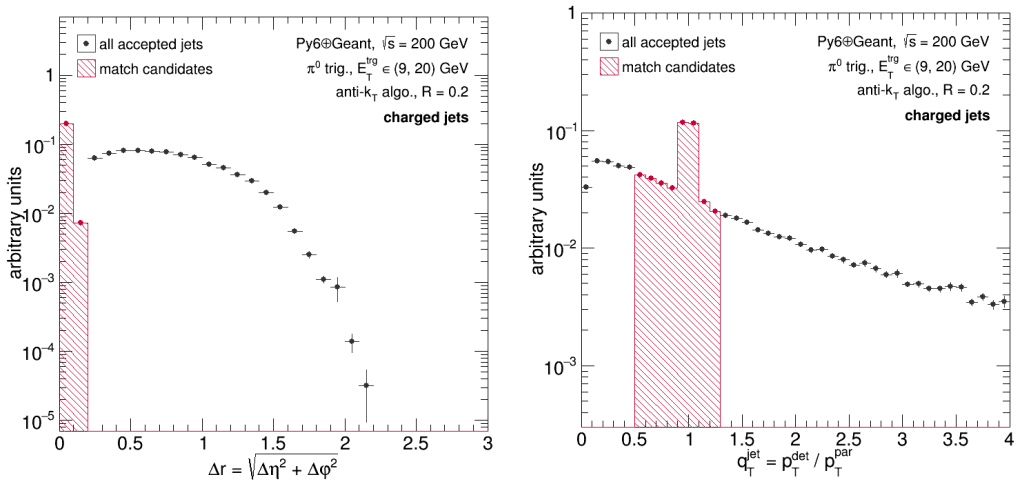

(a) Δr^{jet} (b) $q_{\text{T}}^{\text{jet}}$

Figure 10.1: Δr^{jet} (10.1a) and $q_{\text{T}}^{\text{jet}}$ (10.1b) for $R_{\text{jet}} = 0.2$ charged recoil jets from the Py6⊕Geant framework. Shaded regions indicate the jets selected to be match candidates.

The rationale behind these two parameters is that the only information to characterize jets available at both the particle- and detector-level of the Py6⊕Geant framework are the jet 3-momentum and its area. Since the Py6⊕Geant framework translates simulated particles into simulated detector responses (which have a finite resolution), the mapping between the set of simulated particles and the set of simulated detector responses is not 1-to-1. Thus the only way to assess how well a reconstructed jet matches a simulated jet is how close the two are in $(\eta, \Delta\varphi)$ space and in $p_{\text{T}}^{\text{jet}}$. If a reconstructed jet deviates too much from its simulated counterpart, then it is hard to call the reconstructed jet the "same" jet as the simulated one and thus should be counted as an inefficiency.

In this analysis the parameter ΔR^{match} is set to be R_{jet}, and the parameter $Q_{\text{T}}^{\text{match}}$ is set to be $Q_{\text{T}}^{\text{match}} = (0.5, 1.3)$. The tuning of the $Q_{\text{T}}^{\text{match}}$ parameter will be discussed below. The quantities which these parameters constrain, Δr^{jet} and $q_{\text{T}}^{\text{jet}}$, are visualized in figure 10.1.

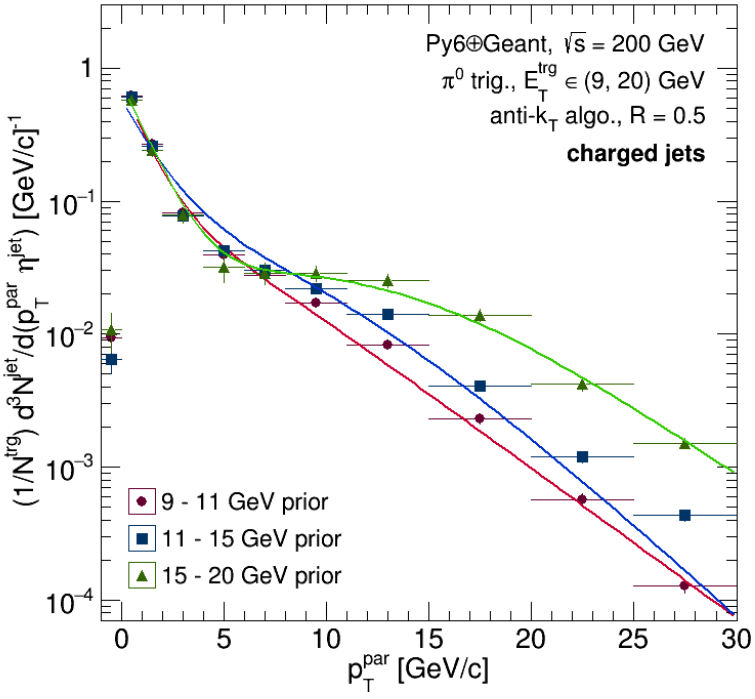

Figure 10.2: Fit functions used to smooth the $R_{\text{jet}} = 0.5$ Py6⊕Geant unfolding priors. Solid lines indicate the fits.

10.2 Smoothing the $R_{\text{jet}} = 0.5$ Response Matrices

In the case of the $R_{\text{jet}} = 0.5$ response matrices, the relatively low statistics of π^0-triggered $R_{\text{jet}} = 0.5$ jets in the Py6⊕Geant framework will result in appreciable bin-to-bin fluctuations in the matrices which will translate into kinks in the unfolded solution. There is no physical reason why these fluctuations should be in R_{ij}, however: they are purely due to the finite statistics of the simulation sample used to train the response matrix. Thus, before unfolding the $R_{\text{jet}} = 0.5$ data, the response matrices will need to be smoothed.

The smoothing proceeds in two steps: the first being to smooth the prior used to train the matrix, and the second being to smooth the matrix itself. To smooth the prior, the particle-level 9 - 11, 11 - 15, and 15 - 20 GeV π^0-triggered $R_{\text{jet}} = 0.5$ recoil jet spectra are

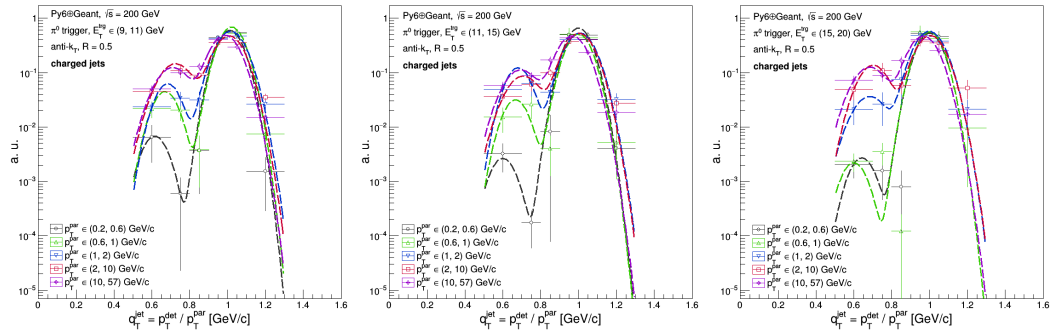

(a) 9 - 11 GeV (b) 11 - 15 GeV (c) 15 - 20 GeV

Figure 10.3: Fit functions used to smooth the $R_{\text{jet}} = 0.5$ response matrices' $q_{\text{T}}^{\text{jet}}$ projections for 9 - 11 (10.3a), 11 - 15 (10.3b), and 15 - 20 GeV (10.3c) π^0 triggers. Solid lines indicate the fits.

fit with functions $P\left(p_{\text{T}}^{\text{par}}|E_{\text{T}}^{\text{trg}}\right)$ which approximate the shape of the spectrum that consist of a combination of exponentials and hyperbolic tangents:

$$P\left(p_{\text{T}}^{\text{par}}|E_{\text{T}}^{\text{trg}}\right) = \left(\sum_{i=0}^{n_{\text{exp}}} e^{c_i + b_i p_{\text{T}}^{\text{par}}}\right) \times \left[\sum_{j=0}^{n_{\text{tan}}} \tanh\left(\frac{p_{\text{T}}^{\text{par}} - p_{\text{T},j}^{0}}{a_j}\right)\right] \tag{10.3}$$

where a_i, b_i, c_j and $p_{\text{T},j}^0$ are parameters, and n_{exp} and n_{tan} set the number of exponentials and hyperbolic tangents to use for a given range of $E_{\text{T}}^{\text{trg}}$. The values of n_{exp} and n_{tan} were arrived at by considering the shape of the prior and trial-and-error. The fit functions are shown in figure 10.2, and the extracted parameters are listed in appendix C. Then $S\left(p_{\text{T}}^{\text{par}}|E_{\text{T}}^{\text{trg}}\right) = \epsilon_{\text{jet}} \times P\left(p_{\text{T}}^{\text{par}}|E_{\text{T}}^{\text{trg}}\right)$ indicates the distribution of unsmeared (particle-level) recoil jet p_{T} after applying the jet matching efficiency.

Next the response matrix itself needs to be smoothed. First, projections of $q_{\text{T}}^{\text{jet}}$ for select ranges of $p_{\text{T}}^{\text{par}}$ were fit using a double Gaussian function, $Q\left(q_{\text{T}}^{\text{jet}}|p_{\text{T}}^{\text{par}}, E_{\text{T}}^{\text{trg}}\right)$. The choice of functional form for these fits may seem odd. However, they do reproduce the general shape of the discrete values of $q_{\text{T}}^{\text{jet}}$ as can be seen in figure 10.3. Moreover, in pp collisions, the number of particles in even $R_{\text{jet}} = 0.5$ jets should be relatively low, especially those at

very low $p_{\mathrm{T}}^{\mathrm{jet}}$. These very soft jets will be dominated by jets with one or two constituents with roughly equal energy. In these cases, one would expect the matching detector-level jet to have either roughly the same $p_{\mathrm{T}}^{\mathrm{jet}}$ ($q_{\mathrm{T}}^{\mathrm{jet}} \sim 1$) as both constituents survived the tracking efficiency, roughly half of the original $p_{\mathrm{T}}^{\mathrm{jet}}$ ($q_{\mathrm{T}}^{\mathrm{jet}} \sim 0.5$) as only one of the constituents survived, or to be completely lost as neither constituent survived. These peaks in $q_{\mathrm{T}}^{\mathrm{jet}}$ at 1 and 0.5 will then be smeared out due to the tracking resolution and the inclusion of jets with more than two constituents.

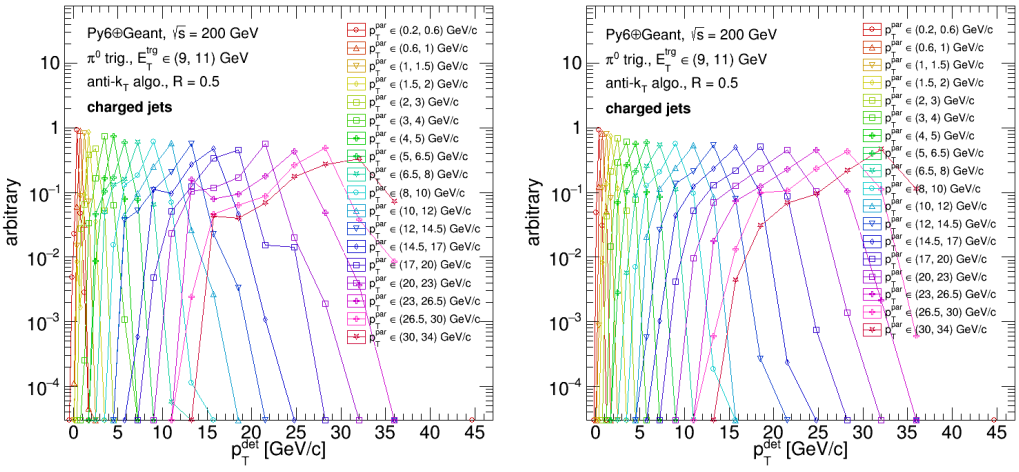

(a) Raw (b) Smoothed

Figure 10.4: Projections of $p_{\mathrm{T}}^{\mathrm{det}}$ for a raw matrix (10.4a) versus its smooth counterpart (10.4b) for 9 - 11 GeV π^0 triggers..

Indeed, this can be seen in the $q_{\mathrm{T}}^{\mathrm{jet}}$ projections at low $p_{\mathrm{T}}^{\mathrm{par}}$ in figure 10.3. As the jet p_{T} increases, these two peaks should become increasingly smeared out as they will become increasingly dominated by jets with substantially more than two constituents, approaching a single peak centered at $q_{\mathrm{T}}^{\mathrm{jet}} = 1$ with a slowly falling tail on the $q_{\mathrm{T}}^{\mathrm{jet}} < 1$ side and a sharply falling tail on the $q_{\mathrm{T}}^{\mathrm{jet}} > 1$ side. This asymmetry is due to the fact that it is substantially

more likely for a jet to lose energy in being reconstructed than it is for it to gain energy. This behavior is also seen in figure 10.3.

The parameters of the functions $Q\left(q_{\mathrm{T}}^{\mathrm{jet}}|p_{\mathrm{T}}^{\mathrm{par}}, E_{\mathrm{T}}^{\mathrm{trg}}\right)$ are listed in appendix C. The algorithm by which the $R_{\mathrm{jet}} = 0.5$ response matrices are smoothed is then described in algorithm 6.

Algorithm 6 The algorithm for smoothing a response matrix R_{ij}.

1: **for** N_{MC} iterations, **do**

2: Randomly sample a value of $p_{\mathrm{T}}^{\mathrm{par}}$ from $S\left(p_{\mathrm{T}}^{\mathrm{par}}|E_{\mathrm{T}}^{\mathrm{trg}}\right)$.

3: Randomly sample a value of $q_{\mathrm{T}}^{\mathrm{jet}}$ from $Q\left(q_{\mathrm{T}}^{\mathrm{jet}}|p_{\mathrm{T}}^{\mathrm{par}}, E_{\mathrm{T}}^{\mathrm{trg}}\right)$.

4: Calculate the corresponding detector-level $p_{\mathrm{T}}^{\mathrm{det}} = p_{\mathrm{T}}^{\mathrm{par}} \times q_{\mathrm{T}}^{\mathrm{jet}}$.

5: Add the pair $\left(p_{\mathrm{T}}^{\mathrm{det}}, p_{\mathrm{T}}^{\mathrm{par}}\right)$ to the smoothed response matrix $\tilde{R}_{ij}$.

6: **end for**

7: Normalize $\tilde{R}_{ij}$ such that $\int \tilde{R}\left(p_{\mathrm{T}}^{\mathrm{det}}, p_{\mathrm{T}}^{\mathrm{par}}\right) dp_{\mathrm{T}}^{\mathrm{det}} = 1$.

The impact of smoothing the response matrix on the matrix itself can be seen in figure 10.4 which shows projections of $p_{\mathrm{T}}^{\mathrm{det}}$ for a raw matrix versus its smoothed counterpart. Then the impact on the unfolded $R_{\mathrm{jet}} = 0.5$ data of smoothing the response matrix can be seen in figure 10.5.

10.3 Retraining the Response Matrix

There are instances when the response matrix needs to be retrained on a prior other than the particle-level Py6⊕Geant recoil jet spectrum. For instance, both the Py6⊕Geant and Py8⊕Param samples used to train the response matrix consist solely of π^0-triggered dijet events. This could produce a bias in the corrected data, especially in the γ_{dir}-triggered data.

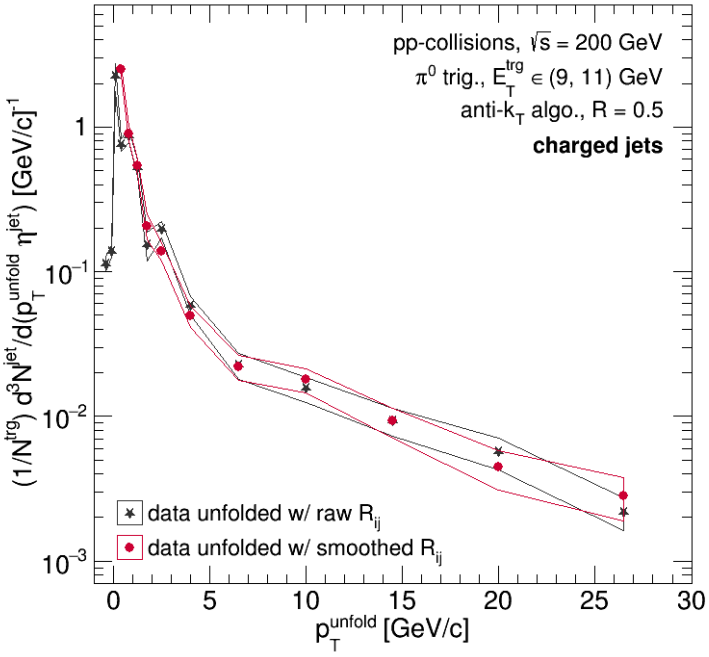

Figure 10.5: 9 - 11 GeV π^0-triggered $R_{\text{jet}} = 0.5$ data unfolded using a raw response matrix (black stars) versus using a smoothed response matrix (red circules).

While this bias is expected to be small due to the robustness of the Bayesian unfolding algorithm and to the fact that (to first order at least) the response matrix should only depend on the jet p_{T} and at most weakly on the shape of the training prior. However, this needs to be checked and will be in Section 11.1.2.

When the need arose, the response matrix was be retrained on a different prior via a fast Monte-Carlo simulation. This procedure will be described in terms of retraining the response matrix on a γ_{dir}-triggered recoil jet spectrum. However, the procedure for retraining the response matrix on something such as a Levy function is identical but with given function substituted for the γ_{dir}-triggered recoil jet spectrum.

First, the $R_{\text{jet}} = 0.2$ and 0.5 γ_{dir}-triggered recoil jet spectra were generated using PYTHIA 8 for all three ranges of $E_{\text{T}}^{\text{trg}}$. Let these spectra be labeled P_i where i runs over

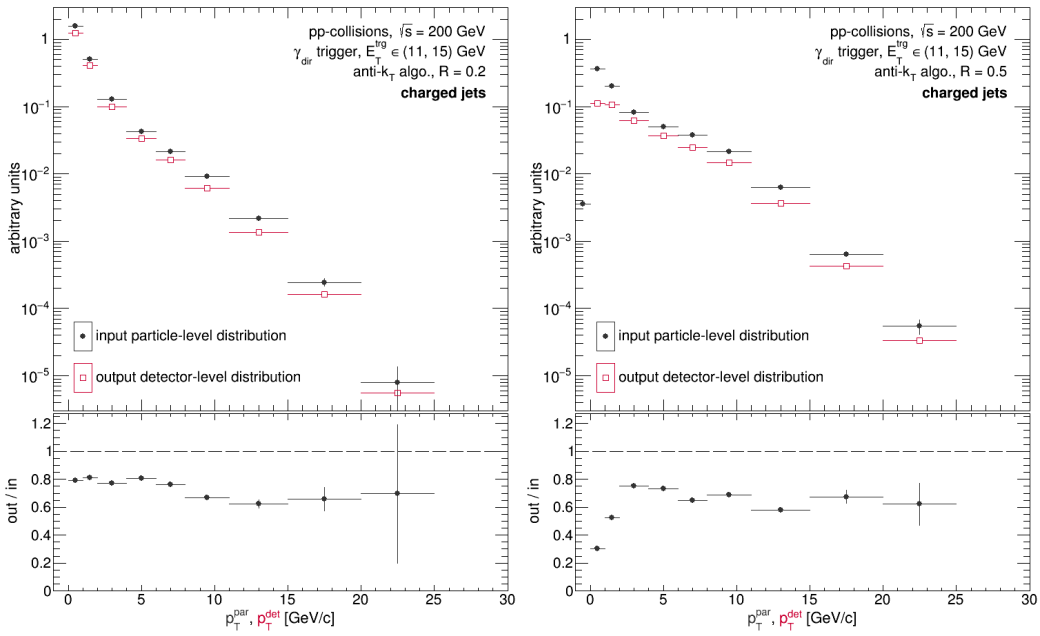

(a) $R_{\text{jet}} = 0.2$ (b) $R_{\text{jet}} = 0.5$

Figure 10.6: Particle-level 11 - 15 GeV γ_{dir}-triggered recoil jet spectrum ("Input") from PYTHIA 8 versus the detector-level recoil jet spectrum ("output") of the fast monte carlo for $R_{\text{jet}} = 0.2$ (10.6a) and 0.5 (10.6b).

the bins of particle-level jet p_{T}. Each spectrum was then multiplied by the corresponding jet-matching efficiency; let the resulting spectrum be labeled $S_i = \epsilon_{\text{jet}} \times P$.

Next, values of unsmeared jet $p_{\text{T}}^{\text{jet}}$ ($p_{\text{T}}^{\text{par}}$) were sampled from S_i. For each sampled $p_{\text{T}}^{\text{par}}$, a smeared jet p_{T} ($p_{\text{T}}^{\text{det}}$) was sampled from the distribution of detector-level jet p_{T} corresponding to the sampled $p_{\text{T}}^{\text{par}}$ from the π^0-triggered response matrix. Each pair $\left(p_{\text{T}}^{\text{det}}, p_{\text{T}}^{\text{par}}\right)$ was then accumulated in a new response matrix, $\tilde{R}_{ij}$, and each sampled $p_{\text{T}}^{\text{det}}$ was accumulated in a new detector-level recoil jet spectrum $\tilde{D}_i$. This sampling procedure was repeated a sufficient number of times such that the region defined by $p_{\text{T}}^{\text{par}} \in \left(-1, E_{\text{T}}^{\text{trg, max}}\right)$ and $p_{\text{T}}^{\text{det}} \in \left(-1, E_{\text{T}}^{\text{trg, max}}\right)$ (where $E_{\text{T}}^{\text{trg, max}}$ is the upper limit of the $E_{\text{T}}^{\text{trg}}$ range) was adequately populated.

Lastly, $\tilde{R}_{ij}$ and $\tilde{D}$ were appropriately normalized. Note that for $R_{\text{jet}} = 0.5$ jets, the

smoothed R_{ij} are used when retraining. Figure 10.6 shows a representative particle-level γ_{dir}-triggered recoil jet spectrum versus the constructed $\tilde{D}_i$ and the $\tilde{R}_{ij}$ from this procedure.

10.4 Bayes' Theorem and Regularized Unfolding

With the response matrices in hand, it is tempting to simply take their mathematical inverse and directly apply them to the measured distribution to obtain the true distribution, i.e.

$$R_{ij}^{-1} m_j = t_i \tag{10.4}$$

where m_i and t_i are the number of measured jets and true jets in bin i of $p_{\text{T}}^{\text{jet}}$. Throughout this section repeated indices will imply summation over the values of those indices. However, as D'Agostini points out in [183], there are issues with this approach:

1. if R_{ij} is singular, there will be issues with inversion;
2. moreover, there is no *a priori* reason why R_{ij}^{-1} should exist; and
3. this approach is not able to handle large statistical fluctuations.

Regarding the last issue, consider that there will inevitably be negative terms in R_{ij}^{-1}. Any large fluctuations in R_{ij} due to statistics could in turn lead to large negative terms in R_{ij}^{-1} which could result in negative entries in the unfolded distribution.

Thus, especially in light of the last issue, the inversion of R_{ij} must be regularized in some fashion. One of the earliest proposals towards regularized unfolding was based on decomposing the R_{ij} into orthogonal polynomials [184]. This method had some technical shortcomings and was not able to handle multidimensional distributions. However, taking seriously the fact that R_{ij} can be interpreted as the conditional probability of obtaining a reconstructed jet with transverse momentum $p_{\text{T}}^{\text{reco}}$ from a true (or simulated) jet of trans-

verse momentum $p_{\mathrm{T}}^{\mathrm{true}}$, Bayes' Theorem offers a natural way to think about this process [183].

As a reminder, Bayes' Theorem states that the probability of an event A occurring given that another event B has occurred is

$$P\left(A|B\right) = \frac{P\left(B|A\right)P\left(A\right)}{P\left(B\right)} \tag{10.5}$$

where $P\left(\star\right)$ indicates the probability of an event occurring, and $P\left(A|B\right)$ is the conditional probability of A occurring given B. For the discussion here, the events under consideration are the observation of a reconstructed jet of $p_{\mathrm{T}}^{\mathrm{reco}}$ and a true jet of $p_{\mathrm{T}}^{\mathrm{true}}$. Their probabilities are:

$$\begin{aligned} P\left(p_{\mathrm{T}}^{\mathrm{true}}\right) &= t_i/N_t \\ P\left(p_{\mathrm{T}}^{\mathrm{reco}}\right) &= m_i/N_m \end{aligned} \tag{10.6}$$

where N_t and N_m are the total number of measured and true jets respectively. We can then state the response matrix in terms of probability [183]:

$$R_{ij} = P\left(p_{\mathrm{T}}^{\mathrm{reco}}|p_{\mathrm{T}}^{\mathrm{true}}\right) \tag{10.7}$$

Now let us consider an "unfolding matrix" U_{ij} which gives the conditional probability of obtaining a *true* jet of $p_{\mathrm{T}}^{\mathrm{true}}$ given a reconstructed jet of $p_{\mathrm{T}}^{\mathrm{reco}}$:

$$U_{ij} = P\left(p_{\mathrm{T}}^{\mathrm{true}}|p_{\mathrm{T}}^{\mathrm{reco}}\right) \tag{10.8}$$

such that the best guess as to what the true distribution is given by

$$\begin{aligned}\hat{t}_i &= U_{ij} m_j \\ \hat{t}_i &= \frac{1}{\epsilon_i} P\left(p_{\mathrm{T},i}^{\mathrm{true}} | p_{\mathrm{T},j}^{\mathrm{reco}}\right) m_j\end{aligned} \tag{10.9}$$

where $\epsilon = \sum_i^{n_m} P\left(p_{\mathrm{T},i}^{\mathrm{reco}} | p_{\mathrm{T}}^{\mathrm{true}}\right) \leq 1$ is the efficiency of reconstructing a jet with $p_{\mathrm{T}}^{\mathrm{true}}$, and n_m is the number of bins of $p_{\mathrm{T}}^{\mathrm{reco}}$. Then making use of Bayes' Theorem gives:

$$\hat{t}_i = \frac{1}{\epsilon_i} \frac{P\left(p_{\mathrm{T},j}^{\mathrm{reco}} | p_{\mathrm{T},i}^{\mathrm{true}}\right) P\left(p_{\mathrm{T},i}^{\mathrm{true}}\right)}{P\left(p_{\mathrm{T},j}^{\mathrm{reco}}\right)} m_j \tag{10.10}$$

Thus, from $\hat{t}$ the estimated total number of true jets $\hat{N}_t$ and their probability distributions:

$$\begin{aligned}\hat{N}_t &= \sum_i^{n_t} \hat{t}_i \\ \hat{P}_t &= \hat{t}_i / \hat{N}_t\end{aligned} \tag{10.11}$$

where n_t is the number of bins of $p_{\mathrm{T}}^{\mathrm{true}}$.

However, the whole motivation behind unfolding is to obtain the underlying true spectrum from measured data. When we make a measurement, we do not know *a priori* what that distribution is. To overcome this, let $P\left(p_{\mathrm{T}}^{\mathrm{true}}\right) \rightarrow P_0\left(p_{\mathrm{T}}^{\mathrm{par}}\right)$ in 10.10 where P_0 is the best guess as to what the true spectrum should be (usually obtained from simulation) and $p_{\mathrm{T}}^{\mathrm{par}}$ is the particle-level jet p_{T}. Then everything is calculable in 10.10, and the simple iterative algorithm described in Algorithm 7 may be used to unfold the measured distribution.

Algorithm 7 An unfolding algorithm based on Bayes' Theorem as implemented in [183].

1: Choose $P_0\left(p_{\mathrm{T}}^{\mathrm{par}}\right)$. Then the initial guess of t is $t_{0,i} = N_m P_0\left(p_{\mathrm{T},i}^{\mathrm{par}}\right)$.

2: Calculate $\hat{t}_i = U_{ij} m_j$ and $\hat{P}\left(p_{\mathrm{T},i}^{\mathrm{par}}\right) / \hat{N}_t$.

3: Make a χ^2/NDF comparison between $\hat{t}$ and t_0.

4: Replace P_0 with $\hat{P}$ and repeat steps 1 - 3.

5: **if** after the 2nd iteration the χ^2/NDF is small enough, **then**

6: Terminate algorithm

7: **else**

8: Replace P_0 with $\hat{P}$ and repeat steps 1 - 4 for an additional $n_{\text{iter}} - 1$ iterations.

9: **end if**

Here n_{iter} be the maximum number of iterations. In the context of this analysis, m_i is the measured data and $P_0\left(p_{\mathrm{T}}^{\mathrm{par}}\right)$ is the particle-level recoil jet distribution from either Py6$\oplus$Geant or Py8$\oplus$Param, and R_{ij} is the calculated response matrix of the previous section.

Note that U_{ij} is *not* the mathematical inverse of R_{ij}. However, in the absence of statistical fluctuations in either t_i or m_i, $UR \to 1$ as the number of iterations in algorithm 7 goes to infinity. If statistical fluctuations are present, though, sending the number of iterations to infinity will result in large fluctuations in the unfolded distribution as $n_{\text{iter}} \to \infty$, $U_{ij} \to R_{ij}^{-1}$. To avoid large fluctuations, one can (1) reduce the number of degrees of freedom in t_i before unfolding; (2) choose an optimal value of n_{iter} before unfolding (usually $n_{\text{iter}} \leq 5$ is sufficient); or (3) smooth $\hat{t}_i$ before feeding it to the next iteration [183]. Option (2) was selected for this analysis.

Lastly, some of the primary benefits of the Bayesian approach to regularized unfolding are that [183]:

1. it can manifestly handle different binnings between the measured and true distribu-

tions;

2. can be applied to multidimensional distributions; and

3. it is robust against the choice of P_0 (even in complete ignorance of the functional form of t_i).

10.5 Applying Corrections to Data

The calculation in Section 10.1 is repeated for each range of $E_{\mathrm{T}}^{\mathrm{trg}}$ and each value of R_{jet}, producing a set of six response matrices and jet-matching efficiencies (ϵ_{jet}). Each pair of R_{ij} and ϵ_{jet} is then used to correct the raw measured π^0 and γ_{dir} data corresponding to the range of $E_{\mathrm{T}}^{\mathrm{trg}}$ and value of R_{jet}. The γ_{dir} data are corrected using the R_{ij} retrained on the γ_{dir}-triggered recoil jet spectra.

Before unfolding $R_{\mathrm{jet}} = 0.5$ data, each corresponding response matrix is smoothed according to the process described in Section 10.2. After unfolding the data ($R_{\mathrm{jet}} = 0.2$ or 0.5), the corresponding jet-matching efficiency is smoothed by fitting it with the function $J\left[\epsilon_{\mathrm{jet}}\right] = \epsilon_0^{\mathrm{jet}}\left(1 - e^{-\sigma_0^{\mathrm{jet}} p_{\mathrm{T}}^{\mathrm{jet}}}\right)$ where $\epsilon_0^{\mathrm{jet}}$ and σ_0^{jet} are fit parameters. The function J is then used to correct the data and perform the backfolding described below.

The unfolding is handled by the RooUnfold framework [185], a plugin for ROOT built to automatically unfold a distribution according to a specified algorithm. It requires four inputs:

1. the "prior," i.e. the original, simulated distribution (in this case the particle-level recoil jet spectra from the Py6$\oplus$Geant sample);

2. the "smeared prior," i.e. the reconstructed simulated distribution with all detector effects applied (the detector-level recoil jet spectra);

3. the response matrix which maps the prior onto the smeared prior;

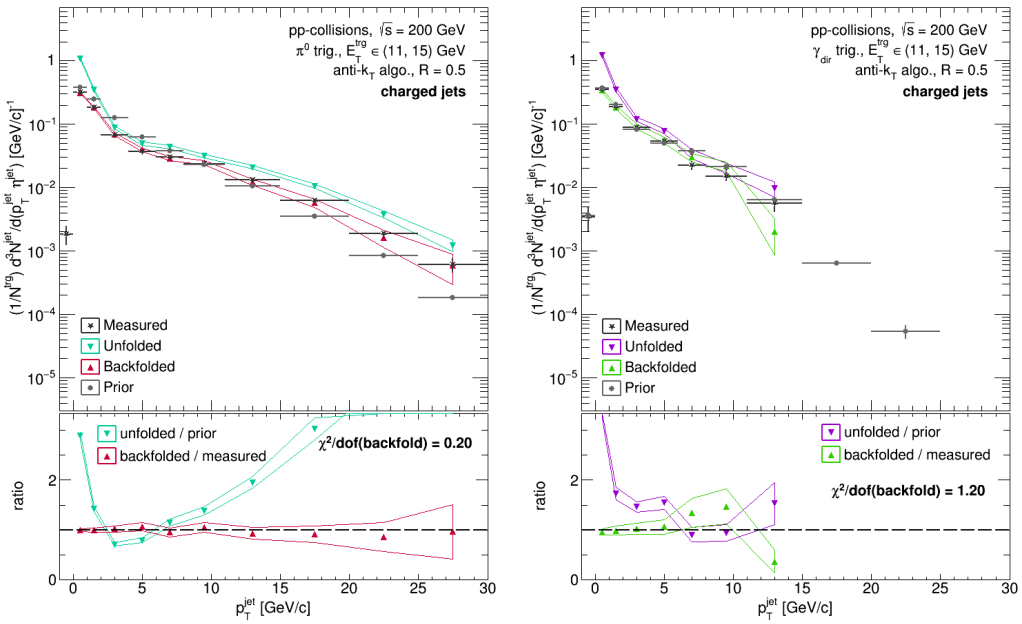

(a) π^0 trigger (b) γ_{dir} trigger

Figure 10.7: Unfolding solutions for 11 - 15 GeV π^0- (10.7a) and γ_{dir}-triggered (10.7b) $R_{\text{jet}} = 0.5$ data versus their corresponding raw data, prior, and backfolded distributions.

4. and the measured data to be unfolded.

RooUnfold provides multiple unfolding algorithms out-of-the-box. However, only the Bayesian algorithm was utilized in this analysis.

The quality of the unfolding is assessed by comparing "backfolded" data against the original, raw data. The data are first unfolded with a fixed regularization parameter and corrected bin-by-bin with the relevant $J\left[\epsilon_{\text{jet}}\right]$. Then the backfolded distribution is accumulated by sampling a random value of $p_{\text{T}}^{\text{unf}}$ according to the unfolded distribution, and then sampling a random value of $p_{\text{T}}^{\text{reco}}$ from the response matrix based on the sampled $p_{\text{T}}^{\text{unf}}$ for a fixed number of iterations. Finally, $J\left[\epsilon_{\text{jet}}\right]$ is applied bin-by-bin to the backfolded distribution which is then normalized to the raw data. Figure 10.7 shows representative unfolding solutions compared against the corresponding raw data, prior, and backfolded

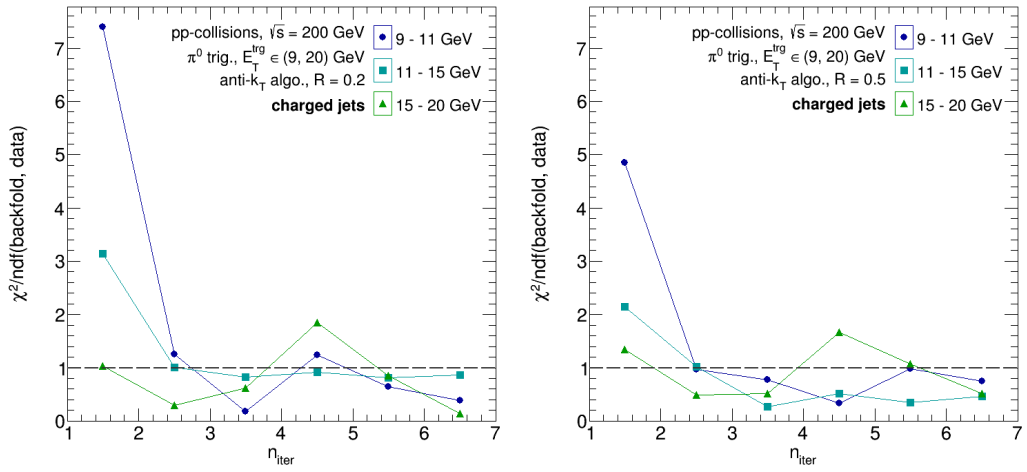

(a) $R_{\text{jet}} = 0.2$ (b) $R_{\text{jet}} = 0.5$

Figure 10.8: The reduced χ^2 between backfolded and raw π^0-triggered $R_{\text{jet}} = 0.2$ (10.8a) and 0.5 (10.8b) data as a function of unfolding n_{iter}.

distributions.

This process is repeated for several values of Bayesian regularization parameter n_{iter} ranging from 1 to 6. Each time a reduced chi-squared, $\chi^2_{\text{N}} = \chi^2/\text{NDF}$, is calculated between the raw data and the backfolded distribution. As n_{iter} increases, χ^2_{N} will eventually converge to a stable value. As stated in the previous section, an optimal value of n_{iter} is determined before unfolding the data by identifying at which n_{iter} χ^2_N begins to converge (i.e. the inflection point of the χ^2_N versus n_{iter} curve) and adding one. Figure 10.8 shows χ^2_N as a function of n_{iter} with the default value of n_{iter}, henceforth denoted n^*_{iter}, indicated. For $R_{\text{jet}} = 0.2$ data, a default value of $n^*_{\text{iter}} = 4$ was used, and for $R_{\text{jet}} = 0.5$ data, a default value of $n^*_{\text{iter}} = 3$ was used.

In the case of the γ_{rich} data, the hadronic background is subtracted *before* performing the unfolding. This is to keep the unfolding stable and to prevent uncertainties on the unfolded data from being artificially inflated by the subtraction process. Ultimately, performing the subtraction before or after unfolding yields the same solution, as can be seen

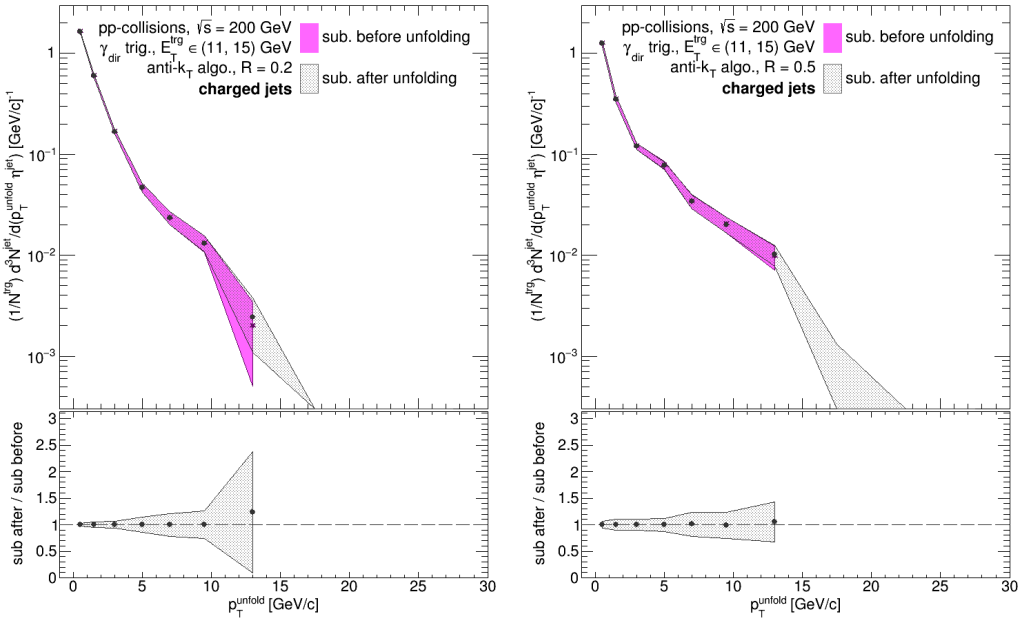

(a) $R_{\text{jet}} = 0.2$ (b) $R_{\text{jet}} = 0.5$

Figure 10.9: Comparison of unfolded 11 - 15 GeV γ_{dir}-triggered $R_{\text{jet}} = 0.2$ (10.9a) and 0.5 (10.9b) data when performing the hadronic subtraction before vs. after after unfolding.

in figure 10.9.

By default, the response matrix and jet-matching efficiency calculated from the Py6⊕ Geant sample is used to correct the data. These can be seen in figures 10.10 and 10.11 respectively. The Py8⊕Param sample is reserved for computing the systematic uncertainties on the corrected data.

The rationale behind choosing the Py6⊕Geant response over the Py8⊕Param response as the default choice for correcting the data is that (1) the sample was generated with an event generator tuned to match STAR data, and (2) it was generated with a detailed Geant simulation of STAR and thus more likely to accurately capture all of the relevant detector effects that might be at play. The raw and corrected per-trigger yields of charged recoil jets are listed in table 10.1. The integrated yields were obtained by integrating the raw and unfolded charged recoil jet spectra over the $p_{\text{T}}^{\text{jet}}$ range of 0 - 30 GeV/c for π^0 triggers and

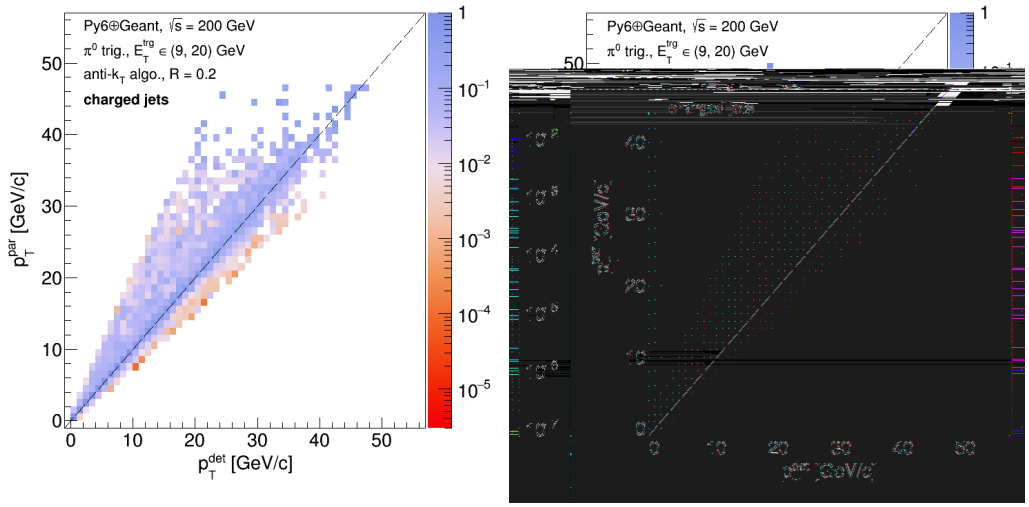

(a) $R_{\text{jet}} = 0.2$ (b) $R_{\text{jet}} = 0.5$

Figure 10.10: Example $R_{\text{jet}} = 0.2$ (10.10a) and 0.5 (10.10b) response matrices calculated from the Py6⊕Geant framework. Note that the matrices used for unfolding are made with the same binning scheme and $E_{\text{T}}^{\text{trg}}$ range as the data to be unfolded.

		9 - 11 GeV		**11 - 15 GeV**		**15 - 20 GeV**	
		0.2	**0.5**	**0.2**	**0.5**	**0.2**	**0.5**
π^0 **trig.**	Raw	1.971	0.702	1.940	0.679	1.731	0.675
	Corrected	2.495	1.598	2.446	1.698	2.206	1.859
γ_{dir} **trig.**	Raw	1.835	0.728	1.975	0.727	2.025	0.609
	Corrected	2.328	1.711	2.490	1.857	2.577	1.460

Table 10.1: Raw vs. corrected per-trigger $R_{\text{jet}} = 0.2$ and 0.5 charged recoil jet yields.

over the $p_{\text{T}}^{\text{jet}}$ range of 0 - 11 GeV/c for 9 - 11 GeV γ_{dir} triggers, 0 - 15 GeV/c for 11 - 15 GeV γ_{dir} triggers, and 0 - 20 GeV/c for 15 - 20 GeV γ_{dir} triggers.

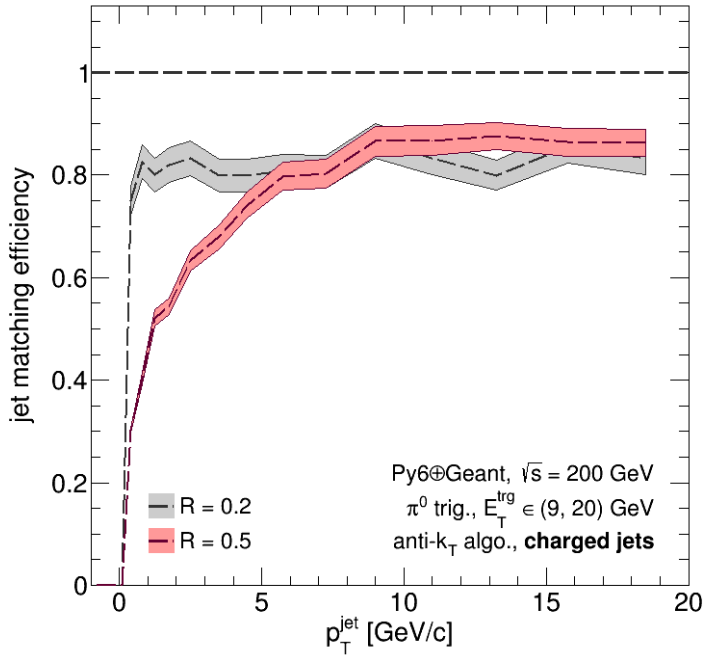

Figure 10.11: The $R_{\text{jet}} = 0.2$ (grey curve) and 0.5 (red curve) jet-matching efficiencies from the Py6$\oplus$Geant simulation. The bands on indicate the systematic uncertainty due to the STAR tracking efficiency.

11. Calculation of Systematic Uncertainties

There are several sources of systematic uncertainty present in the measurements presented in this thesis. The primary sources are the response of the STAR TPC, the unfolding procedure, and the hadronic subtraction applied to the γ_{dir}-triggered data. There is also an additional uncertainty associated with the choice of fragmentation model utilized in the simulation frameworks used to correct the data. In total, there are six sources of uncertainty which are detailed below.

Tracking Efficiency: Past analyses [182] have shown that there is a maximum-extent systematic uncertainty of roughly $\pm 4\%$ absolute on the tracking efficiency of the TPC.

Tracking Resolution: As discussed in section 9.1.2, two methods were deployed in order to estimate the tracking resolution of the TPC. The dependence of this choice can be explored using the Py8$\oplus$Param response.

Regularization: The choice of n_{iter} in the Bayesian unfolding algorithm is arbitrary, and the corrected spectra may be sensitive to this choice.

Unfolding Prior: The Bayesian algorithm requires a prior to be provided in order to train the inverse of the response matrix. Once again, the corrected data may be sensitive to this choice.

Background Level: As detailed in section 7.3, there are systematic uncertainties between 6 and 14% relative on the measured values of $\mathcal{B}$.

Fragmentation Model: Both the Py6$\oplus$Geant and the Py8$\oplus$Param simulations utilize a particular choice of fragmentation model in generating events. This could bias the

training of the response matrix, and thus the corrected data.

These six sources can be grouped into three categories based on how their associated systematic uncertainties are assessed. The *Detector Systematic Uncertainties* include the uncertainties which stem from the response of the TPC, the tracking efficiency and tracking resolution. The approach for evaluating these uncertainties is described in section 11.1.1. The *Unfolding Systematic Uncertainties* include the uncertainties which stem from the unfolding procedure, the choice of regularization and unfolding prior. The approach for evaluating these is described in section 11.1.2. The uncertainty due to the background level $\mathcal{B}$ is assessed alongside the unfolding systematic uncertainties, and the approach to evaluating it is described in section 11.1.3. This leaves only the *Fragmentation Systematic Uncertainty*, which is discussed in section 11.1.4.

While the details differ, the strategy in general for evaluating the systematic uncertainty associated with a particular source is to first generate a new response matrix varied within the uncertainty of interest, and then to unfold the data with this new variant response matrix. The uncertainty is then given by the percent difference between the data unfolded with the variant response matrix and the data unfolded with the default response matrix. After calculation, the systematic uncertainty is applied to data corrected with the response matrix trained on the Py6⊕Geant sample using the default unfolding parameters. Throughout this section, let R_{ij}^{embed} denote a response matrix trained on the Py6⊕Geant sample, and let R_{ij}^{param} denote a response trained on the Py8⊕Param sample.

11.1 Assessing Systematic Uncertainties

11.1.1 The TPC Response

These uncertainties arise from the response of the STAR TPC. The parameterized response functions utilized in the fast simulation allows for the tracking pseudo-efficiency ($\tilde{\epsilon}_{\text{trk}}$) and tracking resolution ($\Delta p_{\text{T}}^{\text{trk}}$) to be varied in order to assess the sensitivity of the

corrected data to each. To do this, five separate response matrices were created using the fast simulation for each value of R_{jet} and range of $E_{\text{T}}^{\text{trg}}$:

1. one with the default $\tilde{\epsilon}_{\text{trk}}$ and default $\Delta p_{\text{T}}^{\text{trk}}$ ($\Delta p_{\text{T}}^{\text{dist}}$) used;
2. one with 4% absolute added to $\tilde{\epsilon}_{\text{trk}}$ across $p_{\text{T}}^{\text{trk}}$ but with default $\Delta p_{\text{T}}^{\text{trk}}$ used;
3. one with 4% absolute subtracted from $\tilde{\epsilon}_{\text{trk}}$ across $p_{\text{T}}^{\text{trk}}$ but with default $\Delta p_{\text{T}}^{\text{trk}}$ used;
4. one with default $\tilde{\epsilon}_{\text{trk}}$ but with $\Delta p_{\text{T}}^{\text{diff}}$ used; and
5. one with default $\tilde{\epsilon}_{\text{trk}}$ but with $\Delta p_{\text{T}}^{\text{Run12}}$ used.

Here $\Delta p_{\text{T}}^{\text{dist, diff, Run12}}$ respectively denote the tracking resolutions parameterized by the R^{dist}, R^{diff}, and Run12 functions from section 9.1.2. The data were then unfolded five times, once with each variant response.

For the sake of clarity, let $R_{ij}^{\text{param}}\left[\tilde{\epsilon}_{\text{trk}}, \Delta p_{\text{T}}^{\text{trk}}\right]$ denote the Py8$\oplus$Param response matrix with the tracking pseudo-efficiency $\tilde{\epsilon}_{\text{trk}}$ and tracking resolution $\Delta p_{\text{T}}^{\text{trk}}$ applied. From hereon the arguments of R_{ij}^{param} will be suppressed when the default $\tilde{\epsilon}_{\text{trk}}$ and $\Delta p_{T}^{\text{trk}}$ are used.

11.1.2 The Unfolding Procedure

These uncertainties arise from the unfolding procedure itself: the choice of n_{iter} and the choice of prior supplied to the Bayesian algorithm. Let n_{iter}^{*} denote the default value of $n_{\text{iter}} = 4$ (for $R_{\text{jet}} = 0.2$) or 3 (for 0.5) used to correct data (see 10.8 and surrounding discussion). Then to assess the uncertainty associated with n_{iter}, the data were unfolded twice: once with $n_{\text{iter}}^{*} - 1$ and once with $n_{\text{iter}}^{*} + 1$. In both cases, the response matrix and prior were unchanged.

The uncertainty associated with the choice of prior poses additional complications, however. A choice of prior that is wildly unphysical (e.g. a sine function) runs the risk of artificially inflating the calculated uncertainty. Thus some amount of care has to be taken

when selecting an alternate prior. For the case of $R_{\text{jet}} = 0.2$, the small jet radius means that a single-particle spectrum is a rough but decent approximation of the jet spectra. Thus $R_{\text{jet}} = 0.2$ jets were generated using particle-level PYTHIA 8 for the three range of $E_{\text{T}}^{\text{trg}}$ for both π^0 and γ_{dir} triggers. Then each generated spectrum was fit with a Lévy function (an example of a Tsallis distribution) [186, 187, 188]:

$$L\left(p_{\text{T}}\right) = \frac{bp_{\text{T}}}{\left[1 + \frac{\sqrt{p_{\text{T}}^2+m^2}-m}{nt}\right]^n}. \tag{11.1}$$

To further probe the space of possible priors, the parameters of these fits were adjusted to obtain a set of alternate Lévy functions. The default parameters extracted for the fit, (b, n, t)[1], and the adjusted alternate parameters, (b', n', t'), are listed in table 11.1. Ultimately, it was found that the corrected data were largely insensitive to the fine details of the choice of prior. Thus both the $R_{\text{jet}} = 0.2$ and 0.5 data were unfolded using variant response matrices retrained on the default and alternate Lévy functions following the procedure of section 10.3.

Lastly, recall that the γ_{dir}-triggered data are corrected with the response matrix retrained on a PYTHIA 8 generated spectrum of γ_{dir}-triggered charged recoil jets. Thus, as an additional point of comparison in evaluating the systematic uncertainty associated with the prior, the γ_{dir} data are unfolded once using the response matrix trained on the π^0-triggered prior, and the π^0 data are unfolded once using the response matrix trained on the γ_{dir} prior in addition to the default choice of prior and the two Lévy functions.

For the sake of clarity let $R_{ij}^{\text{embed}}\left[P\right]$ indicate the Py6$\oplus$Param (smoothed or raw) response matrix trained on the prior $P \in \{\pi^0, \gamma_{\text{dir}}, L_{\text{def}}, L_{\text{alt}}\}$. Here π^0 denotes the Py6$\oplus$Param π^0-triggered charged recoil jet spectrum, γ_{dir} denotes the PYTHIA 8 γ_{dir}-triggered charged

[1]The Lévy function was previously deployed by STAR to fit single particle spectra in [188]. The parameter m was reserved for the particle mass. Here it is fixed to be roughly the mass of a pion, 0.140 GeV/c^2.

Parameter	9 - 11 GeV		11 - 15 GeV		15 - 20 GeV	
	π^0	γ_{dir}	π^0	γ_{dir}	π^0	γ_{dir}
b	3.3	0.7	2.8	0.7	2.4	1.8
b'	3.3	0.7	2.8	0.7	2.4	1.8
n	4.6	11.8	4.3	8.1	3.8	4.5
n'	6.1	25.8	7.2	15.1	6.4	8.5
t	0.4	0.8	0.4	0.8	0.5	0.5
t'	0.5	1.1	0.7	1.1	0.8	0.8

Table 11.1: Lévy function parameters extracted fits to simulated $R_{\text{jet}} = 0.2$ charged recoil jets, (b, n, t), and adjusted parameters, (b', n', t').

recoil jet spectrum, L_{def} denotes the default Lévy function, and L_{alt} denotes the alternate Lévy function. From hereon, the arguments of R_{ij}^{embed} will be suppressed when using the default choice of prior.

11.1.3 The Hadronic Subtraction Scheme

The γ_{rich}-triggered data have an additional source of systematic uncertainty: the value of the measured background level $\mathcal{B}$ used in the hadronic subtraction applied to obtain γ_{dir}-triggered spectra listed in table 7.3. The uncertainty associated with the choice of $\mathcal{B}$ is evaluated in parallel with the uncertainties stemming from the unfolding procedure. For each value of n_{iter} and choice of prior, the γ_{dir} data are unfolded twice: once where the value used to perform the hadronic subtraction is $\mathcal{B} - \delta\mathcal{B}$, where $\delta\mathcal{B}$ is the uncertainty on the background level, and once where the value used to perform the hadronic subtraction is $\mathcal{B} + \delta\mathcal{B}$. The combination of $\mathcal{B} \pm \delta\mathcal{B}$ with the default n_{iter} is included in the Regularization Parameter category.

11.1.4 The Fragmentation Model

The impact of the choice of fragmentation model on the corrected data has yet to be assessed and will not be included in the results presented here. A study is planned and will be carried out in the near future wherein a fast simulation similar to the Py8⊕Param simulation described in section 9.2 will be created, except HERWIG 7 [189, 190] rather than PYTHIA 8 will serve as the event generator.

In PYTHIA 8, fragmentation is handled according to the Lund String Model [54]. This model is inspired by the effective string picture of QCD at high coupling strength: a color string, the color flux tubes of sections 2.1.2, will connect a produced $q\bar{q}$ pair. This string will then snap into pairs of massless (anti-) quarks according to a certain probability. Then hadronization occurs via a simple phenomenological rule assigning (anti-) quark pairs and triplets to meson and baryon states respectively.

In HERWIG, however, fragmentation occurs via the fragmentation model of B. R. Webber [191]. This model simulates hadronization by grouping partons into color-singlet clusters and then allowing them to decay to hadrons according to a simple phase-space model.

Just like with the Py8⊕Param simulation, events will be generated using HERWIG and detector effects will be applied post-hoc via the calculated $\tilde{\epsilon}_{\text{trk}}$ and $\Delta p_{\text{T}}^{\text{trk}}$. A response matrix will then be calculated using this new simulation, Herwig⊕Param, and the data will be unfolded using this new response matrix.

11.2 Calculation of Systematic Uncertainties

In total, for each range of $E_{\text{T}}^{\text{trg}}$ and value of R_{jet} there are 9 π^0-triggered systematic variations and 17 γ_{dir}-triggered systematic variations. These are listed in table 11.2. In every variation, only the Bayesian unfolding algorithm is used.

Let $D_{pp,ijkl}^{\text{var}}$ denote the corrected per-trigger yield of charged recoil jets with unfolded

Category	Source	Reg.	Resp.	Bkgd.	Notes
Detector Sys.	Baseline	n^*_{iter}	R^{param}_{ij}	B	
	Track Eff.	n^*_{iter}	$R^{\text{param}}_{ij}\left[\tilde{\epsilon}_{\text{trk}} + 4\%, \Delta p_{\text{T}}^{\text{trk}}\right]$	B	
		n^*_{iter}	$R^{\text{param}}_{ij}\left[\tilde{\epsilon}_{\text{trk}} - 4\%, \Delta p_{\text{T}}^{\text{trk}}\right]$	B	
	Track Res.	n^*_{iter}	$R^{\text{param}}_{ij}\left[\tilde{\epsilon}_{\text{trk}}, \Delta p_{\text{T}}^{\text{diff}}\right]$	B	
		n^*_{iter}	$R^{\text{param}}_{ij}\left[\tilde{\epsilon}_{\text{trk}}, \Delta p_{\text{T}}^{\text{Run12}}\right]$	B	
Unfolding Sys.	Default	n^*_{iter}	R^{embed}_{ij}	B	
	Regularization	$n^*_{\text{iter}} + 1$	R^{embed}_{ij}	$B \pm \delta B$	
		$n^*_{\text{iter}} - 1$	R^{embed}_{ij}	$B \pm \delta B$	
		n^*_{iter}	R^{embed}_{ij}	$B \pm \delta B$	γ_{dir} only
	Prior	n^*_{iter}	$R^{\text{embed}}_{ij}\left[L_{\text{def}}\right]$	$B \pm \delta B$	
		n^*_{iter}	$R^{\text{embed}}_{ij}\left[L_{\text{alt}}\right]$	$B \pm \delta B$	
		n^*_{iter}	$R^{\text{embed}}_{ij}\left[\gamma_{\text{dir}}\right]$		π^0 only
		n^*_{iter}	$R^{\text{embed}}_{ij}\left[\pi^0\right]$	$B \pm \delta B$	γ_{dir} only

Table 11.2: Systematic variations used in calculating the systematic uncertainty.

jet transverse momentum falling in the i^{th} bin of $p_{\text{T}}^{\text{unfold}}$ of the l^{th} systematic variation of unfolding parameters for the k^{th} uncertainty source of the j^{th} category of systematic uncertainties. Then let $D^{\star}_{pp,ij}$ indicate the same quantity but for the default choice of unfolding parameters for the j^{th} category of systematic uncertainties. For unfolding systematic uncertainties, this is the "Default" line in table 11.2. For the detector systematic uncertainties, the tracking resolution variations were compared against the data unfolded using the combination of parameters listed in the "Baseline" line in table 11.2, and the tracking efficiency variations were compared against the average of the variations. This is to make sure that the uncertainty assigned to the tracking efficiency was not overestimated. Lastly, let $\sigma_{\text{sys},ij} = \{\sigma^{\text{unfold}}_{\text{sys},i}, \sigma^{\text{unfold}}_{\text{sys},i}\}$ denote the systematic uncertainty for the j^{th} category of systematic uncertainty assigned to the i^{th} bin of $p_{\text{T}}^{\text{unfold}}$. Then the systematic uncertainties are calculated according to algorithm 8.

Algorithm 8 The systematic uncertainty calculation.

for each bin i of $p_{\mathrm{T}}^{\mathrm{unfold}}$, **do**
  for each category j of systematic uncertainty, **do**
    for each source of uncertainty k within the category, **do**
      for each variation l within the category, **do**
        Calculate the difference in per-trigger yields between the variation and default unfolding parameters $\delta_{ijkl}^{\mathrm{sys}}$:

$$\delta_{ijk}^{\mathrm{sys}} = |D_{pp,ijkl}^{\mathrm{var}} - D_{pp,ij}^{\star}|$$

      end for
    Take the maximum of $\delta_{ijkl}^{\mathrm{sys}}$ to be the systematic uncertainty $\varsigma_{\mathrm{sys},ijk}$ assigned to source k:

$$\varsigma_{\mathrm{sys},ijk} = \mathrm{Max}\{\delta_{ijkl}^{\mathrm{sys}}\}$$

    end for
    Sum the uncertainties assigned to each source in quadrature to obtain the systematic uncertainty assigned to category j:

$$\sigma_{\mathrm{sys},ij} = \bigoplus_k \varsigma_{\mathrm{sys},ijk}$$

  end for
end for

Algorithm 8 produces a systematic uncertainty as a function of $p_{\mathrm{T}}^{\mathrm{unfold}}$ for each category: the unfolding systematic uncertainty $\sigma_{\mathrm{sys}}^{\mathrm{unfold}}$ and the detector systematic uncertainty $\sigma_{\mathrm{sys}}^{\mathrm{det}}$. Figures 11.1 and 11.2 show representative unfolding and detector systematic variations compared against their baselines (upper panels) and the ratio of the variations over the baselines (lower panels). The assigned systematic uncertainties of each category are shown

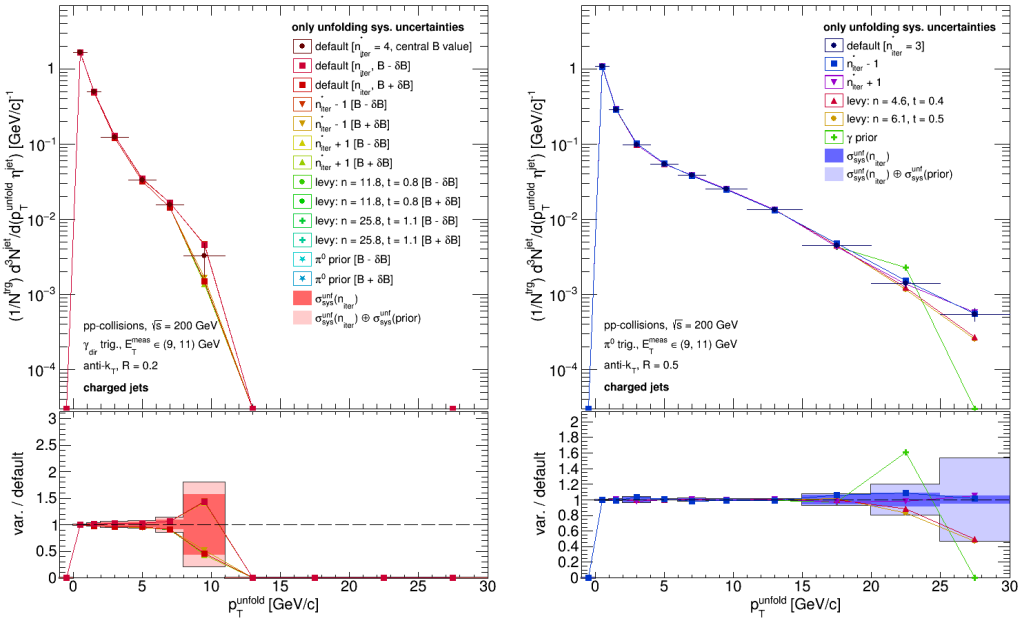

(a) γ_{dir}, $R_{\text{jet}} = 0.2$ (b) π^0, $R_{\text{jet}} = 0.5$

Figure 11.1: Example unfolding systematic variations for $R_{\text{jet}} = 0.2$ (11.1a) and $R_{\text{jet}} = 0.5$ (11.1b). See text for details. Variations visualized without uncertainties.

as solid bands in the lower panels, where the different colors indicate the total accumulated uncertainty as each source is considered. For instance, the darker bands in figure 11.1 show the assigned regularization systematic uncertainty while the lighter bands show the assigned regularization and prior uncertainties added in quadrature. Similar plots for all combinations of trigger species, $E_{\text{T}}^{\text{trg}}$ and R_{jet} can be found in appendix D.

Ultimately, the $n^*_{\text{iter}} + 1$ and n^*_{iter} with background values of $B + \delta B$ variations for the $R_{\text{jet}} = 0.2$ 11 - 15 GeV γ_{dir} data were excluded from the calculation of $\sigma_{\text{sys}}^{\text{unfold}}$. These unfolding solutions produced by these two combinations of unfolded parameters were found to produce poor χ^2/ndf values between the raw data and backfolded solutions and to have unreasonably large unfolding uncertainties. This indicates that the unfolding did not converge, and so were not counted towards the total $\sigma_{\text{sys}}^{\text{unfold}}$.

Furthermore, the γ_{dir} prior variation was excluded from the calculation of the π^0 $\sigma_{\text{sys}}^{\text{unfold}}$

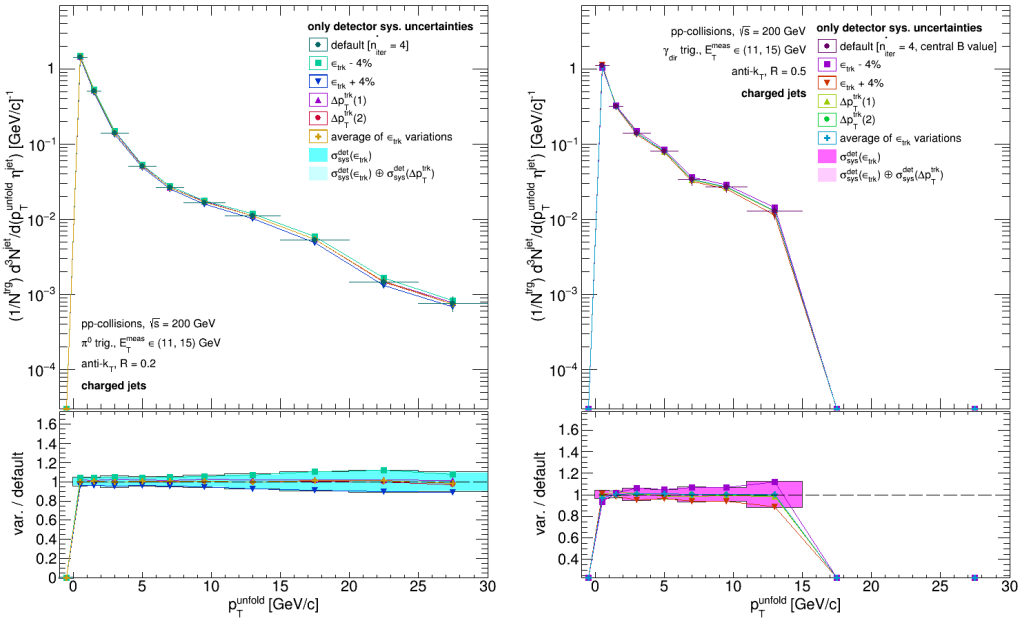

(a) π^0, $R_{\text{jet}} = 0.2$ (b) γ_{dir}, $R_{\text{jet}} = 0.5$

Figure 11.2: Example detector systematic variations for $R_{\text{jet}} = 0.2$ (11.2a) and $R_{\text{jet}} = 0.5$ (11.2b). See text for details. Variations visualized without uncertainties.

for all $E_{\text{T}}^{\text{trg}}$ and R_{jet}. This was done to prevent this variation from artificially inflating the uncertainty at high $p_{\text{T}}^{\text{unfold}}$ where the variation tends to zero yield due to the kinematic reach of the γ_{dir}-triggered prior. As $p_{\text{T}}^{\text{unfold}}$ decreases, though, the γ_{dir} variation quickly converges to the other variations.

Both π^0 Lévy variations end up beneath the default unfolding solution for all combinations of $E_{\text{T}}^{\text{trg}}$ and R_{jet}. This would suggest an asymmetric uncertainty should be assigned to the choice of prior when taken by themselves. However, the γ_{dir} prior results in an unfolding variation which tends quite strongly in the *opposite* direction from both Lévy variations, thereby demonstrating that there do exist possible priors which would result in opposite behavior from the Lévy variations. Thus, the assignation of a symmetric uncertainty due to the choice of prior is justified.

With both $\sigma_{\text{sys}}^{\text{unfold}}$ and $\sigma_{\text{sys}}^{\text{det}}$ calculated, the two are ultimately added in quadrature. How-

ever, the $\sigma_{\text{sys}}^{\text{unfold}}$ was first smoothed such that it only increases monotonically, the rationale being that there was no *a priori* reason why $\sigma_{\text{sys}}^{\text{unfold}}$ should fluctuate bin-to-bin. Moreover, by smoothing, $\sigma_{\text{sys}}^{\text{unfold}}$ will only ever increase with increasing $p_{\text{T}}^{\text{unfold}}$. Thus, the smoothed uncertainties represent a more conservative estimate of $\sigma_{\text{sys}}^{\text{unfold}}$.

The $\sigma_{\text{sys}}^{\text{det}}$, on the other hand, was **not** smoothed before being added in quadrature. This was done in light of the shape of the unfolded spectra: to varying degrees, each spectrum exhibits a plateau at mid p_{T} between the soft region where background dominates and the hard region where signal dominates. This plateau forms a "saddle point" of sorts where the jets are less likely to lose or gain energy due to the detector response. The local minimum in $\sigma_{\text{sys}}^{\text{det}}$ can be seen in figure 11.2 and in the other data shown in appendix D.

Note that the hadronic background subtraction applied to the γ_{rich}-triggered data implies that the subtracted per-trigger yields go to zero for $p_{\text{T}}^{\text{reco}} \gtrsim E_{\text{T}}^{\text{trg}}$ due to momentum conservation. Since γ_{dir} at LO are produced with zero NS yield, i.e. not as part of a jet, the γ_{dir} carries the full energy of the recoiling parton. This means that any jet recoiling from a γ_{rich} trigger with $p_{\text{T}}^{\text{reco}} > E_{\text{T}}^{\text{trg}}$ are generally part of the hadronic background and will be subtracted. As $\mathcal{B}$ is varied to assess the systematic uncertainty of this subtraction, the point where the subtracted yields go to zero will also vary.

This leads to rapidly expanding systematic uncertainties as $p_{\text{T}}^{\text{jet}}$ approaches the upper limit of the $E_{\text{T}}^{\text{trg}}$ range. This effect can be seen in figures D.3 and D.4, and in table 11.4. Tables 11.3 and 11.4 list the largest systematic uncertainty (rounded up to the nearest percent) for a given category over certain ranges of $p_{\text{T}}^{\text{jet}}$. The large unfolding systematic uncertainties of the γ_{dir}-triggered data are driven by the aforementioned effect. Note that the listed cumulative uncertainty are the quadrature-sums of each contribution.

Table 11.3: Systematic uncertainties for π^0-triggered data. See text for details.

$E_{\mathrm{T}}^{\mathrm{trg}}$	R_{jet}	$p_{\mathrm{T}}^{\mathrm{jet}}$	Systematic uncertainty (%)			
[GeV]		[GeV]	TPC Response	Unfolding	Fragmentation	Cumulative
[9, 11]	0.2	[0, 5]	7	1	-	7
		[5, 10]	7	2	-	7
		[10, 15]	9	2	-	10
		[15, 20]	12	4	-	13
		[20, 25]	10	22	-	25
		[25, 30]	14	22	-	27
	0.5	[0, 5]	6	4	-	8
		[5, 10]	6	4	-	8
		[10, 15]	10	4	-	11
		[15, 20]	14	7	-	16
		[20, 25]	15	20	-	25
		[25, 30]	11	54	-	56
[11, 15]	0.2	[0, 5]	6	1	-	7
		[5, 10]	7	1	-	8
		[10, 15]	8	2	-	9
		[15, 20]	10	3	-	11
		[20, 25]	12	20	-	24
		[25, 30]	10	57	-	58
	0.5	[0, 5]	7	5	-	9
		[5, 10]	5	5	-	8
		[10, 15]	9	5	-	11
		[15, 20]	11	9	-	15
		[20, 25]	14	14	-	20
		[25, 30]	16	40	-	44
[15, 20]	0.2	[0, 5]	7	1	-	8
		[5, 10]	6	2	-	7
		[10, 15]	7	4	-	9
		[15, 20]	12	10	-	16
		[20, 25]	2	48	-	49
		[25, 30]	10	50	-	51
	0.5	[0, 5]	7	4	-	9
		[5, 10]	7	9	-	12
		[10, 15]	9	9	-	13
		[15, 20]	8	16	-	18
		[20, 25]	8	22	-	24

Table 11.3 Continued: Systematic uncertainties for π^0-triggered data. See text for details.

$E_{\mathrm{T}}^{\mathrm{trg}}$	R_{jet}	$p_{\mathrm{T}}^{\mathrm{jet}}$	Systematic uncertainty (%)			
[GeV]		[GeV]	TPC Response	Unfolding	Fragmentation	Cumulative
		[25, 30]	13	53	-	55

Table 11.4: Systematic uncertainties for γ_{dir}-triggered data. See text for details.

$E_{\mathrm{T}}^{\mathrm{trg}}$	R_{jet}	$p_{\mathrm{T}}^{\mathrm{jet}}$	Systematic uncertainty (%)			
[GeV]		[GeV]	TPC Response	Unfolding	Fragmentation	Cumulative
[9, 11]	0.2	[0, 5]	7	6	-	10
		[5, 10]	11	80	-	81
	0.5	[0, 5]	6	6	-	9
		[5, 10]	14	82	-	84
[11, 15]	0.2	[0, 5]	6	1	-	7
		[5, 10]	9	21	-	23
		[10, 15]	17	90	-	92
	0.5	[0, 5]	6	6	-	9
		[5, 10]	7	8	-	11
		[10,15]	12	20	-	24
[15, 20]	0.2	[0, 5]	4	7	-	9
		[5, 10]	3	13	-	14
		[10, 15]	2	16	-	17
		[15, 20]	8	20	-	22
	0.5	[0, 5]	7	11	-	14
		[5, 10]	4	12	-	13
		[10, 15]	3	16	-	17
		[15, 20]	2	16	-	17

11.3 Closure Tests

With the measured recoil jets fully corrected and the size of the systematic uncertainties assessed, all that remains is to validate the applied correction scheme. This is done via a *closure test* wherein the simulation sample used to train the response matrix and jet-matching efficiency used to correct the data is divided in half: one half is reserved to train the response (this is the *training sample*), and this response is then used to correct the detector-level of the other half (the *validation sample*) back to the particle-level. Since the FF and RFF sub-samples of the Embedding Sample used in this analysis contain roughly equal statistics, they were used to carry out the closure test. The test was carried out twice: one with the RFF sub-sample serving as the training sample and the FF sub-sample serving as the validation sample, and once with the roles reversed.

The criteria for successful closure here is taken to be that any unfolding solution from the validation sample using any one of the combination of unfolding parameters from table 11.2 associated with the π^0-triggered unfolding systematic uncertainties (excluding the $R_{ij}^{\text{embed}}\left[\gamma_{\text{dir}}\right]$ variation) should agree with the validation sample's particle-level recoil jet distribution within the statistical and systematic precision of the data.

The first step of the test was to account for the difference in statistics between the Py6$\oplus$Geant sample and the data. Since the Py6$\oplus$Geant sample was generated in bins of $\hat{p}_T$, it contains substantially more statistics than do the data at high $E_{\text{T}}^{\text{trg}}$ even after dividing it into the FF and RFF sub-samples (c.f. tables 8.3 and 9.2). Consequently, before any unfolding was carried out, the particle- and detector-level recoil jet distributions of the validation sample were modified to match the corresponding distributions in data. Let $\Delta\eta^{\text{jet}} = 2\left(1 - R_{\text{jet}}\right)$ indicate the width of the jet acceptance window in η, then the algorithm for this process is described in Algorithm 9.

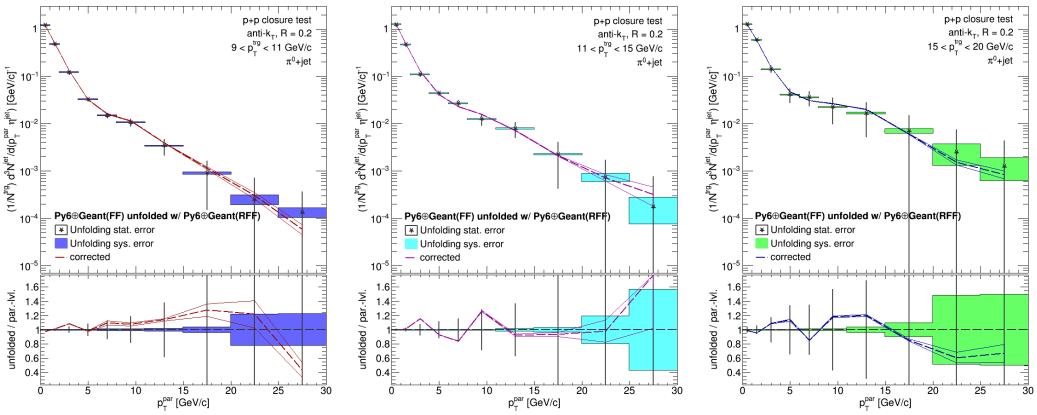

(a) 9 - 11 GeV (b) 11 - 15 GeV (c) 15 - 20 GeV

Figure 11.3: $R_{\text{jet}} = 0.2$ FF closure test for 9 - 11 (11.3a), 11 - 15 (11.3b), and 15 - 20 GeV (11.3c) π^0 triggers. See text for details.

Algorithm 9 The algorithm for modifying the statistics of a provided recoil jet distribution. It requires two inputs: the number of measured triggers ($N_{\text{trg}}^{\text{meas}}$) to match, and the simulated jet distribution S.

1: **for** each $p_{\text{T}}^{\text{reco}}$ bin i in S, **do**

2: Let the per-trigger yield of simulated jets in bin i be $D_{\text{sim}}^{\text{in}}$ and the bin width be $\Delta p_{\text{T}}^{\text{reco}}$

3: Compute the mean of a Poisson distribution μ:

$$\mu = N_{\text{trg}}^{\text{meas}} D_{\text{sim}}^{\text{in}} \Delta p_{\text{T}}^{\text{reco}} \Delta \eta^{\text{jet}}$$

4: The new number of recoil jets in bin i is sampled from the Poisson distribution with mean μ:

$$N_{\text{jet}}^{\text{out}} = \text{Poisson}\left(\mu\right)$$

5: Then the new per-trigger yield in bin i is:

$$D_{\text{sim}}^{\text{out}} = N_{\text{jet}}^{\text{out}} / \left(\Delta p_{\text{T}}^{\text{jet}} \Delta \eta^{\text{jet}}\right)$$

6: And its uncertainty is:

$$\sigma = \sqrt{\mu}$$

7: **end for**

8: Normalize S by the number of measured triggers, $N_{\text{trg}}^{\text{meas}}$.

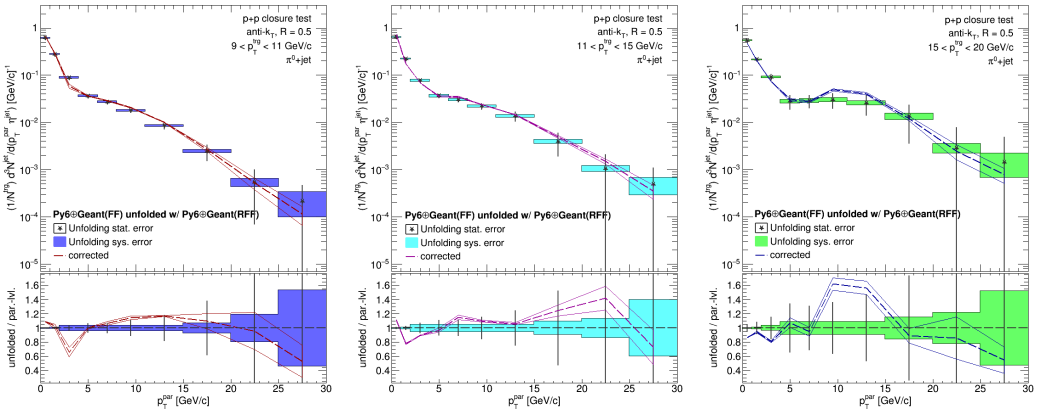

(a) 9 - 11 GeV (b) 11 - 15 GeV (c) 15 - 20 GeV

Figure 11.4: $R_{\text{jet}} = 0.5$ FF closure test for 9 - 11 (11.4a), 11 - 15 (11.4b), and 15 - 20 GeV (11.4c) π^0 triggers. See text for details.

Lastly, the modified detector-level recoil jet distributions were unfolded five times, once with each of the five combinations of unfolding parameters corresponding to the unfolding systematic variations (n_{iter} and unfolding prior) listed in table 11.2. To aid in visualization, the five unfolding variations are averaged together. Figures 11.3 and 11.4 show the averages of the FF unfolding variations (dashed lines) compared against the modified FF particle-level recoil jet spectra (black stars) for $R_{\text{jet}} = 0.2$ and 0.5 respectively. The unfolding systematic uncertainty of the measured data is visualized as solid boxes, and the hollow band on the averages of the FF unfolding variations indicates the maximum deviation of the variations from the average.

For $R_{\text{jet}} = 0.2$, the unfolded modified detector-level FF recoil jet distributions were generally found to agree with the modified particle-level FF recoil jet distributions within the statistical and systematic precision of the data. For $R_{\text{Jet}} = 0.5$, the unfolded modified detector-level FF recoil jet distributions were found to agree with the modified particle-level FF recoil jet distributions within the desired precision only for $p_{\text{T}}^{\text{unfold}} \gtrsim 3$ GeV/c. Beneath this, substantial non-closure was observed. This non-closure will be further investigated in an upcoming publication.

This process was then repeated using the FF sub-sample as the training sample and the RFF sub-sample as the validation sample, the results of which may be seen in appendix E. Similar levels of agreement were found for this test as well. This validates the correction scheme deployed in this analysis.

It should be noted here that the detector systematic uncertainty of the data and the combinations of unfolding parameters associated with the detector systematic uncertainty were excluded here. This is because in the embedding sample, both the tracking efficiency and resolution are known exactly, and so they will be applied and corrected for in the process of moving from particle- to detector-level through the embedding process and back through the unfolding process. Hence they are not relevant for the closure test.

12. The Trigger Energy Scale and Resolution

Chapters 9 to 11 grappled with assessing the impact the physical limitations of STAR have on the measured charged recoil jet spectra. These chapters dealt with determining the **J**et **E**nergy **S**cale (JES) and **J**et **E**energy **R**esolution (JER) of the measurement. The JES quantifies an overall shift in jet energy induced by detector effects, and the JER quantifies the precision with which jet energies are reconstructed.

However, jets are not only objects that are affected by detector effects. The π^0 and γ_{dir} which serve as triggers in this analysis are also subject to a reconstruction efficiency and finite energy resolution. The measured energy distribution of π^0 and γ_{dir} will be distorted by these effects: there is a **T**rigger **E**nergy **S**cale (TES) and **T**rigger **E**nergy **R**esolution (TER). Hence, before the measured jets can be compared against theory, *both* the JES and JER *and* the TES and TER must be accounted for.

In order to assess the TES and TER, a separate fast simulation was constructed to simulate individual π^0 and γ as they pass through STAR. This will be described in section 12.1, section 12.2 will describe how these quantities are calculated, and section 12.3 will describe how the TES and TER are accounted for in the comparison of data and theory.

12.1 Simulation Overview

The simulation framework utilized here consists of single π^0 and γ passing through a Geant3 simulation of STAR. The geometry, detector response, and software options used are identical to those used in the Run9 Dijet Embedding Sample in order to compare with that simulation and the analyzed data.

Each "event" in the simulation consists of either 28 π^0 or 118 γ with a flat E_{T} distribution thrown at random on an (η, φ) grid with spacing of either a_{grid} =0.6 radians (12 BEMC tower lengths), in the case of the π^0, or 0.3 radians, in the case of the γ. The

larger grid spacing in the case of the π^0 is to ensure that a decay γ from one π^0 isn't correlated with one from another. The sample of π^0 and γ are generated such that there are no events containing both π^0 and γ, and generating multiple particles per event improves computational efficiency.

The particular numbers of π^0 and γ simulated per event corresponds to the maximum number of π^0 or γ grid sites that can be fit into the acceptance of the STAR BEMC with two sites reserved for two soft $\pi^{\pm}$. These $\pi^{\pm}$ ensure that a TPC response is generated, which is required for the code that implements the clusterizing algorithm described in chapter 7 to work. They are purely technical, and are not analyzed here.

As this simulation consists of single particles being processed by a Geant simulation of STAR, this simulation framework shall be referred to as Particle$\oplus$Geant.

12.2 Calculation of the Trigger Energy Scale and Resolution

After generating the sample of π^0 and γ, for each particle species there will be a list of events $\mathcal{E} = \{e_i\}$ each with a list of EMC clusters $\mathcal{C}_i = \{c_{ij}\}$ with 3-momentum $(E_{\mathrm{T}}^{\mathrm{reco}}, \eta^{\mathrm{reco}}, \varphi^{\mathrm{reco}})$ and a list of generated particles $\mathcal{P}_i = \{p_{ij}\}$ with 3-momentum $\left(E_{\mathrm{T}}^{\mathrm{sim}}, \eta^{\mathrm{sim}}, \varphi^{\mathrm{sim}}\right)$. Similar to the detector-level jets in the Py6$\oplus$Geant sample, the EMC clusters can only be matched geometrically in (η, φ) space to the simulated particles. Finally, let $\Delta\eta = \eta^{\mathrm{reco}} - \eta^{\mathrm{sim}}$ and $\Delta\varphi = \varphi^{\mathrm{reco}} - \varphi^{\mathrm{sim}}$. Then the algorithm for matching reconstructed EMC clusters (trigger candidates) to their simulated counterparts is described in algorithm 10.

Algorithm 10 The algorithm for matching BEMC clusters to simulated π^0 or γ in the Particle$\oplus$Geant framework.

1: **for** each event $e_i \in \mathcal{E}$, **do**

1: **for** each EMC cluster $c_{ij} \in \mathcal{C}_i$, **do**

2: **if** c_{ij} does *not* satisfy the criteria listed in table 8.2, **continue**

3: **for** each particle $p_{ik} \in \mathcal{P}_i$, **do**

4: **if** p_{ik} does *not* satisfy the criteria listed in table 9.3 excluding the AS criterion, **continue**

5: Calculate the displacement in (η, φ) and energy fraction $q_{\mathrm{T}}^{\mathrm{trg}}$:

$$\Delta r = \sqrt{\Delta\varphi^2 + \Delta\eta^2},$$

$$q_{\mathrm{T}}^{\mathrm{trg}} = E_{\mathrm{T}}^{\mathrm{reco}} / E_{\mathrm{T}}^{\mathrm{sim}}.$$

6: **if** $\Delta r < \Delta R^{\mathrm{match}}$, **then**

7: p_{ik} and c_{ij} are a match, so add the pair (p_{ik}, c_{ij}) to the list of matched particles and EMC clusters $\mathcal{M}$ and remove them from $\mathcal{C}_i$ and $\mathcal{P}_i$.

8: Fill relevant histograms.

9: **break**

10: **end if**

11: **end for**

12: **end for**

13: **end for**

Note that $\Delta R^{\mathrm{match}}$ is a free parameter to be specified in the algorithm. For this analysis, $\Delta R^{\mathrm{match}}$ was set to be $6\sqrt{2} \cdot a_{\mathrm{twr}}$[1] ($\approx 0.41$ rad.) for π^0 and $3\sqrt{2} \cdot a_{\mathrm{tower}}$ (≈ 0.21 rad.) for γ respectively. These values correspond to the hypotenuse of a right triangle with base and height of 2 ½ (1 ½) towers.

Since the particles were simulated with a flat E_{T} distribution, they will need to be weighted to a physical E_{T} distribution post-hoc. Thus all particle-level quantities are weighted according to their $E_{\mathrm{T}}^{\mathrm{sim}}$ by a power law fit to a single particle distribution (π^0 or γ_{dir}) from PYTHIA 8.185 shown in figure 12.1, and all cluster-level quantities are weighted

[1] Here a_{twr} is the side-length of one BEMC tower, 0.05 radians.

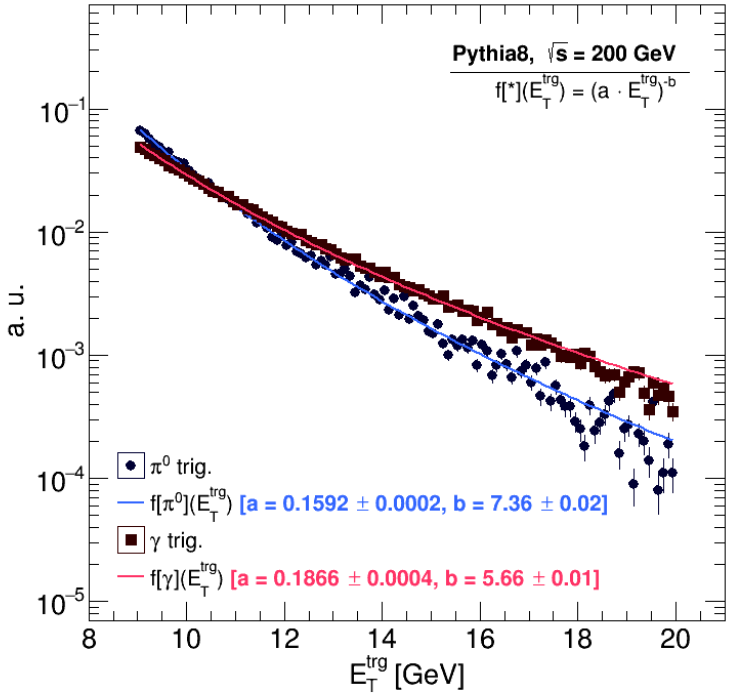

Figure 12.1: Power law fits to single particle π^0 and γ_{dir} $E_{\text{T}}^{\text{trg}}$ distributions from PYTHIA 8 which are used to reweight relevant distributions from the Particle⊕Geant framework.

by the same function according to the $E_{\text{T}}^{\text{sim}}$ of their matched particle. Quantities associated with clusters before matching are not reweighted.

The E_{T} distribution at various stages of the calculation - the input particle spectrum, the spectrum of EMC clusters matched to particles, and the corresponding matched particle spectrum - after weighting can be seen in figure 12.2. Furthermore, after matching each EMC cluster to a particle (and reweighting accordingly), the TES and TER are encoded in the quantity $q_{\text{T}}^{\text{trg}} = E_{\text{T}}^{\text{reco}}/E_{\text{T}}^{\text{sim}}$, the ratio of reconstructed transverse energy in the EMC cluster to the transverse energy of its match, shown in figure 12.3. The TES and TER are extracted from $q_{\text{T}}^{\text{trg}}$ by fitting a gaussian to the peak of the distribution: the TES corresponds to the mean μ of the fit, and the TER corresponds to the width σ of the fit. Table 12.1 lists the calculated TES and TER as a function of $E_{\text{T}}^{\text{reco}}$.

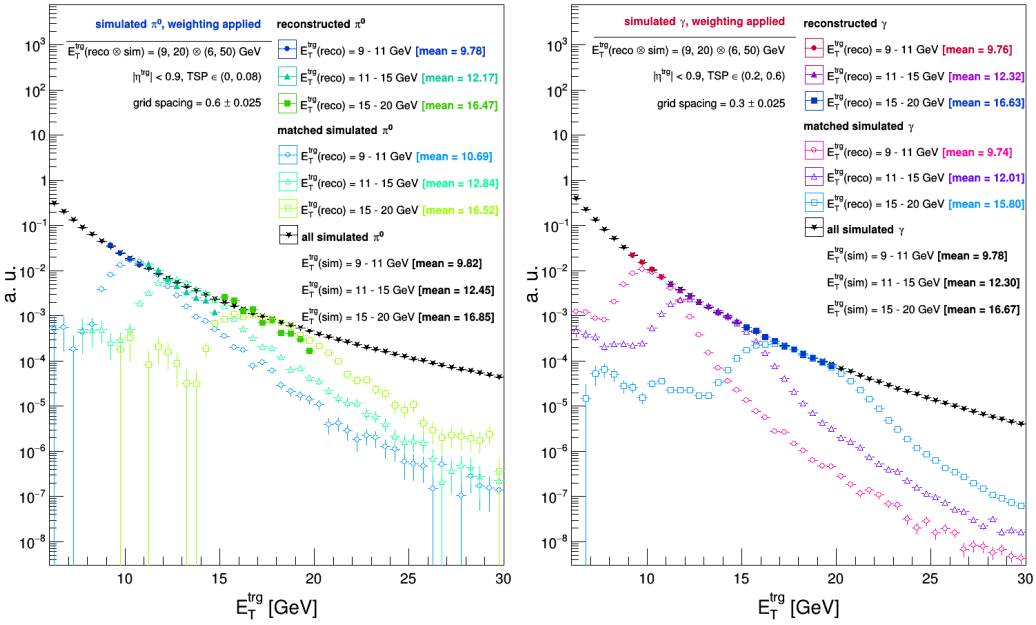

(a) π^0 (b) γ

Figure 12.2: $E_{\mathrm{T}}^{\mathrm{reco}}$ and $E_{\mathrm{T}}^{\mathrm{sim}}$ distributions of matched particle-cluster pairs vs. the input simulated E_{T} spectrum of π^0 (12.2a) and γ (12.2b).

$\mathbf{E_T^{reco}}$ **[GeV]**	π^0		γ	
	TES	**TER**	**TES**	**TER**
9 - 11	92.4 ± 0.2	9.1 ± 0.1	97.97 ± 0.05	8.12 ± 0.03
11 - 15	94.4 ± 0.2	8.4 ± 0.1	97.77 ± 0.03	7.83 ± 0.02
15 - 20	96.9 ± 0.3	8.0 ± 0.2	97.74 ± 0.03	7.56 ± 0.02

Table 12.1: Calculated TES and TER values and their uncertainties as a function of $E_{\mathrm{T}}^{\mathrm{reco}}$ expressed as percentages.

Moreover, by comparing the unweighted input E_{T} distribution to the output reconstructed E_{T} (also unweighted) from the clusterizer algorithm, one can obtain an estimate of the efficiency of the clusterizer algorithm used here. The overall efficiency of the trigger selection of this analysis can be obtained by comparing the input E_{T} distribution to the reconstructed E_{T} after clusterizing and after applying all the trigger QA criteria. These

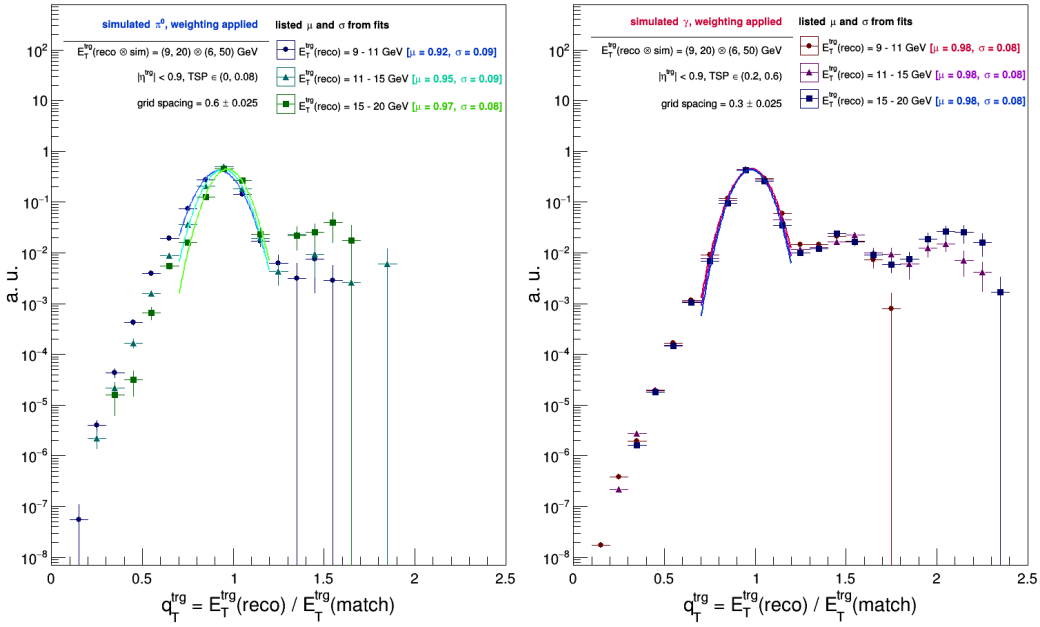

(a) π^0 (b) γ

Figure 12.3: Calculated $q_{\mathrm{T}}^{\mathrm{trg}}$ of matched particle-cluster pairs of π^0 (12.3a) and γ (12.3b) as a function of $E_{\mathrm{T}}^{\mathrm{reco}}$. The peak of each distribution is fit with a gaussian (solid lines) to extract the TES (μ) and TER (σ).

can be seen in figures 12.4 and 12.5 respectively. Note that in figure 12.4, the simulated π^0 and γ were thrown with $E_{\mathrm{T}}^{\mathrm{sim}} \in (9, 20)$ GeV.

12.3 Accounting for the Trigger Energy Scale and Resolution

As the TES is not one and the TER is nonzero, they must be accounted for when comparing unfolded data against particle-level simulation (e.g. PYTHIA 8 or PYTHIA 6). This is accomplished by first approximating the underlying sampled E_{T} distribution of the measured data by "back-smearing" them, i.e. by convoluting the measured E_{T} distributions with the reciprocal of the calculated $q_{\mathrm{T}}^{\mathrm{trg}}$ distributions. Then, the simulation will be weighted such that its E_{T} distributions match the back-smeared data.

In order to quantify the TES and TER, the central peak of $q_{\mathrm{T}}^{\mathrm{trg}}$ distribution, $Q_{\mathrm{T}}^{\mathrm{trg}}$ is

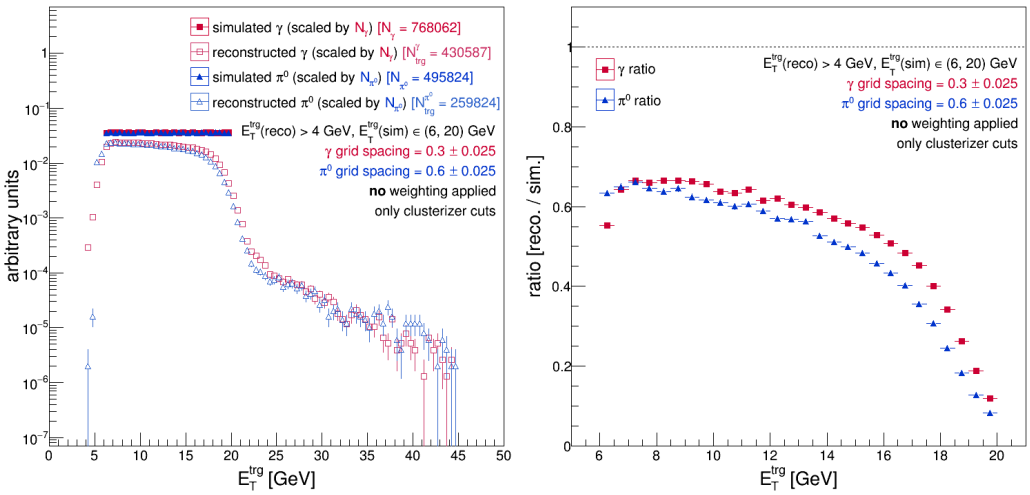

(a) $E_{\mathrm{T}}^{\mathrm{sim}}$ vs. $E_{\mathrm{T}}^{\mathrm{reco}}$ (b) Ratio of $E_{\mathrm{T}}^{\mathrm{reco}}$ to $E_{\mathrm{T}}^{\mathrm{sim}}$

Figure 12.4: Unweighted input $E_{\mathrm{T}}^{\mathrm{sim}}$ vs. unweighted output of the clusterizing algorithm (12.4a), and their ratio (12.4b).

fit with a gaussian to extract its mean and width. However, there are substantial tails extending beyond the central peak of $Q_{\mathrm{T}}^{\mathrm{trg}}$. To assess the extent to which these tails play a role in smearing the E_{T} of a π^0 or γ, the simulated $E_{\mathrm{T}}^{\mathrm{trg}}$ distributions will be convoluted with $Q_{\mathrm{T}}^{\mathrm{trg}}$ twice: once with only the fit to the primary peak, labeled $Q_{\mathrm{T}}^{\mathrm{fit}}$, and once with the whole distribution, labeled $Q_{\mathrm{T}}^{\mathrm{dist}}$.

To validate the TES and TER calculation, the reciprocal of $Q_{\mathrm{T}}^{\mathrm{fit}}$ and $Q_{\mathrm{T}}^{\mathrm{dist}}$ are first convoluted with the output of the Particle⊕Geant framework – the reconstructed E_{T} distributions of the simulated π^0 and γ, labeled $E_{\mathrm{T}}^{\mathrm{reco}}\left[\Delta E_{\mathrm{T}}^{\mathrm{trg}}|\pi^0,\gamma\right]$ (where $\Delta E_{\mathrm{T}}^{\mathrm{trg}}$ indicates the bin of measured $E_{\mathrm{T}}^{\mathrm{trg}}$) – to yield the distributions $\tilde{E}_{\mathrm{TF,D}}^{\mathrm{reco}}\left[\Delta E_{\mathrm{T}}^{\mathrm{trg}}|\pi^0,\gamma\right]$, where the subscripts F and D indicate whether $E_{\mathrm{T}}^{\mathrm{reco}}$ was convoluted with the either the **f**it to or the whole **d**istribution of $Q_{\mathrm{T}}^{\mathrm{trg}}$:

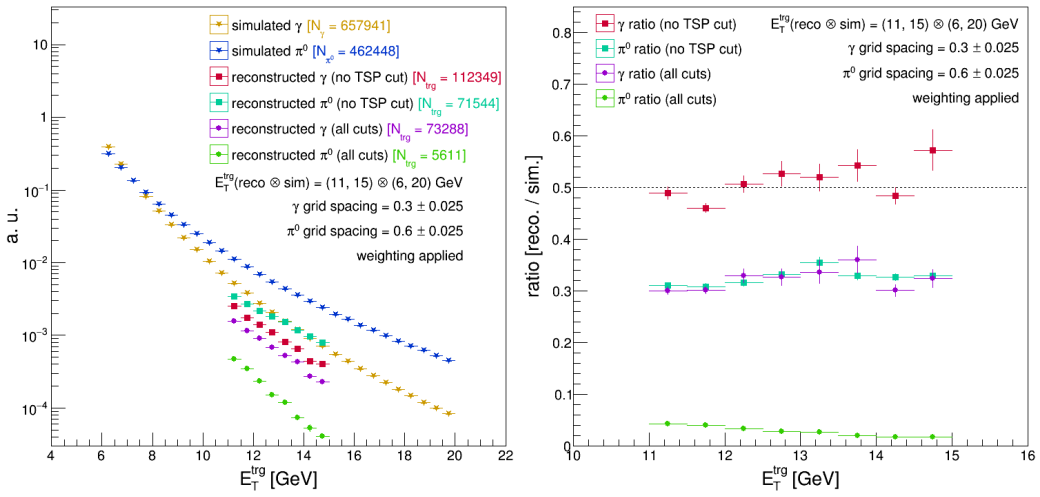

(a) $E_{\mathrm{T}}^{\mathrm{sim}}$ vs. $E_{\mathrm{T}}^{\mathrm{reco}}$ (b) Ratio of $E_{\mathrm{T}}^{\mathrm{reco}}$ to $E_{\mathrm{T}}^{\mathrm{sim}}$

Figure 12.5: Weighted input $E_{\mathrm{T}}^{\mathrm{sim}}$ versus unweighted reconstructed E_{T} after clusterizing and applying trigger QA criteria (12.5a), and their ratio (12.5b), an estimate of the efficiency of the trigger selection of this analysis.

$$\begin{aligned} \tilde{E}_{\mathrm{TF}}^{\mathrm{reco}}\left[\Delta E_{\mathrm{T}}^{\mathrm{trg}}|\pi^0,\gamma\right] &= E_{\mathrm{T}}^{\mathrm{reco}} \circ \frac{1}{Q_{\mathrm{T}}^{\mathrm{fit}}\left[\Delta E_{\mathrm{T}}^{\mathrm{trg}}|\pi^0,\gamma\right]} \\ \tilde{E}_{\mathrm{TD}}^{\mathrm{reco}}\left[\Delta E_{\mathrm{T}}^{\mathrm{trg}}|\pi^0,\gamma\right] &= E_{\mathrm{T}}^{\mathrm{reco}} \circ \frac{1}{Q_{\mathrm{T}}^{\mathrm{dist}}\left[\Delta E_{\mathrm{T}}^{\mathrm{trg}}|\pi^0,\gamma\right]} \end{aligned} \tag{12.1}$$

These back-smeared distributions are then compared against the E_{T} distributions of the simulated π^0 and γ matched to reconstructed BEMC clusters, $E_{\mathrm{T}}^{\mathrm{match}}\left[\Delta E_{\mathrm{T}}^{\mathrm{trg}}|\pi^0,\gamma\right]$. The distributions $E_{\mathrm{T}}^{\mathrm{reco}}$, $\tilde{E}_{\mathrm{T}}^{\mathrm{reco}}$, and $E_{\mathrm{T}}^{\mathrm{match}}$ are shown in figure 12.6.

By back-smearing $E_{\mathrm{T}}^{\mathrm{reco}}$ with $Q_{\mathrm{T}}^{\mathrm{fit}}$, the peaks of the $E_{\mathrm{T}}^{\mathrm{match}}$ distributions are successfully recovered in $\tilde{E}_{\mathrm{T}}^{\mathrm{reco}}$. Furthermore, back-smearing $E_{\mathrm{T}}^{\mathrm{reco}}$ with $Q_{\mathrm{T}}^{\mathrm{dist}}$, the entire $E_{\mathrm{T}}^{\mathrm{match}}$ distributions are successfully recovered, thus validating the TES and TER calculation. Now the weights to be applied to the simulation may be calculated with confidence.

The measured data, labeled $E_{\mathrm{T}}^{\mathrm{meas}}\left[\Delta E_{\mathrm{T}}^{\mathrm{trg}}|\pi^0,\gamma_{\mathrm{rich}}\right]$, are back-smeared by convoluting

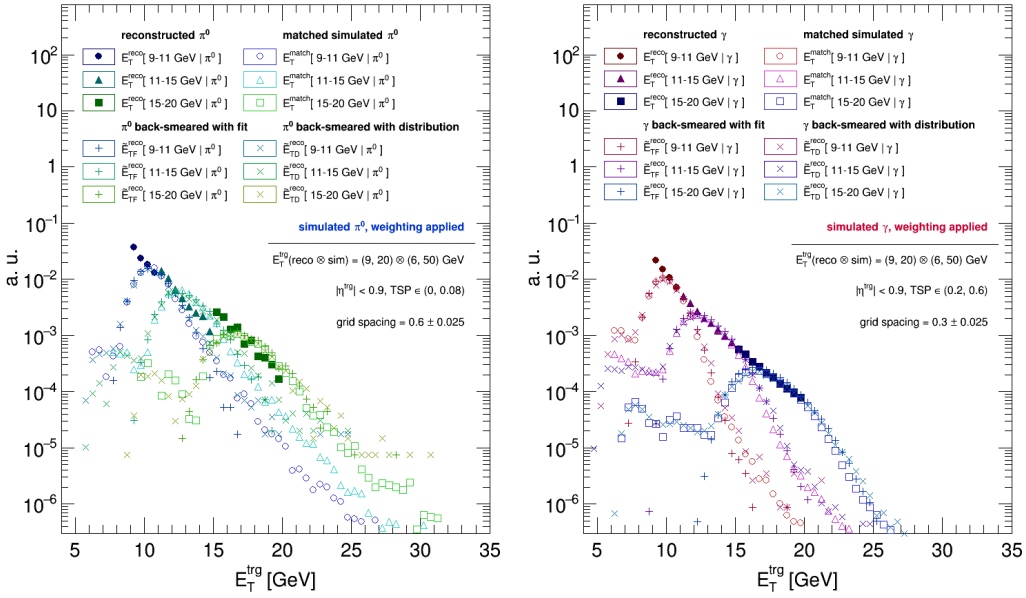

(a) π^0 (b) γ

Figure 12.6: $E_{\mathrm{T}}^{\mathrm{reco}}$, $\tilde{E}_{\mathrm{T}}^{\mathrm{reco}}$, and $E_{\mathrm{T}}^{\mathrm{match}}$ distributions of simulated π^0 (12.6a) and γ (12.6b) from the Particle⊕Geant framework.

$E_{\mathrm{T}}^{\mathrm{meas}}$ with the reciprocal of $Q_{\mathrm{T}}^{\mathrm{fit}}$ and $Q_{\mathrm{T}}^{\mathrm{dist}}$. When normalized to unity, $\tilde{E}_{\mathrm{T}}^{\mathrm{meas}}$ may be interpreted as the probability that a π^0 or γ_{rich} reconstructed by STAR with transverse energy in the range $\Delta E_{\mathrm{T}}^{\mathrm{trg}}$ came from a π^0 or γ_{dir} with transverse energy $\tilde{E}_{\mathrm{T}}^{\mathrm{meas}}$. The back-smeared data, labeled $\tilde{E}_{\mathrm{TF}}^{\mathrm{meas}}$ and $\tilde{E}_{\mathrm{TD}}^{\mathrm{meas}}$ respectively, can be seen in figure 12.7.

In order to compare the fully-corrected data to simulation, the *simulated* recoil jet distributions are reweighted such that the $E_{\mathrm{T}}^{\mathrm{trg}}$ distributions of their correlated triggers match $\tilde{E}_{\mathrm{T}}^{\mathrm{trg}}$. There are two simulation samples which will be compared against the fully corrected data: a sample of "out-of-the-box" PYTHIA 8.185 – i.e. using the Monash Tune described in chapter 9.2 – and a sample of PYTHIA 6.42 tuned to STAR data. These two samples will be labeled Py8 and Py6⋆ respectively. The trigger E_{T} distribution ($E_{\mathrm{T}}^{\mathrm{Py8}}$) extends down to 9 GeV. While in Py6⋆, the trigger E_{T} distribution ($E_{\mathrm{T}}^{\mathrm{Py6\star}}$) extends down to 7 GeV

(for γ triggers) and 6 GeV (for π^0 triggers).

In calculating the weights to be applied to Py8 and Py6$\star$, no cut on E_{T} will be applied to either simulation. First, the distributions $\tilde{E}_{\mathrm{TF}}^{\mathrm{meas}}$, $E_{\mathrm{T}}^{\mathrm{Py8}}$, and $E_{\mathrm{T}}^{\mathrm{Py6}\star}$ are normalized to unity. Then the weights are given by taking the ratio of $\tilde{E}_{\mathrm{TF,D}}^{\mathrm{meas}}$ and $E_{\mathrm{T}}^{\mathrm{Py8,Py6}\star}$:

$$\Delta_{\mathrm{F,D}}^{\mathrm{Py8,Py6}\star}\left[\Delta E_{\mathrm{T}}^{\mathrm{trg}}|\pi^0,\gamma\right] = \frac{\tilde{E}_{\mathrm{TF,D}}^{\mathrm{meas}}\left[\Delta E_{\mathrm{T}}^{\mathrm{trg}}|\pi^0,\gamma\right]}{E_{\mathrm{T}}^{\mathrm{Py8,Py6}\star}\left[\pi^0,\gamma\right]} \tag{12.2}$$

where $\Delta_{\mathrm{F,D}}^{\mathrm{Py8,Py6}\star}$ are the weights corresponding to the data back-smeared with $Q_{\mathrm{T}}^{\mathrm{fit}}$ and $Q_{\mathrm{T}}^{\mathrm{dist}}$ respectively. In total, there are twenty-four sets of weights corresponding to the three bins of measured $E_{\mathrm{T}}^{\mathrm{trg}}$, the two trigger species, the two simulation samples, and the two choices of $q_{\mathrm{T}}^{\mathrm{trg}}$ distributions for convolution. Figure 12.7 shows $\tilde{E}_{\mathrm{TF}}^{\mathrm{meas}}$ versus $E_{\mathrm{T}}^{\mathrm{Py8}}$ and $E_{\mathrm{T}}^{\mathrm{Py6}\star}$, and figure 12.8 the corresponding sets of weights.

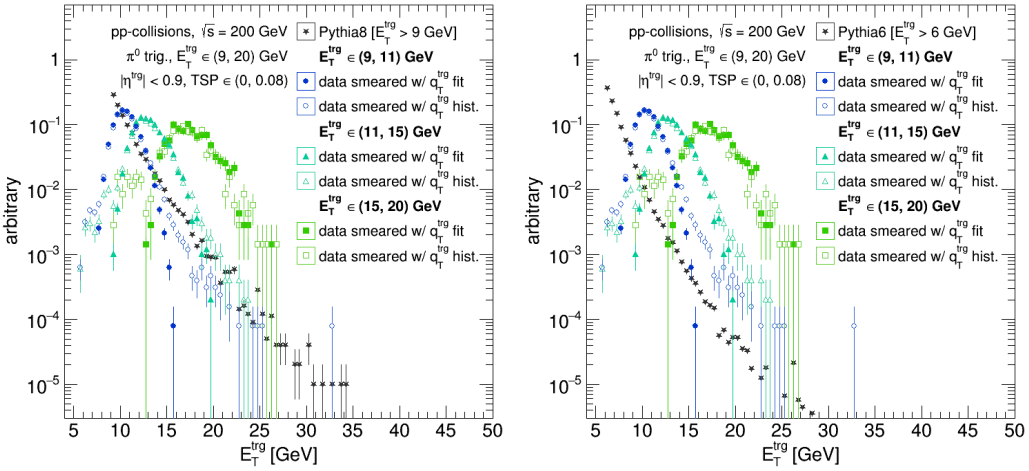

(a) $E_{\mathrm{T}}^{\mathrm{Py8}}\left[\pi^0\right]$ vs. $\tilde{E}_{\mathrm{TF,D}}^{\mathrm{meas}}\left[\Delta E_{\mathrm{T}}^{\mathrm{trg}}|\pi^0\right]$

(b) $E_{\mathrm{T}}^{\mathrm{Py6}\star}\left[\pi^0\right]$ vs. $\tilde{E}_{\mathrm{TF,D}}^{\mathrm{meas}}\left[\Delta E_{\mathrm{T}}^{\mathrm{trg}}|\pi^0\right]$

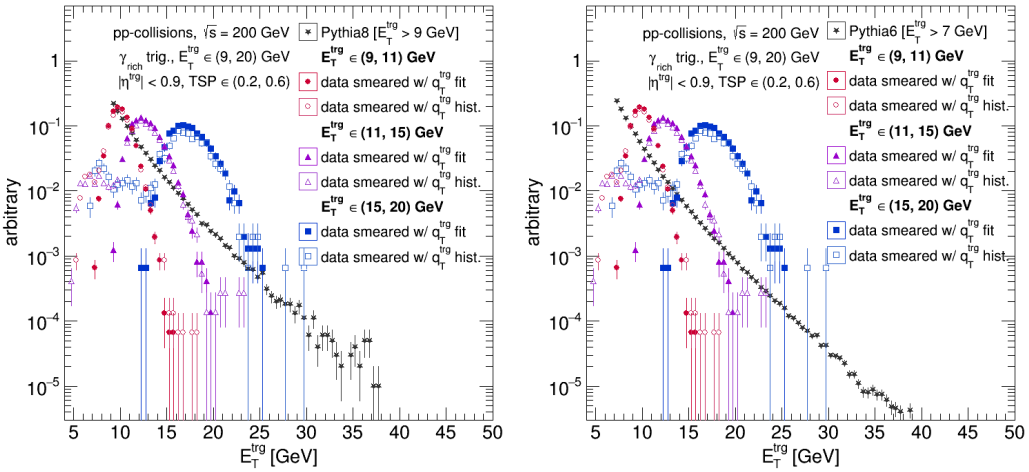

(c) $E_{\mathrm{T}}^{\mathrm{Py8}}\left[\gamma\right]$ vs. $\tilde{E}_{\mathrm{TF,D}}^{\mathrm{meas}}\left[\Delta E_{\mathrm{T}}^{\mathrm{trg}}|\gamma_{\mathrm{dir}}\right]$

(d) $E_{\mathrm{T}}^{\mathrm{Py6}\star}\left[\gamma\right]$ vs. $\tilde{E}_{\mathrm{TF,D}}^{\mathrm{meas}}\left[\Delta E_{\mathrm{T}}^{\mathrm{trg}}|\gamma_{\mathrm{dir}}\right]$

Figure 12.7: Py8 (12.7a, 12.7c) and Py6⋆ (12.7b, 12.7d) π^0 (12.7a, 12.7b) and γ (12.7c, 12.7d) $E_{\mathrm{T}}^{\mathrm{trg}}$ distributions compared against back-smeared data.

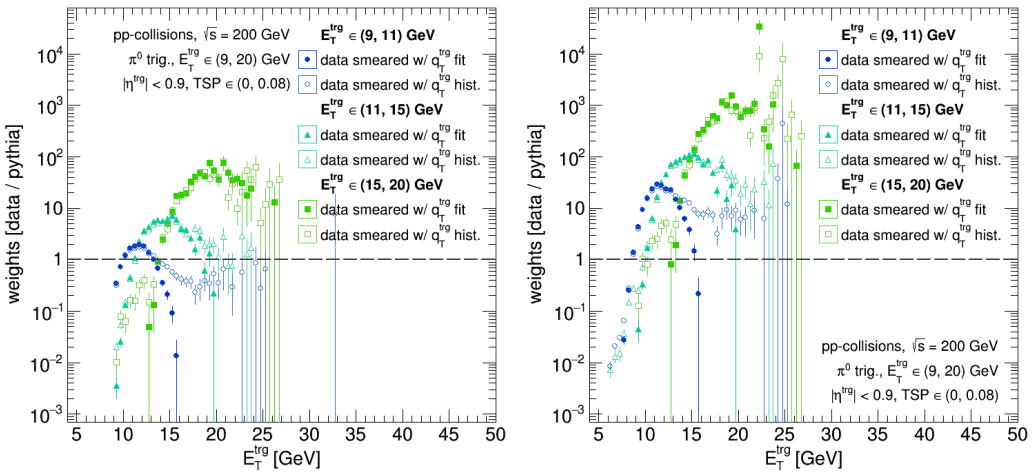

(a) $\Delta_{F,D}^{Py8}\left[\Delta E_T^{trg}|\pi^0\right]$

(b) $\Delta_{F,D}^{Py6\star}\left[\Delta E_T^{trg}|\pi^0\right]$

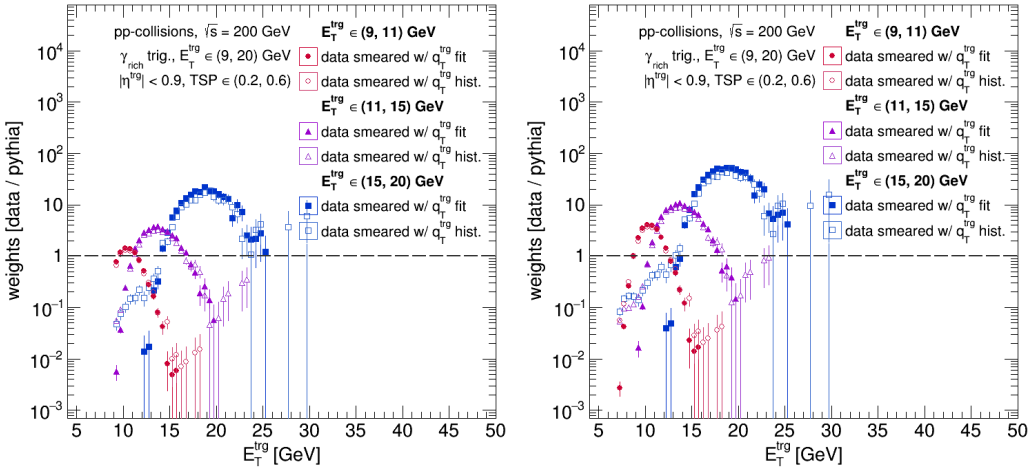

(c) $\Delta_{F,D}^{Py8}\left[\Delta E_T^{trg}|\gamma\right]$

(d) $\Delta_{F,D}^{Py6\star}\left[\Delta E_T^{trg}|\gamma\right]$

Figure 12.8: The weights $\Delta_{F,D}^{Py8,Py6\star}$ which map the Py8 (12.8a, 12.8c) and Py6⋆ (12.8b, 12.8d) π^0 (12.8a, 12.8b) and γ (12.8c, 12.8d) E_T^{trg} distributions onto the back-smeared data.

13.1 Comparison to Fully Corrected Data

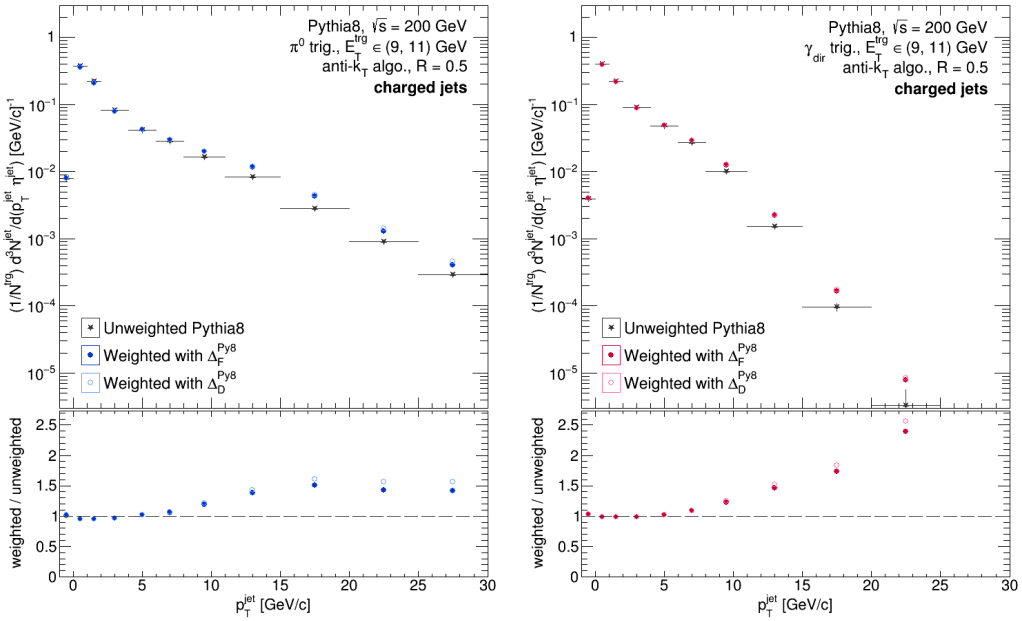

(a) π^0 (b) γ_{dir}

Figure 13.1: Weighted vs. unweighted PYTHIA 8.185 9 - 11 GeV π^0- (13.1a) and γ-triggered (13.1b) recoil jet p_{T} distributions. Weighted distributions visualized without uncertainties.

Once the weights $\Delta_{\text{F,D}}^{\text{Py8}}$ and $\Delta_{\text{F,D}}^{\text{Py6}\star}$ have been calculated, they may be applied to the relevant PYTHIA π^0- and γ_{dir}-triggered charged recoil jet distributions. For the sake of illustration, only Py8 will be discussed here and compared against the fully corrected data. The comparison between the fully corrected data and Py6$\star$ will be reserved for an upcoming publication.

As the range of $\tilde{E}_{\text{T}}^{\text{meas}}$ extends well past the small bins of $E_{\text{T}}^{\text{meas}}$ used to select triggers

(9 - 11, 11 - 15, and 15 - 20 GeV), the selected Py8 π^0 and γ_{dir} triggers are allowed to have any transverse energy. Figure 13.1 shows the weighted 9 - 11 GeV Py8 distributions compared against the corresponding unweighted π^0- and γ_{dir}-triggered Py8 charged recoil jet distributions. The triggers of the unweighted spectra were required to have a transverse energy falling within the corresponding bin of measured transverse energy, e.g. 9 - 11 GeV.

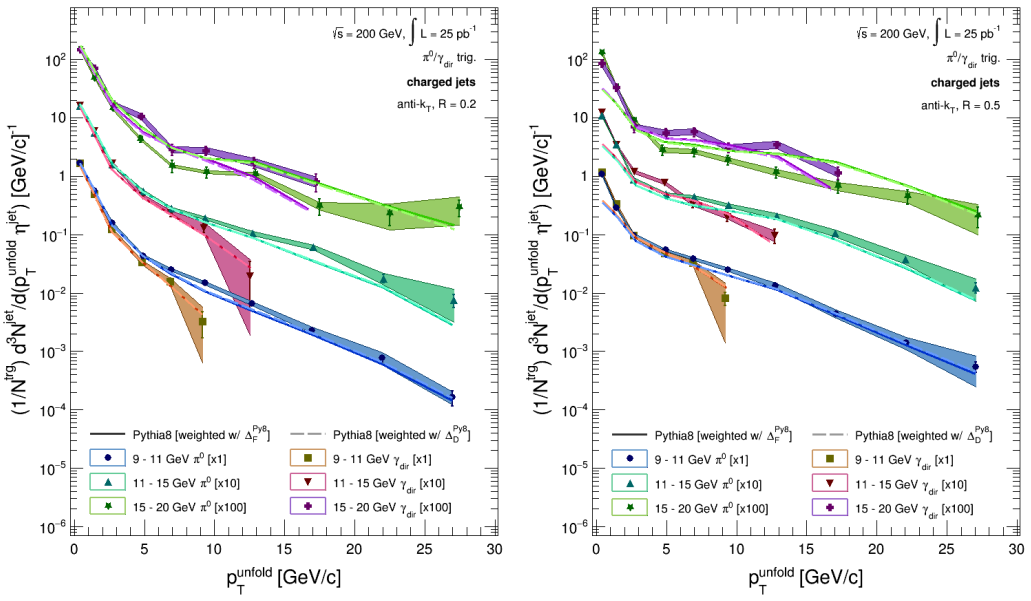

(a) $R_{\text{jet}} = 0.2$ (b) $R_{\text{jet}} = 0.5$

Figure 13.2: Fully corrected $R_{\text{jet}} = 0.2$ (13.2a) and 0.5 (13.2b) data vs. weighted PYTHIA 8.185 recoil jet spectra. The bars and shaded bands respectively indicate the statistical and systematic uncertainty of the measured data.

Figure 13.2 shows the corrected data compared against the weighted Py8 recoil jet spectra. To account for the wide $p_{\text{T}}^{\text{jet}}$, the data and weighted PYTHIA are plotted at their barycenters rather than at their bin centers. The barycenters of the bins were determined according to the algorithm presented in [192]. Agreement is observed between the cor-

rected data and weighted Py8 spectra for 9 - 11 and 11 - 15 GeV π^0 and γ_{dir} triggers and for the 15 - 20 GeV γ_{dir} trigger. However, there is a surprising differences between the weighted simulation and the corrected 15 - 20 GeV π^0 data. Both the $R_{\text{jet}} = 0.2$ and 0.5 15 - 20 GeV π^0 data are systematically lower than the weighted Py8 spectra. This could be due to the Particle$\oplus$Geant simulation not accurately simulating the TSP for 15 - 20 GeV π^0: these π^0 have a small opening angle, and so have on average larger TSP values than the lower energy π^0. It could be that this effect has not been reproduced in the simulation. If so, this would have a large impact on the 15 - 20 GeV weighted Py8 spectra, and so warrants further investigation.

13.2 Summary

The per-trigger yield of charged recoil jets opposite π^0 and γ_{dir} triggers were measured with high precision to furnish a vacuum fragmentation reference for a forthcoming measurement of I_{AA} of π^0- and γ_{dir}-triggered charged recoil jets. These per-trigger yields were corrected using a regularized unfolding procedure carried out at the level of ensemble-averaged distributions as described in chapter 10. This enabled a semi-inclusive measurement of charged recoil jets over a broad range of jet transverse momentum with well-controlled uncertainties.

The energy scale and resolution of the π^0 and γ_{dir} triggers were assessed using a simulation of the STAR electromagnetic calorimeter. The simulation determined that using the π^0 and γ_{dir} identification techniques described in chapter 7, STAR is able to on average reconstruct roughly 97% of the energy of a γ_{dir} and between 92% to 96% of the energy of a π^0. Weights were calculated which enabled the comparison of the fully corrected data to π^0- and γ_{dir}-triggered recoil jet distributions generated by Py8 while accounting for the effects of the finite trigger energy scale and resolution in the measured data. The weighted Py8 semi-inclusive charged recoil jet distributions were found to agree with the fully cor-

rected 9 - 11 and 11 - 15 GeV π^0-triggered data and the γ_{dir}-triggered data. However, there are currently substantial differences between the fully corrected 15 - 20 GeV π^0 data and the weighted PYTHIA spectra, and will be the subject of further studies.

In summary, the measured data will be a valuable vacuum fragmentation baseline for the corresponding measurement of charged recoil jet per-trigger yields in AuAu-collisions and for the measurement of I_{AA} for π^0- and γ_{dir}-triggered charged recoil jets. Moreover, it would be interesting to compare the fully corrected data against NLO calculations.

REFERENCES

[1] MissMJ, "Standard Model of Elementary Particles." https://en.wikipedia.org/wiki/File:Standard_Model_of_Elementary_Particles.svg, 2021. Accessed: November 8th, 2021.

[2] TriTertButoxy, "Elementary Particle Interactions." https://en.wikipedia.org/wiki/File:Elementary_particle_interactions.svg, 2007. Accessed: November 8th, 2021.

[3] **The DOE/NSF Nuclear Science Advisory Committee**, "The Frontiers of Nuclear Science, a Long Range Plan," 2008. arXiv:0809.3137 [nucl-ex].

[4] M. Cacciari, G. P. Salam, and G. Soyez, "The anti-k_t jet clustering algorithm," *Journal of High Energy Physics*, vol. 2008, p. 063, 2008. doi:10.1088/1126-6708/2008/04/063.

[5] **STAR Collaboration**, J. Adams, *et al.*, "Evidence from $d+$ Au Measurements for Final-State Suppression of High-p_T in Au+Au Collisions at RHIC," *Physical Review Letters*, vol. 91, p. 072304, 2003.

[6] **Particle Data Group**, P. A. Zyla, *et al.*, "The Review of Particle Physics (2021)," *Progress of Theoretical and Experimental Physics*, p. 083C01, 2020.

[7] **PHENIX Collaboration**, S. Afanasiev, *et al.*, "Measurement of Direct Photons in Au+Au Collisions at $\sqrt{s_{NN}} = 200$ GeV," *Physical Review Letters*, vol. 109, p. 152302, 2012.

[8] X.-N. Wang, Z. Huang, and I. Sarcevic, "Jet Quenching in the Opposite Direction of a Tagged Photon in High-Energy Heavy-Ion Collisions," *Physical Review Letters*, vol. 77, pp. 231–234, 1996.

[9] **STAR Collaboration**, L. Adamczyk, *et al.*, "Jet-like correlations with direct-photon and neutral-pion triggers at $\sqrt{s_{NN}} = 200$ GeV," *Physics Letters B*, vol. 760, pp. 689–696, 2016.

[10] **PHENIX Collaboration**, A. Adare, *et al.*, "Medium Modification of Jet Fragmentation in Au+Au Collisions at $\sqrt{s_{NN}} = 200$ GeV Measured in Direct Photon-Hadron Correlations," *Physical Review Letters*, vol. 111, p. 032301, 2013.

[11] **PHENIX Collaboration**, U. Acharya, *et al.*, "Measurement of jet-medium interactions via direct photon-hadron correlations in Au+Au and d+Au collisions at $\sqrt{s_{NN}} = 200$ GeV," *Physical Review C*, vol. 102, p. 054910, 2020.

[12] **STAR Collaboration**, L. Adamczyk, *et al.*, "Jet-Hadron Correlations in $\sqrt{s_{NN}} = 200$ GeV p+p and Central Au+Au Collisions," *Physical Review Letters*, vol. 112, p. 122301, 2014.

[13] "RHIC Complex." `https://www.flickr.com/photos/brookhavenlab/7979381212/in/album-72157613690851651/`, 2011. Accessed: November 8th, 2021.

[14] "STAR Detector." `https://www.flickr.com/photos/brookhavenlab/3253562970/in/album-72157613690851651/`, 2009. Accessed: November 8th, 2021.

[15] `https://www.star.bnl.gov/public/img/images/star/star_detector.gif`, 2000. Accessed: November 8th, 2021.

[16] **STAR Collaboration**, L. Adamczyk, *et al.*, "Longitudinal and transverse spin asymmetries for inclusive jet production at mid-rapidity in polarized $p + p$ collisions at $\sqrt{s} = 200$ GeV," *Physical Review D*, vol. 86, p. 032006, 2012.

[17] M. Anderson *et al.*, "The STAR Time Projection Chamber: A Unique Tool for Studying High Multiplicity Events at RHIC," *Nuclear Instruments and Methods in Physics Research A*, vol. 499, pp. 659–678, 2003.

[18] M. Beddo *et al.*, "The STAR Barrel Electromagnetic Calorimeter," *Nuclear Instruments and Methods in Physics Research A*, vol. 499, pp. 725–739, 2003.

[19] **STAR Collaboration**, L. Adamczyk, *et al.*, "Di-Jet Imbalance Measurements at $\sqrt{s_{NN}} = 200$ GEV at STAR," *Physical Review Letters*, vol. 119, p. 062301, 2017.

[20] B. Spinoza, *The Ethics, Treatise on the Emendation of the Intellect, and Selected Letters*. Hackett Publishing Company, 1992.

[21] G. Deleuze and F. Guattari, *What Is Philosophy?* Columbia University Press, 1996.

[22] C. Quigg, "The Double Simplex," 2005. FERMILAB-CONF-05/371-T.

[23] J. H. Christenson, J. W. Cronin, V. L. Fitch, and R. Turlay, "Evidence for the 2π Decay of the K_2^0 Meson," *Physical Review Letters*, vol. 13, p. 138, 1964.

[24] **LHCb Collaboration**, R. Aaij, *et al.*, "Observation of CP Violation in Charm Decays," *Physical Review Letters*, vol. 122, p. 211803, 2019.

[25] **STAR Collaboration**, J. Adams, *et al.*, "Experimental and theoretical challenges in the search for the quark-gluon plasma: the STAR Collaboration's critical assessment of the evidence from RHIC collisions," *Nuclear Physics A*, vol. 757, pp. 102–183, 2005.

[26] T. Lancaster and S. J. Blundell, *Quantum Field Theory for the Gifted Amateur*. Oxford University Press, 2014.

[27] A. Zee, *Quantum Field Theory in a Nutshell*. Princeton University Press, 2003.

[28] R. P. Feynman, "Space-Time Approach to Quantum Electrodynamics," *Physical Review*, vol. 76, p. 769, 1949.

[29] S. Mandelstam, "Determination of the Pion-Nucleon Scattering Amplitude from Dispersion Relations and Unitarity. General Theory.," *Physical Review*, vol. 112, p. 1344, 1958.

[30] H. Yukawa, "On the Interaction of Elementary Particles. I," *Proceedings of the Physico-Mathematical Society of Japan*, vol. 17, pp. 48–57, 1935.

[31] M. Gell-Mann, "A schematic model of baryons and mesons," *Physics Letters*, vol. 8, pp. 214–215, 1964.

[32] G. Zweig, "An SU(3) Model for Strong Interaction Symmetry and its Breaking," 1964. CERN-8182/TH-401.

[33] G. Zweig, "An SU(3) Model for Strong Interaction Symmetry and its Breaking II," 1964. CERN-8419/TH-412.

[34] R. P. Feynman, "The Behavior of Hadron Collisions at Extreme Energies," in *High Energy Collisions: Third International Conference at Stony Brook, N.Y.*, (Stony Brook, New York), pp. 237–249, Gordn & Breach, 1969.

[35] **LHCb Collaboration**, R. Aaij, *et al.*, "Observation of structure in the J/ψ-pair mass spectrum," *Science Bulletin*, vol. 65, p. 1983, 2020.

[36] **LHCb Collaboration**, R. Aaij, *et al.*, "Observation of $J/\psi p$ resonances consistent with pentaquark states $\Lambda_b^0 \to J/\psi K^- p$ decays," *Physical Review Letters*, vol. 115, p. 072001, 2015.

[37] F. Halzen and A. D. Martin, *Quarks & Leptons: an Introductory Course in Modern Particle Physics*. John Wiley & Sons, Inc., 1984. pg.s 9 - 12 and 167 - 171.

[38] B. L. Inscoe and J. L. Lancaster, "Introducing SU(3) color charge in undergraduate quantum mechanics," *American Journal of Physics*, vol. 89, p. 172, 2021.

[39] D. Griffiths, *Introduction to Elementary Particles*. John Wiley & Sons, Inc., 1987. pg.s 279 - 281.

[40] D. J. Gross and F. Wilczek, "Ultraviolet Behavior of Non-Abelian Gauge Theories," *Physical Review Letters*, vol. 30, p. 1343, 1973.

[41] H. D. Politzer, "Reliable Perturbative Results for Strong Interactions?," *Physical Review Letters*, vol. 30, p. 1346, 1973.

[42] K. Yagi, T. Hatsuda, and Y. Miake, *Quark-Gluon Plasma: From Big Bang to Little Bang*. Cambridge University Press, 2005.

[43] J. Letessier and J. Rafelski, *Hadrons and Quark-Gluon Plasma*. Cambdridge Unversity Press, 2002.

[44] F. Karsch, E. Laermann, and A. Peikert, "Quark mass and flavour dependence of the QCD phase transition," *Nuclear Physics B*, vol. 605, pp. 579–599, 2001.

[45] F. Karsch, "Lattice results on QCD thermodynamics," *Nuclear Physics A*, vol. 698, pp. 199–208, 2002.

[46] W. Busza, K. Rajagopal, and W. v. d. Schee, "Heavy Ion Collisions: The Big Picture and the Big Questions," *Annual Review of Nuclear and Particle Science*, vol. 68, pp. 339–376, 2018.

[47] T. Ludlam and L. McLerran, "What Have We Learned From the Relativistic Heavy Ion Collider?," *Physics Today*, vol. 56, p. 48, 2003.

[48] S. D. Drell, D. J. Levy, and T.-M. Yan, "Theory of Deep-Inelastic Lepton-Nucleon Scattering and Lepton-Pair Annihilation Processes I," *Physical Review*, vol. 187, p. 2159, 1969.

[49] S. D. Drell, D. J. Levy, and T. M. Yan, "Theory of Deep-Inelastic Lepton-Nucleon Scattering and Lepton-Pair Annihilation Processes II," *Physical Review D*, vol. 1, p. 1617, 1970.

[50] N. Cabibbo, G. Parisi, and M. Testa, "Hadron production in e^+e^- collisions," *Lettere al Nuovo Cimento*, vol. 4, pp. 35–39, 1970.

[51] J. D. Bjorken and S. J. Brodsky, "Statistical Model for Electron-Positron Annihilation into Hadrons," *Physical Review D*, vol. 1, p. 1416, 1970.

[52] G. Hanson *et al.*, "Evidence for Jet Structure in Hadron Production by e^+e^- Annihilation," *Physical Review Letters*, vol. 35, p. 1609, 1975.

[53] R. F. Schwitters *et al.*, "Azimuthal Asymmetry in Inclusive Hadron Production by e^+e^- Annihilation," *Physical Review Letters*, vol. 35, p. 1320, 1975.

[54] B. Andersson, G. Gustafson, G. Ingelman, and T. Sjöstrand, "Parton Fragmentation and String Dynamics," *Physics Reports*, vol. 97, pp. 31–145, 1983.

[55] A. Metz and A. Vossen, "Parton fragmentation functions," *Progress in Particle and Nuclear Physics*, vol. 91, pp. 136–202, 2016.

[56] **Particle Data Group**, M. Tanabashi, *et al.*, "Fragmentation Functions in e^+e^-, ep, and pp Collisions," *Physical Review D*, vol. 98, p. 030001, 2018.

[57] J. J. Ethier and E. R. Nocera, "Parton Distributions in Nucleons and Nuclei," *Annual Review of Nuclear and Particle Science*, vol. 70, pp. 43–76, 2020.

[58] J. E. Huth *et al.*, "Towards a standardization of jet definitions," in *1990 DPF Summer Study on High-energy Physics: Research Directions for the Decade (Snowmass 90)*, (Snowmass, Colorado), pp. 0134–0136, World Scientific, 1992.

[59] G. Blazey *et al.*, "Run II Jet Physics: Proceedings of the Run II QCD and Weak Boson Physics Workshop," 2000. arXiv:hep-ex/0005012.

[60] G. P. Salam and G. Soyez, "A practical seedless infrared-safe cone jet algorithm," *Journal of High Energy Physics*, vol. 2007, p. 086, 2007.

[61] S. Sapeta, "QCD and jets at hadron colliders," *Progress in Particle and Nuclear Physics*, vol. 89, pp. 1–55, 2016.

[62] S. D. Ellis and D. E. Soper, "Successive Combination Jet Algorithm For Hadron Collisions," *Physical Review D*, vol. 48, p. 3160, 1993.

[63] Y. L. Dokshitzer, G. D. Leder, S. Moretti, and B. R. Webber, "Better Jet Clustering Algorithms," *Journal of High Energy Physics*, vol. 1997, p. 001, 1997.

[64] M. Cacciari, G. P. Salam, and G. Soyez, "The Catchment Area of Jets," *Journal of High Energy Physics*, vol. 2008, p. 005, 2008.

[65] M. Cacciari and G. P. Salam, "Pileup subtraction using jet areas," *Physics Letters B*, vol. 659, pp. 119–126, 2008.

[66] **ALICE Collaboration**, B. Abelev, *et al.*, "Charged jet cross-sections and properties in proton-proton collisions at $\sqrt{s} = 7$ TeV," *Physical Review D*, vol. 91, p. 112012, 2015.

[67] Z. Chang, *Inclusive Jet Longitudinal Double-Spin Asymmetry A_{LL} Measurements in 510 GeV Polarized pp Collisions at STAR*. PhD thesis, Texas A&M University, College Station, TX, December 2016.

[68] **STAR Collaboration**, J. Adam, *et al.*, "Longitudinal double-spin asymmetry for inclusive jet and dijet production in pp collisions at $\sqrt{s} = 510$ GeV," *Physical Review D*, vol. 100, p. 052005, 2019.

[69] M. Connors, C. Nattrass, R. Reed, and S. Salur, "Review of Jet Measurements in Heavy Ion Collisions," *Reviews of Modern Physics*, vol. 90, p. 025005, 2018.

[70] J. D. Bjorken, "Energy Loss of Energetic Partons in Quark - Gluon Plasma: Possible Extinction of High p(t) Jets in Hadron - Hadron Collisions," 1982. FERMILAB-PUB-82-059-THY, FERMILAB-PUB-82-059-T.

[71] S. Peigné and A. V. Smilga, "Energy losses in relativistic plasmas: QCD versus QED," *Physics-Uspekhi*, vol. 52, p. 659, 2009.

[72] G.-Y. Qin, J. Ruppert, C. Gale, J. Sangyong, G. D. Moore, and M. G. Mustafa, "Radiative and Collisional Jet Energy Loss in the Quark-Gluon Plasma at the BNL Relativistic Heavy Ion Collider," *Physical Review Letters*, vol. 100, p. 072301, 2008.

[73] L. D. Landau and I. I. Pomeranchuk, "The limits of applicability of the theory of Bremsstrahlung by electrons and of the creation of pairs at large energies," *Doklady Akademii Nauk SSSR*, vol. 92, pp. 586–588, 1953.

[74] A. B. Migdal, "Bremsstrahlung and pair production in Condensed Media at High Energies," *Physical Review*, vol. 103, p. 1811, 1956.

[75] D. d'Enterria, *Jet Quenching*. Switzerland: Springer Verlag, 2010.

[76] N. Armesto, B. Cole, C. Gale, W. A. Horowitz, P. M. Jacobs, S. Jeon, M. v. Leeuwen, A. Majumder, B. Müller, G.-Y. Qin, C. A. Salgado, B. Schenke, M. Verweij, X.-N. Wang, and U. A. Wiedemann, "Comparison of jet quenching formalisms for a quark-gluon plasma brick," *Physical Review C*, vol. 86, p. 064904, 2012.

[77] G.-Y. Qin and X.-N. Wang, "Jet quenching in high-energy heavy-ion collisions," *International Journal of Modern Physics E*, vol. 24, p. 1530014, 2015.

[78] P. Arnold, "Simple Forumla for High-Energy Gluon Bremsstrahlung in a Finite, Expanding Medium," *Physical Review D*, vol. 79, p. 065025, 2009.

[79] P. Arnold and W. Xiao, "High-energy jet quenching in weakly-coupled quark-gluon plasmas," *Physical Review D*, vol. 78, p. 125008, 2008.

[80] R. Baier and Y. Mehtar-Tani, "Jet quenching and broadening: the transport coefficient $\hat{q}$ in an anisotropic plasma," *Physical Review C*, vol. 78, p. 064906, 2008.

[81] R. Baier, Y. L. Dokshitzer, A. H. Mueller, S. Peigné, and D. Schiff, "Radiative energy loss of high-energy quarks and gluons in a finite volume quark-gluon plasma," *Nuclear Physics B*, vol. 483, pp. 291–320, 1997.

[82] R. Baier, Y. L. Dokshitzer, A. H. Mueller, S. Peigné, and D. Schiff, "Radiative energy loss and $p_\perp$-broadening of high energy partons in nuclei," *Nuclear Physics B*, vol. 484, pp. 265–282, 1997.

[83] B. G. Zakharov, "Fully quantum treatment of the Landau-Pomeranchuk-Migdal effect in QED and QCD," *Journal of Experimental and Theoretical Physics Letters*, vol. 63, pp. 952–957, 1996.

[84] C. A. Salgado and U. A. Wiedemann, "Calculating quenching weights," *Physical Review D*, vol. 68, p. 014008, 2003.

[85] M. Gyulassey, P. Levai, and I. Vitev, "Jet quenching in thin quark-gluon plasmas I: formalism," *Nuclear Physics B*, vol. 571, pp. 197–233, 2000.

[86] M. Gyulassey, P. Levai, and I. Vitev, "Non-Abelian energy loss at finite opacity," *Physical Review Letters*, vol. 85, pp. 5535–5538, 2000.

[87] M. Gyulassey, P. Levai, and I. Vitev, "Reaction operator approach to non-Abelian energy loss," *Nuclear Physics B*, vol. 594, pp. 371–419, 2001.

[88] U. A. Wiedemann, "Gluon radiation off hard quarks in a nuclear environment: opacity expansion," *Nuclear Physics B*, vol. 588, pp. 303–344, 2000.

[89] U. A. Wiedemann, "Jet quenching versus jet enhancement: a quantitative study of the BDMPS-Z gluon radiation spectrum," *Nuclear Physics A*, vol. 690, pp. 731–751, 2001.

[90] I. Vitev, "Jet quenching in relativistic heavy ion collisions," *Journal of Physics: Conference Series*, vol. 50, p. 014, 2006.

[91] M. Djordjevic and U. W. Heniz, "Radiative energy loss in a finite dynamical QCD medium," *Physical Review Letters*, vol. 101, p. 022302, 2008.

[92] X.-F. Guo and X.-N. Wang, "Multiple scattering, parton energy loss and modified fragmentation functions in deeply inelastic eA scattering," *Physical Review Letters*, vol. 85, pp. 3591–3594, 2000.

[93] X.-F. Guo and X.-N. Wang, "Multiple parton scattering in nuclei: Parton energy loss," *Nuclear Physics A*, vol. 696, pp. 788–832, 2001.

[94] A. Majumder, "Hard collinear gluon radiation and multiple scattering in a medium," *Physical Review D*, vol. 85, p. 014023, 2012.

[95] P. Arnold, G. D. Moore, and L. G. Yaffe, "Photon Emission from Quark-Gluon Plasma: Complete Leading Order Results," *Journal of High Energy Physics*, vol. 2001, p. 009, 2001.

[96] P. Arnold, G. D. Moore, and L. G. Yaffe, "Photon Emission from Ultrarelativistic Plasmas," *Journal of High Energy Physics*, vol. 2001, p. 057, 2001.

[97] P. Arnold, G. D. Moore, and L. G. Yaffe, "Photon and gluon emission from relativistic plasmas," *Journal of High Energy Physics*, vol. 2002, p. 030, 2002.

[98] P. Romatschke, "Do nuclear collisions create a locally equilibrated quark-gluon plasma?," *The European Physical Journal C*, vol. 77, 2017. Article number: 21.

[99] S. Caron-Huot and C. Gale, "Finite-size effects on the radiative energy loss of a fast parton in hot and dense strongly interacting matter," *Physical Review C*, vol. 82, p. 064902, 2010.

[100] H. Li, F. Liu, G.-l. Ma, X.-N. Wang, and Y. Zhu, "Mach cone induced by γ-triggered jets in high-energy heavy-ion collisions," *Physical Review Letters*, vol. 106, p. 012301, 2011.

[101] X.-N. Wang and Y. Zhu, "Medium Modification of γ-Jets in High-Energy Heavy-Ion Collisions," *Physical Review Letters*, vol. 111, p. 062301, 2013.

[102] Y. He, T. Luo, X.-N. Wang, and Y. Zhu, "Linear Boltzmann Transport for Jet Propagation in the Quark-Gluon Plasma: Elastic Processes and Medium Recoil," *Physical Review C*, vol. 91, p. 054908, 2015.

[103] A. Jaiswal and V. Roy, "Relativistic Hydrodynamics in High Energy Heavy-Ion Collisions: General Aspects and Recent Developments," *Advances in High Energy Physics*, vol. 2016, 2016. Article ID: 9623034.

[104] C. Shen and L. Yan, "Recent development of hydrodynamic modeling in heavy-ion collisions," *Nuclear Science and Techniques*, vol. 31, 2020. Article number: 122.

[105] C. Gale, S. Jeon, and B. Schenke, "Hydrodynamic Modeling of Heavy-Ion Collisions," *International Journal of Modern Physics A*, vol. 28, p. 1340011, 2013.

[106] W. Chen, S. Cao, T. Luo, L.-G. Pang, and X.-N. Wang, "Effects of jet-induced medium excitation in γ-hadron correlation in $A + A$ collisions," *Physics Letters B*, vol. 777, p. 86, 2018.

[107] E. Shuryak, "Why does the quark-gluon plasma at RHIC behave as a nearly ideal fluid?," *Progress in Particle and Nuclear Physics*, vol. 53, pp. 273–303, 2004.

[108] T. D. Lee, "The strongly interacting quark-gluon plasma and future physics," *Nuclear Physics A*, vol. 750, pp. 1–8, 2005.

[109] M. Gyulassey and L. McLerran, "New forms of QCD matter discovered at RHIC," *Nuclear Physics A*, vol. 750, pp. 30–63, 2005.

[110] J. M. Maldacena, "The Large N Limit of Superconformal Field Theories and Supergravity," *International Journal of Theoretical Physics*, vol. 38, pp. 1113–1133, 1999.

[111] E. Witten, "Anti-de Sitter Space, Thermal Phase Transition, and Confinement in Gauge Theories," *Advances in Theoretical and Mathematical Physics*, vol. 2, pp. 505–532, 1998.

[112] I. Y. Aref'eva, "Holographic approach to quark-gluon plasmas in heavy ion collisions," *Physics-Uspekhi*, vol. 57, p. 527, 2014.

[113] H. Liu, K. Rajagopal, and U. A. Wiedemann, "Calculating the Jet Quenching Parameter," *Physical Review Letters*, vol. 97, p. 182301, 2006.

[114] H. Liu, K. Rajagopal, and U. A. Wiedemann, "Wilson loops in heavy ion collisions and their calculation in AdS/CFT," *Journal of High Energy Physics*, vol. 2007, p. 066, 2007.

[115] J. Casalderrey-Solana and C. A. Salgado, "Introductory lectures on jet quenching in heavy ion collisions," *Acta Physica Polonica B*, vol. 38, pp. 3731–3794, 2007.

[116] G. David, "Direct real photons in relativistic heavy ion collisions," *Reports on Progress in Physics*, vol. 83, p. 046301, 2020.

[117] J. F. Owens, "Large Momentum Transfer Production of Direct Photons, Jets, and Particles," *Reviews of Modern Physics*, vol. 59, p. 465, 1987.

[118] L. McLerran and B. Schenke, "The Glasma, Photons and the Implications of Anisotropy," *Nuclear Physics A*, vol. 929, pp. 71–82, 2014.

[119] J. Berges, K. Reygers, N. Tanji, and R. Venugopalan, "Parametric estimate of the relative photon yields from the glasma and the quark-gluon plasma in heavy-ion collisions," *Physical Review C*, vol. 95, p. 054904, 2017.

[120] J. I. Kapusta, P. Lichard, and D. Seibert, "High-energy photons from quark-gluon plasma versus hot hadronic gas," *Physical Review D*, vol. 44, pp. 2774–2788, 1991.

[121] C. Y. Wong, *Introduction to high-energy heavy ion collisions*. World Scientific, 1994. pg. 422.

[122] J. W. Harris and B. Müller, "The Search for the Quark-Gluon Plasma," *Annual Review of Nuclear and Particle Science*, vol. 46, pp. 71–107, 1996.

[123] **CMS Collaboration**, S. Chatrchyan, *et al.*, "Measurement of isolated photon production in pp and PbPb collisions at $\sqrt{s_{NN}} = 2.76$ TeV," *Physics Letters B*, vol. 710, pp. 256–277, 2012.

[124] **ATLAS Collaboration**, G. Aad, *et al.*, "Centrality, rapidity and transverse momentum dependence of isolated prompt photon production in lead-lead collisions at $\sqrt{s_{NN}} = 2.76$ TeV measured with the ATLAS detector," *Physical Review C*, vol. 93, p. 034914, 2016.

[125] **ALICE Collaboration**, J. Adam, *et al.*, "Direct photon production in Pb-Pb collisions at $\sqrt{s_{NN}} = 2.76$ TeV," *Physics Letters B*, vol. 754, pp. 235–248, 2016.

[126] **PHENIX Collaboration**, A. Adare, *et al.*, "Suppression Pattern of Neutral Pions at High Transverse Momentum in Au + Au Collisions at $\sqrt{s_{NN}} = 200$ GeV and Constraints on Medium Transport Coefficients," *Physical Review Letters*, vol. 101, p. 232301, 2008.

[127] J. Binnewies, B. A. Kniehl, and G. Kramer, "Next-to-Leading Order Fragmentation Functions for Pions and Kaons," *Zeitschrift für Physik C Particles and Fields*, vol. 65, pp. 471–480, 1995.

[128] M. J. Tannenbaum, "Measurement of $\hat{q}$ in Relativistic Heavy ion Collisions using di-hadron correlations," *Physics Letters B*, vol. 771, pp. 553–557, 2017.

[129] M. Xie, S.-Y. Wei, G.-Y. Qin, and H.-Z. Zhang, "Extracting jet transport coefficient via single hadron and dihadron productions in high-energy heavy-ion collisions," *The European Physical Journal C*, vol. 79, p. 7, 2019.

[130] **JET Collaboration**, K. M. Burke, *et al.*, "Extracting the jet transport coefficient from jet quenching in high-energy heavy-ion collisions," *Physical Review C*, vol. 90, p. 014909, 2014.

[131] T. Sjöstrand, S. Mrenna, and P. Skands, "A brief introduction to PYTHIA 8.1," *Computer Physics Communications*, vol. 178, pp. 852–867, 2008.

[132] T. Renk, "Towards jet tomography: γ-hadron correlations," *Physical Review C*, vol. 74, p. 034906, 2006.

[133] H. Zhang, J. F. Owens, E. Wang, and X.-N. Wang, "Tomography of High-Energy Nuclear Collisions with Photon-Hadron Correlations," *Physical Review Letters*, vol. 103, p. 032302, 2009.

[134] **STAR Collaboration**, L. Adamczyk, *et al.*, "Experimental studies of di-jets in Au+Au collisions using angular correlations with respect to back-to-back leading hadrons," *Physical Review C*, vol. 87, p. 044903, 2013.

[135] D. de Florian, R. Sassot, M. Epele, R. J. Hernandez-Pinto, and M. Stratmann, "Parton-to-Pion Fragmentation Reloaded," *Physical Review D*, vol. 91, p. 014035, 2015.

[136] T. Kaufmann, A. Mukherjee, and W. Vogelsang, "Hadron Fragmentation Inside Jets in Hadronic Collisions," *Physical Review D*, vol. 92, p. 054015, 2015.

[137] D. de Florian, R. Sassot, and M. Stratmann, "Global analysis of fragmentation functions for pions and kaons and their uncertainties," *Physical Review D*, vol. 75, p. 114010, 2007.

[138] G.-Y. Qin, C. Gale, S. Jeon, G. D. Moore, and J. Ruppert, "Jet energy loss and high p_T photon production in hot quark-gluon plasma," *Nuclear Physics A*, vol. 830, pp. 459c–462c, 2009.

[139] X.-F. Chen, C. Greiner, E. Wang, X.-N. Wang, and Z. Xu, "Bulk matter evolution and extraction of jet transport parameters in heavy-ion collisions at energies available at the BNL Relativistic Heavy Ion Collider (RHIC)," *Physical Review C*, vol. 81, p. 064908, 2010.

[140] T. Renk, "γ-hadron correlations as a tool to trace the flow of energy lost from hard partons in heavy-ion collisions," *Physical Review C*, vol. 80, p. 014901, 2009.

[141] B. W. Harris and J. F. Owens, "Two cutoff phase space slicing method," *Physical Review D*, vol. 65, p. 094032, 2002.

[142] Z. Xu and C. Greiner, "Thermalization of gluons in ultrarelativistic heavy ion collisions by including three-body interactions in a parton cascade," *Physical Review C*, vol. 71, p. 064901, 2005.

[143] Z. Xu and C. Greiner, "Transport rates and momentum isotropization of gluon matter in ultrarelativistic heavy-ion collisions," *Physical Review C*, vol. 76, p. 024911, 2007.

[144] T. Renk, "Parton shower evolution in a 3D hydrodynamical medium," *Physical Review C*, vol. 78, p. 034908, 2008.

[145] T. Renk, "Jet modification in 200 AGeV Au-Au collisions," 2008. arXiv:0808.1803 [hep-ph].

[146] T. Renk, "A comparison of medium-modified QCD shower evolution scenarios," *Physical Review C*, vol. 79, p. 054906, 2009.

[147] N. Borghini and U. A. Wiedemann, "Distorting the hump-backed plateau of jets and dense QCD matter," 2005. arXiv:hep-ph/0506218.

[148] T. Renk, "Theoretical assessment of jet-hadron correlations," *Physical Review C*, vol. 87, p. 024905, 2013.

[149] `https://www.agsrhichome.bnl.gov/RHIC/Runs/index.html#RHIC_Summary`, 2021. Accessed: March 15th, 2022.

[150] **PHOBOS Collaboration**, B. B. Back, *et al.*, "The PHOBOS detector at RHIC," *Nuclear Instruments and Methods in Physics Research A*, vol. 499, p. 603, 2003.

[151] **PHOBOS Collaboration**, B. B. Back, *et al.*, "Charged particle multiplicity near mid-rapidity in central Au + Au collisions at $S^{1/2} = 56$-A/GeV," *Physical Review Letters*, vol. 85, pp. 3100–3104, 2000.

[152] **PHOBOS Collaboration**, B. B. Back, *et al.*, "Charged-Particle Pseudorapidity Density Distributions from Au+Au Collisions at $\sqrt{s_{NN}} = 130$ GeV," *Physical Review Letters*, vol. 87, p. 102303, 2001.

[153] **BRAHMS Collaboration**, M. Adamczyk, *et al.*, "The BRAHMS experiment at RHIC," *Nuclear Instruments and Methods in Physics Research A*, vol. 499, pp. 437–468, 2003.

[154] **BRAHMS Collaboration**, I. Arsene, *et al.*, "Evolution of the nuclear modification factors with rapidity and centrality in d+Au at $\sqrt{s_{NN}} = 200$ GeV," *Physical Review Letters*, vol. 93, p. 242303, 2004.

[155] **BRAHMS Collaboration**, I. Arsene, *et al.*, "Quark Gluon Plasma and Color Glass Condensate at RHIC? The perspective from the BRAHMS experiment.," *Nuclear Physics A*, vol. 757, pp. 1–27, 2005.

[156] **PHENIX Collaboration**, K. Adcox, *et al.*, "PHENIX detector overview," *Nuclear Instruments and Methods in Physics Research A*, vol. 499, pp. 469–479, 2003.

[157] **PHENIX Collaboration**, S. S. Adler, *et al.*, "Suppressed π^0 production at large transverse momentum in central Au + Au collisions at $\sqrt{S_{NN}} = 200$ GeV," *Physical Review Letters*, vol. 91, p. 072301, 2003.

[158] **sPHENIX Collaboration**, A. Adare, *et al.*, "sPHENIX: an upgrade concept from the PHENIX Collaboration," 2012. arXiv:1207.6378 [nucl-ex].

[159] **$\mathbf{A_N}$DY Collaboration**, L. C. Bland, *et al.*, "Cross sections and transverse single-spin asymmetries in forward jet production from proton collisions at $\sqrt{s} = 500$ GeV," *Physics Letters B*, vol. 750, pp. 660–665, 2015.

[160] **pp2pp Collaboration**, S. Bueltmann, *et al.*, "First Measurement of Proton-Proton Elastic Scattering at RHIC," *Physics Letters B*, vol. 579, pp. 245–250, 2004.

[161] **STAR Collaboration**, L. Adamczyk, *et al.*, "Single spin asymmetry A_N in polarized proton-proton elastic scattering at $\sqrt{s} = 200$ GeV," *Physics Letters B*, vol. 719, pp. 62–69, 2013.

[162] K. H. Ackermann *et al.*, "STAR detector overview," *Nuclear Instruments and Methods in Physics Research A*, vol. 499, pp. 624–632, 2003.

[163] F. Bergsma *et al.*, "The STAR detector magnet subsystem," *Nuclear Instruments and Methods in Physics Research A*, vol. 499, pp. 633–639, 2003.

[164] F. S. Bieser *et al.*, "The STAR trigger," *Nuclear Instruments and Methods in Physics Research A*, vol. 499, pp. 766–777, 2003.

[165] E. G. Judd *et al.*, "The evolution of the STAR Trigger System," *Nuclear Instruments and Methods in Physics Research A*, vol. 902, pp. 228–237, 2018.

[166] J. Kiryluk, "Relative Luminosity Measurement in STAR and Implications for Spin Asymmetry Determinations," vol. 675 of *AIP Conference Proceedings*, p. 424, American Institute of Physics, 2003.

[167] C. Adler, A. Denisov, E. Garcia, M. Murray, H. Strobele, and S. White, "The RHIC zero-degree calorimeters," *Nuclear Instruments and Methods in Physics Research A*, vol. 461, pp. 337–340, 2001.

[168] W. J. Llope *et al.*, "The STAR Vertex Position Detector," *Nuclear Instruments and Methods in Physics Research A*, vol. 759, pp. 23–28, 2014.

[169] L. C. Bland *et al.*, "Future of low-x forward physics at RHIC," *The European Physical Journal C*, vol. 43, pp. 427–435, 2005.

[170] W. J. Llope, "Multigap RPCs in the STAR experiment at RHIC," *Nuclear Instruments and Methods in Physics Research A*, vol. 661, pp. S110–S113, 2012. Supplement 1.

[171] R. Bellwied *et al.*, "The STAR Silicon Vertex Tracker: a large area Silicon Drift Detector," *Nuclear Instruments and Methods in Physics Research A*, vol. 499, pp. 640–651, 2003.

[172] S. Bouvier, "The silicon strip detector for STAR," *Nuclear Instruments and Methods in Physics Research A*, vol. 549, pp. 27–32, 2005.

[173] K. H. Ackermann *et al.*, "The Forward Time Projection Chamber (FTPC) in STAR," *Nuclear Instruments and Methods in Physics Research A*, vol. 499, pp. 713–719, 2003.

[174] C. E. Allgower *et al.*, "The STAR endcap electromagnetic calorimeter," *Nuclear Instruments and Methods in Physics Research A*, vol. 499, pp. 740–750, 2003.

[175] A. H. Hamed, *Elliptic Flow Measurements of Inclusive Photons and Neutral Pion Reconstructions*. PhD thesis, Wayne State University, Detroit, MI, July 2006.

[176] **STAR Collaboration**, B. I. Abelev, *et al.*, "Parton energy loss in heavy-ion collisions via direct-photon and charged-particle azimuthal correlations," *Physical Review C*, vol. 82, p. 034909, 2010.

[177] M. Cacciari, G. P. Salam, and G. Soyez, "Fastjet user manual," *The European Physical Journal C*, vol. 72, p. 1896, 2012.

[178] **STAR Collaboration**, L. Adamczyk, *et al.*, "Measurement of jet quenching with semi-inclusive hadron+jet distributions in Au+Au collisions at $\sqrt{s_{NN}}$ = 200 GeV," *Physical Review C*, vol. 96, p. 024905, 2017.

[179] T. Sjöstrand, S. Mrenna, and P. Skands, "PYTHIA 6.4 Physics and Manual," *Journal of High Energy Physics*, vol. 2006, p. 026, 2006.

[180] P. Z. Skands, "Tuning Monte Carlo generators: The Perugia tunes," *Physical Review D*, vol. 82, p. 074018, 2010.

[181] R. Brun, R. Hagelberg, M. Hansroul, and J. C. Lassalle, "Simulation program for particle physics experiments, GEANT: user guide and reference manual," 1978. CERN-DD-78-2.

[182] L. Huo, "In-Jet Tracking Efficiency Analysis for the STAR Time Projection Chamber in Polarized Proton-Proton Collisions at $\sqrt{s} = 200$ GeV," Master's thesis, Texas A&M University, October 2011.

[183] G. D'Agostini, "A Multidimensional unfolding method based on Bayes' theorem," *Nuclear Instruments and Methods in Physics Research A*, vol. 362, pp. 487–498, 1995.

[184] V. Blobel, "Unfolding methods in high energy physics experiments," in *Proceedings of the "1984 CERN School of Computing"*, (Aiguablava, Catalonia, Spain), pp. 88–127, CERN, 1985.

[185] T. Adye, "Unfolding algorithms and tests using RooUnfold," in *Proceedings of the PHYSTAT 2011 Workshop*, (Geneva, Switzerland), pp. 313–318, CERN, 2011.

[186] C. Tsallis, "Possible generalization of Boltzmann-Gibbs statistics," *Journal of Statistical Physics*, vol. 52, pp. 479–487, 1988.

[187] G. Wilk and Z. Włodarczyk, "Interpretation of the Nonextensivity Parameter q in Some Applications of Tsallis Statistics and Lévy Distributions," *Physical Review Letters*, vol. 84, p. 2770, 2000.

[188] **STAR Collaboration**, B. I. Abelev, *et al.*, "Strange particle production in $p + p$ collisions at $\sqrt{s} = 200$ GeV," *Physical Review C*, vol. 75, p. 064901, 2007.

[189] M. Bähr, S. Gieseke, M. A. Gigg, D. Grellscheid, K. Hamilton, O. Latunde-Dada, S. Plätzer, P. Richardson, M. H. Seymour, A. Sherstnev, and B. R. Webber, "Herwig++ physics and manual," *The European Physical Journal C*, vol. 58, pp. 639–707, 2008.

[190] J. Bellm, S. Gieseke, D. Grellscheid, S. Plätzer, M. Rauch, R. Christian, P. Richardson, P. Schichtel, M. H. Seymour, A. Siódmok, A. Wilcock, N. Fischer, M. A. Harrendorf, G. Nail, A. Papaefstathiou, and D. Rauch, "Herwig 7.0/Herwig++ 3.0 release note," *The European Physical Journal C*, vol. 76, 2016. Article number: 196.

[191] B. R. Webber, "A QCD model for jet fragmentation including soft gluon interference," *Nuclear Physics B*, vol. 238, pp. 492–528, 1984.

[192] G. D. Lafferty and T. R. Wyatt, "Where to stick your data points: The treatment of measurements within wide bins," *Nuclear Instruments and Methods A*, vol. 355, pp. 541–547, 1995.

APPENDIX A

DATA PRODUCTION DETAILS AND BAD RUN/TOWER LISTS

As stated, the analysis presented in this thesis makes use of data (pp-collisions) recorded by STAR during the running year 2009 (Run9). Specifically, this analysis makes use of data from the P11id MuDSTs for the L2gamma trigger (the `st_gamma` stream). The relevant query for the STAR file catalog is:

```
get_file_list.pl -keys node,path,filename -cond
trgsetupname=commission2009_200Gev_Hi||
production2009_200GeV_Hi||
production2009_200GeV_noendcap||
production2009_200GeV_Single||
tof_production2009_single, production=P11id,
filetype=daq_reco_MuDst,filename~st_gamma,
storage!=HPSS -limit 0
```

Furthermore, L2gamma events from this data-set which were recorded during any of the runs whose IDs are listed below were excluded from this analysis:

10114082, 10120093, 10159043, 10166054, 10126064, 10128094, 10128102, 10131009, 10131075, 10131087, 10132004, 10135072, 10136036, 10138049, 10140005, 10140011, 10142012, 10142035, 10142093, 10144038, 10144074, 10149008, 10150005, 10151001, 10152010, 10156090, 10157015, 10157053, 10158047, 10160006, 10161006, 10161016, 10161024, 10162007, 10165027,

10165077, 10166024, 10169033, 10170011, 10170029, 10170047, 10171011, 10172054, 10172059, 10172077

These runs were excluded based on six event-wise observables:

- the average pseudorapidity of all accepted primary tracks;
- the average azimuthal angle of all accepted primary tracks;
- the average number of interaction vertices;
- the average reference-multiplicity, the number of global tracks with $\eta \in (-0.5, 0.5)$;
- the average total energy in the BEMC;
- and the average z-component of the primary interaction vertex.

The runs excluded are outliers in one or more of these observables. The same criteria was applied to identify bad runs in the AuAu data, and is the same list of bad runs used in [9].

And lastly, any L2gamma event from this data-set whose associated trigger cluster contains one of the towers whose IDs are listed below is also excluded from this analysis:

34, 106, 113, 160, 266, 267, 275, 280, 282, 286, 287, 293, 410, 504, 533, 541, 555, 561, 562, 594, 615, 616, 629, 633, 637, 638, 647, 650, 653, 657, 671, 673, 743, 789, 790, 791, 792, 806, 809, 810, 811, 812, 813, 814, 821, 822, 823, 824, 829, 830, 831, 832, 837, 841, 842, 843, 844, 846, 849, 850, 851, 852, 857, 875, 897, 899, 903, 939, 953, 954, 956, 993, 1026, 1046, 1048, 1080, 1081, 1100, 1125, 1130, 1132, 1180, 1197, 1198, 1199, 1200, 1207, 1217, 1218, 1219, 1220, 1221, 1222, 1223, 1224, 1237, 1238, 1240, 1241, 1242, 1243, 1244, 1257, 1258, 1259, 1260, 1312, 1348, 1353, 1354, 1388, 1407, 1409, 1434, 1448, 1537, 1567, 1574, 1597, 1612, 1654, 1668, 1713,

1762, 1765, 1766, 1877, 1878, 1984, 2032, 2043, 2054, 2073, 2077, 2092, 2093, 2097, 2107, 2162, 2168, 2214, 2305, 2392, 2409, 2415, 2439, 2459, 2589, 2590, 2633, 2652, 2749, 2834, 2961, 2969, 3005, 3017, 3070, 3071, 3186, 3220, 3289, 3360, 3493, 3494, 3495, 3508, 3588, 3604, 3611, 3668, 3678, 3679, 3690, 3692, 3732, 3738, 3838, 3840, 3927, 3945, 4005, 4006, 4013, 4018, 4019, 4053, 4059, 4124, 4331, 4355, 4357, 4458, 4464, 4500, 4677, 4678, 4684, 4768, 360, 493, 779, 1284, 1306, 1337, 1438, 1709, 2027, 2445, 3407, 3720, 4217, 4288, 95, 96, 296, 316, 443, 479, 555, 562, 637, 671, 709, 740, 743, 796, 857, 897, 899, 915, 953, 1130, 1132, 1294, 1318, 1337, 1348, 1359, 1378, 1427, 1429, 1440, 1537, 1563, 1574, 1709, 1763, 1773, 1819, 1854, 1874, 1936, 1938, 2018, 2043, 2098, 2099, 2256, 2259, 2294, 2514, 2520, 2552, 2589, 2598, 2680, 2706, 2799, 2880, 2897, 2917, 2969, 3020, 3028, 3310, 3319, 3375, 3399, 3504, 3539, 3541, 3679, 3690, 3692, 3718, 3719, 3720, 3738, 3806, 3838, 3840, 3928, 4013, 4017, 4038, 4053, 4057, 4058, 4079, 4097, 4099

These are towers which have been identified as being *hot*, registering an anomalously large number of counts (a signal above a determined threshold) over the entirety of a data-taking period.

APPENDIX B

ADDITIONAL TRIGGER AND TRACK DISTRIBUTIONS

This appendix compiles additional figures which show various event, trigger, and track distributions on which the selection criteria in chapter 8 are applied. Figure B.1 shows the primary vertex v_z, v_x, and v_y distributions of the recorded data and the selection criteria applied to v_z. Figure B.2 shows the trigger $E_{\mathrm{T}}^{\mathrm{trg}}$ versus the trigger η^{trg} and φ^{trg}. Lastly, figure B.3 shows the distribution of trigger $E_{\mathrm{T}}^{\mathrm{trg}}$ and TSP and the selection criteria applied to them.

Figure B.4 shows the number of primary tracks for all events selected for analysis. Figure B.5 shows the distribution of the number of used fit points and the ratio of used fit points to total possible fit points for primary tracks and the selection criteria applied to the distributions. Figure B.6 shows the distribution of global DCA (i.e. the distance of closest approach of the track to the IV calculated with respect to the IP) for primary tracks and the selection criteria applied. Figure B.7 shows the distribution of primary track $p_{\mathrm{T}}^{\mathrm{trk}}$ and η^{trk} and the selection criteria applied. Figure B.8 and B.9 show the $\Delta\varphi^{\mathrm{trk}}$ and η^{trk} distributions of primary tracks as a function of the track $p_{\mathrm{T}}^{\mathrm{trk}}$ for both π^0 and γ_{rich} triggers. Figure B.10 shows the $\left(\eta^{\mathrm{trk}}, \Delta\varphi^{\mathrm{trk}}\right)$ distribution of all primary tracks selected for jet reconstruction. Lastly, figure B.11 shows the distribution of $p_{\mathrm{T}}^{\mathrm{trk}}$ for all primary tracks selected for jet reconstruction for both π^0 and γ_{rich} triggers.

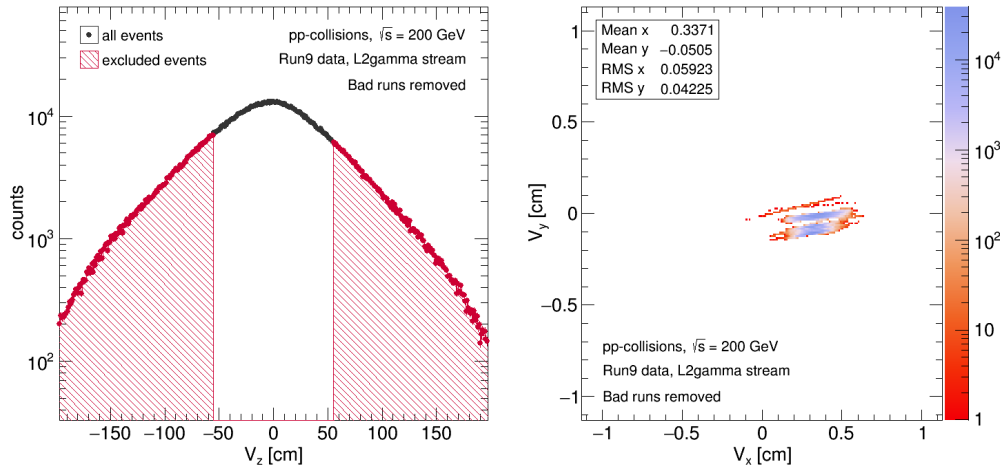

(a) Primary vertex v_z.

(b) Primary vertex v_x and v_y.

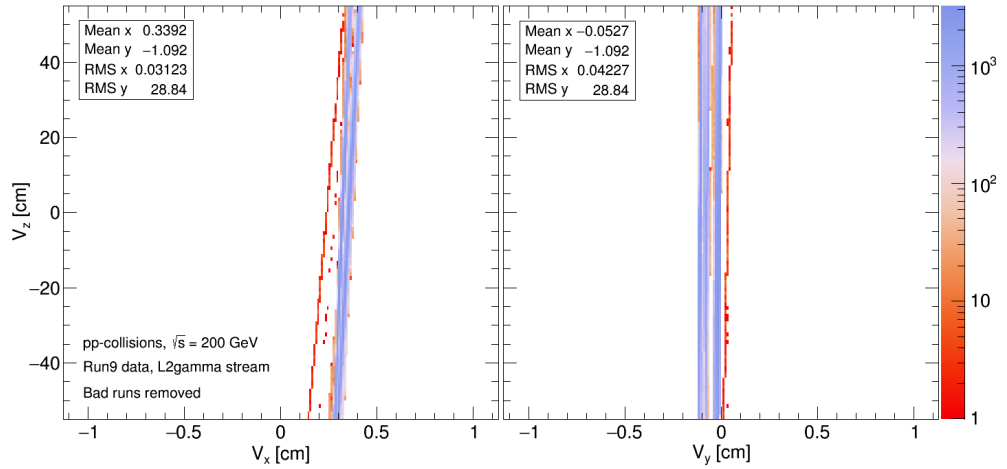

(c) v_y and v_x vs. v_z of primary vertices.

Figure B.1: Primary vertex coordinates (v_x, v_y, v_z) of all events. The shaded regions in B.1a indicate events excluded by the v_z selection criterion. All events satisfy the v_r selection criterion.

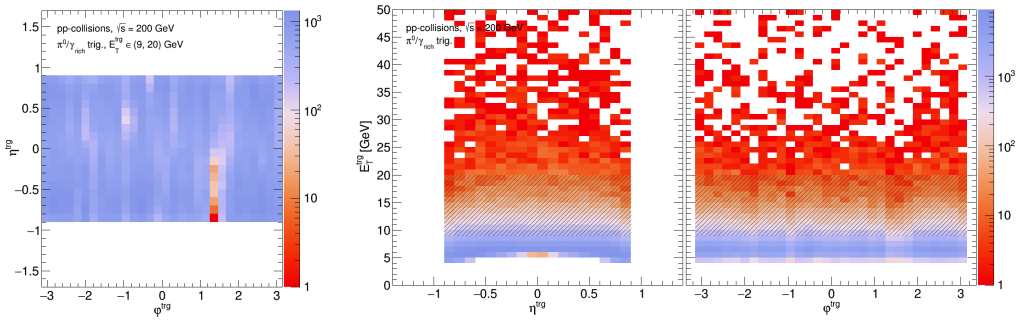

(a) Trigger $(\eta^{\mathrm{trg}}, \varphi^{\mathrm{trg}})$ (b) Trigger $E_{\mathrm{T}}^{\mathrm{trg}}$ vs. $(\eta^{\mathrm{trg}}, \varphi^{\mathrm{trg}})$

Figure B.2: Trigger $(\eta^{\mathrm{trg}}, \varphi^{\mathrm{trg}})$ (B.2a) and $E_{\mathrm{T}}^{\mathrm{trg}}$ vs. $(\eta^{\mathrm{trg}}, \varphi^{\mathrm{trg}})$ (B.2b). The shaded regions of B.2b indicate the $E_{\mathrm{T}}^{\mathrm{trg}}$ selection window.

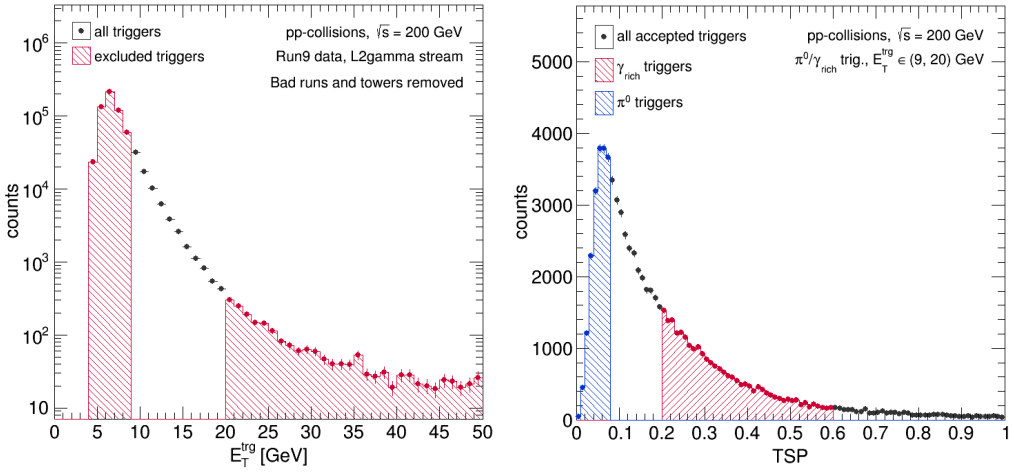

(a) Trigger $E_{\mathrm{T}}^{\mathrm{trg}}$ (b) Trigger TSP

Figure B.3: $E_{\mathrm{T}}^{\mathrm{trg}}$ and TSP distributions from data. The shaded regions in B.3a indicate triggers excluded by the $E_{\mathrm{T}}^{\mathrm{trg}}$ trigger selection criterion, and the shaded regions in B.3b indicate identified π^0 and γ_{rich} triggers.

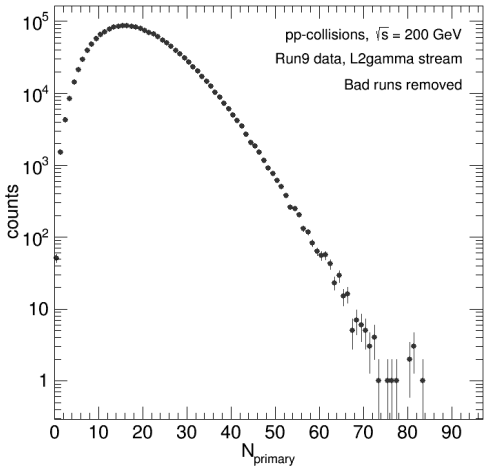

Figure B.4: Number of primary tracks.

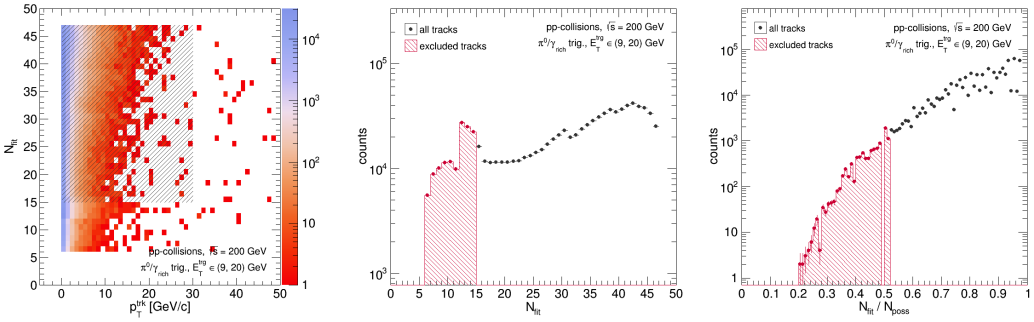

(a) Track N_{fit} vs. $p_{\text{T}}^{\text{trk}}$ (b) Track N_{fit} (c) Track $N_{\text{fit}}/N_{\text{poss}}$

Figure B.5: Track N_{fit} and $N_{\text{fit}}/N_{\text{poss}}$ distributions The shaded region in B.5a indicates tracks satisfying the $p_{\text{T}}^{\text{trk}}$ vs. N_{fit} selection window, and the shaded regions in B.5b and B.5c indicate tracks excluded by the N_{fit} and $N_{\text{fit}}/N_{\text{poss}}$ track acceptance criteria.

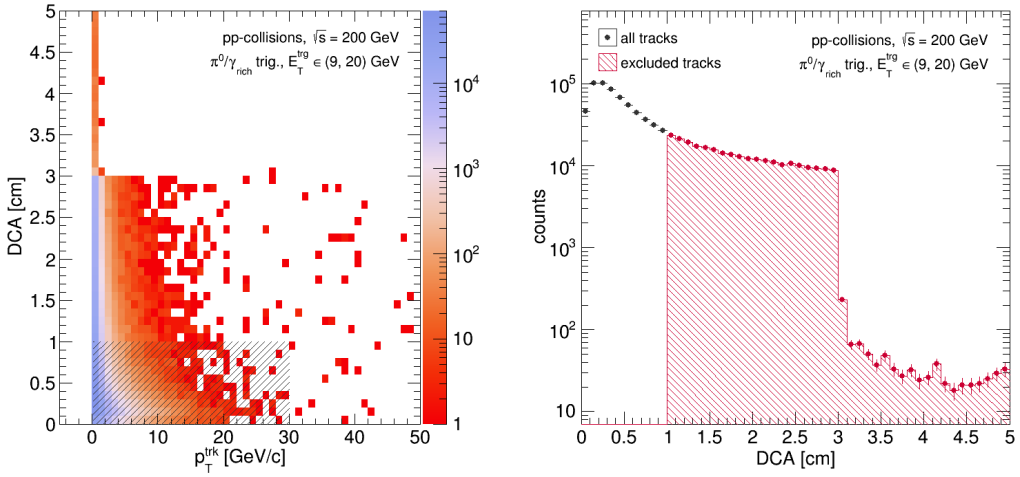

(a) Track DCA vs. $p_{\mathrm{T}}^{\mathrm{trk}}$ (b) Track DCA

Figure B.6: Global DCA of all tracks. The shaded region in B.6a indicates the $p_{\mathrm{T}}^{\mathrm{trk}}$ vs. DCA selection window, and the shaded region in B.6b indicates tracks excluded by the DCA selection criterion.

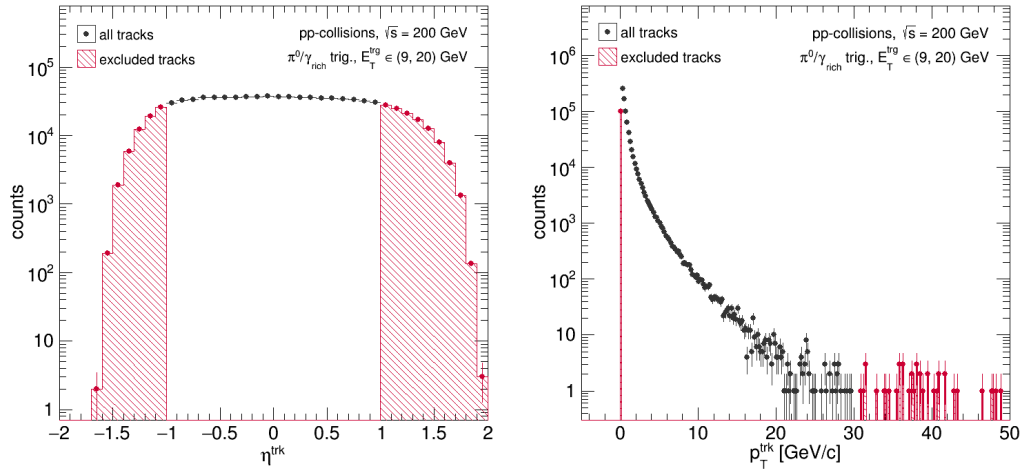

(a) Track η^{trk} (b) Track $p_{\mathrm{T}}^{\mathrm{trk}}$

Figure B.7: The pseudorapidity and transverse momentum distributions of all tracks. The shaded regions indicate tracks excluded by the η^{trk} and $p_{\mathrm{T}}^{\mathrm{trk}}$ track selection criteria.

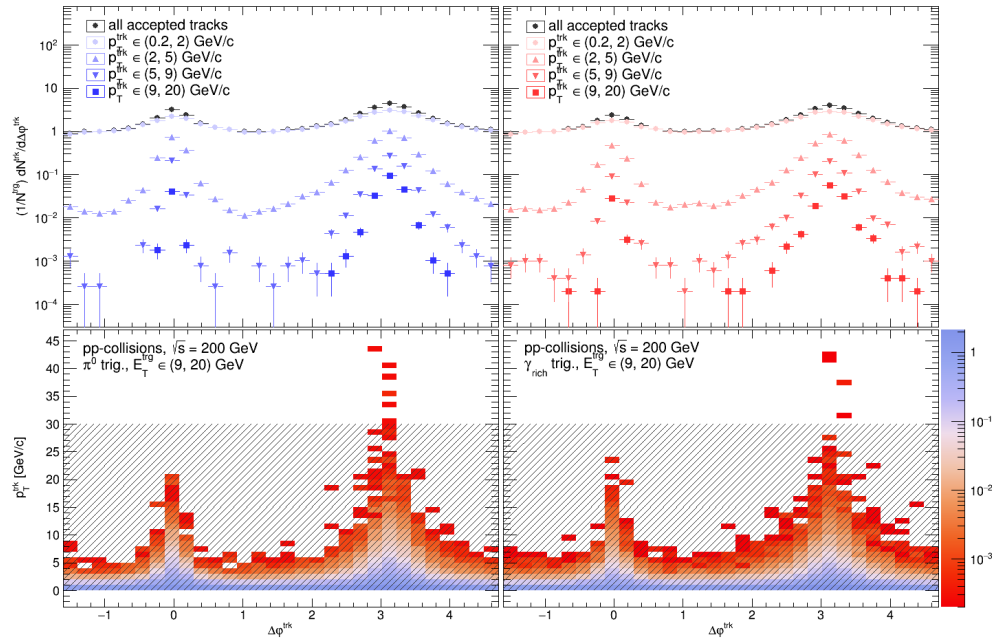

Figure B.8: $\Delta\varphi^{\mathrm{trk}}$ of all accepted tracks (top panels) and $\Delta\varphi^{\mathrm{trk}}$ vs. $p_{\mathrm{T}}^{\mathrm{trk}}$ (lower panels) for all tracks correlated with π^0 and γ_{rich} triggers. The shaded regions in the lower panels indicate the $p_{\mathrm{T}}^{\mathrm{trk}}$ selection window.

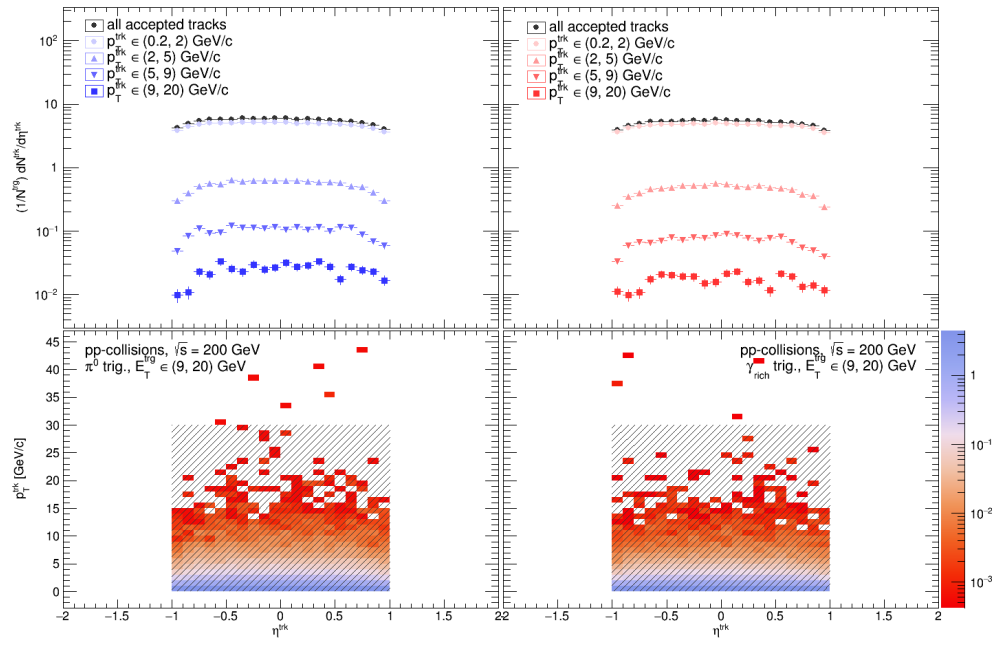

Figure B.9: η^{trk} of all accepted tracks (top panels) and η^{trk} vs. $p_{\mathrm{T}}^{\mathrm{trk}}$ (lower panels) for all tracks correlated with π^0 and γ_{rich} triggers. Shaded regions indicate the $p_{\mathrm{T}}^{\mathrm{trk}}$ vs. η^{trk} selection window.

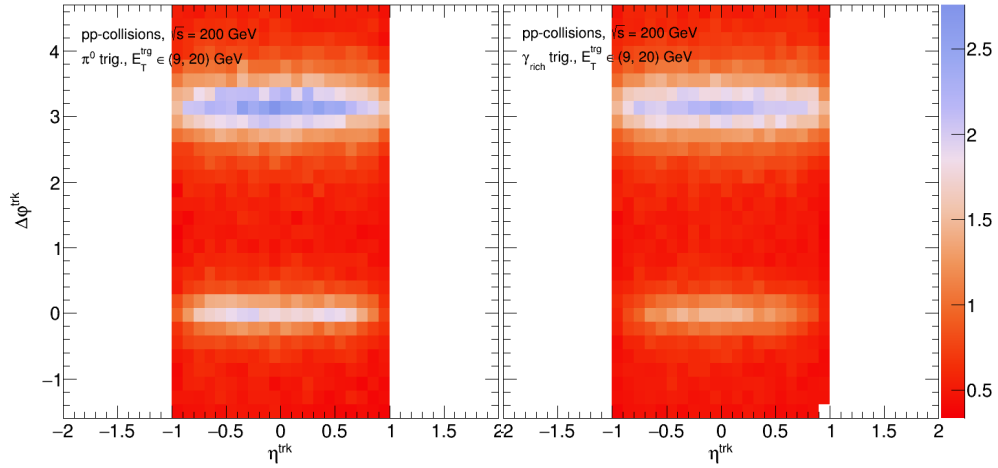

Figure B.10: η^{trk} vs. $\Delta\varphi^{\mathrm{trk}}$ of all accepted tracks for π^0 and γ_{rich} triggers.

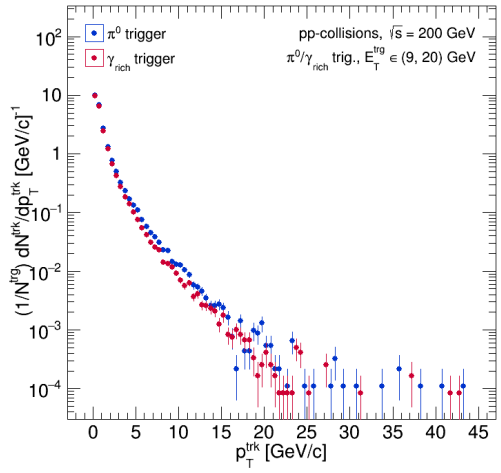

Figure B.11: $p_{\mathrm{T}}^{\mathrm{trk}}$ for π^0 and γ_{rich} triggers.

APPENDIX C

FIT PARAMETERS FOR SMOOTHING RESPONSE MATRICES

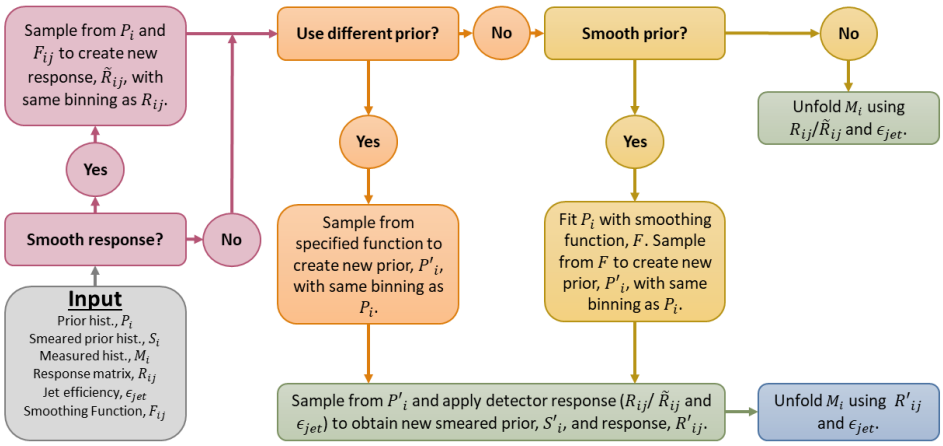

Figure C.1: A flow chart which illustrates the layout of the unfolding code.

This appendix compiles tables of the parameters extracted from the fits to the $R_{\text{jet}} = 0.5$ Py6⊕Geant unfolding priors and $q_{\text{T}}^{\text{jet}}$ distributions used to smooth the $R_{\text{jet}} = 0.5$ response matrices. Table C.1 lists the parameters for the exponential piece of the prior fits, and table C.2 lists the parameters for the hyperbolic tangent piece of the prior fits. Tables C.3, C.4, C.5, C.6, C.7 list the parameters extracted from the double Gaussian fits to the $q_{\text{T}}^{\text{jet}}$ distributions for $p_{\text{T}}^{\text{par}} = 0.2$ - 0.6, 0.6 - 1, 1 - 2, 2 - 10, and 10 - 57 GeV/c respectively. Figure C.1 illustrates the structure of the code used to perform the unfolding described in chapters 10 and 11. It also illustrates the order of operations when smoothing the prior, smoothing the response matrix, and retraining the response matrix.

E_T^{trg} [GeV]	n_{exp}	c_i	b_i
9 - 11	2	$(0.39, -1.78)$	$(-1.17, -0.260)$
11 - 15	3	$(0.39, -2.44, -1.78)$	$(-1.17, -0.14, -0.260)$
15 - 20	4	$(0.31, -1.36, -3.81, -0.49)$	$(-1.18, -0.39, 0.01, -0.22)$

Table C.1: Exponential fit parameters used to the smooth the $R_{\text{jet}} = 0.5$ Py6⊕Geant unfolding priors.

E_T^{trg} [GeV]	n_{tan}	p_T^0	a_i
9 - 11	1	(-8.12)	(10.70)
11 - 15	2	$(7.14, 7.33)$	$(13.29, -13.34)$
15 - 20	2	$(9.07, 9.28)$	$(8.15, -8.15)$

Table C.2: Hyperbolic tangent parameters used to smooth the $R_{\text{jet}} = 0.5$ Py6⊕Geant unfolding priors.

E_T^{trg} [GeV]	Low q_T^{jet}			High q_T^{jet}		
	A	μ	σ	A	μ	σ
9 - 11	0.007	0.67	0.06	0.59	1.01	0.06
11 - 15	0.003	0.60	0.06	0.66	1.00	0.06
15 - 20	0.003	0.64	0.06	0.53	1.00	0.06

Table C.3: Fit parameters for $p_T^{par} \in (0.2, 0.6)$ GeV/c used to smooth the q_T^{jet} projections of the $R_{\text{jet}} = 0.5$ Py6⊕Geant response matrix.

E_T^{trg} [GeV]	Low q_T^{jet}			High q_T^{jet}		
	A	μ	σ	A	μ	σ
9 - 11	0.04	0.67	0.06	0.68	1.02	0.06
11 - 15	0.03	0.67	0.06	0.51	1.00	0.06
15 - 20	0.002	0.60	0.06	0.56	1.00	0.06

Table C.4: Fit parameters for $p_T^{par} \in (0.6, 1)$ GeV/c used to smooth the q_T^{jet} projections of the $R_{\text{jet}} = 0.5$ Py6⊕Geant response matrix.

E_T^{trg} [GeV]	Low q_T^{jet}			High q_T^{jet}		
	A	μ	σ	A	μ	σ
9 - 11	0.06	0.68	0.06	0.57	1.02	0.07
11 - 15	0.12	0.68	0.06	0.53	1.01	0.07
15 - 20	0.04	068	0.06	0.57	1.00	0.07

Table C.5: Fit parameters for $p_T^{par} \in (1, 2)$ GeV/c used to smooth the q_T^{jet} projections of the $R_{jet} = 0.5$ Py6$\oplus$Geant response matrix.

E_T^{trg} [GeV]	Low q_T^{jet}			High q_T^{jet}		
	A	μ	σ	A	μ	σ
9 - 11	0.15	0.73	0.08	0.47	1.01	0.07
11 - 15	0.09	0.71	0.08	0.52	1.00	0.07
15 - 20	0.14	0.70	0.07	0.48	1.00	0.07

Table C.6: Fit parameters for $p_T^{par} \in (2, 10)$ GeV/c used to smooth the q_T^{jet} projections of the $R_{jet} = 0.5$ Py6$\oplus$Geant response matrix.

E_T^{trg} [GeV]	Low q_T^{jet}			High q_T^{jet}		
	A	μ	σ	A	μ	σ
9 - 11	0.12	0.71	0.08	0.48	0.99	0.07
11 - 15	0.11	0.69	0.08	0.47	0.97	0.07
15 - 20	0.13	0.68	0.08	0.47	0.97	0.07

Table C.7: Fit parameters for $p_T^{par} \in (10, 57)$ GeV/c used to smooth the q_T^{jet} projections of the $R_{jet} = 0.5$ Py6$\oplus$Geant response matrix.

APPENDIX D

ADDITIONAL SYSTEMATIC VARIATIONS

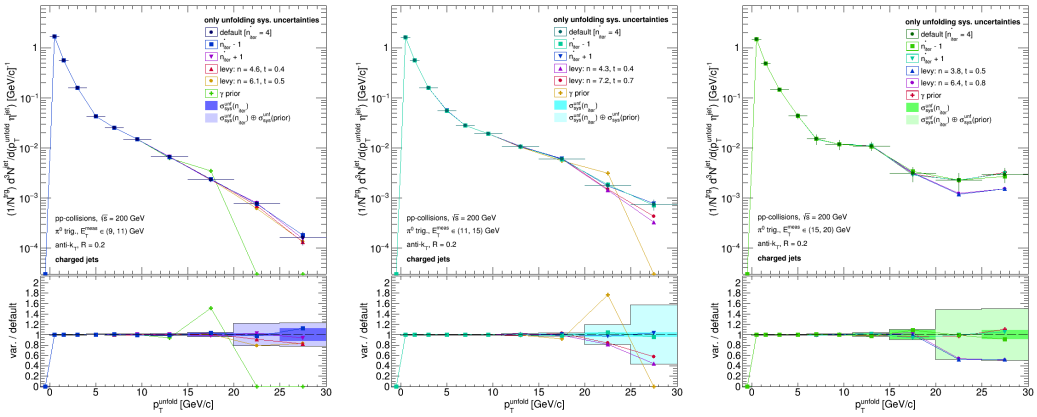

(a) 9 - 11 GeV (b) 11 - 15 GeV (c) 15 - 20 GeV

Figure D.1: Unfolding systematic variations for 9 - 11 (D.1a), 11 - 15 (D.1b), and 15 - 20 GeV (D.1c) π^0-triggered $R_{\text{jet}} = 0.2$ data. Variations visualized without uncertainties.

This appendix compiles plots showing unfolding and detector systematic variations compared against the respective baselines and their assigned uncertainties for each combination of trigger species, $E_{\text{T}}^{\text{trg}}$ range, and R_{jet}. As described in section 11.2, the solid bands in the lower panels of each plot show the total accumulated uncertainty as each source is considered. Figures D.1 and D.2 show the unfolding systematic variations for π^0-triggered $R_{\text{jet}} = 0.2$ and 0.5 data respectively. Figures D.3 and D.4 show the same but for γ_{dir} triggers. Figures D.5 and D.5 show the detector systematic variations for π^0-triggered $R_{\text{jet}} = 0.2$ and 0.5 data respectively. Lastly, figures D.7 and D.8 show the same but for γ_{dir} triggers.

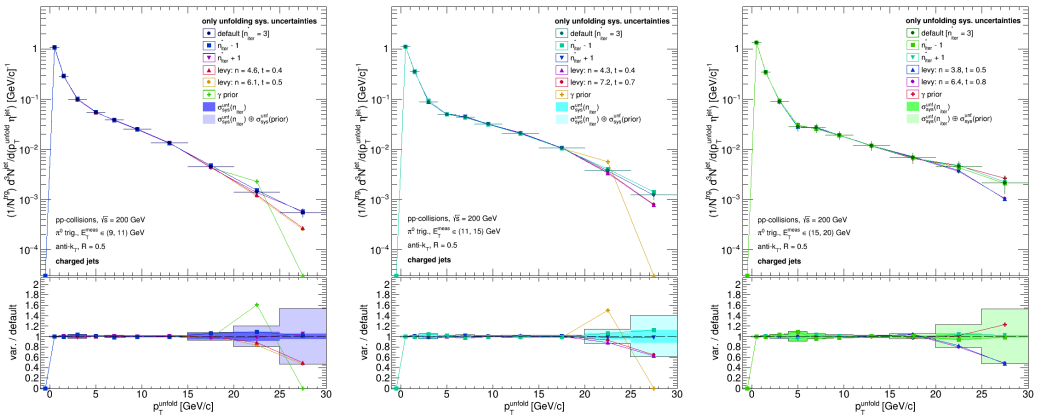

(a) 9 - 11 GeV (b) 11 - 15 GeV (c) 15 - 20 GeV

Figure D.2: Unfolding systematic variations for 9 - 11 (D.2a), 11 - 15 (D.2b), and 15 - 20 GeV (D.2c) π^0-triggered $R_{\text{jet}} = 0.5$ data. Variations visualized without uncertainties.

As was mentioned in section 11.2, the γ_{dir} prior variation was excluded from the calculation of $\sigma_{\text{sys}}^{\text{unfold}}$ for all $E_{\text{T}}^{\text{trg}}$ and $R_{\text{jet}} = 0.2$. Similarly, the $n_{\text{iter}}^{*} + 1$ and n_{iter}^{*} with background values of $B + \delta B$ variations for 11 - 15 GeV γ_{dir} were excluded as the solutions did not converge.

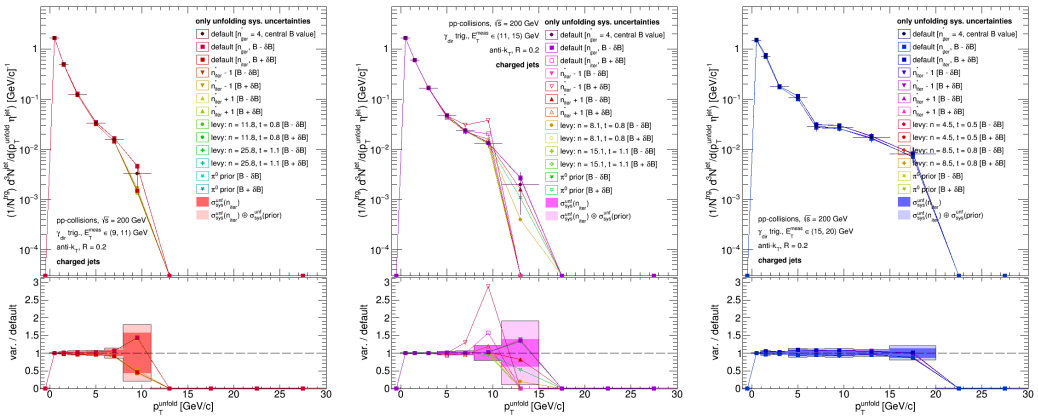

(a) 9 - 11 GeV (b) 11 - 15 GeV (c) 15 - 20 GeV

Figure D.3: Unfolding systematic variations for 9 - 11 (D.3a), 11 - 15 (D.3b), and 15 - 20 GeV (D.3c) γ_{dir}-triggered $R_{\text{jet}} = 0.2$ data. Variations visualized without uncertainties.

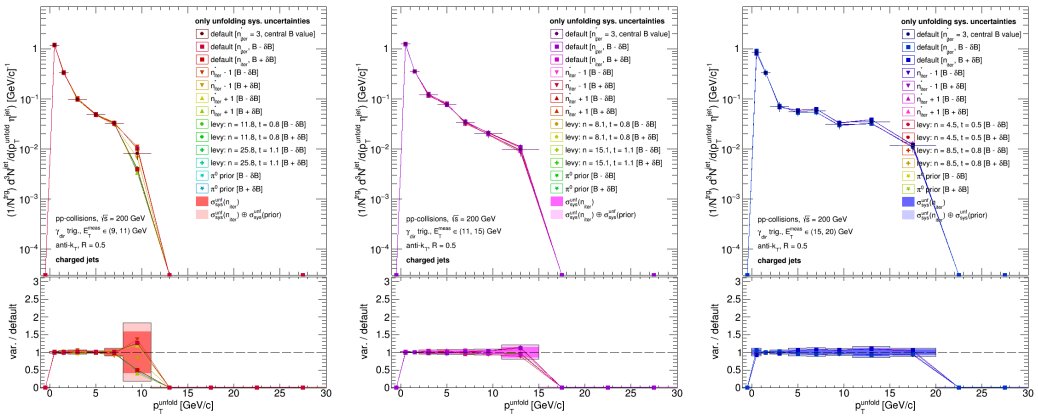

(a) 9 - 11 GeV (b) 11 - 15 GeV (c) 15 - 20 GeV

Figure D.4: Unfolding systematic variations for 9 - 11 (D.4a), 11 - 15 (D.4b), and 15 - 20 GeV (D.4c) γ_{dir}-triggered $R_{\text{jet}} = 0.5$ data. Variations visualized without uncertainties.

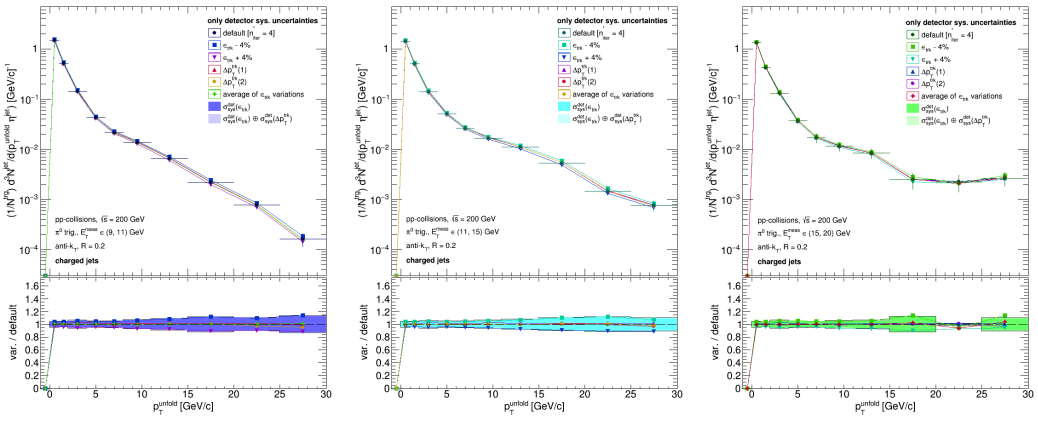

(a) 9 - 11 GeV (b) 11 - 15 GeV (c) 15 - 20 GeV

Figure D.5: Detector systematic variations for 9 - 11 (D.5a), 11 - 15 (D.5b), and 15 - 20 GeV (D.5c) π^0-triggered $R_{\text{jet}} = 0.2$ data. Variations visualized without uncertainties.

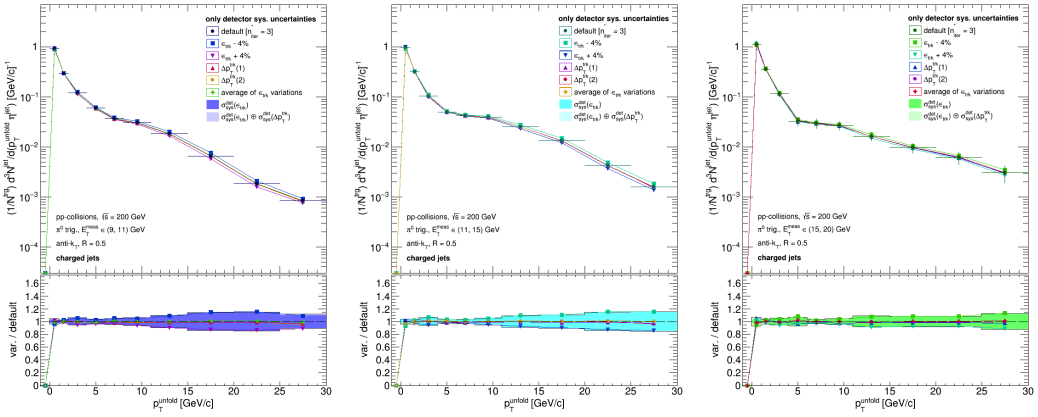

(a) 9 - 11 GeV (b) 11 - 15 GeV (c) 15 - 20 GeV

Figure D.6: Detector systematic variations for 9 - 11 (D.6a), 11 - 15 (D.6b), and 15 - 20 GeV (D.6c) π^0-triggered $R_{\text{jet}} = 0.5$ data. Variations visualized without uncertainties.

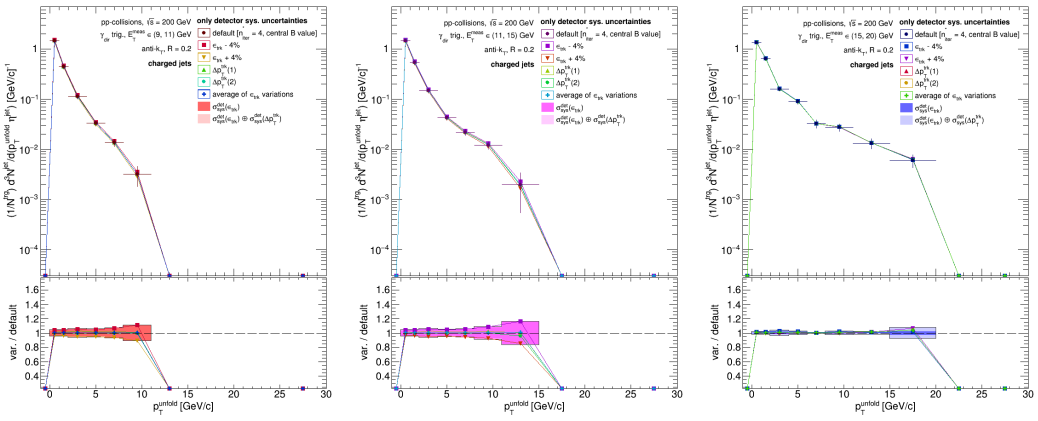

(a) 9 - 11 GeV (b) 11 - 15 GeV (c) 15 - 20 GeV

Figure D.7: Detector systematic variations for 9 - 11 (D.7a), 11 - 15 (D.7b), and 15 - 20 GeV (D.7c) γ_{dir}-triggered $R_{\text{jet}} = 0.2$ data. Variations visualized without uncertainties.

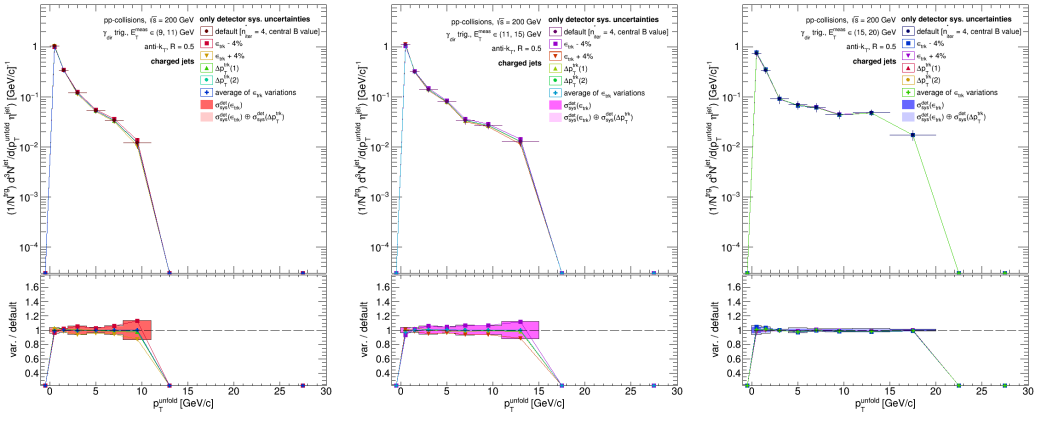

(a) 9 - 11 GeV (b) 11 - 15 GeV (c) 15 - 20 GeV

Figure D.8: Detector systematic variations for 9 - 11 (D.8a), 11 - 15 (D.8b), and 15 - 20 GeV (D.8c) γ_{dir}-triggered $R_{\text{jet}} = 0.5$ data. Variations visualized without uncertainties.

APPENDIX E

ADDITIONAL CLOSURE TESTS

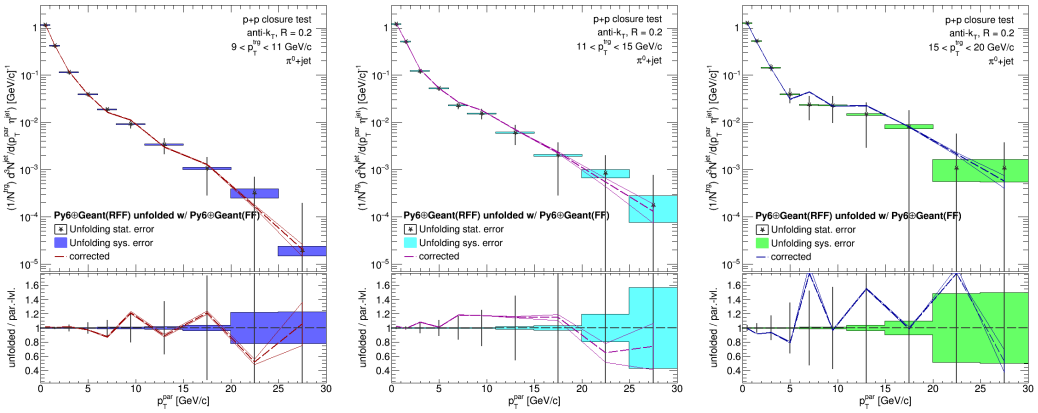

(a) 9 - 11 GeV (b) 11 - 15 GeV (c) 15 - 20 GeV

Figure E.1: $R_{\text{jet}} = 0.2$ RFF closure test for 9 - 11 (E.1a), 11 - 15 (E.1b), and 15 - 20 GeV (E.1c) π^0 triggers. See text for details.

The closure test described in section 11.3 was performed twice: once with the FF sub-sample of the Py6⊕Geant simulation serving as the validation sample and the RFF sub-sample serving as the training sample, and once with the roles reversed. The results of the closure test with reversed roles may be seen in figures E.1 and E.2. As before, the dashed lines indicate the averages for the five unfolding variations of the modified RFF detector-level and the black stars indicate the modified RFF particle-level, the solid boxes indicate the unfolding systematic uncertainty of the measured data, and the hollow bands indicate the maximum deviation of the unfolding variations from the average.

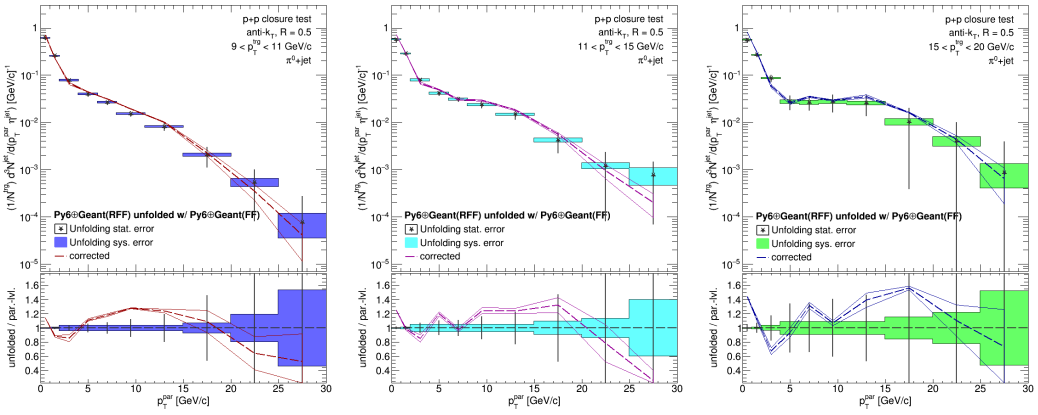

(a) 9 - 11 GeV (b) 11 - 15 GeV (c) 15 - 20 GeV

Figure E.2: $R_{\text{jet}} = 0.5$ RFF closure test for 9 - 11 (E.2a), 11 - 15 (E.2b), and 15 - 20 GeV (E.2c) π^0 triggers. See text for details.